Department of Material Sciences

THESIS

Presented by:

Boumezrag Maria Nor Elyakin

To obtain the diploma of:

DOCTORATE

Title:

Study of mechanical and physical properties Of thermoelectric materials for energy conversion.

Board of Examiners:

Mr Tibermacine Toufik	Professor	University of Biskra	President
Mr LAKEL Said	Professor	University of Biskra	Supervisor
Mme ALMI Kenza	MCA	University of Biskra	Co-Supervisor
Mr. Ibrir Miloud	Professor	University of M'sila	Examiner
Mr. Belahssen Okba	Professor	University of Biskra	Examiner

Academic Year : 2024-2025

Acknowledgements

First and foremost, I am grateful to Allah Ta'ala, whose Grace has allowed me to carry out this work and overcome every obstacle. God blessings and peace upon our Prophet Mohammed (peace and blessings of Allah be upon him), who encourages us to pursue knowledge and science.

I would like to express my sincere gratitude to my supervisor **Prof. Said Lakel** for his guidance and support. I express my deepest and heart felt gratitude to him for the valuable guidance, timely suggestions, moral support and encouragement given by him during the course of the research work.

My sincere thanks go also to my co-supervisor **Prof.AlmiKenza** for guiding me throughout achieving this work.

Besides, I owe my sincere thanks to the **Prof. Tibermacine Toufik.**, **Prof.Ibrir Miloud** and **Prof. Belahssen Okba** for their acceptance to judge this modest work.

My sincere thanks also go to my parents for their infinite patience and for providing me with an ideal working environment. This project was made possible thanks to their support.

Finally, I would like to express my deepest thanks to all the academic and administrative staff of the Physics department at MOHAMED Keider University - Biskra.

Boumezrag Maria Nor Elyakin

Contents

Contents

Contents

Contents

List of Figures

List of Figures

List of Figures

List of Figures

List of Figures

List of Tables

List of Tables

List of Tables

Table IV.10. The calculated bulk modulus (B), shear modulus (G), Pugh's ratio (G/B), Young's modulus (E), Poisson's ratio, longitudinal (V_l), shear (V_t), average (V_m) elastic wave velocities and Debye temperature (θ_D) of CuO in monoclinic phase.

Table IV.11. The maximum and minimum values of Young's modulus (E, in GPa), linear compressibility (β, in TPa^{-1}), shear modulus (G, in GPa) and Poisson's ratio (ν) of monoclinic CuO.

General introduction

In recent years, there has been significant progress in developing technologies aimed at enhancing the efficiency of renewable energy systems, particularly in areas such as thermal power plants and solar energy generation. A substantial portion of energy produced in these systems is lost as waste heat, which leads to reduced overall efficiency and output [1]. This realization has prompted scientific research to focus on harnessing waste heat through the utilization of thermal energy [2], opening up new avenues for applications such as thermoelectric cooling [3], thermoelectric generator [4], and automotive power generation [5]. Thermoelectric materials play a crucial role in this energy conversion process, as they can effectively transform temperature differences into electrical energy, leveraging the Seebeck effect and Peltier effect [6].

Traditionally, materials such as bismuth telluride (BiTe) and lead telluride (PbTe) have been employed in thermoelectric applications [7]. However, their high production costs and the environmental toxicity associated with lead have led researchers to seek alternative materials that are less harmful and more cost-effective. Transition metal oxides, particularly copper oxide (CuO), have emerged as promising candidates [8]. CuO, characterized by its monoclinic crystal structure and p-type semiconductor behavior, possesses a band gap of approximately 1.2 eV [9].

developing high-quality materials and mastering their properties pose significant challenges in the field of materials science. In this context, our research is primarily focused on the properties of copper oxide (CuO) thin films. We aim to elucidate the experimental factors that must be considered during sample handling and preparation, tailored to meet the specific requirements dictated by various applications. We begin by examining the influence of precursor materials on film quality, as the choice of materials can significantly impact the crystallinity and overall performance of the thin films. Subsequently, we explore the effect of doping with alkali metals, specifically lithium (Li) [10], sodium (Na), and potassium (K) [11], on the thermoelectric properties of CuO. potentially leading to improved thermoelectric efficiency.

Our goal is to discuss the potential of CuO as an effective thermoelectric material for waste energy recovery, emphasizing its viability for future applications in energy conversion technologies.

This thesis is organized into four chapters:

Chapter One: presents a comprehensive literature survey on copper oxide (CuO) thin films, outlining their various properties and applications.

Chapter Two: focuses on the experimental details related to the deposition of CuO films and the characterization techniques employed in this research, with particular emphasis on the methods utilized throughout the study.

Chapter Three: investigates the influence of solvent choice, number of layers, and annealing temperature on the properties of CuO thin films.

Chapter Four: is dedicated to presenting and discussing the results obtained from alkali-doped CuO thin films, specifically those doped with lithium (Li), sodium (Na), and potassium (K) at concentrations of 3%, 6%, 9%, and 12%. This chapter covers the structural, optical, and electrical properties of the doped films.

Finally, the dissertation concludes with a section that summarizes the key findings and highlights potential directions for future research.

References

[1]   G. J. Snyder and E. S. Toberer, "Complex thermoelectric materials," *Nature materials,* vol. 7, pp. 105-114, 2008.

[2]   I. Dincer and M. Rosen, "Thermal Energy Storage and," *Thermal Energy Storage: Systems and Applications,* p. 235, 2002.

[3]   J. Mao, G. Chen, and Z. Ren, "Thermoelectric cooling materials," *Nature Materials,* vol. 20, pp. 454-461, 2021.

[4]   Y. Lyu, A. Siddique, S. H. Majid, M. Biglarbegian, S. Gadsden, and S. Mahmud, "Electric vehicle battery thermal management system with thermoelectric cooling," *Energy Reports,* vol. 5, pp. 822-827, 2019.

[5]   J. Yang and T. Caillat, "Thermoelectric materials for space and automotive power generation," *MRS bulletin,* vol. 31, pp. 224-229, 2006.

[6]   I. Petsagkourakis, K. Tybrandt, X. Crispin, I. Ohkubo, N. Satoh, and T. Mori, "Thermoelectric materials and applications for energy harvesting power generation," *Science and technology of advanced materials,* vol. 19, pp. 836-862, 2018.

[7]   T. Tavrina, E. Rogacheva, and V. Pinegin, "Structural, thermoelectric and galvanomagnetic properties of PbTe-BiTe semiconductor solid solutions," *Mold. J. Phys. Sci,* vol. 4, pp. 430-434, 2005.

[8]   N. Silva, S. Ramírez, I. Díaz, A. Garcia, and N. Hassan, "Easy, quick, and reproducible sonochemical synthesis of CuO nanoparticles," *Materials,* vol. 12, p. 804, 2019.

[9]   B. Balamurugan and B. Mehta, "Optical and structural properties of nanocrystalline copper oxide thin films prepared by activated reactive evaporation," *Thin solid films,* vol. 396, pp. 90-96, 2001.

[10]   P. Chand, A. Gaur, A. Kumar, and U. K. Gaur, "Structural and optical study of Li doped CuO thin films on Si (1 0 0) substrate deposited by pulsed laser deposition," *Applied surface science,* vol. 307, pp. 280-286, 2014.

[11]   H. Siddiqui, M. R. Parra, M. Qureshi, M. Malik, and F. Z. Haque, "Studies of structural, optical, and electrical properties associated with defects in sodium-doped copper oxide (CuO/Na) nanostructures," *Journal of materials science,* vol. 53, pp. 8826-8843, 2018.

Chapter I

*Review of thin films,
Copper Oxide properties
and their applications.*

I.1. Introduction

This review focuses on the properties of CuO thin films, aiming to outline the key experimental factors necessary for careful sample handling and preparation tailored to specific applications. It begins by discussing the influence of preparation materials and methods, guiding through to the completion of form-ready samples. Additionally, the review highlights the potential of CuO as a promising material for future applications, particularly in energy conversion technologies, as demonstrated by various researchers' findings.

I.2. Cupric oxide

Copper naturally forms two oxides: cuprous oxide (Cu_2O) and cupric oxide (CuO). Both are semiconductors, with Cu_2O having a band gap of 2.0 eV and CuO a band gap of 1.2 eV, making them suitable for various applications [1]. These band gaps are ideal for photovoltaic devices, including solar cells and water-splitting devices for hydrogen production [2,3]. Additionally, they are promising materials optoelectronic devices [4].

Table I.1. Different properties of CuO.

Cupric Oxide CuO	
Chemical names	Copper (II) oxide Cupric oxide Copper monoxide Copper oxide (CuO)
Mineral	tenorite
Molecular Formula	CuO
Appearance	Black powder
Solubility in water	Insoluble
Molecular Mass	79.55 g / mol
Density	ρ= 6.32 g / cm3
Relative permittivity	12
Melting point	1134 °C
Boiling point	2000 °C

I.3. Properties of cupric oxide thin films

I.3.1. Structural properties

It has noteworthy that CuO can be found mainly in monoclinic structures, with a crystallographic space group for the unit cell of C2/c [5]. on the monoclinic crystal structure, CuO has a coordination geometry. where the copper atom is coordinated with four coplanar oxygen atoms situated at the corners of a rectangular parallelogram, which form chains by sharing edges. Similarly, each oxygen atom is coordinated by four copper atoms situated at the corners of a distorted tetrahedron. **Figure I.1**. demonstrates the crystal structure of CuO.
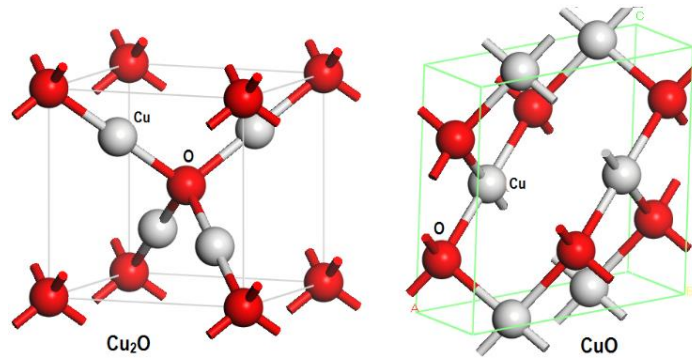
Figure I.1. crystal structure of CuO and Cu_2O.

Table I.2. Crystallographic properties of CuO.

CuO	
Unit Cell	Monoclinic a =4.6837 Å b =3.4226 Å c =5.1288 Å β =99.54° α =γ=99.54°
Shortest inter-atomic distance	
Cu-O	1.95 Å
O-O	2.62 Å
Cu-Cu	2.90 Å
Cell volume	81.08 Å^3
Cell content	4 [CuO]

In order to describe copper oxide, monoclinic indices can be used based on a three-coordinate system with indices (hkl). where, the three main reflections from the XRD spectrum of copper oxide using the three coordinate systems (hkl) are the (100), (101), and the (002) planes.

It is well argued that thin film growth is strongly related to the deposition conditions and the used method. Among them oxygen partial pressure, annealing time and the deposition temperature which are main parameters that should be controlled to achieve high film quality.

As a matter of fact, Temperature significantly impacts the structural properties of copper oxide films, influencing their optical, electrical, and morphological characteristics. Numerous studies have shown that as the temperature rises from room temperature to higher levels, the phases of these films undergo transformations. When Cu_2O thin films are annealed, molecular vibrations increase, and lattice oscillations lead to the breaking of weaker bonds, resulting in a transition to the more stable CuO crystal structure. This structural stability arises due to the enhanced bond strength in CuO [6, 7]. Thus, higher temperatures cause substantial oxidation of pure copper in air, as demonstrated in (Equation I.1). Further temperature increases lead to additional oxidation of copper nanoparticles, as illustrated in (Equation I.2) [8].

$$4Cu + O_2 \quad \longrightarrow 2Cu_2O \tag{I.1}$$

$$2Cu_2O + O2 \quad \longrightarrow 4 \, CuO \tag{I.2}$$
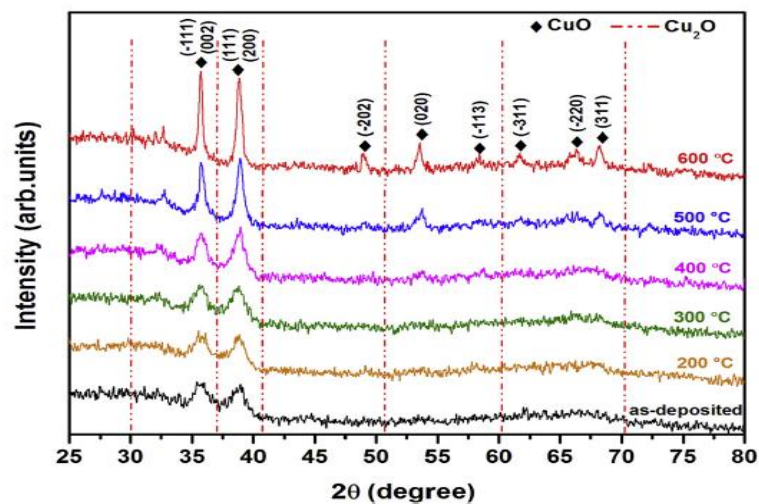
Figure I.2. XRD patterns of copper oxide thin films deposited on glass substrates by spin-coating and annealed at various temperatures [9].

where A. Loubaba. et al demonstrated that CuO NPs were synthesized by sol-gel combustion method. X-ray diffraction measurements revealed that the crystallite size, lattice parameters and crystallinity of CuO nanoparticles have enhanced with the elevation in annealing temperature. and that intensity of crystalline peaks increases with the increase in temperature. Further, it can also be seen that the major peaks (002) and (111) located at 2θ values [10]. The table below provides illustration of impact of the annealing temperature on the structural properties of copper oxide deposited by different techniques.

Noteworthiness, Raman spectrometry was used to analyze the phase of the material prepared. The copper (II) oxide phase crystallizes in a tenorite structure (monoclinic crystal system), which is represented by symmetry group C2/c C_{2h}^6 n∘15. Its Bravais space cell is composed of two-unit formulas; Cu atoms occupy C_i symmetry sites, and O atoms are placed in C_2 symmetry sites [11, 12]. The metal cation copper forms four coplanar bonds with oxygen, which again self-coordinated by four copper atoms, forming two sets of chains directed along (110) direction [12, 13]. The factor group analysis yields [14]:

Cu: Γ = 3 Au + 3Bu.

O: Γ= Ag + 2Bg + Au + 2Bu.

This crystal has 12 degrees of freedom with the following irreducible representation:

$4A_u + 5B_u + A_g + 2B_g$.

3 acoustic modes: $A_u + 2B_u$.

3 Raman activity modes: $(A_g + 2B_g)$.

6 IR activity modes $(3A_u + 3B_u)$. three well know peaks of copper oxide (296, 346, 632) cm^{-1} they are assigned to A_g and $2B_g$ CuO phonon peaks [9]

Cu_2O crystallizes in a cuprite structure (cubic crystal system), represented by symmetry group Pn3m(O_h^4) n∘ 224. Its Bravais space cell is composed of two-unit formulas, with Cu atoms occupying D_{3d} symmetry sites while O atoms are placed in T_d symmetry sites. This crystal has 18 degrees of freedom represented by the following irreducible representation [15]

Cu_2O: $A_{2u} + 3T_{1u} + E_u + T_{2u} + T_{2g}$.

Acoustic modes: T_{1u}.

Raman active modes: T_{2g}.

Infrared (IR) active modes: T_{1u}.

Silent modes: $A_{2u}+E_u + T_{2u}$.

B.Balamurugan et al. studied raman spectra of Cu_2O, they reported two relatively strong peaks at 570 cm^{-1} and 618 cm^{-1}. These correspond to the Cu2O phase [16].fig.6 shows Raman spectra of CuO nanostructures at different annealing temperatures.
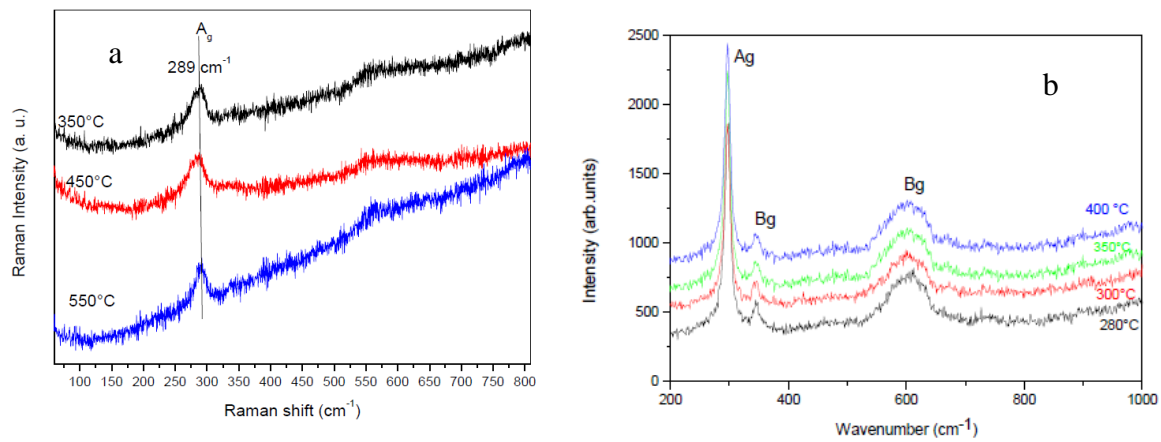
Figure.I.3. Raman spectra of CuO thin films at different annealing temperatures : a [17],b [18]

Table I.3. summary on the effect of the annealing temperature on the structural properties of the copper oxide thin films.

Method	Temperature	Structure	Size(nm)	(hkl) plan	Ref
Sol gel (Nebulizer spray Pyrolysis)	250 °C 280 °C 310 °C 320 °C	Cu_2O Cu_2O Cu_2O CuO	20 25 22 33	(111) (111) (−111) (111) (−111) (111) (−202) (−113) (−220).	[19]
a remote plasma sputtering	As deposited 250°C 350°C 450 °C	CuO thin films have a monoclinic structure	13 14.3 14.8 14.8	(−111) (002) /(111) (−111) (002) /(111) (−111) (002) /(111) (−111) (002) /(111)	[20]

	as-deposited 200 °C 300°C 400°C	Cu₂O Cu₂O decrease of Cu₂O and increasing in CuO CuO	increase	(111) CuO/ (200) Cu₂O (111) CuO/ (200) Cu₂O (111) CuO/ (200) Cu₂O (111) (020) (113)/(220) (222)	[15]
continuous current electrodepo--sition					
Sol gel (spin coating)	350 °C 450°C 550°C	CuO CuO CuO	19.99 27.06 31.47	$(\bar{1}10)$ (002) (111)	[21]
heat treatment approach	500°C 600°C 700°C 800°C	CuO monoclinic phase	9 14 18 23	(110) (002) (111) $(\bar{1}12)$ $(\bar{2}02)$ (020) (202) $(\bar{1}13)$ (022) $(\bar{3}11)$ (113) (311) (004)	[22]
SILAR	As grown 200 °C 300°C 400°C	CuO thin films have a monoclinic structure.	11.09 12.05 13.86 14.88	(110) $(\bar{1}11)$ (200) $(\bar{2}02)$ (202) $(\bar{1}13)$ (110) $(\bar{1}11)$ (200) $(\bar{2}02)$ (202) $(\bar{1}13)$ (300) (020) (220)	[23]

From this table, it is evident that temperature significantly influences the structural properties of copper oxide films. Numerous studies have shown that as temperature increases from room temperature to higher levels, the film phases shift from Cu_2O to a pure CuO thin film with a monoclinic structure. Pure Cu_2O thin films typically form at lower temperatures (around 200 °C), while pure CuO films require higher temperatures, generally between 300 and 500 °C. The formation of the Cu_4O_3 phase mixed with other CuO compounds is rare.

In other conditions, the annealing duration at a specific temperature greatly influences the structural properties of copper oxide thin films. Prolonged annealing allows for more thorough oxidation and diffusion, resulting in a more stable and crystalline CuO structure. This process enhances phase purity and reduces defects, which in turn impacts the film's optical, electrical, and morphological properties. Additionally, extended annealing promotes grain growth and improves crystalline orientation. Singh et al. observed this structural change by adjusting the deposition time. They found that CuO thin films deposited with a 10-minute

deposition time were initially amorphous, but as the spray time increased, the films transitioned to a polycrystalline structure with enhanced crystallinity [24].

Under other circumstances. in a study by M. Umar et al., copper oxide thin films were grown on silicon substrates using radio frequency magnetron sputtering in an oxygen-argon environment at two different oxygen partial pressures (15% and 23%). The research explored the effect of varying oxygen pressure on film growth and the impact of vacuum annealing to promote the formation of pure-phase cuprous oxide (Cu_2O) Figure.I.5. The results showed that lower oxygen pressure favors the formation of Cu_2O, while higher oxygen pressure leads to the conversion of CuO to Cu_2O upon annealing above 350°C due to the limited availability of oxygen during deposition [5].
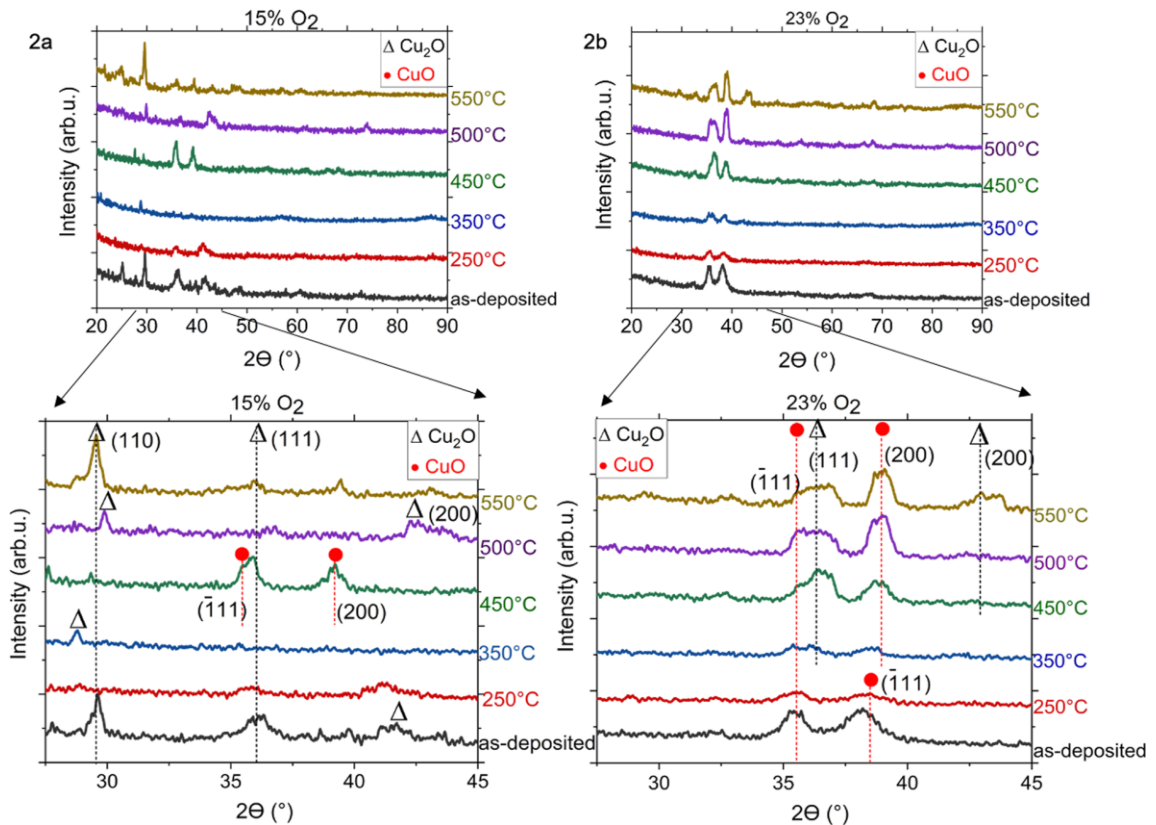
Figure. I.4. Stacked XRD patterns of thin films prepared on Si substrates by RF-magnetron sputtering at 15% (panel 2a) and 23% (panel 2b) O2 partial pressure. The bottom panels offer a magnified view of the top panels, in the region 27-45°. Triangles and circles indicate peaks attributed to Cu_2O or CuO, respectively, and the dashed lines highlight their evolution. Annealing temperature of each sample is indicated on the right side [5].

within this framework. Ooi et al. investigated the impact of oxygen percentage on the structural properties of CuO thin films and identified three distinct phases of copper oxide: Cu_2O, Cu_4O_3, and CuO. The formation of these phases was heavily influenced by the oxygen content. At lower oxygen percentages, pure Cu_2O thin films with a cubic structure were obtained, whereas at higher oxygen percentages, pure CuO thin films with a monoclinic structure were formed. These results suggest that higher temperature, oxygen partial pressure, and annealing time significantly enhance the oxidation kinetics of pure copper [25].

In another study examining the factors affecting structural properties, researchers found that solvents significantly influence these characteristics. Variations in solvent evaporation rates impact the drying and crystallization process: fast-evaporating solvents tend to cause rapid nucleation, resulting in finer grain structures, whereas slower-evaporating solvents allow for extended particle arrangement, promoting larger grain growth and greater crystallinity. This effect was demonstrated by Foo et al., who observed an increased preferred orientation in the (002) plane, associated with solvents with higher boiling points [26].

Additionally, the polarity of the solvent and its interaction with the solute play a crucial role in particle formation. Solvents with high solvating abilities enhance precursor dispersion, which leads to smaller particle sizes and improved crystallinity, as shown by Leekumjorn et al., who confirmed that strong solvent-solute interactions contribute to a finer and more uniform crystalline structure [27].

I.4.2. Electrical properties

As-grown CuO thin films have consistently been found to exhibit p-type conductivity. The electrical conductivity and hole density of CuO films are influenced by the density of copper vacancies, which act as shallow acceptors [28]. These copper vacancies are particularly prominent in non-stoichiometric cupric oxide due to the volatility of copper during the formation of the material [29-31]. It is well established that copper vacancies generate shallow acceptor states just above the valence band of CuO, which is a key factor in inducing p-type behavior [32, 33]. This means that when a copper atom is missing from the lattice, it creates a "hole" or a vacancy that can accept electrons, leading to a surplus of positively charged carriers (holes), which is characteristic of p-type semiconductors.

Copper vacancies are the most significant defects in cupric oxide, primarily because copper tends to evaporate or volatilize more easily than oxygen during the synthesis process. This volatility results in a CuO lattice that is naturally deficient in copper, thereby creating these vacancies, which in turn play a crucial role in the material's electrical properties.

To better understand how different deposition conditions affect the electrical properties of CuO thin films, several experimental studies have been conducted. These studies reveal that the resistivity of CuO films depends on the method of preparation. For instance, films prepared via thermal deposition typically have resistivities in the range of 10^2 to 10^4 $\Omega \cdot$cm, while those produced by electrochemical deposition tend to exhibit higher resistivities, in the range of 10^4 to 10^6 Ω. cm.

In terms of the charge carrier mobility and concentration, experimental measurements indicate that the hole mobility in these films can vary between 10 and 100 cm²/V·s, and the free carrier concentration can range from 10^{10} to 10^{16} cm^{-3}[34]. These variations are influenced by both the deposition technique and the specific conditions under which the films are prepared, such as temperature, pressure, and electrolyte composition during deposition.

The following table summarizes some experimental results related to the electrical properties of CuO thin films deposited using different methods. These results provide a comprehensive overview of how the deposition process affects the performance of CuO films in electronic applications.

Table I.4. Electrical proprieties of CuO thin films deposited by various deposition method.

Method	Parameters	Conductivity/ Resistivity	Other electrical properties	ref
Sol gel Nebulizer spray pyrolysis	**Temperatures** 250 °C 280 °C 310 °C 320 °C	**Conductivity** 4.26×10^{-4} 8.66×10^{-4} 1.66×10^{-3} 2.66×10^{-3}	**Mobility (cm ^{2} /Vs):** 0.41, 0.55, 0.61,1 **Carrier concentration (cm$^{-3}\times10^{-15}$):** 6.35, 9.67, 10.89, 13.53	[19]
Remote Plasma Sputtering	**Temperatures** As deposited 250°C 350°C 450 °C		**carrier concentration (cm$^{-3}\times10^{-15}$):** decrease from 42 to 5.3 **mobility (cm ^{2} /vs):** increase from 0.8 to 2.3 with increasing of the temperatures	[20]

SILAR	**Temperatures** As deposited 100°C 300°C 500 °C	**Resistivity** 6.12×10^4 7.44×10^3 8.23×10^3 5.11×10^2	**Mobility (cm ^{2} /Vs):** 4.2, 9.42, 20,25, 31.87	[35]
Spray pyrolysis Technique	**Molarity** 0.05 0.10 0.15	**Conductivity** 17.25 14.69 19.24	**Hall coefficient R_H** (10^2 cm^3/C°): 1.69 9.51 34.25	[36]
Spray pyrolysis Technique	**Thickness** 970 1730 1950 2270 2900	**Resistivity** 94.26 65.37 43.41 8.51 24.7	**Mobility (cm ^{2} /Vs):** 2.19, 14.67, 22.44, 54.56, 34.13	[37]
Reactive RF sputtering	**Oxygen percentage (%)** 10 20 30 40 50	**Resistivity** 0.001×10^3 0.130×10^3 0.700×10^3 1×10^3 2.5×10^3		[25]
Spray pyrolysis Technique	**Precursor** Copper chloride Copper acetate	**Conductivity** 3.46 10-3 1.46 10-4	**Free carrier concentration (cm^{-3}):** 7.73×10^{17} 9.37×10^{13}	[38]

As observed in the table above, the molarity of the precursor solution plays a critical role in shaping the properties of CuO thin films. Studies indicate that increasing the molarity leads to larger grain sizes, which reduces grain boundary scattering. This reduction in scattering facilitates greater mobility of charge carriers, thereby improving electrical conductivity. As a result, films produced with higher molarity tend to have lower resistivity. Additionally, higher molarity has been shown to enhance carrier concentration, further contributing to the improved conductivity of the films [36].

Annealing temperature also significantly impacts the properties of CuO thin films. Increasing the annealing temperature results in larger crystallites, which minimizes the effect of grain boundaries. These boundaries can trap free carriers, so reducing their number extends carrier lifetimes and decreases resistance. Valladares L. et al. reported that for CuO films

prepared by thermal oxidation, the resistivity dropped from 4.2×10^{-2} $\Omega \cdot cm$ at 150°C to 1.8×10^{-11} $\Omega \cdot cm$ when the annealing temperature was raised to 1000°C [39]. This enhancement in conductivity is attributed to the increase in free carriers, which is believed to be caused by copper atoms occupying interstitial positions and the creation of oxygen vacancies.

The thickness of CuO films is another important factor affecting their electrical properties. Thicker films typically have larger grain sizes, which results in fewer grain boundaries. Since grain boundaries can act as traps for free carriers and impede their transport, reducing their density by increasing the grain size improves carrier mobility and enhances conductivity. This results in a decrease in resistivity, mainly due to the increased carrier density and mobility associated with larger grains. This trend is supported by the findings of Shariffudin S.S. et al. [40]. However, if the grain size decreases further or if other discontinuities are introduced into the film, it can lead to increased scattering of carriers, which would cause an increase in resistance.
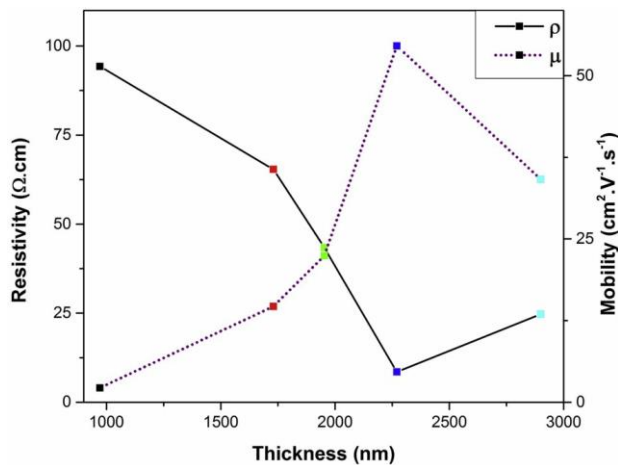
Figure. I. 5. The variation of the resistivity (ρ) and Hall mobility (μ) as a function of CuO thin film thickness [37].
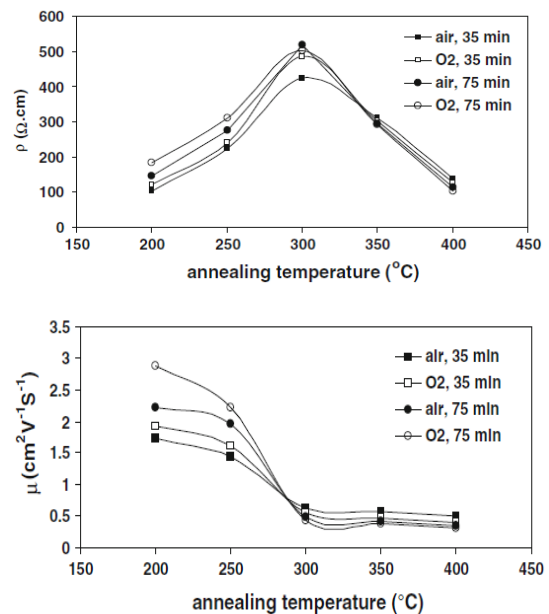
Figure I.6. Variation in Resistivity and Hall mobility of the samples produced at different annealing times and in different environments as a function of annealing temperature [41]

I.3.3. Optical properties

Copper oxide (CuO) thin films have unique optical properties, with strong absorption across the visible spectrum, giving them a characteristic black appearance [42]. These films typically exhibit around 20% transmittance in the visible region, which can increase up to 90% at higher wavelengths due to the material's refractive index, which ranges from 2 to 2.5[40].

CuO is a direct bandgap semiconductor, with a bandgap ranging from 1.3 to 3.7 eV at room temperature, depending on the deposition and preparation conditions [43]. This bandgap energy enables electron excitation from the valence band (VB) to the conduction band (CB). The band structure of CuO, influenced by its crystallographic properties and the electronic configurations of copper and oxygen, determines this energy range.

Various studies have explored luminescence in CuO to identify defect states, which contribute to different recombination levels. Luminescence is the process by which the material returns to energy equilibrium after excitation through photoluminescence (light wave) or cathodoluminescence (electron bombardment) at energies equal to or greater than the bandgap. This excitation creates an electron-hole pair, known as an exciton, which can interact with different impurities or defects, including copper and oxygen vacancies or interstitials, as well as antisite defects [44].

CuO thin films display distinct emission peaks in the visible and UV regions due to these defects. Specific studies have linked emission peaks to various defect states: Chand et al. reported band edge emissions at 371, 349, and 369 nm [45], while others have attributed UV emissions to excitonic transitions and defect-related recombination. For instance, Saravanan et al. observed that increasing the annealing temperature improved transmittance in undoped CuO films prepared by spray pyrolysis[46].

Additionally, deposition parameters like precursor concentration and film thickness impact CuO's optical transmittance and bandgap. Chafi et al. found that increasing precursor molarity decreased transmittance, likely due to the resulting increase in film thickness, which reduces light penetration[47]. Similarly, Akaltun et al. noted that thicker films displayed a reduced bandgap, observing a decrease from 2.03 eV to 1.79 eV as thickness increased from 120 to 310 nm[48].
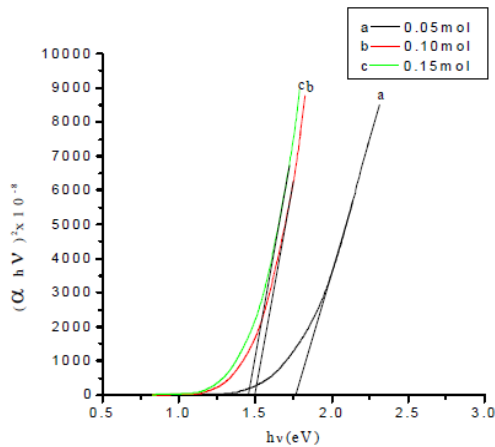
Figure. I.7. Variation of $(\alpha h\nu)^2$ as the incident photon energy (hν) of CuO films at different molar concentrations[49].
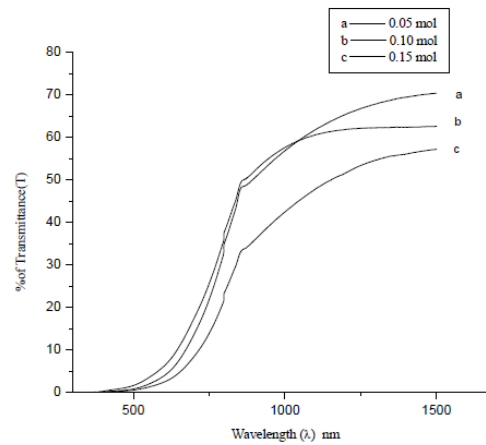
Figure. I.8. Optical transmittance spectra of CuO at different molar concentrations[49].

Substrate temperature also affects the optical bandgap **figure I. 7** Several studies [50] [51]reported that lower deposition temperatures can induce stress in the film, broadening the bandgap. For CuO films prepared on glass substrates, Gopalakrishna et al. documented a decrease in bandgap energy from 1.8 to 1.2 eV as the substrate temperature rose from 250°C to 350°C, attributing this to variations in film morphology and crystallite size [36].
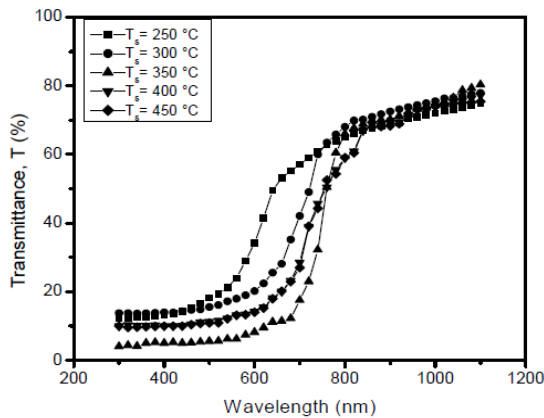
Figure. I. 9. Optical transmittance vs. wavelength of CuO thin films at various Ts [52].
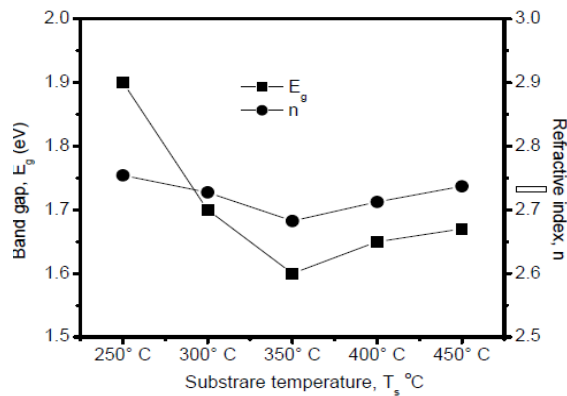
Figure. I. 10. Variation of band gap and refractive index with Ts[52].

Overall, CuO's optical properties can be finely tuned through careful control of deposition parameters, allowing researchers to optimize these films for applications in optoelectronics and photonic devices.

I.3.4. Mechanical properties

The mechanical properties of CuO thin films, such as hardness, elastic modulus, adhesion, and fracture toughness, are influenced by various factors, including film thickness, grain size, crystallite structure, doping elements, and annealing conditions.

The hardness (HN) and elastic modulus (Er) of CuO thin films are crucial indicators of their resistance to deformation and structural integrity. Generally, these values increase with optimized crystallite and particle sizes, which is often achieved through controlled deposition parameters and doping. For instance, F. Bayansal et al. proposed using lithium (Li) doping at various concentrations to improve the mechanical and structural properties of CuO films. With increased Li doping, both hardness (HN) and elastic modulus (Er) values rose, corresponding to changes in particle and crystallite size. The Hall-Petch relationship suggests that smaller crystallite sizes, resulting in more grain boundaries, restrict dislocation movement, thereby increasing hardness. Moreover, the observed peak broadening and decreased intensity suggest fine-grain formation, further indicating that Li doping effectively enhances the mechanical strength of CuO films [53].
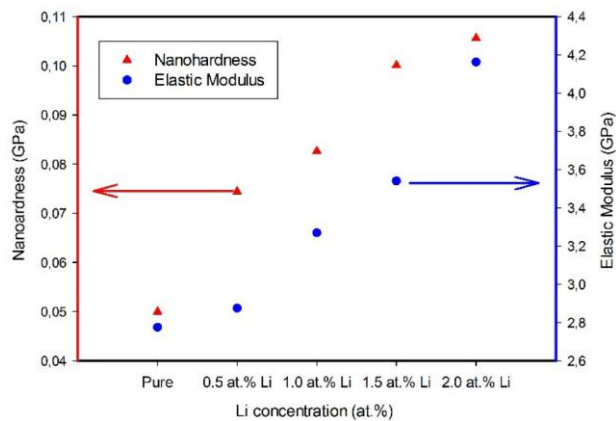
Figure. I. 11. Nanohardness and Elastic Modulus variation of CuO films as a function of Li concentration.
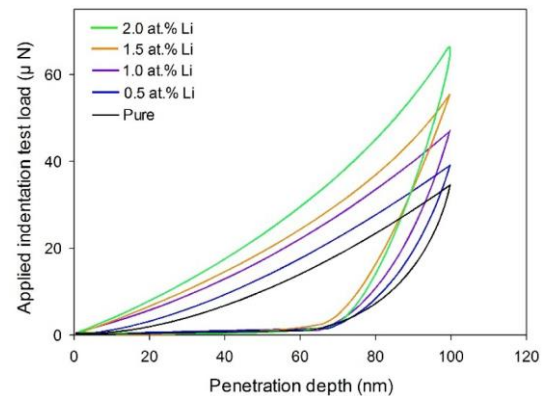
Figure I. 12. Applied indentation test load versus penetration depth curves of CuO films, as a function of Li concentration.

Within the contact, G.D. Sim reported that increasing the temperature significantly reduced the elastic modulus of copper thin films with a columnar structure. This reduction is partly due to grain boundary sliding, which occurs as the grain boundaries soften at higher temperatures [54].

I.4. CuO doping

From the literature, the use of extrinsic elements on CuO has been widespread. Where, the presence of impurity at the interfaces, vacancy, vacancy cluster at the grain and grain boundaries can play an important role in the behavior of the material. These defects offer a scope to tune the useful material properties in order to improve it. It is well known that interstitial oxygen Oi and free copper V_{Cu} are defined as the acceptors in CuO and that these acceptors can take the place of lattice defects and atomic impurities.

In this regard, various elements of large and small radius such as lanthanide ions (La^{3+}, Ce^{3+}, Pr^{3+}, Sm^{3+}, Nd^{3+}, Gd^{3+}, Tb^{3+}, Dy^{3+}) [55-59], transition metals (Mn^{2+}, Cd^{2+}, Zn^{2+}, Ni^{2+}, Fe^{3+}, Y^{3+}, Cr^{2+}, Pd^{2+}, Ag^+, Ti^{4+}) [60-66] post-transition metals (Al^{3+}, Ga^{3+} and In) [67, 69], semimetals (Sn^{3+}, Pb^{3+}) [70, 71], and alkali metals (Li^+, Na^+, and K^+) [72] are incorporated into CuO lattice for different applications as ferromagnetic oxide, conductivity improvements or photocatalytic properties. In this part, we review the most important studies related to the dopant effect on the performance of films.

Numerous experimental studies emphasized that the properties variation can be due to the effect of major synthesis processing parameters such as Precursor Solution, annealing temperature, and thickness of the nanomaterial

Table I.5. proprieties of doped CuO thin films

Method	Dopants	Main results	Ref
Sol-gel	0, 1, 3, 5, 7 % mol CuO/Na	Alteration from monoclinic to cubic symmetry beyond 3%; Crystallite size (nm): 31.9, 29.8, 28.3, 30.6, 33.2; Strain ($\times 10^{-3}$): 2.822, 3.624, 4.0837, 4.01, 4.013; Dislocation density ($D \times 10^{-15}$) 1.25, 2.57, 3.26, 4.01, 2.36; Band gap (eV): 1.49, 1.41.46, 1.51, 1.53; AC conductivity exhibits a general trend of increasing with the frequency of applied ac field for all the samples.	[73].
solvothe rmal	$K_\chi Cu_{1-\chi} O_{1-\delta}$ ($\chi = 0$, 0.1)	monoclinic structure; nanoparticle size: in range of 50–100 nm, 25–50 nm;	[74]

		specific capacity: 68.9 mA h g−1at 3.2 C, 162.3 mA h g−1at 3.2 C.	
spray pyrolysis-spin coating	0 at%, 0.5 at %, 2 at %, 3.5 at % and 5 at % Li/CuO		[75]
sol–gel dip-coating	0%, 1%, 2%,3%, 4%,5% wt% Ce/CuO	double-phase (CuO and Cu2O); Thickness (µm): 4.58, 4.30, 3.15, 3.19, 4.09, 3.88; Crystallite size CuO (nm) :28.82, 27.98, 48.91, 27.98, 30.72, 26.06; Transmittance: 28, 25, 37, 23, 21 and 16%; Band gap (eV): 3.50, 3.46, 3.48, 3.45, 3.26, 3.25; Urbach energy (eV): 0.07, 0.1, 0.14, 0.12, 0.21, 0.11; Dielectric constant: 1.61, 1.51, 1.23, 1.08, 1.66, 1.69; AC Conductivity (µS/m): 0.13, 0.08, 0.03, 0.07, 0.29, 0.19; Photocatalytic activity increases with an increase in cerium dopant percentage; 3 at. wt. % Ce best bactericidal effect against four bacterial strains.	[76]
the chemical reduction	0%, 3%, 5%, 7%, 9%, 15% Ni/CuO	monoclinic structure of CuO Crystallite size (nm): 20, 18, 17, 16, 15, 13;	[77]
the Successive Ionic Layer Adsorption and Reaction method	0, 0.27, 0.36, 0.37, 0.46, 0.75 at % Pb/CuO	the monoclinic crystal structure with (¯111) and (111), reflections; Average grain size (nm):9.94, 17.22, 16.21, 15.79, 13.07, 8.98; Microstrain ($\times10^{-3}$): 3.896, 2.15, 2.254, 2.297, 4.083, 5.119; band gap: 1.43, 1.80, 1.76, 1.72, 1.68, 1.65 eV; the morphology of the film surface was changed from plate-like to coral-like nanostructures with increasing Pb;	[78]
sol gel	0, 0.5, 1; 1.5, 2 mol% Sn/CuO	monoclinic CuO phase with (110), (¯111), (111), (310) and (220) reflections; Band gap: 2, 1.99, 2, 1,94, 1.97; Hall mobility:19,10.5, 7.58, 6.18, 7.14 (cm2/Vs); Resistivity: 108, 64.8, 54.7, 47.4, 77.5 (Ω.cm); Carrier concentration ($\times10^{15}$ /cm3): 3.06, 9.14, 15.1, 21.4, 10.8.	[79]

I.5. Applications of copper oxide

CuO is alluring material for applications in electronics, photonics sensing, and acoustics due to its advantages such as easy synthesis, low cost, compact size, durability, easy tenability, low power consumption, and small drift in signal over a long.

I.5.1. Gaz sensing

Gas sensors are essential in industrial processes like safety monitoring, chemical control, and environmental pollution detection, where their functionality relies on changes in electrical conductivity caused by the adsorption and desorption of target gases in the environment [80]. A typical metal oxide gas sensor consists of two primary components: a sensitive element (a metal oxide layer) where the reaction with the gaseous species occurs, and a transducer system, which converts this interaction into a measurable electrical signal [81].

Recently, CuO thin film gas sensors have been investigated for detecting a variety of compounds, including nitrogen oxides, carbon oxides, hydrogen sulfide, ammonia, and various volatile organic compounds across multiple applications, such as agriculture. These CuO thin film sensors demonstrated excellent sensitivity, selectivity, and stability—the "3-S" parameters. Additionally, they were shown to operate effectively at room temperature with long-term stability, making CuO an attractive material for gas-sensing applications, including exhaled breath analysis. Table I.6 shows a summary of the information presented in this review.

Table I.6. Summary of information on CuO-based gas sensors discussed in this paper.

Material	Target gas	Concentration (ppm)	Operating Temp. (°C)	Highest sensitivity (%)	Ref
CuO	NO	300- 500	300	40	[82]
CuO	NO_2	10- 40	75	5600	[83]
CuO	NO_2	100	180	3.25	[84]
CuO	NO_2	20	210	3.25	[85]
CuO	NO_2	1-100	R. T	80	[85]
CuO/r GO	NO_2	1-75	R. T	52.5	[86]
CuO/ CuFe$_2$O$_4$	H_2S	10-75	240	75	[87]
CuO: Pd	H_2S	1-50	80	119	[88]

CuO: Pt	H_2S	1-10	40	134	[89]
CuO/ TiO_2	CO	10	300	1400	[90]
CuO	CO	100	180	2.25	[91]
CuO/ ZnO	CO_2	400-4000	300	32.5	[92]
CuO	C_2H_5OH	100	300	9	[93]
CuO/ Li	C_2H_5OH	1000	300	2.5	[94]
CuO/ Fe	C_2H_5OH	1000	300	<1	[94]
SnO_2/ CuO	C_3H_6O	10-400	280	70	[95]
CuO/ Cr	C_3H_6O	0.4-3.2	450	3.25	[96]
(CuO- Cu_2O) ZnO/Al	$C_4H_{10}O$	100	350	200	[97]
(Al/ZnO)/CuO	NH_3	100-500	R. T	3000	[98]

Copper oxides have recently become a popular material for detecting gases. These sensors can find gases like nitrogen oxides, carbon oxides, ammonia, hydrogen sulfide, and some organic compounds, as well as measure humidity. They are used across different industries and can detect a wide range of concentrations, from very low (less than 1 part per million, or ppm) to high levels (over 1000 ppm). However, the levels required to detect some gases, like NOx and H_2S, are sometimes higher than needed for practical use.

The best way to make copper oxide thin films with precise thickness is through vacuum-based methods, but these are usually expensive. More affordable options, like sol-gel methods, are easier and great for making quick prototypes. A key advantage of CuO thin film gas sensors is their ability to work at low or room temperatures for extended periods. New research shows that both pure and modified CuO films can be created using different methods, which expands their potential for various gas detection applications.
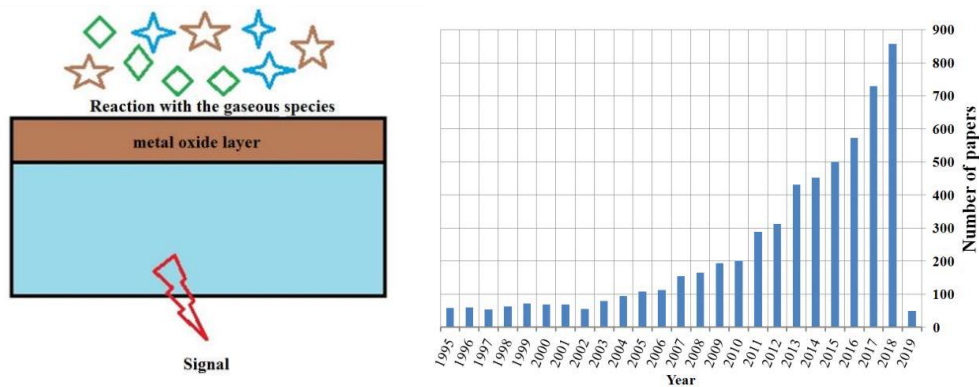
Figure I.13. Schematic of a gas sensor based on metal oxide [99]. b- the number of papers related to CuO-based gas sensors from 1995–2019 [80].

I.5.2. Photo- catalysis

In this process, an electron-hole pair is produced below the intensity of light by means of oxidation or reduction reactions taking place on the surface of the catalyst. In the presence of a photocatalyst, an organic pollutant can be oxidized directly by means of a photogenerated hole or indirectly via a reaction with characteristic reactive groups (ROS) [100] , for example, the hydroxyl radical OH and O_2, produced in solution [101]. it can be clearly that generated O_2 and OH radicals reacted with aniline pollutants and degraded them into a nontoxic product.

Accordingly, aniline was degraded into intermediate compounds such as diamidine, 4-anilino phenol, and azobenzol. After that, the benzene ring of generated intermediate products was deboned by OH radicals, and some low molecular weight compounds such as phenyl succinic acid, maleic acid, and other organic compounds were generated [102]. Lastly, the latter compounds were degraded into nontoxic products (CO_2 and H_2O).the photocatalytic activities of CuO can be modified to achieve efficient degradation of contaminants [103-104].Thus, CuO metal oxide has been proven to be an effective visible-range active photocatalyst for the photodegradation of contaminants without the addition of H_2O_2 [105].
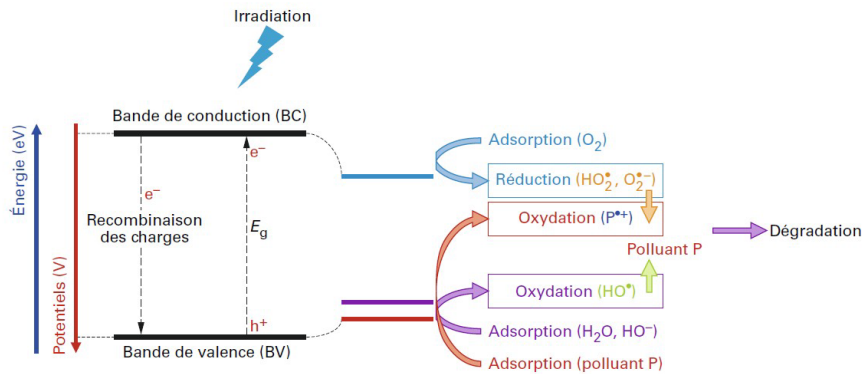
Figure I.13. Summary of the process of photocatalysis by a semiconductor according to the techniques of the engineer Guillard [106].

I.5.3. Solar cells

There are two main types of solar cells: p-n junction (conventional) and photoelectrochemical [107]. Copper Oxide is an attractive material for photovoltaic applications. It is naturally a P-type semiconductor due to negatively charged Copper vacancies with a direct band gap of approximately 2 eV, it is abundant on earth, nontoxic, and exhibits fairly high minority carrier diffusion lengths, high absorption coefficient in the visible region, and large exciton binding energy. The theoretical photoelectric conversion efficiency is 31%.

Early attempts focused on metal CuO Schottky solar cells because CuO is natively p-type and is hard to doped n-type.

little research on CuO solar cells has been published until recently, In 2012, Gao et al.

reported a p-CuO/n-Si heterojunction solar cell fabricated by the reactive magnetron sputtering technique, under AM 1.5G illumination, the current density voltage (J-V) characteristic showed a modest photovoltaic effect and an η of 0.41% was measured for a Cu/p-CuO/n-Si/Al device structure[108].

Vinay. Kumar et al. proposed that using the RF magnetron sputtering method, p-CuO/n-Si heterojunction prepared after thermal treatment at 300 C°. The solar cell with p-CuO and n-Si exhibits an open-circuit voltage of 340 mV and a short-circuit current of 1mA/cm^2 [109].

Another study by R Bhunia et al. focuses on the fabrication of Glass/Cu/Cu2O/CuO/ZnO/Al-ZnO/Ag heterojunction solar cell structure by magnetron sputtering on glass substrates[110].

there has been other work in this field reported by Masudy-Panah et al. The heterostructure studied was Al/Ti/n-Si/p-CuO/Ti/Al, the CuO heterojunction solar cell with PCE approaching 1%.

Solar cells employing this heterojunction structure demonstrated a power conversion efficiency exceeding 5.6% and an open-circuit voltage of 0.57V. where the CuO appeared a good absorber layer, they linked the higher quality factors (n>2) are connected with mechanisms like interface recombination and tunneling-enhanced interface recombination [69]

p-n heterojunction using p-CuO and n-ZnO films was fabricated in the structure ITO/n-ZnO/p-CuO/Au which showed rectification behavior with a turn-on voltage of 2.5 V and an ideality factor of 3.15[111].

Masudy-Panah et al. fabricated p-CuO(Ti)/n-Si solar cells using sputter deposition at room temperature followed by rapid thermal annealing. Their study examined the effect of titanium (Ti) doping on the photovoltaic (PV) properties of copper (I) oxide, with Ti concentrations ranging from approximately 0.049% to 0.598%. They assessed the potential of Ti doping to enhance the PV performance and conductivity of CuO devices. The CuO (Ti) thin films were analyzed using atomic force microscopy, Raman spectroscopy, X-ray diffraction (XRD), X-ray photoelectron spectroscopy (XPS), high-resolution transmission electron microscopy (HRTEM), and I-V characterization of the p-CuO(Ti)/n-Si heterojunction solar cells. The cell efficiency ranged from 0.06% to 0.39%, with the highest efficiency (0.39%) obtained at a Ti concentration of 0.099 [66].

Masudy-Panah et al. developed p-CuO/n-Si solar cells using rapid thermal annealing combined with conventional sputtering. Their study focused on how thermal treatment and working pressure during deposition influenced the photovoltaic (PV) properties of copper-oxide-based devices. The highest efficiency achieved was 1.0%, with an open-circuit voltage (Voc) of 4.9 V, short-circuit current density (JSC) of 6.4 mA/cm², and a fill factor (FF) of 32% for solar cells annealed at 300°C for 1 minute. They concluded that increasing the working pressure during deposition could enhance crystalline structure quality, improve interface properties, and reduce carrier recombination rates [112].

Table I.7. Summary of information on CuO-based Solar cells discussed in this paper.

Heterojunction	V oc (mV)	I sc (mA)	FF (%)	η (%)	Ref
CuO/Si thin films	200	0.0073	24	9.7×10^{-3}	[113]
CuO/ZnO: Sn thin films	480	1.82	0.63	0.232	[114]
CuO/C$_{60}$ thin films	0.24	0.067	0.25	2.3×10^{-4}	[115]
CuO/Cu$_2$O thin films	210	0.310	0.26	0.02	[116]

I.5.4. Thermoelectric application

Recent studies have explored innovative approaches to thermoelectric materials. Virgil Andrei, et al., [117] developed thermoelectric pastes composed of graphite, copper(I) oxide, and polychlorotrifluoroethene. Their pastes exhibited a Seebeck coefficient ranging from 10 to 600 μVK^{-1} and electrical conductivity between 10^{-4} to 102 Sm^{-1}, achieving a power factor of $5.69 \times 10^{-4} \pm 0.70 \times 10^{-4}$ $\mu Wm^{-1}K^{-2}$. This study demonstrates the practical application of these materials by successfully fabricating a flexible thermoelectric sensor, positioning thermoelectric pastes as a viable alternative to traditional methods.

In parallel, D. Hartung and colleagues investigated CuxO thin films synthesized via rf-sputter deposition, varying oxygen flux across compositions ($1 \leq x \leq 2$). They identified three crystalline phases—stable cuprous oxide (Cu2O), cupric oxide (CuO), and metastable paramelaconite (Cu$_4$O$_3$)—and analyzed their thermoelectric properties, determining that the highest ZT values at room temperature were linked to the stable phases CuO and Cu2O[118].
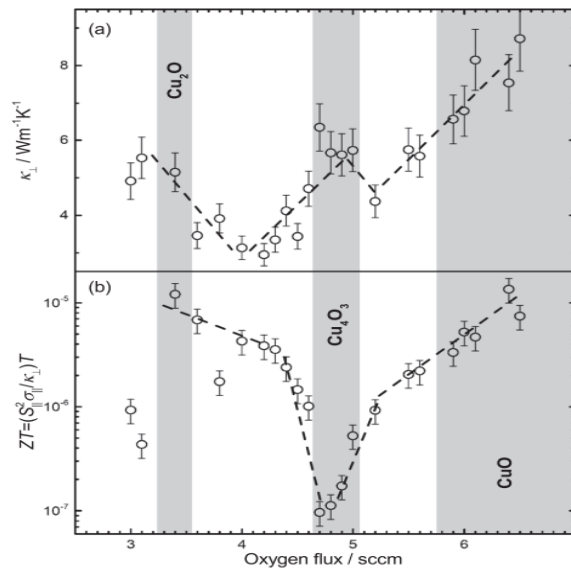
Figure I.14. Cross-plane measured thermal conductivities and (b) calculated minimum ZT with in-plane and cross-plane parameters at room temperature of Cu_xO on sapphire substrate against variation of oxygen flux during the sputtering process. The grey regions denote the main phase regions and the dashed lines are a guide to the eye.

Reference

[1]   G. Filipič and U. Cvelbar, "Copper oxide nanowires: a review of growth," *Nanotechnology,* vol. 23, p. 194001, 2012.

[2]   N. D. Hoa, N. Van Quy, H. Jung, D. Kim, H. Kim, and S.-K. Hong, "Synthesis of porous CuO nanowires and its application to hydrogen detection," *Sensors and Actuators B: Chemical,* vol. 146, pp. 266-272, 2010.

[3]   Z. Chen, T. F. Jaramillo, T. G. Deutsch, A. Kleiman-Shwarsctein, A. J. Forman, N. Gaillard, R. Garland, K. Takanabe, C. Heske, and M. Sunkara, "Accelerating materials development for photoelectrochemical hydrogen production: Standards for methods, definitions, and reporting protocols," *Journal of Materials Research,* vol. 25, pp. 3-16, 2010.

[4]   S. Saleem, A. H. Jabbar, M. H. Jameel, A. Rehman, Z. H. Kareem, A. H. Abbas, Z. Ghaffar, S. A. Razzaq, R. A. Pashameah, and E. Alzahrani, "Enhancement in structural, morphological, and optical properties of copper oxide for optoelectronic device applications," *Nanotechnology Reviews,* vol. 11, pp. 2827-2838, 2022.

[5]   M. Umar, M. Y. Swinkels, M. De Luca, C. Fasolato, L. Moser, G. Gadea, L. Marot, T. Glatzel, and I. Zardo, "Morphological and stoichiometric optimization of Cu2O thin films by deposition conditions and post-growth annealing," *Thin Solid Films,* vol. 732, p. 138763, 2021.

[6]   K. Khojier and A. Behju, "Annealing temperature effect on nanostructure and phase transition of copper oxide thin films," 2012.

[7]   L. Yuan, Y. Wang, R. Mema, and G. Zhou, "Driving force and growth mechanism for spontaneous oxide nanowire formation during the thermal oxidation of metals," *Acta Materialia,* vol. 59, pp. 2491-2500, 2011.

[8]   I. Ezenwa, "Optical analysis of chemical bath fabricated CuO thin films," *Res. J. Recent Sci,* vol. 1, pp. 46-50, 2012.

[9]   F. A. Akgul, G. Akgul, N. Yildirim, H. E. Unalan, and R. Turan, "Influence of thermal annealing on microstructural, morphological, optical properties and surface electronic structure of copper oxide thin films," *Materials Chemistry and Physics,* vol. 147, pp. 987-995, 2014.

[10]   L. Attou, B. Jaber, and H. Ez-Zahraouy, "Effect of annealing temperature on structural, optical and photocatalytic properties of CuO nanoparticles," *Mediterranean Journal of Chemistry,* vol. 7, pp. 308-316, 2018.

[11]   G. Tunell, E. Posnjak, and C. Ksanda, "Geometrical and optical properties, and crystal structure of tenorite," *Zeitschrift für Kristallographie-Crystalline Materials,* vol. 90, pp. 120-142, 1935.

[12]   S. Åsbrink and L.-J. Norrby, "A refinement of the crystal structure of copper (II) oxide with a discussion of some exceptional esd's," *Acta Crystallographica Section B: Structural Crystallography and Crystal Chemistry,* vol. 26, pp. 8-15, 1970.

[13]   D. Volanti, D. Keyson, L. Cavalcante, A. Z. Simões, M. Joya, E. Longo, J. A. Varela, P. Pizani, and A. Souza, "Synthesis and characterization of CuO flower-nanostructure processing by a domestic hydrothermal microwave," *Journal of Alloys and Compounds,* vol. 459, pp. 537-542, 2008.

[14]   G. Pezzotti, "Raman spectroscopy of piezoelectrics," *Journal of Applied Physics,* vol. 113, p. 8_1, 2013.

[15]   Y. H. Ribeiro, J. d. S. Pereira, D. G. David, and M. V. da Silva, "Growth, characterization, and photovoltaic application of copper oxide thin films," *Thin Solid Films,* vol. 757, p. 139381, 2022.

[16]   B. Balamurugan, B. Mehta, D. Avasthi, F. Singh, A. K. Arora, M. Rajalakshmi, G. Raghavan, A. Tyagi, and S. Shivaprasad, "Modifying the nanocrystalline characteristics—structure, size, and surface states of copper oxide thin films by high-energy heavy-ion irradiation," *Journal of applied physics,* vol. 92, pp. 3304-3310, 2002.

[17]   N. TOUKA, "Effect of annealing temperature on structural and optical properties of copper oxide thin films deposited by sol-gel spin coating method," 2019.

[18]   M. L. Zeggar, M. Aida, and N. Attaf, "Copper oxide thin films deposition by spray pyrolysis," *Journal of New Technology and Materials,* vol. 277, pp. 1-3, 2014.

[19]   R. D. Prabu, S. Valanarasu, V. Ganesh, M. Shkir, S. AlFaify, A. Kathalingam, S. Srikumar, and R. Chandramohan, "An effect of temperature on structural, optical, photoluminescence and electrical properties of copper oxide thin films deposited by nebulizer spray pyrolysis technique," *Materials Science in Semiconductor Processing,* vol. 74, pp. 129-135, 2018.

[20]   X. Zhang, Z. Li, and J. Fan, "An effect of rapid post-annealing temperature on the properties of cupric oxide thin films deposited by a remote plasma sputtering technique," *Materials Science in Semiconductor Processing,* vol. 137, p. 106227, 2022.

[21]   N. Touka, D. Tabli, and K. Badari, "Effect of annealing temperature on structural and optical properties of copper oxide thin films deposited by sol-gel spin coating method," *Journal of Optoelectronics and Advanced Materials,* vol. 21, pp. 698-701, 2019.

[22]   A. A. Baqer, K. A. Matori, N. M. Al-Hada, H. M. Kamari, A. H. Shaari, E. Saion, and J. L. Y. Chyi, "Copper oxide nanoparticles synthesized by a heat treatment approach with structural, morphological and optical characteristics," *Journal of Materials Science: Materials in Electronics,* vol. 29, pp. 1025-1033, 2018.

[23]   T. Çayir Taşdemirci, "Copper oxide thin films synthesized by SILAR: role of varying annealing temperature," *Electronic Materials Letters,* vol. 16, pp. 239-246, 2020.

[24]   I. Singh and R. Bedi, "Studies and correlation among the structural, electrical and gas response properties of aerosol spray deposited self assembled nanocrystalline CuO," *Applied surface science,* vol. 257, pp. 7592-7599, 2011.

[25]   P. Ooi, S. Ng, M. Abdullah, H. A. Hassan, and Z. Hassan, "Effects of oxygen percentage on the growth of copper oxide thin films by reactive radio frequency sputtering," *Materials Chemistry and Physics,* vol. 140, pp. 243-248, 2013.

[26]   K. L. Foo, M. Kashif, U. Hashim, and W.-W. Liu, "Effect of different solvents on the structural and optical properties of zinc oxide thin films for optoelectronic applications," *Ceramics International,* vol. 40, pp. 753-761, 2014.

[27]   S. Leekumjorn, S. Gullapalli, and M. S. Wong, "Understanding the solvent polarity effects on surfactant-capped nanoparticles," *The Journal of Physical Chemistry B,* vol. 116, pp. 13063-13070, 2012.

[28]   B. Meyer, A. Polity, D. Reppin, M. Becker, P. Hering, P. Klar, T. Sander, C. Reindl, J. Benz, and M. Eickhoff, "Binary copper oxide semiconductors: From materials towards devices," *physica status solidi (b),* vol. 249, pp. 1487-1509, 2012.

[29]   Y. Gong, C. Lee, and C. Yang, "Atomic force microscopy and Raman spectroscopy studies on the oxidation of Cu thin films," *Journal of Applied Physics,* vol. 77, pp. 5422-5425, 1995.

[30]   L. Huanga, S. Yanga, T. Lia, B. Gua, Y. Dua, Y. Lub, and S. Shi, "Preparation of large-scale cupric oxide nanowires by thermal evaporation," *J. Cryst. Growth,* vol. 260, pp. 130-135, 2004.

[31]   J.-H. Lee, B.-W. Yeo, and B.-O. Park, "Effects of the annealing treatment on electrical and optical properties of ZnO transparent conduction films by ultrasonic spraying pyrolysis," *Thin Solid Films,* vol. 457, pp. 333-337, 2004.

[32]   C. Luyo, I. Fábregas, L. Reyes, J. L. Solís, J. Rodríguez, W. Estrada, and R. J. Candal, "SnO2 thin-films prepared by a spray–gel pyrolysis: Influence of sol properties on film morphologies," *Thin Solid Films,* vol. 516, pp. 25-33, 2007.

[33]   S. Kose, F. Atay, V. Bilgin, and I. Akyuz, "Some physical properties of copper oxide films: The effect of substrate temperature," *Materials Chemistry and Physics,* vol. 111, pp. 351-358, 2008.

[34]   F. M. Li, R. Waddingham, W. I. Milne, A. J. Flewitt, S. Speakman, J. Dutson, S. Wakeham, and M. Thwaites, "Low temperature (< 100 C) deposited P-type cuprous oxide thin films: Importance of controlled oxygen and deposition energy," *Thin Solid Films,* vol. 520, pp. 1278-1284, 2011.

[35]   D. Ozaslan, O. Erken, M. Gunes, and C. Gumus, "The effect of annealing temperature on the physical properties of Cu2O thin film deposited by SILAR method," *Physica B: Condensed Matter,* vol. 580, p. 411922, 2020.

[36]   D. Gopalakrishna, K. Vijayalakshmi, and C. Ravidhas, "Effect of annealing on the properties of nanostructured CuO thin films for enhanced ethanol sensitivity," *Ceramics International,* vol. 39, pp. 7685-7691, 2013.

[37]   H. B. Saâd, M. Ajili, S. Dabbabi, and N. T. Kamoun, "Investigation on thickness and annealing effects on physical properties and electrical circuit model of CuO sprayed thin films," *Superlattices and Microstructures,* vol. 142, p. 106508, 2020.

[38]   M. L. Zeggar, F. Bourfaa, A. Adjimi, F. Boutbakh, M. Aida, and N. Attaf, "CuO thin films deposition by spray pyrolysis: influence of precursor solution properties," *International Journal of Mathematical, Computational, Physical, Electrical and Computer Engineering,* vol. 9, pp. 610-13, 2015.

[39]   L. D. L. S. Valladares, D. H. Salinas, A. B. Dominguez, D. A. Najarro, S. Khondaker, T. Mitrelias, C. Barnes, J. A. Aguiar, and Y. Majima, "Crystallization and electrical

resistivity of Cu2O and CuO obtained by thermal oxidation of Cu thin films on SiO2/Si substrates," *Thin solid films,* vol. 520, pp. 6368-6374, 2012.

[40]   S. Shariffudin, S. Khalid, N. Sahat, M. Sarah, and H. Hashim, "Preparation and characterization of nanostructured CuO thin films using sol-gel dip coating," in *IOP Conference Series: Materials Science and Engineering*, 2015, p. 012007.

[41]   K. Khojier, H. Savaloni, and Z. Sadeghi, "A comparative investigation on growth, nanostructure and electrical properties of copper oxide thin films as a function of annealing conditions," *Journal of Theoretical and Applied Physics,* vol. 8, pp. 1-8, 2014.

[42]   A. Ogwu, T. Darma, and E. Bouquerel, "Electrical resistivity of copper oxide thin films prepared by reactive magnetron sputtering," *Journal of achievements in materials and manufacturing engineering,* vol. 24, pp. 172-177, 2007.

[43]   M. Dhaouadi, M. Jlassi, I. Sta, I. B. Miled, G. Mousdis, M. Kompitsas, and W. Dimassi, "Physical properties of copper oxide thin films prepared by sol–gel spin–coating method," *Am. J. Phys. Appl,* vol. 6, pp. 43-50, 2018.

[44]   L. Ozawa, *Cathodoluminescence and photoluminescence: theories and practical applications* vol. 2: CRC Press, 2018.

[45]   P. Chand and P. Kumar, "Effect of precursors medium on structural, optical and dielectric properties of CuO nanostructures," *Optik,* vol. 156, pp. 743-753, 2018.

[46]   V. Saravanakannan and T. Radhakrishnan, "Structural, electrical and optical characterization of CuO thin films prepared by spray pyrolysis technique," *International Journal of ChemTech Research,* vol. 6, pp. 306-310, 2014.

[47]   R. Shabu, A. M. E. Raj, C. Sanjeeviraja, and C. Ravidhas, "Assessment of CuO thin films for its suitablity as window absorbing layer in solar cell fabrications," *Materials Research Bulletin,* vol. 68, pp. 1-8, 2015.

[48]   Y. Akaltun, "Effect of thickness on the structural and optical properties of CuO thin films grown by successive ionic layer adsorption and reaction," *Thin Solid Films,* vol. 594, pp. 30-34, 2015.

[49]   A. S. Kumar, K. Perumal, and P. Thirunavukkarasu, "Structural and optical properties of chemically sprayed CuO thin films," *Optoelec. Advan. Mater.–Rapid Commun,* vol. 4, pp. 831-833, 2010.

[50]   L. Huang, S. Yang, T. Li, B. Gu, Y. Du, Y. Lu, and S. Shi, "Preparation of large-scale cupric oxide nanowires by thermal evaporation method," *Journal of Crystal Growth,* vol. 260, pp. 130-135, 2004.

[51]   F. J. Arregui, *Sensors based on nanostructured materials* vol. 10: Springer, 2009.

[52]   S. Roy, A. Bhuiyan, and J. Podder, "Optical and electrical properties of copper oxide thin films synthesized by spray pyrolysis technique," *Sensors & Transducers,* vol. 191, p. 21, 2015.

[53]   F. Bayansal, O. Şahin, and H. Çetinkara, "Mechanical and structural properties of Li-doped CuO thin films deposited by the successive ionic layer adsorption and reaction method," *Thin Solid Films,* vol. 697, p. 137839, 2020.

[54]   G.-D. Sim, J.-H. Park, M. D. Uchic, P. A. Shade, S.-B. Lee, and J. J. Vlassak, "An apparatus for performing microtensile tests at elevated temperatures inside a scanning electron microscope," *Acta materialia,* vol. 61, pp. 7500-7510, 2013.

[55]   L. V. Devi, S. Sellaiyan, S. Sankar, and K. Sivaji, "Structural and optical investigation of combustion derived La doped copper oxide nanocrystallites," *Materials Research Express,* vol. 5, p. 024002, 2018.

[56]   I. Singh, S. Dey, S. Santra, K. Landfester, R. Muñoz-Espí, and A. Chandra, "Cerium-doped copper (II) oxide hollow nanostructures as efficient and tunable sensors for volatile organic compounds," *ACS omega,* vol. 3, pp. 5029-5037, 2018.

[57]   N. Sankar, V. Sankaranarayanan, L. Vaidhyanathan, G. Rangarajan, R. Srinivasan, K. Thomas, U. Varadaraju, and G. S. Rao, "Specific heat of praseodymium doped yttrium barium copper oxide," *Solid state communications,* vol. 67, pp. 391-395, 1988.

[58]   B. M. Abu-Zied, S. M. Bawaked, S. A. Kosa, and W. Schwieger, "Impact of Gd-, La-, Nd-and Y-doping on the textural, electrical conductivity and N2O decomposition activity of CuO catalyst," *Int. J. Electrochem. Sci,* vol. 11, pp. 2230-2246, 2016.

[59]   B. M. Abu-Zied, S. M. Bawaked, S. A. Kosa, and W. Schwieger, "Effect of some rare earth oxides doping on the morphology, crystallite size, electrical conductivity and N2O decomposition activity of CuO catalyst," *Int J Electrochem Sci,* vol. 11, pp. 1568-1580, 2016.

[60]   D. Wang, Y. Wang, T. Jiang, H. Jia, and M. Yu, "The preparation of M (M: Mn2+, Cd2+, Zn2+)-doped CuO nanostructures via the hydrothermal method and their

properties," *Journal of Materials Science: Materials in Electronics,* vol. 27, pp. 2138-2145, 2016.

[61]   C. Meneses, J. Duque, L. Vivas, and M. Knobel, "Synthesis and characterization of TM-doped CuO (TM= Fe, Ni)," *Journal of non-crystalline solids,* vol. 354, pp. 4830-4832, 2008.

[62]   S. Baig, P. Kumar, J. Ngai, Y. Li, and S. Ahmed, "Yttrium doped copper (II) oxide hole transport material as efficient thin film transistor," *ChemPhysChem,* vol. 21, pp. 895-907, 2020.

[63]   M. Ariëns, L. van de Water, A. I. Dugulan, E. Brück, and E. J. Hensen, "Copper promotion of chromium-doped iron oxide water-gas shift catalysts under industrially relevant conditions," *Journal of Catalysis,* vol. 405, pp. 391-403, 2022.

[64]   W. Wang, Z. Li, W. Zheng, J. Yang, H. Zhang, and C. Wang, "Electrospun palladium (IV)-doped copper oxide composite nanofibers for non-enzymatic glucose sensors," *Electrochemistry communications,* vol. 11, pp. 1811-1814, 2009.

[65]   H. Absike, M. Hajji, H. Labrim, A. Abbassi, and H. Ez-Zahraouy, "Electronic, electrical and optical properties of Ag doped CuO through modified Becke-Johnson exchange potential," *Superlattices and Microstructures,* vol. 127, pp. 128-138, 2019.

[66]   S. Masudy-Panah, K. Radhakrishnan, H. R. Tan, R. Yi, T. I. Wong, and G. K. Dalapati, "Titanium doped cupric oxide for photovoltaic application," *Solar Energy Materials and Solar Cells,* vol. 140, pp. 266-274, 2015.

[67]   R. M. Thyab, M. A. H. Al-Hilo, F. A. Yasseen, H. Alshater, E. G. Blall, and M. A. Abdel-Lateef, "Influence of Aluminum Doping on Structural and Optical Properties of the Nanostructured Copper Oxide Thin Films Prepared by CSP Method," *NeuroQuantology,* vol. 20, pp. 99-104, 2022.

[68]   J. H. Bae, J. H. Lee, S. P. Park, T. S. Jung, H. J. Kim, D. Kim, S.-W. Lee, K.-S. Park, S. Yoon, and I. Kang, "Gallium doping effects for improving switching performance of p-type copper (I) oxide thin-film transistors," *ACS applied materials & interfaces,* vol. 12, pp. 38350-38356, 2020.

[69]   A. Yildiz, Ş. Horzum, N. Serin, and T. Serin, "Hopping conduction in In-doped CuO thin films," *Applied Surface Science,* vol. 318, pp. 105-107, 2014.

[70]   S. Yang, Z. Liu, H. An, S. Arnouts, J. de Ruiter, F. Rollier, S. Bals, T. Altantzis, M. C. Figueiredo, and I. A. Filot, "Near-Unity Electrochemical CO2 to CO Conversion over
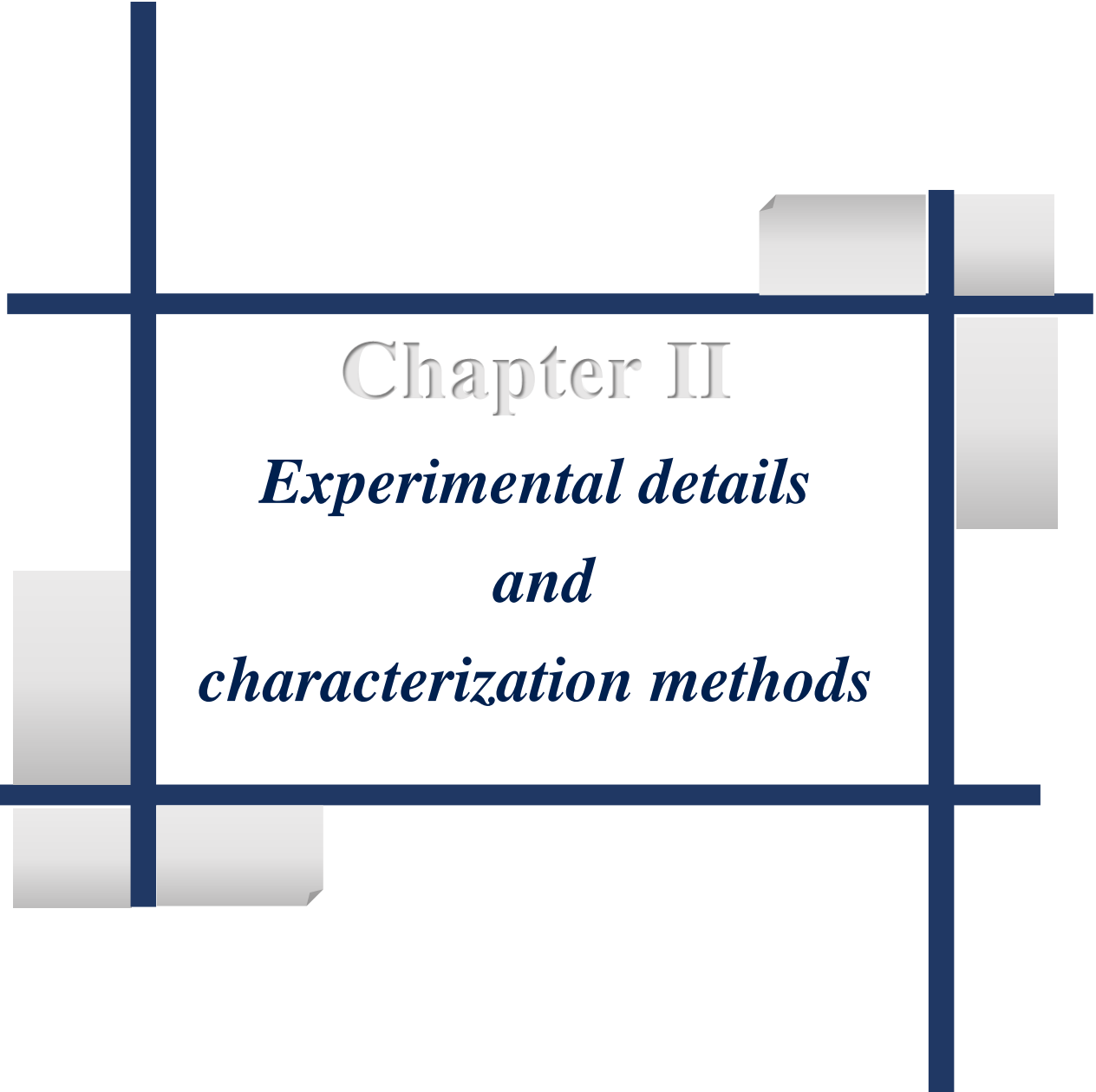
Sn-Doped Copper Oxide Nanoparticles," *ACS catalysis,* vol. 12, pp. 15146-15156, 2022.

[71]   D. Tabli, N. Touka, K. Baddari, and N. Selmi, "Pb-Doped CuO Thin Films Synthetized by Sol-Gel Method," *Advances in Materials Science,* vol. 22, pp. 5-13, 2022.

[72]   H. Siddiqui, M. Qureshi, and F. Z. Haque, "Alkali metals doped Cu0. 95X0. 05O (X= Li, Na and K) nanoparticles: Facile synthesis, structural, optical properties and solar cell application," *Materials letters,* vol. 275, p. 128090, 2020.

[73]   H. Siddiqui, M. R. Parra, M. Qureshi, M. Malik, and F. Z. Haque, "Studies of structural, optical, and electrical properties associated with defects in sodium-doped copper oxide (CuO/Na) nanostructures," *Journal of materials science,* vol. 53, pp. 8826-8843, 2018.

[74]   T. V. Thi, A. K. Rai, J. Gim, and J. Kim, "Potassium-doped copper oxide nanoparticles synthesized by a solvothermal method as an anode material for high-performance lithium ion secondary battery," *Applied surface science,* vol. 305, pp. 617-625, 2014.

[75]   C.-Y. Chiang, Y. Shin, and S. Ehrman, "Li doped CuO film electrodes for photoelectrochemical cells," *Journal of The Electrochemical Society,* vol. 159, p. B227, 2011.

[76]   Z. N. Kayani, W. Chaudhry, R. Sagheer, S. Riaz, and S. Naseem, "Effect of Ce doping on crystallite size, band gap, dielectric and antibacterial properties of photocatalyst copper oxide Nano-structured thin films," *Materials Science and Engineering: B,* vol. 283, p. 115799, 2022.

[77]   J. Eppakayala, P. Donta, J. R. Madireddy, L. Eppakayala, M. R. Mettu, and R. Golconda, "Synthesis, structural and optical properties of Ni doped CuO nanoparticles," *Materials Today: Proceedings,* 2023.

[78]   F. Bayansal, Y. Gülen, B. Şahin, S. Kahraman, and H. Çetinkara, "CuO nanostructures grown by the SILAR method: influence of Pb-doping on the morphological, structural and optical properties," *Journal of Alloys and Compounds,* vol. 619, pp. 378-382, 2015.

[79]   J. Wu, K. Hui, K. Hui, L. Li, H.-H. Chun, and Y. Cho, "Characterization of Sn-doped CuO thin films prepared by a sol–gel method," *Journal of Materials Science: Materials in Electronics,* vol. 27, pp. 1719-1724, 2016.

[80]   A. Rydosz, "The use of copper oxide thin films in gas-sensing applications," *Coatings,* vol. 8, p. 425, 2018.

[81]   D. Ju, H. Xu, Z. Qiu, J. Guo, J. Zhang, and B. Cao, "Highly sensitive and selective triethylamine-sensing properties of nanosheets directly grown on ceramic tube by forming NiO/ZnO PN heterojunction," *Sensors and Actuators B: Chemical,* vol. 200, pp. 288-296, 2014.

[82]   M. R. Mullen and P. K. Dutta, "Building selectivity for NO sensing in a NOx mixture with sonochemically prepared CuO structures," *Chemosensors,* vol. 4, p. 1, 2015.

[83]   D. N. Oosthuizen, D. E. Motaung, and H. Swart, "In depth study on the notable room-temperature NO2 gas sensor based on CuO nanoplatelets prepared by sonochemical method: Comparison of various bases," *Sensors and Actuators B: Chemical,* vol. 266, pp. 761-772, 2018.

[84]   C. Chou and W. H. Organization, *Hydrogen sulfide: human health aspects*: World Health Organization, 2003.

[85]   G. J. Dugbartey, "H2S as a possible therapeutic alternative for the treatment of hypertensive kidney injury," *Nitric Oxide,* vol. 64, pp. 52-60, 2017.

[86]   Z. Li, Y. Liu, D. Guo, J. Guo, and Y. Su, "Room-temperature synthesis of CuO/reduced graphene oxide nanohybrids for high-performance NO2 gas sensor," *Sensors and Actuators B: Chemical,* vol. 271, pp. 306-310, 2018.

[87]   X. Hu, Z. Zhu, Z. Li, L. Xie, Y. Wu, and L. Zheng, "Heterostructure of CuO microspheres modified with CuFe2O4 nanoparticles for highly sensitive H2S gas sensor," *Sensors and Actuators B: Chemical,* vol. 264, pp. 139-149, 2018.

[88]   X. Hu, Z. Zhu, C. Chen, T. Wen, X. Zhao, and L. Xie, "Highly sensitive H2S gas sensors based on Pd-doped CuO nanoflowers with low operating temperature," *Sensors and Actuators B: Chemical,* vol. 253, pp. 809-817, 2017.

[89]   Q. Tang, X.-B. Hu, M. He, L.-L. Xie, Z.-G. Zhu, and J.-Q. Wu, "Effect of platinum doping on the morphology and sensing performance for CuO-based gas sensor," *Applied Sciences,* vol. 8, p. 1091, 2018.

[90]   J.-H. Lee, J.-H. Kim, and S. S. Kim, "CuO–TiO2 p–n core–shell nanowires: Sensing mechanism and p/n sensing-type transition," *Applied Surface Science,* vol. 448, pp. 489-497, 2018.

[91]   A. Rydosz, A. Czapla, W. Maziarz, K. Zakrzewska, and A. Brudnik, "CuO and CuO/TiO2-y thin-film gas sensors of H2 and NO2," in *2018 XV International Scientific Conference on Optoelectronic and Electronic Sensors (COE)*, 2018, pp. 1-4.

[92]   N. Tanvir, O. Yurchenko, E. Laubender, and G. Urban, "Investigation of low temperature effects on work function based CO2 gas sensing of nanoparticulate CuO films," *Sensors and Actuators B: Chemical,* vol. 247, pp. 968-974, 2017.

[93]   A. Umar, J.-H. Lee, R. Kumar, O. Al-Dossary, A. A. Ibrahim, and S. Baskoutas, "Development of highly sensitive and selective ethanol sensor based on lance-shaped CuO nanostructures," *Materials & Design,* vol. 105, pp. 16-24, 2016.

[94]   Y.-H. Choi, D.-H. Kim, and S.-H. Hong, "p-Type aliovalent Li (I) or Fe (III)-doped CuO hollow spheres self-organized by cationic complex ink printing: structural and gas sensing characteristics," *Sensors and Actuators B: Chemical,* vol. 243, pp. 262-270, 2017.

[95]   B. Zhang, W. Fu, X. Meng, A. Ruan, P. Su, and H. Yang, "Synthesis of actinomorphic flower-like SnO2 nanorods decorated with CuO nanoparticles and their improved isopropanol sensing properties," *Applied Surface Science,* vol. 456, pp. 586-593, 2018.

[96]   A. Szkudlarek, K. Kollbek, S. Klejna, and A. Rydosz, "Electronic sensitization of CuO thin films by Cr-doping for enhanced gas sensor response at low detection limit," *Materials Research Express,* vol. 5, p. 126406, 2018.

[97]   M. Hoppe, N. Ababii, V. Postica, O. Lupan, O. Polonskyi, F. Schütt, S. Kaps, L. F. Sukhodub, V. Sontea, and T. Strunskus, "(CuO-Cu2O)/ZnO: Al heterojunctions for volatile organic compound detection," *Sensors and Actuators B: Chemical,* vol. 255, pp. 1362-1375, 2018.

[98]   Y. Zhao, M. Ikram, J. Zhang, K. Kan, H. Wu, W. Song, L. Li, and K. Shi, "Outstanding gas sensing performance of CuO-CNTs nanocomposite based on asymmetrical schottky junctions," *Applied Surface Science,* vol. 428, pp. 415-421, 2018.

[99]   A. Noua and R. Guemini, "Preparation and characterization of thin films nanostructures based on ZnO and other oxides," 2019.

[100]   N. Mukwakwa, "Desposition of zinc oxide thin films by spin coating and examination of their structural, electrical and optical characteristics for solar cell application," The University of Zambia, 2017.

[101]   S. Norzaee, B. Djahed, R. Khaksefidi, and F. K. Mostafapour, "Photocatalytic degradation of aniline in water using CuO nanoparticles," *Journal of Water Supply: Research and Technology—Aqua,* vol. 66, pp. 178-185, 2017.

[102]   Y. Li, F. Wang, G. Zhou, and Y. Ni, "Aniline degradation by electrocatalytic oxidation," *Chemosphere,* vol. 53, pp. 1229-1234, 2003.

[103]   R. Gusain and O. P. Khatri, "Ultrasound assisted shape regulation of CuO nanorods in ionic liquids and their use as energy efficient lubricant additives," *Journal of Materials Chemistry A,* vol. 1, pp. 5612-5619, 2013.

[104]   A. Bhaduri and K. Kajal, "Facile synthesis and characterization of cupric oxide (CuO) nanoparticles: Inexpensive and abundant candidate for light harvesting," in *AIP Conference Proceedings*, 2019.

[105]   M. R. Hoffmann, S. T. Martin, W. Choi, and D. W. Bahnemann, "Environmental applications of semiconductor photocatalysis," *Chemical reviews,* vol. 95, pp. 69-96, 1995.

[106]   C. Guillard, B. Kartheuser, and S. Lacombe, "La photocatalyse: dépollution de l'eau ou de l'air et matériaux autonettoyants," *Tech. Ing. Génie Procédés Prot. Environ,* 2011.

[107]   S. Waita, "Dye sensitized TiO2 solar cells," *Department of Physics, University of Nairobi, Kenya (PhD Thesis),* 2008.

[108]   F. Gao, X.-J. Liu, J.-S. Zhang, M.-Z. Song, and N. Li, "Photovoltaic properties of the p-CuO/n-Si heterojunction prepared through reactive magnetron sputtering," *Journal of applied physics,* vol. 111, 2012.

[109]   V. Kumar, S. Masudy-Panah, C. Tan, T. Wong, D. Chi, and G. Dalapati, "Copper oxide based low cost thin film solar cells," in *2013 IEEE 5th international nanoelectronics conference (INEC)*, 2013, pp. 443-445.

[110]   R. Bhunia, S. Dolai, R. Dey, S. Das, S. Hussain, R. Bhar, and A. Pal, "Fabrication and characterization of cu/Cu2O/CuO/ZnO/Al–ZnO/ag heterojunction solar cells," *Semiconductor Science and Technology,* vol. 33, p. 105007, 2018.

[111]   R. R. Prabhu, A. Saritha, M. Shijeesh, and M. Jayaraj, "Fabrication of p-CuO/n-ZnO heterojunction diode via sol-gel spin coating technique," *Materials Science and Engineering: B,* vol. 220, pp. 82-90, 2017.

[112]   S. Masudy-Panah, G. K. Dalapati, K. Radhakrishnan, A. Kumar, H. R. Tan, E. Naveen Kumar, C. Vijila, C. C. Tan, and D. Chi, "p-CuO/n-Si heterojunction solar cells with high open circuit voltage and photocurrent through interfacial engineering," *Progress in Photovoltaics: Research and Applications,* vol. 23, pp. 637-645, 2015.

[113] J.-P. Kim, "Electric properties and chemical bonding states of pnjunction p-CuO/n-Si by sol-gel method," *Journal of Ceramic Processing Research,* vol. 13, pp. 96-99, 2012.

[114] E. Omayio, P. Karimi, W. Njoroge, and F. Mugwanga, "Current-voltage characteristics of p-CuO/n-ZnO: Sn Solar cell," *Int. J. Thin Film Sci. Tec,* vol. 2, pp. 25-28, 2013.

[115] T. Oku, R. Motoyoshi, K. Fujimoto, T. Akiyama, B. Jeyadevan, and J. Cuya, "Structures and photovoltaic properties of copper oxides/fullerene solar cells," *Journal of Physics and Chemistry of Solids,* vol. 72, pp. 1206-1211, 2011.

[116] R. P. Wijesundera, M. Hidaka, K. Koga, J.-Y. Choi, and N. E. Sung, "Structural and electronic properties of electrodeposited heterojunction of CuO/Cu 2 O," *Ceramics-silikàty,* vol. 54, pp. 19-25, 2010.

[117] V. Andrei, K. Bethke, and K. Rademann, "Adjusting the thermoelectric properties of copper (i) oxide–graphite–polymer pastes and the applications of such flexible composites," *Physical Chemistry Chemical Physics,* vol. 18, pp. 10700-10707, 2016.

[118] D. Hartung, F. Gather, P. Hering, C. Kandzia, D. Reppin, A. Polity, B. Meyer, and P. Klar, "Assessing the thermoelectric properties of CuxO (x= 1 to 2) thin films as a function of composition," *Applied Physics Letters,* vol. 106, 2015.

Chapter II

Experimental details
and
characterization methods

II.1. Introduction

This section deal, a short discussion about several steps were involved in the preparation of the CuO thin films such as preparation of solution and substrates, deposition process, preheating, annealing process, and characterization. The steps are explained in details as below.

II.2. Sol gel process

Sol is a colloid solution containing very small particles whose size ranges from 1 nm to hundred nm. A gel is a solid, interconnected three-dimensional network with submicrometric pores and cross-linked chains having an average length larger than a micrometre.

The sol-gel method involves firstly the formation of sols through hydrolysis and condensation of inorganic or metal-organic precursors. Secondly, liquid sols undergo a series of chemical reactions and transform into solid skeletons within the liquid phase.

Metal oxides can be obtained when the liquid phase is further removed. Three approaches have been conducted to fabricate oxides through sol-gel process:

(i) gelation of colloidal particles;

(ii) hypercritical drying of gels formed through hydrolysis and condensation of alkoxide precursors;

(iii) aging and drying of gels formed through hydrolysis and condensation of alkoxide precursors;

The formation of oxide from molecular precursor via a soul-gel process generally involves four main steps:

(1) Mixing alkoxide precursors with water to initiate hydrolysis

and condensation reactions. The polymeric framework of sols can be obtained by linking metal ions through M-O-M bonds.

(2) Linking the sols together through prolonging reaction time (gelation). Three-dimensional gels can thus be formed.

(3) Coarsening the solid by spontaneous polycondensation and dissolution/recrystallization processes (aging).

(4) Removing the liquid (drying).

The presentation of the various steps of the formation of the oxide will then make it possible to understand the role of each constituent of the elaborated solutions.

Precursors used in sol-gel reactions generally involve metal alkoxides M(OR)n, where R represents an alkyl group. The reactivity of precursors arises from the electronegativity of alkoxo groups which results in high reactivity of metal ions towards nucleophilic attack. Therefore, metal alkoxides can react with water to form metal oxides.

Hydrolysis reaction

In order for the alkoxides to condense at room temperature, the hydrolysis of the -OR groups must begin the reaction process. This step is necessary to give rise to hydroxyl groups –OH

$$\text{M-(OR)}_n + \text{H}_2\text{O} \rightarrow \text{HO-M-(OR)}_{n-1} + \text{R-OH} \qquad\qquad\qquad (\text{II.1})$$

Hydrolysis is a nucleophilic substitution of a -OH ligand for a -OR ligand. It is accompanied by water consumption and alcohol release. During this step, the functionality of the precursor with respect to the polycondensation is created.

Condensation reaction

The -OH groups generated during the hydrolysis are good nucleophiles and go during the condensation, resulting in the creation of M-O-M bridges:

Alcoxolation:

$$\text{(OR)}_{n-1}\text{-M-OH} + \text{RO-M-(OR)}_{n-1} \rightarrow \text{(OR)}_{n-1}\text{- M-O-M-(OR)}_{n-1} + \text{R-OH.} \qquad (\text{II.2})$$

Ox olation:

$$\text{(OR)}_{n-1}\text{-M-OH} + \text{HO-M-(OR)}_{n-1} \rightarrow \text{(OR)}_{n-1}\text{- M-O-M-(OR)}_{n-1} + \text{H}_2\text{O} \qquad (\text{II.3})$$
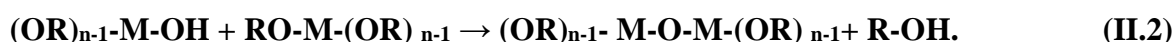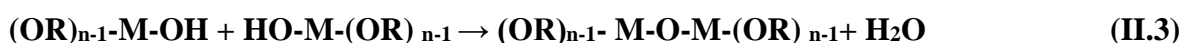
As the reactions go on, the number of M-O-M bonds increases leading to a decrease of the flexibility of the network and thus the viscosity rises. Parameters such as the nature, length and branch of the R group, difference in electronegativity between M and O as well as the ability of M to increase its coordination number through dative bond with other alkoxide molecules, affect the reactivity of the alkoxides in nucleophilic substitutions. If the gelation time is too long, it is possible to resort to the use of catalysts, typically Brønsted acids and bases, to facilitate polymerization. If an acid is used as catalyst, the hydrolysis is promoted:

$$\text{(RO)n M-OR} + \text{H3O}^+ \longrightarrow \text{(RO)n M-OH} + \text{H}^+ + \text{ROH} \qquad\qquad (\text{II.4})$$
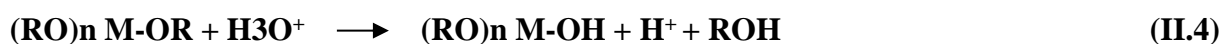
In the base-catalyzed reactions, condensation reactions are promoted because the deprotoned M-OR groups are better nucleophiles:

$$(RO)_n \text{ M-OR} + OH^- \longrightarrow (RO)_n \text{ M-OH} + RO^- \tag{II.5}$$

The hydrolysis and condensation reactions for highly reactive alkoxides, such as titanium alkoxide, must be instead slowed down and in order to achieve this goal a suitable solvent and/or a chelant (i.e. b-diketones, b-keto esters and carboxylic acids) can be used.

However, non-aqueous sol-gel routes are often chosen for several reasons such as the achievement of uniform metal oxide nanoparticles which can be easily dispersed in organic solvents.

In non-aqueous sol-gel routes, different kinds of aprotic condensation reactions occur.

Two metal alkoxide can react with resulting ether elimination (Equation **II.6**):

$$(RO)_n \text{ M-OR} + \text{R-O-M(OR)}_n \longrightarrow (RO)_n \text{ M-O-M(OR)}_n + ROR \tag{II.6}$$

Or metal acetates and metal alkoxides can react under ester elimination (Equation **II.7**):

$$(RO)_n \text{ M-OOCR1} + \text{R-O-M(OR)}_n \longrightarrow (RO)n \text{ M-O-M(OR)}_n + ROOCR_1 \tag{II.7}$$

Metal alkoxides can also react with metal halides leading to the elimination of alkyl halide:

$$(RO)_n \text{ M-X} + \text{R-O-M(OR)}_n \longrightarrow (RO)n \text{ M-O-M(OR)}_n + RX \tag{II.8}$$

where X indicates the halogen element. In non-aqueous acid-catalyzed systems, the initialization of the hydrolysis can occur as a result of the esterification reaction between alcohol and carboxylic acid:

$$RCOOH + R_1OH \longrightarrow RCOOR_1 + H_2O \tag{II.9}$$

Although aqueous and non-aqueous routes present different advantages and disadvantages, they both can be used to prepare ceramic and glass materials in a wide variety of forms (e.g., ultra-fine powders, thin films coatings, ceramic fibers, microporous inorganic membranes and monoliths).
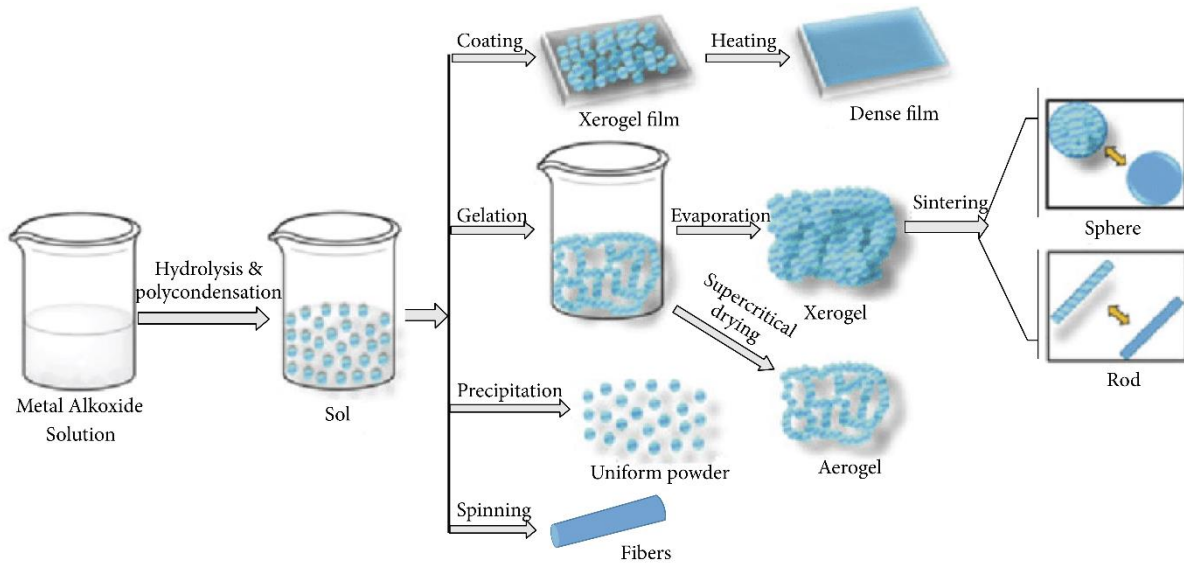
Figure II.1. An overview of the types of processes that can be done with the sol-gel method and the products of each process [1].

II.3. Parameters influencing reaction kinetics

the synthesis process involves two steps; hydrolysis and condensation to obtain the precursor solution that can be deposited by one of the sol-gel techniques (in our case, the dip-coating method), after the deposition, a heat treatment is applied to the thin films to obtain a better crystalline structure.

The entire process can be affected by many parameters, including:

❖ The precursor (nature and concentration),
❖ The nature of the solvent,
❖ Aging time,
❖ The coating method (deposition rate).

II.3.8. spin-coating technique

Spin coating is a widely-used, efficient method for creating uniform thin films on flat substrates, making it popular in both research and industrial applications. This technique is especially valuable in fields that demand precise thickness control and uniformity, such as microelectronics, photovoltaics, and thermoelectric materials. It's frequently applied to

materials like glass, silicon wafers, and polymers due to its ease of implementation and relatively low cost.

The spin coating process involves depositing an excess amount of solution onto a substrate, which is then spun to achieve a thin, uniform film[2]. This method is effective on flat surfaces, typically with dimensions around a few square centimeters. The spin coating process can be divided into four key phases:

1.Deposition: A controlled amount of solution is applied to the centre of the substrate.

2. Spin-up: During the initial acceleration, centrifugal forces spread the liquid outward from the centre to the edges.

3. Spin-off: At a constant rotation speed, excess solution is ejected as droplets, and film thickness decreases uniformly across the substrate.

4. Evaporation: The volatile solvents evaporate, which further reduces film thickness and helps stabilize the final layer [3].
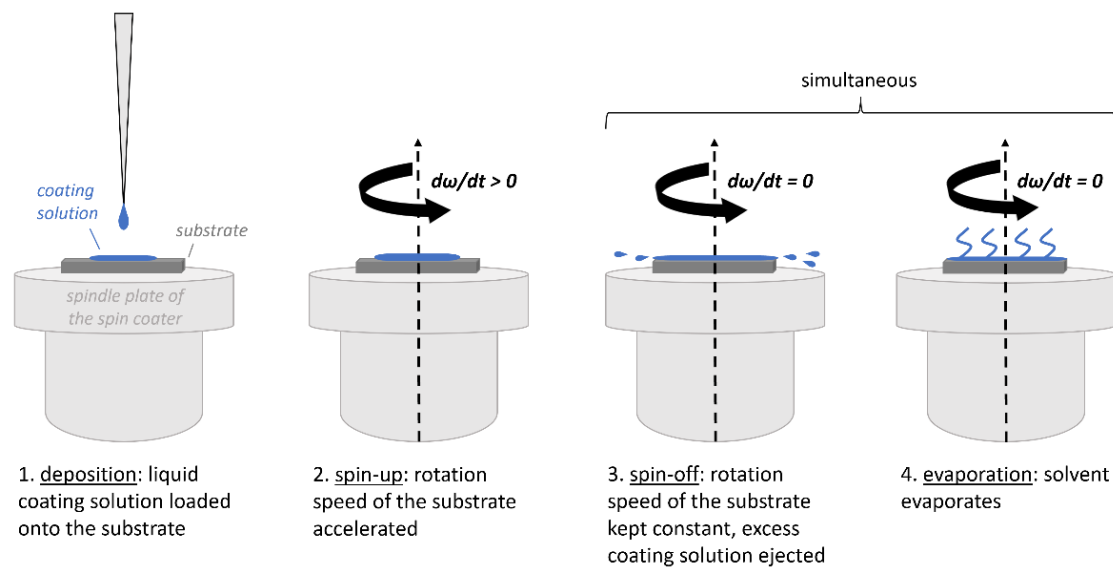
Figure II.2. The four stages of the spin coating procedure.**[4]**

This process ensures a uniform film thickness, with the final properties influenced by various parameters like spin speed, spin duration, and solution viscosity.

1. Spin Speed

Research consistently shows that increasing spin speed results in thinner films, as the higher centrifugal force drives more solution off the substrate. Higher speeds can also improve film smoothness by spreading the material more evenly across the surface. This smoother film quality is crucial in optoelectronic applications, where surface roughness can scatter light and reduce device efficiency[5]. For example, a study by H. Hashim et al. demonstrated the effectiveness of spin coating for depositing copper oxide thin films on quartz substrates. They found that at 1000 rpm, the films achieved maximum thickness and minimal surface roughness, which improved electrical conductivity **figure II.2**. On the other hand, films spun at 3000 rpm exhibited a lower optical band gap **figure II.3**., emphasizing the influence of spin speed on both the structural and optical properties of thin films [6].
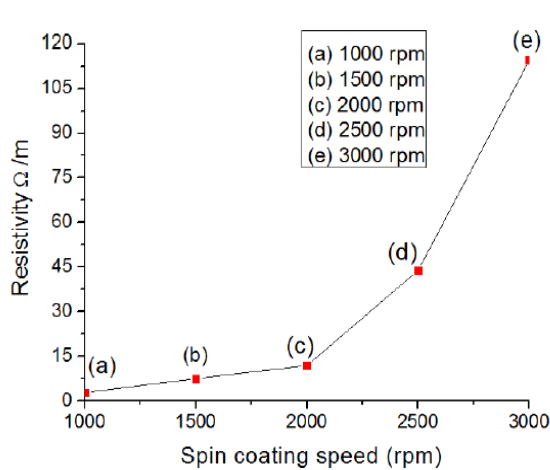
Figure II.3. The plot of resistivity of copper oxide thin films versus spin coating speeds.
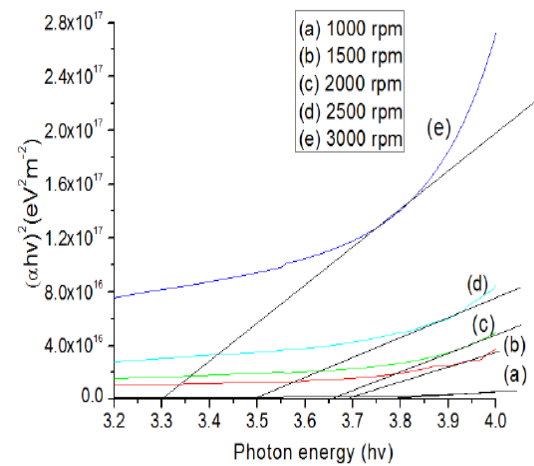
Figure II.4. The plot of optical band gap energy versus photon energy.

2. Spin Duration

Extending the spin time allows more solvent evaporation, leading to a thinner, more stable film. Burmann et al. showed that while the solvent evaporation effect is important when employing spin-coating for membrane casting, the rotational duration had little impact on membrane thickness [7].

3. Viscosity of Solution, additives and concentration

Higher concentrations and viscosities in the coating solution generally produce thicker films but can compromise film smoothness, as increased concentration may lead to particle

aggregation during the drying process. Thus, optimizing both concentration and viscosity is essential for achieving the desired film properties.

A study by M. Dhaouadi et al. on spin-coated copper oxide (CuO) thin films demonstrated that increasing the solute concentration in the solution directly increased the final film thickness. Higher-viscosity solutions, which resist centrifugal forces more effectively during spinning, tend to yield thicker films. However, this increased viscosity can also lead to greater surface roughness [8]. This is in good agreement with other research work [9].On the other hand, highly viscous solvents can slow the reaction and extend the gelation period by limiting the mobility of catalysts and reactants within the solution. This resistance to particle motion can lead to particle agglomeration, as particles stay close to their initial positions. Conversely, with a low-viscosity solvent, particles move more freely, and surface tension can encourage aggregation. This aggregation of particles may trap solvent between them, which can slow down solvent evaporation and impact the gel formation process. Ultimately, the final film's available gel amount depends on both the extent of particle agglomeration and the rate of solvent evaporation. Higher viscosity generally promotes thicker films due to resistance against centrifugal forces, but it may also cause uneven surfaces. Balancing these factors is crucial for achieving desired film thickness and smoothness in CuO thin films. [10, 11].

Are employed to simplify the complete dissolution of the precursor-alcoholic medium the formation of a stable sol [12] . They act as basic or acid and/or chelating agent. Alkali metal hydroxides, alkanolamines, alkylamines, carboxylic acids, acetylacetone and polyalcohols are used for this purpose [13].

The authors reported that the deposition efficiency and crystallinity of the films deposited by adding additives which act as stabilizers or catalyst during the reaction was improved. D. S. C. Halin et al, have shown the addition of polyethylene glycol will increase the viscosity of solution due to chain length effects, Since the polyethylene glycol additive can avoid the particle aggregation occurring in the sol-gel solution the grain size was reducing from 104 nm to 83 nm. also, the addition of polyethylene glycol will produce crack free films with high optical absorbance [14]. whereas, P. Samarasekara et al, demonstrated that Ethylene glycol is a better additive compared with the polyethylene glycol[15].

instead, hydroxide and potassium hydroxide are base agent which provides hydroxyl ion which is strongly associated with reactions that form nanocrystals[16]. This explained by the increase

in OH$^-$ ions with the pH, accelerates the process of CuOH formation (equation 5) provoking a faster crystallization of Cu$_2$O (equation 6) [17]. This fast crystallization reduces interstitial defects, allowing to the interstitial atoms move to the boundaries, relaxing the crystal and consequently reducing its size[18] [19].

$$Cu^+ + OH^- \longrightarrow CuOH \tag{II.10}$$

$$2CuOH \longrightarrow Cu_2O + H_2O \tag{II.11}$$

within the search of the authors, at bath pH~9.0, the (100) plane are produced and in higher bath pH~11.0, the (111) are produced [20-22].

Other common additives are the alkanolamines i.e., monoethanolamine [MEA; (HOCH$_2$CH$_2$) NH$_2$] [23], diethanolamine [DEA; (HOCH$_2$CH$_2$)$_2$NH] [15], triethanolamine [TEA; (HOCH$_2$CH$_2$)$_3$ N] [24] are the most widely used in the CuO thin film fabrication. Likewise, acetic acid (Ac. Ac.; CH$_3$COOH) [25] and lactic acid (Lactic Ac.; CH$_3$CHOHCOOH) [26] tartaric acid [27], oxalic acid [27], malic acid [27-28] also added as complexing agent. Sometimes, it is preferable to use only a single additive in certain circumstance for better dissolution of the mixture.

4.   Preheating During Spin Coating

Preheating the substrate before spin coating enhances film adhesion and decreases drying time, which is particularly beneficial when using low-volatility solvents. Liu et al. (2014) demonstrated that preheating the substrate to approximately 50°C prior to deposition reduced drying time and improved film uniformity in thin films.

II.4. CuO thin films preparation

The aim of this study is to deposit and characterize CuO thin films using the spin coating technique. This research explores the impact of various parameters specific to this technique on the resulting film properties. The study details the experimental process of preparing films via spin coating, as well as the range of characterization methods employed to analyse the films. Additionally, it covers the synthesis of copper oxide thin films using the sol-gel method, the effects of doping with Group I metals (Li, Na, K) on their thermoelectric properties, and

discusses the potential of CuO as a promising thermoelectric material for energy recovery from waste heat.

Unlike other deposition techniques, spin coating offers a wide range of parameters to adjust, allowing for in-depth study. This investigation focuses on the key parameters affecting CuO thin films, specifically: annealing temperature, solvent type, and film thickness. Six sets of samples were prepared, with each set varying only one parameter while keeping the others constant, enabling an isolated analysis of each factor's influence.

To deposit the CuO thin films, a prepared CuO solution was spin-coated onto glass substrates at a rate of 3000 rpm for 30 seconds. To fully evaporate the solvent and eliminate any organic residues, the films were preheated in a furnace at 250°C for 15 minutes.

Glass Substrate Cleaning Procedure:

1. First Cleaning in Methanol: The glass substrates were first cleaned ultrasonically in methanol to remove surface impurities, such as grease or dust, in three cycles of 10 minutes each.

2. Second Cleaning in Distilled Water: Next, the substrates were ultrasonically cleaned in distilled water to remove any remaining traces of methanol, also in three cycles of 10 minutes each.

3. Drying: The cleaned glass substrates were then dried with a dryer.

Tables II.1 (a-c) summarize the specific deposition parameters for each set. The variations include:

- Sets 1: Annealing temperature was varied.

- Set 2: Solvent type was altered.

- Set 3: Different numbers of layers (6, 9, and 12) were deposited to analyze thickness variation

In this section, the copper oxide network is infused with an alkali metal. In Table II.1. d

- Set 4: The doping source (Li, Na, K) and concentration were varied to examine the effect of different Group I dopants on CuO's thermoelectric properties.

Table II.1-a Deposition parameters of the first series of CuO samples.

Samples	Annealing temperature	Number of layers	Solvent
S1	230°C	9 time	Ethanol
S2	400°C		
S3	450°C		
S4	550°C		
S5	600°C		

Table II.1-b Deposition parameters of the Second series of CuO samples

Samples	solvent	Number of layers	Annealing temperature
S1	Methanol	9 time	550 C°
S2	Ethanol		
S3	1-propanol		
S4	Isopropanol		
S5	Methoxyethanol		
S6	Pentanol		

Table II.1.c Deposition parameters of the thirdly series of CuO samples**.**

Samples	Number of layers	Annealing temperature	Solvent
S1	6 layers	500°C	Ethanol
S2	9 layers		
S3	12 layers		

Table II.1-d Deposition parameters of the fourthly series of CuO samples.

Samples	group 1 impurity			Number of layers	Solvent	Annealing temperature
Undoped				9 time	Ethanol	500° C
3%	(LiNO₃.	(NaNO₃.	(KNO₃.			
6%	H₂O)	H₂O)	H₂O)			
9%						
12%						

II.5. Characterization methods

II.5.1. Physico-chemical characterizations

II.5.1.1. Thin Film's thickness Measurement

The thickness of the prepared thin films was determined using the mass difference method. This involved measuring the mass of the samples twice: first, the mass of the bare glass slides before thin film deposition, and second, the mass after the deposition of the thin films [29]. The difference in mass, denoted as (∆m) provided the mass of the thin film deposited on the substrate. The density of CuO is 2.5 g/cm³, and the volume of the glass substrate is $75 \times 25 \times 1$ mm³. The thickness of the thin films was then calculated using the following equation [30]:

$$t = \frac{\Delta m}{\rho\, A} \qquad\qquad\qquad \textbf{(II.12)}$$

Where: t is the thickness, **A** is the area of the thin film, **ρ** is the density of the thin film material CuO, and **∆m** is the mass of the deposited thin films. The calculated thickness of the prepared thin films varies approximately depending on the preparation conditions.

II.5.1.2. X-ray diffraction (XRD)

II.5.1.2.1. Definition and principle of the technique

XRD is a powerful and non-destructive characterization technique. It makes it possible to obtain information on the chemical nature, the structure as well as the characteristics to be sent an X-ray beam on the sample to be analysed. When this beam comes into contact with the electronic

clouds of atoms, the scattering phenomenon occurs. According to the directions of space, the interferences of the rays can be constructive or crystallographic of the crystalline or semi-crystalline materials analysed. Its principle is destructive. The directions with which the interferences are constructive constitute what are called "diffraction peaks", and obey Bragg's law Figure II.5.

$$2\,dhkl\,\sin(\theta) = n\,\lambda \qquad\qquad \textbf{(II.13)}$$

With

d_{hkl}: interreticular distance (in nm)

h, k and l: Miller indices (which are the direction indices)

θ: angle of incidence of X-rays (degree)

n: diffraction order, often equal to 1

λ: X-ray wavelength
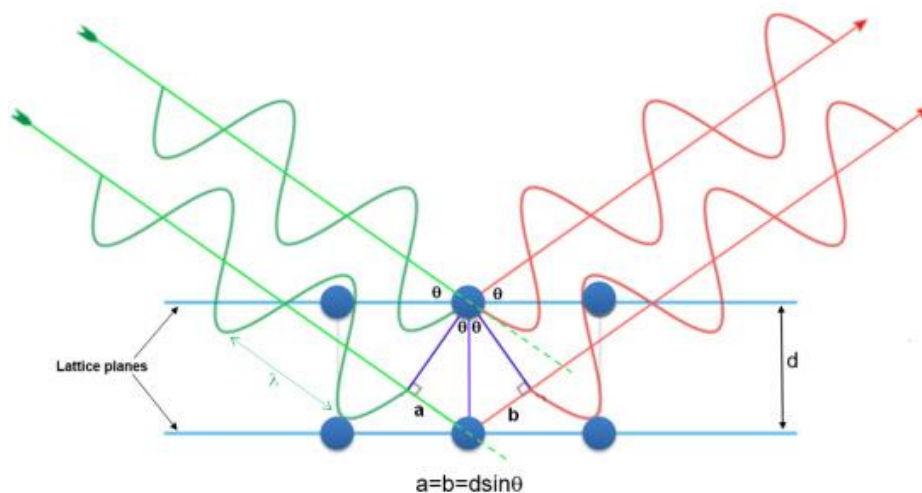
Figure II.5. Bragg's Law

Consequently, the positions of the peaks as well as their recorded intensities make it possible to identify the nature of the sample and to draw several crystallographic information from it.

II.5.1.2.2. Diffractometer and conditions used

XRD analyses were performed with a Bruker D8 Advance diffractometer (Figure 23). The X-ray source is a copper anticathode ($\lambda CuK\alpha = 0.154046$ nm) powered by a generator (40 kV, 40 mA). The diffractometer is controlled by the "Diffract Plus XRD Commander" application version 2.6.1 within a diffraction angle range $2\theta = 30$–$80°$.

The XRD spectra or the diffractograms recorded by the detector are curves which represent the intensities of the diffracted rays as a function of the angles 2θ. These spectra provide a set of information thanks to the databases integrated into the operating software. In our case, the data was used with Eva software version 14.0.0.0 provided by the manufacturer.

II.5.1.2.3. Data analysis

Among the information that can be obtained from these spectra:

II.5.1.2.4. Crystallite size

There are several methods for determining the size of crystallites. Among them, the Rietveld method, the Williamson-Hall method and the Scherrer method, the latter being the most used method and involving the equation

$$D_{hkl} = \frac{n\lambda}{\beta \cos\theta} \qquad \textbf{(II.14)}$$

where D is the crystallite size, n is a constant 0.9, λ is the X-ray wave length of Cu which is 1.5418Å, β is full width at half maximum (FWHM) of the peak and θ is the Bragg's angle in radians.

The line (hkl) generally used to determine the average size of the crystallites is the line of the most intense peak.

The lattice parameter

A crystal lattice is universally represented by a direct trihedron, with sides a, b and c and angles α, β and γ. The determination of the lattice parameters is therefore a determination of these different sides and different angles. Whatever the type of crystal lattice, there is a general relationship linking the lattice parameters with the interreticular distance, in our case, the crystallographic structure is monoclinic. Therefore: $(a \neq b \neq c)\alpha = \gamma = 90^0 \neq \beta$

$$\frac{1}{d^2} = \frac{1}{sin^2\beta}\left(\frac{h^2}{a^2} + \frac{k^2\,sin}{b^2} + \frac{l^2}{c}\right) + \frac{2h\,l\,cos\beta}{a.c} \tag{II.15}$$

II.5.1.2.5. Dislocation density

A dislocation is a linear defect, a discontinuity in the arrangement of the crystal structure of materials. Dislocations are significant factors for semiconductor materials since they influence their electronic properties.

The dislocation density (δ) is expressed in nm^{-2}. It is calculated by the Williamson and Smallman method from the crystallite size in nm determined by the Scherrer method by the following relationship

$$\delta = \frac{1}{D^2} \tag{II.16}$$

II.5.1.2.6. Micro-deformations

is defined as the strain occurring within a material or the small-scale deformation. It is also possible thanks to the XRD spectra, to determine the micro deformations (ε) of the analysed materials (quantity without unit) using the following equation:

$$\varepsilon = \frac{\beta}{4\,cos\,\theta} \tag{II.17}$$

II.5.1.3. Scanning electron microscopy (SEM)

Scanning electron microscopy (SEM) is a surface-imaging technique that produces images of a sample by scanning it with a focused beam of electrons. The incident electrons interact with the sample and generate signals that reflect direct images and the atomic composition of the scanned surface. These interactions cause the emission of elastically backscattered electrons (BS), secondary inelastically scattered electrons, and characteristic X-rays from the atoms on the sample surface. The most common mode in SEM is the detection of secondary electrons; by collecting these electrons with a special detector, a detailed image of the sample is created.

Optical microscopes use visible light sources and lenses or mirrors to produce magnified images at the micrometer scale. In contrast, electron microscopes are frequently used to provide direct images and chemical information of materials at the nanoscale. Due to the small de Broglie wavelength of electrons, electron microscopes are capable of imaging at significantly higher resolutions than light microscopes [31].
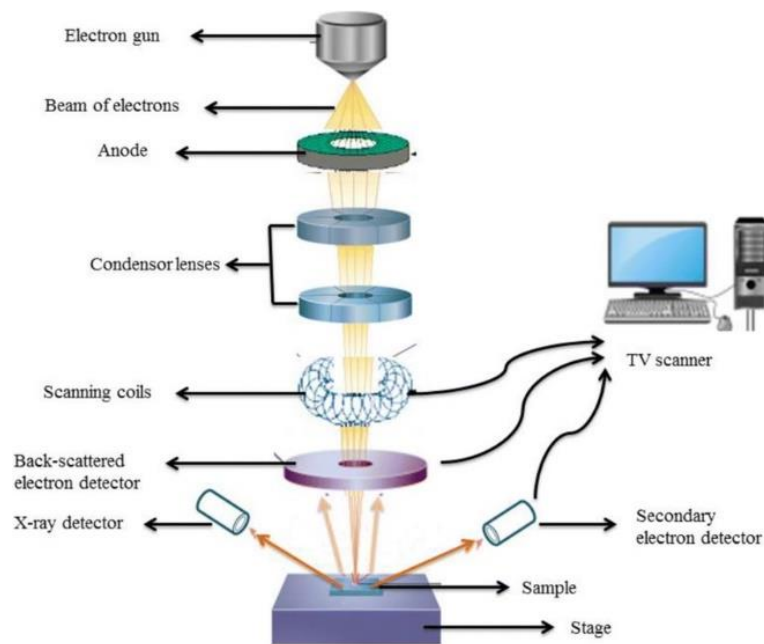
Figure II.6. Schematic diagram of SEM [32].

II.5.1.4. Energy-Dispersive Spectrometry (EDS)

EDS analysis is also called energy dispersive X-ray analysis or energy dispersive X-ray microanalysis. It is an analytical technique used for the elemental analysis or chemical characterization of a sample. It relies on an interaction of some source of X-ray excitation and a sample. Its characterization capabilities are due in large part to the fundamental principle that each element has a unique atomic structure allowing a unique set of peaks on its X-ray emission spectrum [33].
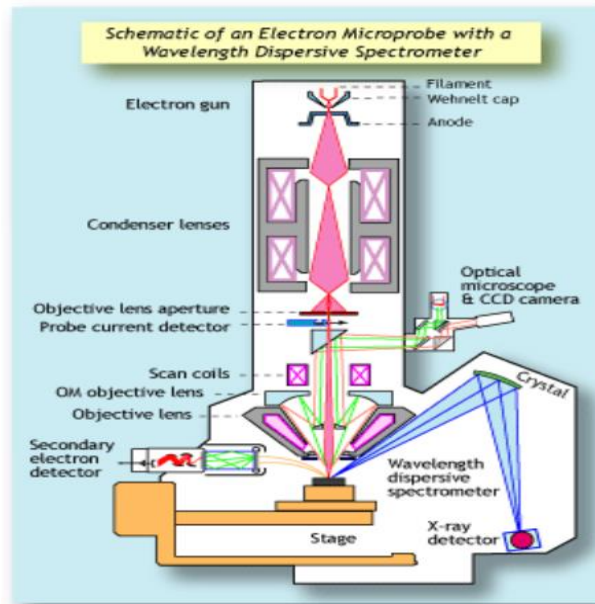
Figure II.7. Schematic diagram of Energy dispersion X-Ray (EDX) [34]

A technique called energy dispersive X-ray spectroscopy (EDX) is integrated into most modern SEM systems and is used to analyze the elemental composition of surfaces at the micrometer scale. The combined use of SEM and EDX techniques is highly beneficial, as it provides information on the size, shape, surface texture, and elemental composition of samples in a relatively short time.

II.5.1.5. UV –Visible spectroscopy

Optical transmission measurements are used to evaluate and test certain optical constants of materials that are critical for system fabrication and analysis. Among these optical constants:

the absorption coefficients, the bandgap energy, refractive index and Urbach energy, dielectric index, it can also provide information on the thickness of the sample. Furthermore, optical transmission or absorption measurements are used to detect certain impurities present in a material as some impurities have characteristic absorption lines[35].

The UV-vis absorption spectroscopy provides information on absorption light as a function of wavelength, which describes the electronic transitions occurring in the measured samples. where a substance absorbs light in the ultraviolet and visible domains, the energy absorbed causes disturbances in the electronic structure of atoms, ions, or molecules. These electron transitions are in the visible range, from 350 to 800 nm and ultraviolet between 200 and 350

nm. One or more electrons absorb this energy to jump from a low energy level to a high energy level [36, 37].

These electronic transitions result in modifications of the light transmitted and reflected by the material. In the case of materials deposited in thin layers on transparent substrates, the transmitted and reflected light will also be modulated in intensity by interference phenomena linked to multiple reflections at the film/substrate and film/air interfaces [38].
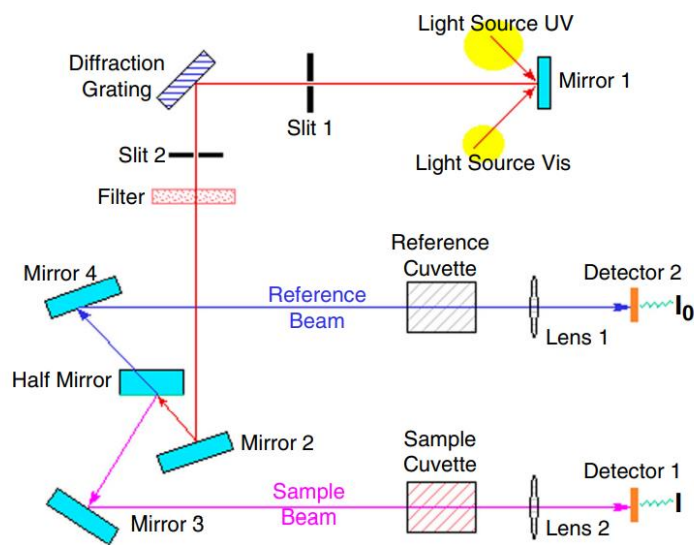
Figure II.8. A diagram of an ultraviolet/visible spectrophotometer.

There are two light sources; one for ultraviolet light and one for visible light. A mirror is used to select the proper light source. The diffraction grating is the monochromator that selects specific wavelengths of light. The two detectors are coupled so that reference absorptions can be subtracted from sample absorptions [39].

II.5.1.5.1. Absorption coefficient

In the spectral range where the light is absorbed, and knowing the thickness of the films, we can determine the absorption coefficient for each value of the transmittance T in (%) which corresponds to an energy according to Beer- Lambert

$$T = e^{-\alpha d} \tag{II.18}$$

d: is the film thickness, T: is the transmittance in (%), α: id the absorption coefficient(cm^{-1}),
k: is the extinction coefficient (without unity).

$$\alpha = \frac{1}{d} ln \frac{1}{T} \quad , \quad k = \frac{\alpha\lambda}{4\pi} \qquad\qquad (II.19)$$

Knowing the thickness of the films, d, it is therefore possible to determine the absorption coefficient for each value of the transmittance which corresponds to an energy [40].

II.5.1.5.2. Optical band gap energy

An electronic transition between the conduction and valence bands in the crystal starts at the absorption edge which equals the least energy variation between the highest maximum of the valence band and the lowest minimum of the conduction band is known as band gap energy (Eg). If these extrema lie at a similar point of the k-space then the transition is called direct. If this is not, then only phonon-assisted transitions called indirect transitions are possible as depicted in **Figure II.9**.
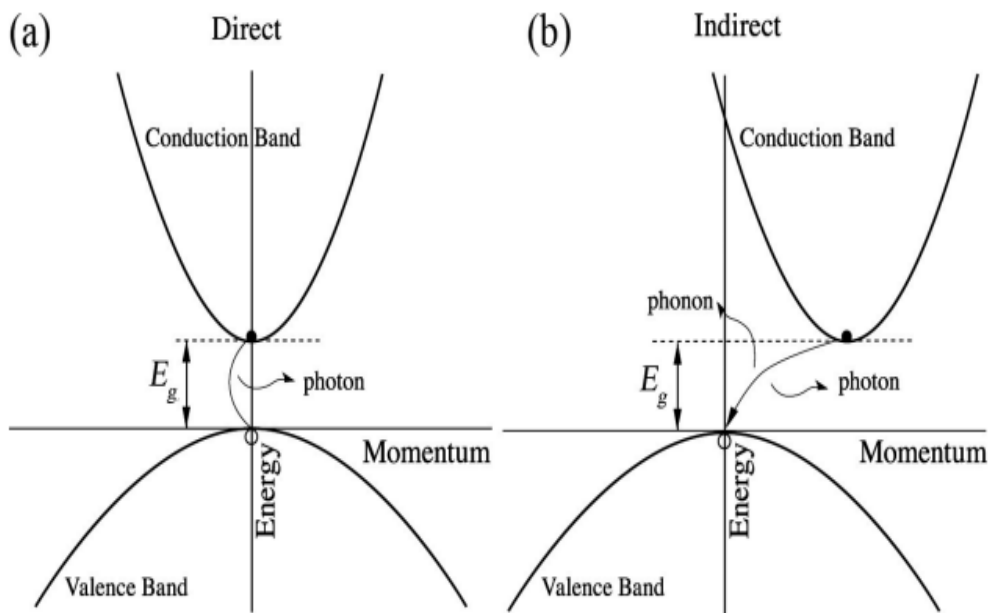
Figure II.9. E-K diagram showing (a) direct band and (b) indirect band transition [41]

In high energy, absorption results from electronic transitions between wide states of band to band. It is usually described by Tauc law.

$$(\alpha h\nu)^n = A (\alpha h\nu - Eg) \qquad\qquad (II.20)$$

Where:

$h\nu$: the photon energy

Eg: the optical gap

n and A are constants, n characterizes the optical type of transition and takes the values 2, 1/2 (2 for allowed direct transitions or 1/2 for allowed indirect transitions). In order to determine the nature of the transition from the films that are produced in this study, we will plot the curves $(\alpha h\nu)2 = f\ (h\nu)$ [20]. We can obtain Eg value as it showing in **figure II.10**:
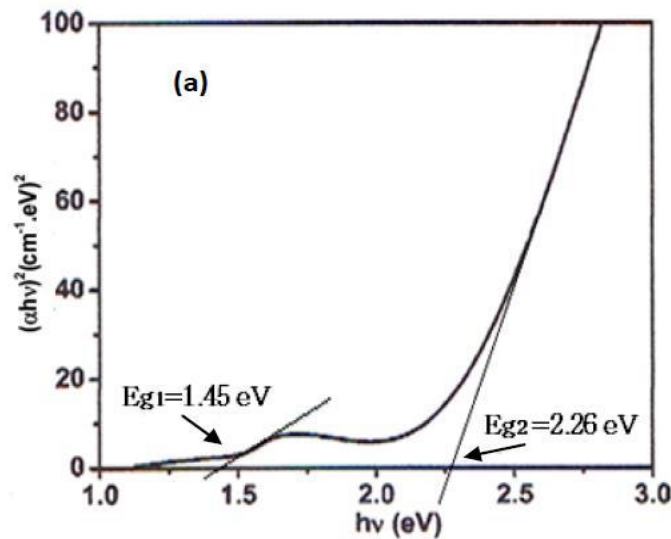
Figure II.10. Curve represent the function $(\alpha h\nu)^2 = f(h\nu)$.

II.5.1.5.3. Urbach Energy

When in a material there are variations in interatomic distances, bond lengths, or angles, what is called "disorder" occurs. In this case, the band edges described in the case of crystal lattices and delimited by "Ev" and "Ec" may disappear. We observe what are called localized states formed in band tails at the boundaries of the forbidden band in the valence and conduction bands. For energies higher than Ec and lower than Ev, extended states are found. **(figure II. 10).**

When the disorder becomes too great (for example, with the appearance of dangling bonds or impurities in the material), the tails can encroach. We will then define the notion of the Urbach

parameter (Eu), which corresponds to transitions between the extended states of the valence band and the localized states of the conduction band[42].
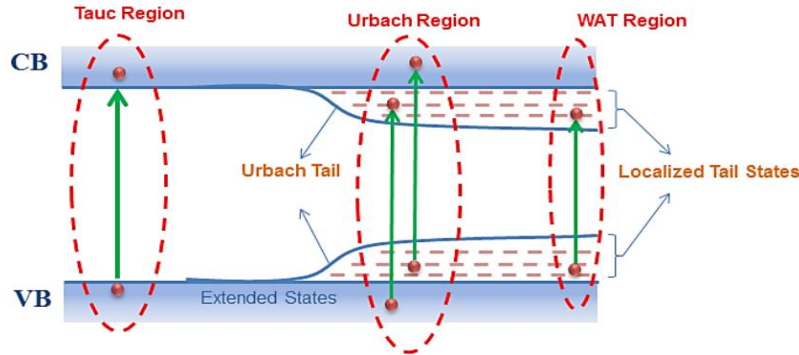
Figure II.11. Schematic representation of various transitions between valence band (VB) and conduction band (CB). Tauc region, Urbach region and weak absorption tail region are highlighted with dotted circles[43].

According to Urbach's law, the expression of the absorption coefficient is of the form:

$$\boldsymbol{\alpha = \alpha_0 \exp\left(\frac{h\nu}{Eu}\right)} \tag{II.21}$$

By plotting $\boldsymbol{ln\,\alpha}$ as a function of $\boldsymbol{h\nu}$.

$$\boldsymbol{ln\,\alpha = ln\,\alpha_0 + \frac{1}{E_u} h\nu} \tag{II.22}$$

whereby, it is expressed by inverse of the slope ($\boldsymbol{E_u = \frac{\Delta(h\nu)}{\Delta[ln(a)]}}$)for linear fit of the logarithm of the absorption intensity (ln(α)) as a function of photon energy (hν) in the absorption edge region[44].

II.5.2. Electrical characterization techniques:

Electrical conductivity σ describes a material's ability to conduct electricity and is inversely related to resistivity ρ, where =1/σ. In semiconductors, conductivity depends on charge carrier mobility and concentration (electrons or holes). Various measurement techniques exist, often influenced by temperature.

In semiconductors, conductivity increases with temperature due to greater carrier generation, while in metals, it decreases as increased lattice scattering hinders electron

movement. Additionally, conductivity is influenced by crystal structure, as electronic properties are closely tied to crystallographic orientation. In polycrystalline materials, grain size plays a crucial role, affecting carrier scattering and, at very small scales, modifying electronic properties.

II.5.2.1. Resistivity measurements

Four-point probe measurements are used to determine the resistivity of a bulk or thin film sample. The use of four contacts instead of two, as in a traditional resistance measurement, allows one to disregard the resistance of the points and only measure the resistance of the sample. **Figure II.12.** illustrates the four-point probe measurement setup. As shown in **Figure II.12**, a current, I, is passed through the sample, and the voltage, V, is measured. The specific resistivity of the sample can then be calculated. When the distance between the limits is significantly greater than the thickness of the thin film (d<<a) The lateral dimensions can be thought of as infinite [45].

Figure II.12. (a)Diagram representing the principle of the four points method; (b) "KEYSIGHT" semiconductor device analyses type "B1500A".

In this case, a bi-dimensional conduction model is considered and provides

$$\frac{U}{I} = K\frac{\rho}{d} \qquad \text{(II.23)}$$

Were ρ is the resistivity and d: is the thickness of the films. An important surface electrical property in the field of TCOs is the surface resistance R_S defined as the ratio of the resistivity to the thickness of the thin film depending on the relationship were R_{sq} (a).

$$R_{sq} = K\frac{U}{I} = \frac{\rho}{d} \qquad \text{(II.24.a)}$$

K: is a coefficient and R_{sq}: is the ratio between voltage U and current I. considering a cylindrical propagation of the field lines in the thin film, the coefficient K is ln (2)/π is equal to 4.532. According to the relation **(II.24.a)** and the previous considerations, we have the formula **(II.24.b)** to deduce the resistivity ρ (b) from the measurement four points knowing the thickness:

$$\rho = \left(\frac{\ln (2)}{\pi} . \frac{U}{I}\right) . d = R_{sq} . d \qquad \textbf{(II.24.b)}$$

II.5.2.2. Conductivity measurements

The electrical measurements that we have taken are mostly about current-tension characteristics I (V). To calculate the resistance of the layer, the calculation of the electrical conductivity depends on the electrical resistance, R of the intrinsic layer, thus even geometric parameters (inter-electrode distance L, the thickness d and the section of the conductive thin film S) [46]. The conductivity σ is related to these parameters by the following relationship

$$\sigma = \left(\frac{L}{S}\right)\left(\frac{1}{R}\right) \qquad \textbf{(II.25)}$$

the measurements of electrical resistivity of the synthetized films were carried out using four probe methods with using "KEYSIGHT" semiconductor device analyses type "B1500A" at room temperature.

II.6. DFT characterization of mechanical properties
II.6.1. Introduction

The elastic and mechanical properties of any material are among the key properties that must be thoroughly investigated to facilitate the proper integration of that material into the emerging technology. One way to analyze the elastic and mechanical response of materials is via the first-principles density-functional theory (DFT) calculations. The success of DFT [47] [48] [49] not only enabled us to predict the properties of materials from ab-intio calculations, but it also expedited the discovery and design of novel materials with a given set of properties for desired practical applications. Modern DFT codes, e:g:; ABINIT [50, 51], VASP [52, 53], SIESTA [54], Quantum Espresso [55, 56], exciting [57], WIEN2k [58], CASTEP [59], ELK [60], CRYSTAL [61, 62] offer the capability to efficiently compute the elastic stiffness tensor of materials to a remarkable accuracy (i.e., to the accuracy of the employed DFT method). In fact, such calculations have been performed in recent years and materials databases containing the DFT calculated elastic tensor of hundreds of bulk and two-dimensional materials have been

developed [63-69]. Further, various software tools such as ELATE [70], AELAS [71], ElaStic [72], and ELAM [73], to the best of our knowledge, have been developed to carry out the analysis of elastic properties from first-principles calculations.

II.6.2 Method of calculating elastic constants

The study of elastic constants allows us to deduce important information on the dynamic and mechanical properties of solid materials such as the stability of phases and the nature of forces interacting between nearest neighbor atoms [74-75]. Ab initio calculations of these constants are generally done by two approaches:

(i)   Energy-strain approach.

(ii)   Stress-strain approach.

The first one where we calculate the total energy of crystals for deformed structures with a suitable choice of strains. For this approach the elastic constants can be obtained by analyzing energies under different small stresses.

In the second approach and with a judicious choice of strain applied to the system, the stress tensor components can be calculated by an ab initio method. So we retain the elastic constants C_{ij} based on the linear Hock law. Applying a given homogeneous strain and calculating the resulting stress requires much less computational effort, since the unit cell is fixed and only the ionic positions require optimization. The CASTEP code uses the latter approach for calculating elastic constants of crystal structures [76].

In this work, we have used the method of plane wave pseudo-potential, based on density functional theory (DFT) [77]. This method was applied using CASTEP codes [78]. In order to exchange-correlation potential, the generalized gradient approximation (GGA) parametrized by Perdew–Burke–Ernzerhof [79]was chosen.

The power of the cut and the k point number (in particular used to merge the Brillouin (BZ)region on the accuracy of the calculation The plane wave cutoff energy in reciprocal space was taken as 900 eV. The BZ with Monkhorst – Pack scheme at special k-points [80] of $7 \times 8 \times 7$.

The tolerances for geometry optimization are set as follows: The difference of the total energy is within $5 * 10^{-6}$ eV/atom, the maximum force is 0.01 eV/Å. Elastic constants at the equilibrium volumes are calculated using the stress–strain method [81]. The method implemented in CASTEP is setting homogeneous deformation (strain) to a finite value, reoptimizing any free parameters and calculating the resulting stress. The elastic stiffness constant Cij and compliance

constants S_{ij} for monoclinic CuO were determined from the stress-strain relationship calculations.

Reference

[1]   D. Bokov, A. Turki Jalil, S. Chupradit, W. Suksatan, M. Javed Ansari, I. H. Shewael, G. H. Valiev, and E. Kianfar, "Nanomaterial by sol-gel method: synthesis and application," *Advances in Materials Science and Engineering,* vol. 2021, pp. 1-21, 2021.

[2]   M. Tyona, "A theoritical study on spin coating technique," *Advances in materials Research,* vol. 2, p. 195, 2013.

[3]   M. Abdelhafid, "Etude des couches minces d'' Oxyde de Zinc dopé Aluminium et Cobalt élaborées par le technique sol gel-spin coating. Application à la photodétection et au photocourant," *Universite Freres Mentouri-Constantine,* 2015.

[4]   S. Moschetto, "Functional engineering of hybrid heterostructures for application in electronic, optical and optoelectronic nanostructured devices," 2023.

[5]   B. Shivaraj, H. N. Murthy, M. Krishna, and S. Sharma, "Investigation of influence of spin coating parameters on the morphology of ZnO thin films by taguchi method," *Int. j. thin film sci. tec,* vol. 2, pp. 143-154, 2013.

[6]   H. Hashim, S. Shariffudin, P. Saad, and H. Ridah, "Electrical and optical properties of copper oxide thin films by sol-gel technique," in *IOP Conference Series: Materials Science and Engineering*, 2015, p. 012032.

[7]   P. Burmann, B. Zornoza, C. Téllez, and J. Coronas, "Mixed matrix membranes comprising MOFs and porous silicate fillers prepared via spin coating for gas separation," *Chemical Engineering Science,* vol. 107, pp. 66-75, 2014.

[8]   M. Dhaouadi, M. Jlassi, I. Sta, I. B. Miled, G. Mousdis, M. Kompitsas, and W. Dimassi, "Physical properties of copper oxide thin films prepared by sol–gel spin–coating method," *Am. J. Phys. Appl,* vol. 6, pp. 43-50, 2018.

[9]   H. Hashim, S. Shariffudin, M. Sarah, and N. Nasir, "The characterization of copper oxide with different molar concentration using sol-gel spin coating," in *2016 IEEE International Conference on Semiconductor Electronics (ICSE)*, 2016, pp. 224-227.

[10]   V. Solyanikov and L. Petrov, "The Rate of the Oxygen Absorption by the Styrene Epoxide–p-Toluene Sulfonic Acid Double System Depending on the Structure of the Aliphatic Tail of the Alcohol Solvent," *Russian Journal of Physical Chemistry B,* vol. 17, pp. 1259-1264, 2023.

[11]   T. Munekata, T. Suzuki, S. Yamakawa, and R. Asahi, "Effects of viscosity, surface tension, and evaporation rate of solvent on dry colloidal structures: A lattice Boltzmann study," *Physical Review E—Statistical, Nonlinear, and Soft Matter Physics,* vol. 88, p. 052314, 2013.

[12]   E. Benrezgua, B. Deghfel, Z. Abdelhalim, W. J. Basirun, R. Amari, A. Boukhari, M. K. Yaakob, S. Kheawhom, and A. A. Mohamad, "Synthesis and properties of copper doped zinc oxide thin films by sol-gel, spin coating and dipping: A characterization review," *Journal of Molecular Structure,* p. 133639, 2022.

[13]   L. Znaidi, "Sol–gel-deposited ZnO thin films: A review," *Materials Science and Engineering: B,* vol. 174, pp. 18-30, 2010.

[14]   D. Halin, I. Talib, A. Daud, and M. Hamid, "Characterizations of cuprous oxide thin films prepared by sol-gel spin coating technique with different additives for the photoelectrochemical solar cell," *International Journal of Photoenergy,* vol. 2014, 2014.

[15]   P. Samarasekara and N. Premasiri, "Optical properties of spin coated and sol-gel dip coated cupric oxide thin films," *arXiv preprint arXiv:1806.03976,* 2018.

[16] T. Jiang, Y. Wang, D. Meng, X. Wu, J. Wang, and J. Chen, "Controllable fabrication of CuO nanostructure by hydrothermal method and its properties," *Applied Surface Science,* vol. 311, pp. 602-608, 2014.

[17] S. Chaurasiya, J. Udaya Bhanu, and P. Thangadurai, "Precursor dependent structural phase evolution in hydrothermally prepared Cu2O octahedrons and cu micro-flakes and their structural and optical properties," *Transactions of the Indian Institute of Metals,* vol. 71, pp. 1185-1191, 2018.

[18] O. Reyes, D. Maldonado, J. Escorcia-García, and P. Sebastian, "Effect of temperature and pH on direct chemical bath deposition of cuprous oxide thin films," *Journal of Materials Science: Materials in Electronics,* vol. 29, pp. 15535-15545, 2018.

[19] S. Farhad, S. Majumder, M. A. Hossain, N. Tanvir, R. Akter, and M. A. Patwary, "Effect of solution pH and post-annealing temperatures on the optical bandgap of the copper oxide thin films grown by modified SILAR method," *MRS Advances,* vol. 4, pp. 937-944, 2019.

[20] V. Avrutin, N. Izyumskaya, and H. Morkoç, "Semiconductor solar cells: Recent progress in terrestrial applications," *Superlattices and Microstructures,* vol. 49, pp. 337-364, 2011.

[21] A. Rakhshani, A. Al-Jassar, and J. Varghese, "Electrodeposition and characterization of cuprous oxide," *Thin Solid Films,* vol. 148, pp. 191-201, 1987.

[22] L. Olsen, F. Addis, and W. Miller, "Experimental and theoretical studies of Cu2O solar cells," *Solar cells,* vol. 7, pp. 247-279, 1982.

[23] G. Sığırcık and T. Tüken, "ZnO/CuO hybrid films synthesized by sequential application of electrochemical and spin coating technique," *Journal of Materials Science: Materials in Electronics,* vol. 31, pp. 17855-17871, 2020.

[24] Z. N. Kayani, W. Chaudhry, R. Sagheer, S. Riaz, and S. Naseem, "Effect of Ce doping on crystallite size, band gap, dielectric and antibacterial properties of photocatalyst copper oxide Nano-structured thin films," *Materials Science and Engineering: B,* vol. 283, p. 115799, 2022.

[25] A. Maini and M. Shah, "Sol-Gel Fabricated CuO Thin Film: Characterization for Device Application," 2021.

[26] K. Iimura, Y. Ishikawa, T. Kikuchi, T. Takai, H. Satone, and M. Suzuki, "Preparation of yttrium barium copper oxide superconductive fibers via electrospinning through a lactic-acid gel route," *Journal of the Ceramic Society of Japan,* vol. 125, pp. 634-637, 2017.

[27] T. Fujiwara, T. Nakaue, and M. Yoshimura, "Direct fabrication and patterning of Cu2O film by local electrodeposition method," *Solid State Ionics,* vol. 175, pp. 541-544, 2004.

[28] Q. Zhu, Y. Zhang, J. Wang, F. Zhou, and P. K. Chu, "Microwave synthesis of cuprous oxide micro-/nanocrystals with different morphologies and photocatalytic activities," *Journal of Materials Science & Technology,* vol. 27, pp. 289-295, 2011.

[29] M. Imran, G. Asghar, G. H. Tariq, A. W. Faridi, S. Bano, M. S. Shifa, and S. Ullah, "Investigation of annealing effects on physical properties of chemically prepared copper oxide thin films," *Results in Optics,* vol. 10, p. 100331, 2023.

[30] N. Beji, M. Souli, M. Ajili, S. Azzaza, S. Alleg, and N. K. Turki, "Effect of iron doping on structural, optical and electrical properties of sprayed In2O3 thin films," *Superlattices and Microstructures,* vol. 81, pp. 114-128, 2015.

[31] A. Barhoum and M. L. García-Betancourt, "Physicochemical characterization of nanomaterials: Size, morphology, optical, magnetic, and electrical properties," in

Emerging applications of nanoparticles and architecture nanostructures, ed: Elsevier, 2018, pp. 279-304.

[32] N. Munir, M. Hanif, D. A. Dias, and Z. Abideen, "The role of halophytic nanoparticles towards the remediation of degraded and saline agricultural lands," *Environmental Science and Pollution Research,* vol. 28, pp. 60383-60405, 2021.

[33] G. C. Wang, *The utilization of slag in civil infrastructure construction*: Woodhead Publishing, 2016.

[34] S. Benhamida, "Caractérisation Des Couches Minces D'oxyde De Nickel (NiO) Elaboré Par Spray Pyrolyse," Université Mohamed Khider-BISKRA, 2018.

[35] W. Allag, "Study of thin films for photovoltaic solar cells," 2023.

[36] P. Miles, "High transparency infrared materials," *Optical Engineering,* vol. 15, pp. 451-459, 1976.

[37] R. A. Vasudev, "Synthesis and characterization of nanocrystalline ZnO Gas Sensor," 2015.

[38] M. C. BENACHOUR, "Elaboration et caractérisation des couches minces de matériau CZTS (Cu2ZnSnS4) obtenues par voie sol gel: Applications a la photovoltaïque," ecole polytechnique, 2020.

[39] M. M. Houck and J. A. Siegel, "Chapter 5 - Light and Matter," in *Fundamentals of Forensic Science (Third Edition)*, M. M. Houck and J. A. Siegel, Eds., ed San Diego: Academic Press, 2015, pp. 93-119.

[40] F. Khediri, "Etude expérimental des propriétés physiques des couches minces de ZnO," Université Echahid Cheikh Larbi-Tebessi-Tébessa, 2022.

[41] M. D. Jawad, "Senior Year Project: Fabrication and Optimization of Quantum Dots based Photonic devices," 2022.

[42] K. Derrar and M. Zaabat, "Elaboration et caractérisation des oxydes métalliques," 2020.

[43] N. Sharma, K. Prabakar, S. Ilango, S. Dash, and A. Tyagi, "Optical band-gap and associated Urbach energy tails in defected AlN thin films grown by ion beam sputter deposition: Effect of assisted ion energy," *Advanced Materials Proceedings,* vol. 2, pp. 342-346, 2017.

[44] H. Touhami, K. Almi, and S. Lakel, "Experimental and theoretical investigation of the effect of alkali (Li, Na and K) doping on the properties of nickel oxide thin films: Comparative study," *Main Group Chemistry,* pp. 1-15.

[45] S. Amara, "Caractérisation optique et structurale des couches minces d'oxydes complexes pour applications photoniques," 2018.

[46] A. Hafdallah and N. Attaf, "Étude du dopage des couches minces de ZnO élaborées par spray ultrasonique," 2007.

[47] J. Hafner, C. Wolverton, and G. Ceder, "Toward computational materials design: the impact of density functional theory on materials research," *MRS bulletin,* vol. 31, pp. 659-668, 2006.

[48] X. Gonze, F. Jollet, F. A. Araujo, D. Adams, B. Amadon, T. Applencourt, C. Audouze, J.-M. Beuken, J. Bieder, and A. Bokhanchuk, "Recent developments in the ABINIT software package," *Computer physics communications,* vol. 205, pp. 106-131, 2016.

[49] S. Curtarolo, D. Morgan, and G. Ceder, "Accuracy of ab initio methods in predicting the crystal structures of metals: A review of 80 binary alloys," *Calphad,* vol. 29, pp. 163-211, 2005.

[50] X. Gonze, B. Amadon, P.-M. Anglade, J.-M. Beuken, F. Bottin, P. Boulanger, F. Bruneval, D. Caliste, R. Caracas, and M. Côté, "ABINIT: First-principles approach to

material and nanosystem properties," *Computer Physics Communications,* vol. 180, pp. 2582-2615, 2009.

[51] A. H. Romero, D. C. Allan, B. Amadon, G. Antonius, T. Applencourt, L. Baguet, J. Bieder, F. Bottin, J. Bouchet, and E. Bousquet, "ABINIT: Overview and focus on selected capabilities," *The Journal of chemical physics,* vol. 152, 2020.

[52] G. Kresse and J. Furthmüller, "Efficient iterative schemes for ab initio total-energy calculations using a plane-wave basis set," *Physical review B,* vol. 54, p. 11169, 1996.

[53] G. Kresse and D. Joubert, "From ultrasoft pseudopotentials to the projector augmented-wave method," *Physical review b,* vol. 59, p. 1758, 1999.

[54] J. M. Soler, E. Artacho, J. D. Gale, A. García, J. Junquera, P. Ordejón, and D. Sánchez-Portal, "The SIESTA method for ab initio order-N materials simulation," *Journal of Physics: Condensed Matter,* vol. 14, p. 2745, 2002.

[55] P. Giannozzi, O. Andreussi, T. Brumme, O. Bunau, M. B. Nardelli, M. Calandra, R. Car, C. Cavazzoni, D. Ceresoli, and M. Cococcioni, "Advanced capabilities for materials modelling with Quantum ESPRESSO," *Journal of physics: Condensed matter,* vol. 29, p. 465901, 2017.

[56] P. Giannozzi, S. Baroni, N. Bonini, M. Calandra, R. Car, C. Cavazzoni, D. Ceresoli, G. L. Chiarotti, M. Cococcioni, and I. Dabo, "QUANTUM ESPRESSO: a modular and open-source software project for quantum simulations of materials," *Journal of physics: Condensed matter,* vol. 21, p. 395502, 2009.

[57] A. Gulans, S. Kontur, C. Meisenbichler, D. Nabok, P. Pavone, S. Rigamonti, S. Sagmeister, U. Werner, and C. Draxl, "Exciting: a full-potential all-electron package implementing density-functional theory and many-body perturbation theory," *Journal of Physics: Condensed Matter,* vol. 26, p. 363202, 2014.

[58] P. Blaha, K. Schwarz, F. Tran, R. Laskowski, G. K. Madsen, and L. D. Marks, "WIEN2k: An APW+ lo program for calculating the properties of solids," *The Journal of chemical physics,* vol. 152, 2020.

[59] S. J. Clark, M. D. Segall, C. J. Pickard, P. J. Hasnip, M. I. Probert, K. Refson, and M. C. Payne, "First principles methods using CASTEP," *Zeitschrift für kristallographie-crystalline materials,* vol. 220, pp. 567-570, 2005.

[60] A. Sanna, J. A. Flores-Livas, A. Davydov, G. Profeta, K. Dewhurst, S. Sharma, and E. Gross, "Ab initio Eliashberg theory: making genuine predictions of superconducting features," *Journal of the Physical Society of Japan,* vol. 87, p. 041012, 2018.

[61] W. Perger, J. Criswell, B. Civalleri, and R. Dovesi, "Ab-initio calculation of elastic constants of crystalline systems with the CRYSTAL code," *Computer Physics Communications,* vol. 180, pp. 1753-1759, 2009.

[62] R. Dovesi, A. Erba, R. Orlando, C. M. Zicovich-Wilson, B. Civalleri, L. Maschio, M. Rérat, S. Casassa, J. Baima, and S. Salustro, "Quantum-mechanical condensed matter simulations with CRYSTAL," *Wiley Interdisciplinary Reviews: Computational Molecular Science,* vol. 8, p. e1360, 2018.

[63] W. Setyawan, R. M. Gaume, S. Lam, R. S. Feigelson, and S. Curtarolo, "High-throughput combinatorial database of electronic band structures for inorganic scintillator materials," *ACS combinatorial science,* vol. 13, pp. 382-390, 2011.

[64] A. Jain, G. Hautier, C. J. Moore, S. P. Ong, C. C. Fischer, T. Mueller, K. A. Persson, and G. Ceder, "A high-throughput infrastructure for density functional theory calculations," *Computational Materials Science,* vol. 50, pp. 2295-2310, 2011.

[65] A. Jain, S. P. Ong, G. Hautier, W. Chen, W. D. Richards, S. Dacek, S. Cholia, D. Gunter, D. Skinner, and G. Ceder, "Commentary: The Materials Project: A materials genome approach to accelerating materials innovation," *APL materials,* vol. 1, 2013.

[66] M. De Jong, W. Chen, T. Angsten, A. Jain, R. Notestine, A. Gamst, M. Sluiter, C. Krishna Ande, S. Van Der Zwaag, and J. J. Plata, "Charting the complete elastic properties of inorganic crystalline compounds," *Scientific data,* vol. 2, pp. 1-13, 2015.

[67] F.-X. Coudert and A. H. Fuchs, "Computational characterization and prediction of metal–organic framework properties," *Coordination Chemistry Reviews,* vol. 307, pp. 211-236, 2016.

[68] K. Choudhary, I. Kalish, R. Beams, and F. Tavazza, "High-throughput identification and characterization of two-dimensional materials using density functional theory," *Scientific reports,* vol. 7, p. 5179, 2017.

[69] K. Choudhary, G. Cheon, E. Reed, and F. Tavazza, "Elastic properties of bulk and low-dimensional materials using van der Waals density functional," *Physical Review B,* vol. 98, p. 014107, 2018.

[70] R. Gaillac, P. Pullumbi, and F.-X. Coudert, "ELATE: an open-source online application for analysis and visualization of elastic tensors," *Journal of Physics: Condensed Matter,* vol. 28, p. 275201, 2016.

[71] S. Zhang and R. Zhang, "AELAS: Automatic ELAStic property derivations via high-throughput first-principles computation," *Computer Physics Communications,* vol. 220, pp. 403-416, 2017.

[72] R. Golesorkhtabar, P. Pavone, J. Spitaler, P. Puschnig, and C. Draxl, "ElaStic: A tool for calculating second-order elastic constants from first principles," *Computer Physics Communications,* vol. 184, pp. 1861-1873, 2013.

[73] A. Marmier, Z. A. Lethbridge, R. I. Walton, C. W. Smith, S. C. Parker, and K. E. Evans, "ElAM: A computer program for the analysis and representation of anisotropic elastic properties," *Computer Physics Communications,* vol. 181, pp. 2102-2115, 2010.

[74] M. Born and K. Huang, *Dynamical theory of crystal lattices*: Oxford university press, 1996.

[75] Z. Zhou and B. Joós, "Stability criteria for homogeneously stressed materials and the calculation of elastic constants," *Physical Review B,* vol. 54, p. 3841, 1996.

[76] C. Kittel, "Introduction to Solid State Physics John Wiley & Sons Inc," *New York,* 2005.

[77] L. J. Sham and W. Kohn, "One-particle properties of an inhomogeneous interacting electron gas," *Physical Review,* vol. 145, p. 561, 1966.

[78] M. Segall, P. J. Lindan, M. a. Probert, C. J. Pickard, P. J. Hasnip, S. Clark, and M. Payne, "First-principles simulation: ideas, illustrations and the CASTEP code," *Journal of physics: condensed matter,* vol. 14, p. 2717, 2002.

[79] J. P. Perdew, K. Burke, and M. Ernzerhof, "Generalized gradient approximation made simple," *Physical review letters,* vol. 77, p. 3865, 1996.

[80] H. J. Monkhorst and J. D. Pack, "Special points for Brillouin-zone integrations," *Physical review B,* vol. 13, p. 5188, 1976.

[81] R. K. Wang, S. Kirkpatrick, and M. Hinds, "Phase-sensitive optical coherence elastography for mapping tissue microstrains in real time," *Applied Physics Letters,* vol. 90, 2007.

Chapter III

The solvent, number of layers and annealing temperature influence on CuO thin films properties.

III.1. Solvent effect

III.1.1. Introduction

The solvent significantly influences the optical and structural characteristics of CuO thin films, making it essential to study the solvent effect on their morphology and optical properties. Numerous studies have been conducted on the impact of solvents on CuO thin films. In this section, we explore the effects of different solvents on the structural, optical, and electrical properties of CuO thin films fabricated using the spin-coating method.

Table III. 1. Dielectric constants and boiling points for some alcohols [1] [2].

Samples	Alcohol	Formula	Dielectric constant at 20 C°	Boiling point (C°)
S1	Methanol	CH_3OH	32.35	64.7
S2	Ethanol	CH_3CH_2OH	25.00	78.3
S3	1-propanol	$CH_3CH_2CH_2OH$	20.81	97.2
S4	Isopropanol	$CH_3CH(OH)CH_3$	18.62	82.2
S5	Methoxyethanol	CH_3OCH_2CHOH	16.90	124.6
S6	Pentanol	$CH_3CH_2CH_2CH_2CH_2OH$	13.9 (at 25 C°)	138

The reaction mechanism can be understood as the thermal decomposition of copper acetate monohydrate into copper oxide in the presence of water, heat, and air. Different solvents used in this study, such as 1-propanol, 2-propanol, ethanol, methanol, and 2-methoxyethanol and influence this process, leading to the following formations:

- Reaction of copper acetate monohydrate with 1-propanol:

$$Cu\ (CH_3COO)_2 \cdot H_2O + C_3H_7OH \xrightarrow{\text{Heat}} CuO + CH_3COCH_3\uparrow + CO_2\uparrow + H_2O\uparrow + CH_3CH_2CHO\uparrow$$
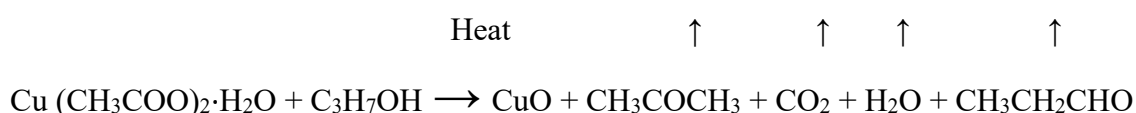
- Reaction of copper acetate monohydrate with 2-propanol:

Heat   ↑   ↑

$$Cu\,(CH3COO)_2 \cdot H2O + C_3H_7OH \longrightarrow CuO + 2CH_3COOH + H2O$$
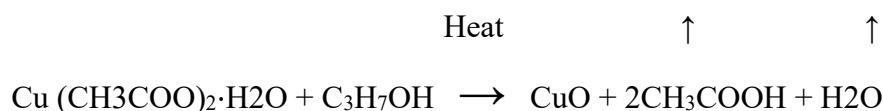
- Reaction of copper acetate monohydrate with ethanol:

Heat   ↑   ↑   ↑   ↑

$$Cu\,(CH_3COO)_2 \cdot H_2O + C_2H_5OH \longrightarrow CuO + CH_3COCH_3 + CO_2 + H2O + CH_3CHO$$
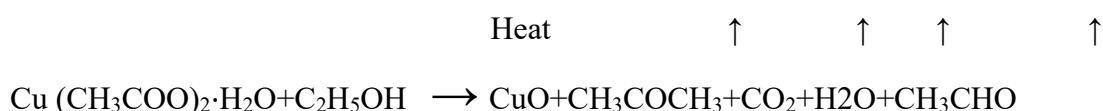
- Reaction of copper acetate monohydrate with methanol:

Heat   ↑   ↑   ↑   ↑

$$Cu\,(CH_3COO)_2 \cdot H_2O + CH_3OH \longrightarrow CuO + 2CH_3COOH + H_2O + CH_4 + CO2$$
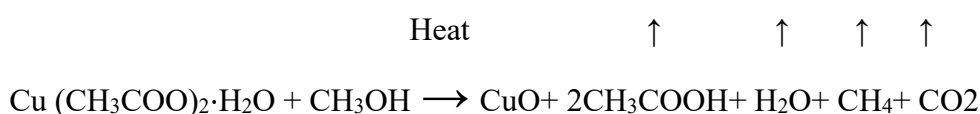
- Reaction of copper acetate monohydrate with 2-methoxyethanol:

Heat   ↑   ↑   ↑   ↑

$$Cu\,(CH_3COO)_2 \cdot H_2O + C_3H_8O_2 \longrightarrow CuO + 2CH_3COOH + H_2O + CH_3O - C_2H_5 + CO_2$$
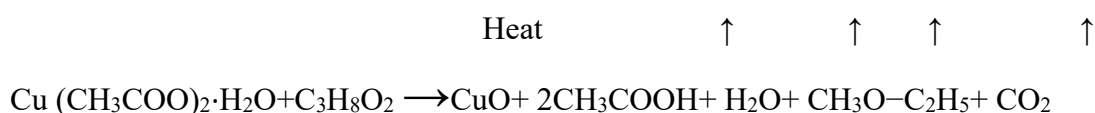
Reaction of copper acetate monohydrate with Pentanol:

Heat   ↑   ↑   ↑   ↑

$$Cu\,(CH_3COO)_2 \cdot H_2O + C_5H_{11}OH \longrightarrow CuO + 2CH_3COOH + H_2O + C_4H_{10} + CO2$$
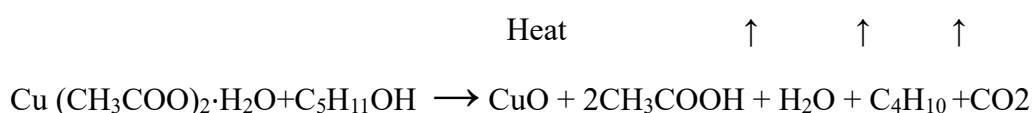
III.1.2. Result and discussions

III.1.2. 1. Structural properties:

The XRD patterns of CuO thin films synthesized using different solvents were observed within the diffraction angle range of 30° to 80°. All films exhibited a polycrystalline nature with a monoclinic crystal structure. The diffraction data were in good agreement with JCPDS card of CuO (JCPDS no.98-004-3179) [3], Two main peaks corresponding to the (100) and (002) planes were detected for all the solvents. No impurity peaks related to other phases, such as $Cu\,(OH)_2$, Cu_2O, or Cu, were observed in the XRD patterns, confirming the successful synthesis of pure and well-crystalline CuO nanoparticles without impurities are in good agreement with previously reported studies [4, 5].

The CuO films synthesized using 1-Propanol, Isopropanol, ethanol, and 2-Methoxyethanol showed the highest intensity at the (002) plane, indicating preferential crystal growth along the c-axis (002 orientation). In contrast, films synthesized using pentanol and Methanol exhibited high intensity in the (111) plane, suggesting that these solvents promote a different preferential orientation, likely influenced by their evaporation dynamics. Where, Solvents with higher boiling points evaporate more slowly during the heating phase, allowing the film to grow in a more controlled manner and favouring growth along the natural crystal orientation. In comparison, low boiling point solvents evaporate more rapidly, leading to faster deposition and less control over the crystal growth direction. As a result, the films tend to grow in multiple directions rather than a single preferred orientation. Foo. K.L et al., confirmed this behaviour by observing an increase in preferred orientation in the (002) plane, which is related to boiling points [6].

Additionally, the diffraction patterns demonstrate that all peaks exhibit broadening, as evidenced by an increase in full width at half maximum (FWHM) values. This broadening is influenced by the solvent and is attributed to a combination of small crystallite size and the presence of stresses and lattice defects within the films.
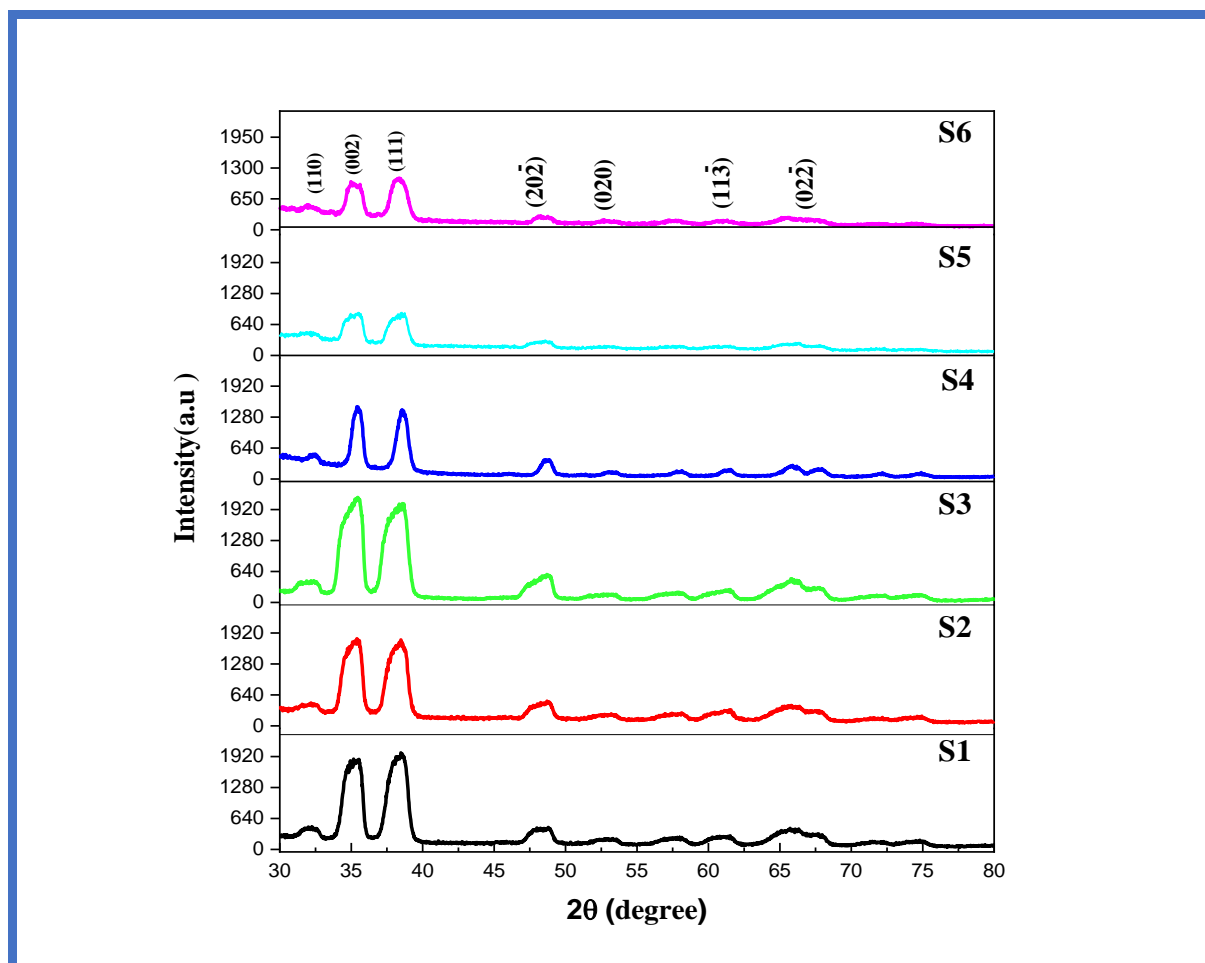
Figure III.1. X-ray diffraction pattern of CuO nanoparticles synthesized by sol-gel route with different solvents.

The average crystallite size (D) of the CuO films was calculated using the (002) peak diffraction and Scherrer's formula [7]. Table III.2**.** demonstrates a clear correlation between crystallite size and the solvent used for synthesis. isopropanol-based films exhibit the largest crystallite size, Hamidi et al. attribute this enhancement primarily due to the solvent's lower dielectric constant and lower polarity. These properties influence nucleation, growth kinetics, and hydrolysis rates, creating a favourable environment for the formation of larger crystallites [8]. However, Kumar and Mithal observed a positive correlation between crystallite size and the number of hydroxyl groups [9].

Table III.2. *The calculated values of crystallite size (D), lattice strain (ε) and dislocation density (δ$_{dislo}$) in CuO thin films.*

Samples	Average Grain size D (nm)	Dislocation density δ × 10^{-3}	Strain ε × 10^{-4}	Lattice parameter (Å)			
				a =	b=	c=	V=
Methanol	4.61	47.03	73.66	4.4509	3.4333	5.0731	76.4602
Ethanol	4.96	40.54	69.32	4.4874	3.4446	5.1373	78.3197
1-propanol	5.37	34.677	64.57	4.5090	3.4731	5.1283	79.2088
Isopropanol	8.76	13.03	39.56	4.4953	3.4813	5.1383	79.3089
Methoxyethanol	5.75	33.56	60.21	4.5082	3.4695	5.1300	79.1389
Pentanol	5.87	29.02	59.06	4.5176	3.4719	5.1555	79.7533

Table III.2. presents the strain and dislocation density values for CuO nanoparticles synthesized using various solvents. As shown, CuO nanoparticles prepared with methanol exhibit higher strain. This can be attributed to the smaller crystallite size associated with methanol, which leads to an increased density of grain boundaries and dislocations, resulting in elevated lattice strain [10].

As previously discussed, factors like boiling point [11], dielectric constant [8], and solvent polarity can affect crystallite size. This, in turn, influences lattice parameters, which were calculated using equation (2) and are presented in the aforementioned table

III.1.2.2. Optical properties:
Transmittance properties

The study aims to explore the impact of different solvents on the optical properties of CuO thin films, using UV-Vis-NIR (ultraviolet-visible-near infrared) spectroscopy to assess these effects. As shown in **Figure III.2.**, all films deposited on glass substrates are opaque, exhibiting lower transmission in the visible region, with a notable reduction in transmittance across infrared regions. This decrease may be attributed to factors such as surface roughness, structural defects, porosity, film thickness, crystallinity, film color, and surface structure.

The film produced using isopropanol as the solvent showed improved transmittance, which is attributed to its preferred c-axis orientation and larger crystallite size, as confirmed by XRD analysis. A greater grain size and preferred c-axis orientation typically enhance transmittance. Additionally, the optical transparency of the CuO thin films is significantly influenced by the boiling point of the solvents used. Solvents with higher boiling points tend to produce films with better optical transparency. Methanol, ethanol, and 1-propanol have comparatively lower boiling points than solvents like 2-methoxyethanol and pentanol. As a result, when solvents with lower boiling points are used, the CuO particles agglomerate quickly during evaporation, causing the film to become opaquer and reducing its transmittance. This explains why the film prepared with isopropanol exhibited higher transmittance compared to the others, as its boiling point allows for more controlled particle deposition and less agglomeration.

We conclude that isopropanol is the most effective solvent for regulating the growth orientation of CuO thin films, demonstrating its superiority in producing CuO films with exceptional structural and optical characteristics. R. Bekkari. Et al., has observed similar behaviour in ZnO [12].
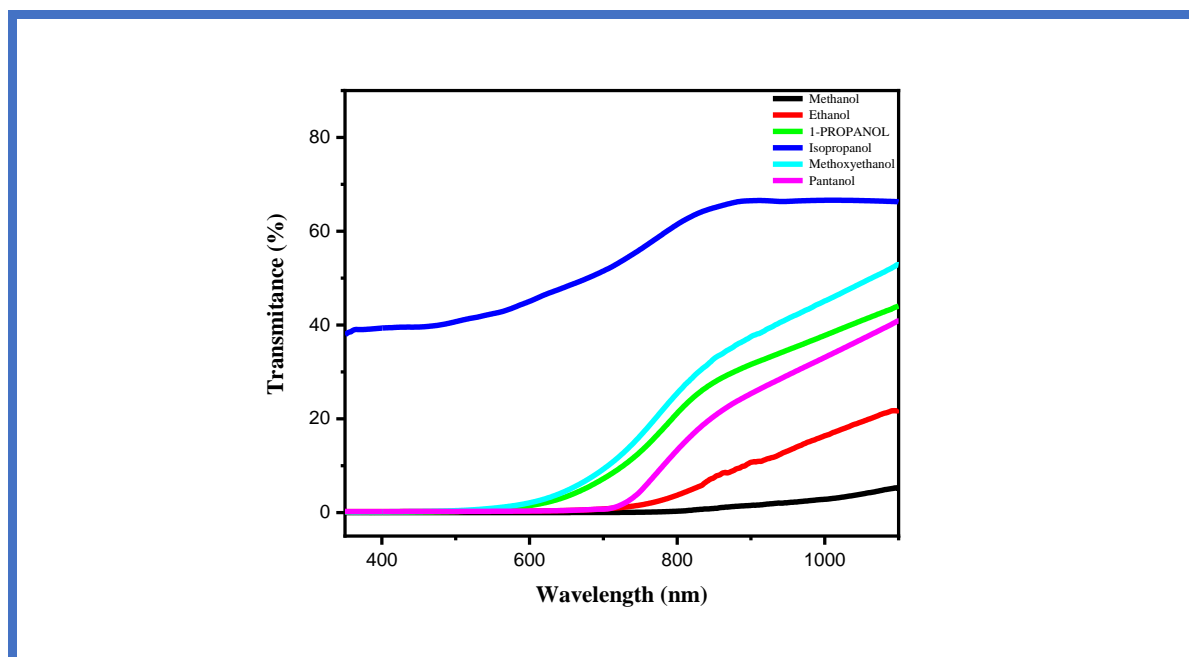
Figure III.2. Optical transmittance spectra of CuO thin films prepared with different solvents.

Band gap energy (Eg) and Urbach energy (Eu)

The optical bandgap of the films is determined by plotting $(\alpha h v)^2$ against photon energy hv. The bandgap energy Eg is calculated by extending the linear portion of the plot to the x-axis (photon energy) and finding its intersection point. This value, expressed in electron volts (eV), is depicted in **Figure III.3.** From these graphs, it's clear that the direct gap energy variation for different solvents can be related to the film structure that affects the film's inter-atomic bonds. Where, the direct gap energy variation for different solvents is primarily influenced by how these solvents affect the film's structure during synthesis. Smaller grains or amorphous regions lead to more grain boundaries and defects, which can introduce localized states in the band structure, narrowing or broadening the optical band gap. Films deposited using methanol and ethanol may have a smaller grain size, leading to higher defect density, while those formed with propanol or methoxyethanol may exhibit better crystallinity and larger grain sizes. Additionally, the variation in solvent properties such as polarity and boiling point can also influence the electronic properties, including the band gap [13]. In the case of methanol, ethanol, and propanol, these smaller alcohols have shorter carbon chains and higher polarity compared to pentanol and methoxyethanol. Their higher polarity can lead to stronger interactions with the film-forming materials, potentially influencing the film's crystal structure and interatomic bonding. This could result in a higher band gap. Conversely, isopropanol, methoxyethanol, and pentanol have longer carbon chains and lower polarity, which might result in weaker interactions with the film-forming materials. This could lead to a less ordered film structure and potentially a narrower bandgap.

The choice of solvent during the deposition of copper oxide thin films significantly impacts their microstructure, crystallinity, and defect density. Polar solvents like methanol and ethanol can lead to finer grain sizes and higher defect densities, resulting in increased Urbach energy due to localized states near the band edge. Conversely, less polar solvents like propanol or methoxyethanol promote better crystallinity, leading to lower Urbach energy values due to fewer defects and more ordered structures. Therefore, the solvent's polarity plays a crucial role in determining the film's microstructure and defect density, which ultimately influence the Urbach energy.
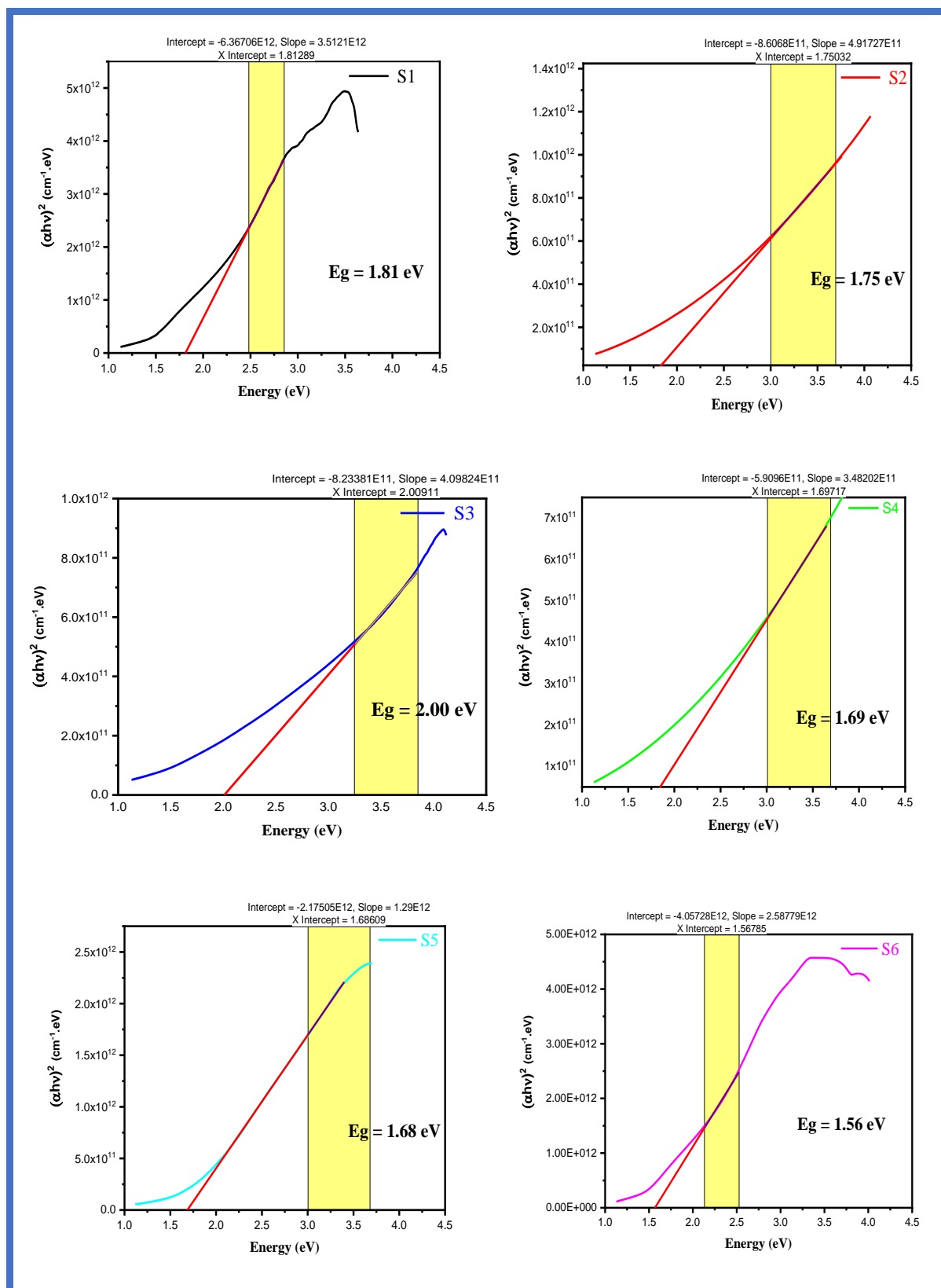
Figure III.3. Plots of $(\alpha h\upsilon)^2$ against $h\upsilon$ of CuO thin films prepared with different solvent
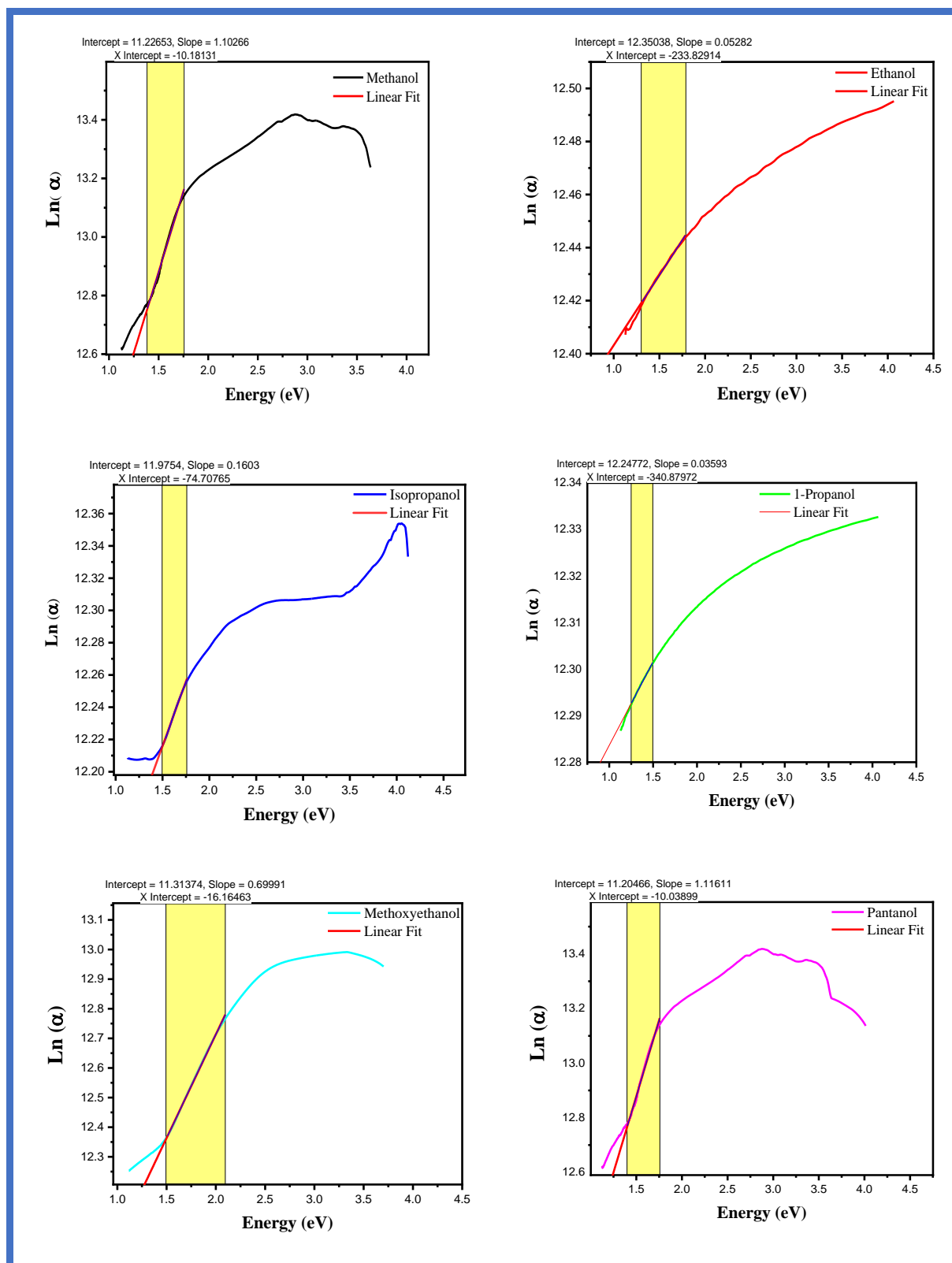
Figure III.4. Plots of Ln (α)against *hʋ* of CuO thin films prepared with different solvents

III.1.2.3. Electrical properties

Resistivity and conductivity values of CuO thin films deposited by the sol-gel technique using various precursor solvents were tabulated **Table III.3.** Conductivity values were found to be higher in samples prepared with methanol and ethanol solvents. This can be attributed to the higher dielectric constants of these solvents. A higher dielectric constant can reduce the electrostatic attraction between ions, increasing their mobility and decreasing resistivity. Additionally, the crystallite size of the CuO thin films may also influence conductivity. Smaller crystallites can lead to lower resistivity due to increased grain boundary scattering, which can hinder the movement of charge carriers.

Table III.3. Resistivity (ρ) and Conductivity (σ) of the CuO thin films prepared with different solvents.

solvents	Resistivity (Ω.cm)	Conductivity (Ω.cm)$^{-1}$
Methanol	1.722×10^3	5.807×10^{-4}
Ethanol	6.035×10^3	1.657×10^{-4}
1-propanol	9.154×10^3	1.0924×10^{-4}
Isopropanol	7.327×10^3	1.3648×10^{-4}
Methoxyethanol	12.780×10^3	0.7824×10^{-4}
Pentanol	18.431×10^3	0.5426×10^{-4}

III.2. Thickness effect

III.2.1. Introduction

Understanding and controlling the influence of thickness on CuO thin films is crucial for optimizing their properties to suit advanced technological applications. Consequently, this study explores how variations in the thickness of CuO thin films affect their structural and optical properties, with an emphasis on uncovering the mechanisms responsible for these changes.

III.2.2. Result and discussions

III.2.2.1. Thin film's thickness Measurement

Accurately determining the thickness of thin films is essential, as it significantly influences their properties and performance across various applications. The thickness of the prepared thin films was measured using the mass difference method.
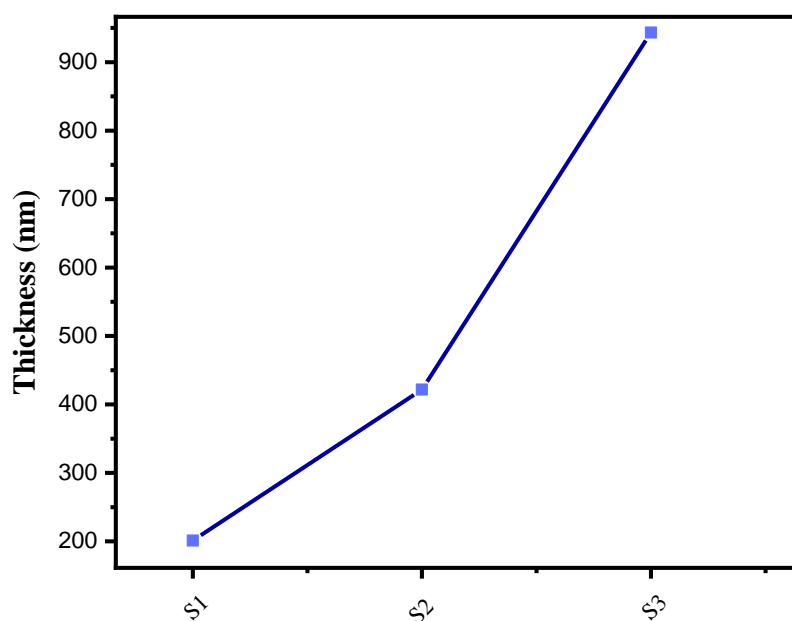
Figure III.5. Variation of CuO thin film thickness as a function of number of layers.

Figure III.5. and **Table III.4.** show the variation in film thickness with the number of layers. The results reveal an approximately linear increase in film thickness as the number of layers rises. This trend is likely due to the fact that each additional layer of material contributes to the overall thickness. As the number of layers increases, the total material volume grows, which can enhance inter-layer interactions and contribute to the overall structural integrity of the films.

Table III.4. Variation of CuO thin film thickness as a function of number of layers.

Samples	S1 (6 layers)	S2 (9 layers)	S3 (12 layers)
Thickness (nm)	201.060	421.748	943.23

III.2.2. 2. Structural properties:

XRD analysis

The X-ray diffraction (XRD) patterns of the CuO thin films with varying thicknesses, prepared using the spin coating technique, are presented in **Figure III.6**. The well-resolved diffraction peaks demonstrate the high crystallographic quality of all the CuO thin layers.

All the deposited films exhibit a polycrystalline nature, evidenced by the presence of multiple peaks. These peaks correspond to the JCPDS reference data for CuO (JCPDS No. 98-004-3179), confirming the monoclinic crystal structure and tenorite phase. Notably, no additional phases of copper oxide, such as Cu_2O, were detected in any of the samples.

As the film thickness increases up to 421.748 nm, more material becomes available for diffraction, which typically leads to an increase in peak intensity. This is because, in the initial stages of film deposition, the crystallites (or grains) become better ordered as the film thickens, particularly in processes like spin coating. This enhanced crystallinity results in sharper, more intense diffraction peaks. Moreover, the two main peaks around 35.6° and 38.7° correspond to the (111) and (111) crystallographic planes, respectively, of the CuO monoclinic structure. These are specific diffraction angles that are characteristic of CuO's crystal structure. Similar results were found by other authors [14]. However, we can see that beyond a certain thickness (up to 421.748 nm), the intensity of the XRD peaks starts to decrease. This decrease can be

attributed to several factors, including material saturation. Once the film reaches a certain thickness, additional layers do not significantly contribute to the diffraction intensity. The X-rays are already strongly diffracting from the existing crystallographic planes, and adding more material does not substantially increase the amount of diffraction material for the X-rays to interact with.

For thinner films, the intensity of the diffraction peaks typically increases with thickness due to the higher number of crystallites, more ordered crystallographic planes, and greater material density. However, for films thicker than a critical threshold, the intensity begins to drop due to factors such as saturation of diffraction signals, the formation of defects, reduced crystallinity, and the limited ability of X-rays to penetrate deeper into the thicker layers effectively.
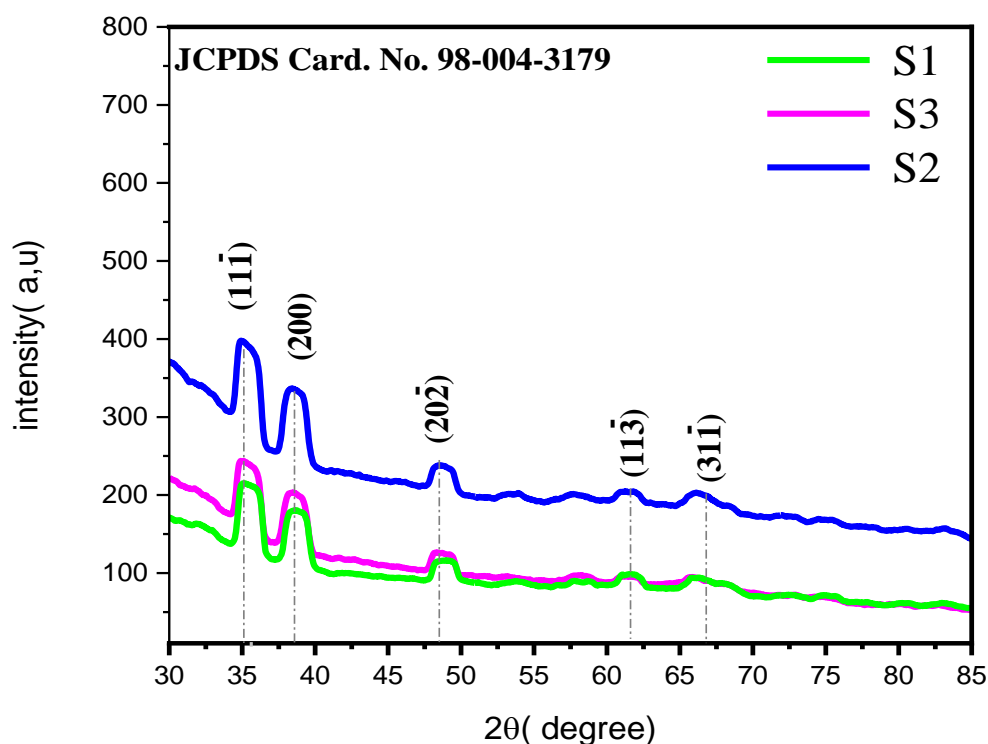
Figure III.6. X-ray diffraction pattern of CuO nanoparticles synthesized by sol-gel route with different thicknesses.

Chapter III
*The solvent, number of layers and annealing temperature
influence on CuO thin films properties.*

Crystallite size

The average crystallite size was calculated using Scherrer's formula, and the results are summarized in **Table III.5.** The data show a slight increase in crystallite size from 10.285 nm (6 layers) to 15.115 nm (9 layers) with increasing film thickness. However, for 12 layers, the crystallite size decreased slightly to 10.14 nm. As additional layers are deposited, the crystallization of the film may evolve. Typically, the initial layers form a highly ordered crystalline structure, and with the addition of more layers, the crystallites may grow larger, resulting in a denser and more uniform film. Conversely, excessive thickness can adversely affect the film quality, potentially disrupting crystallization and uniformity.

Table III.5. Structural parameter variations of CuO thin films as a function of thickness

Samples	2θ (°)	Plan (hkl)	Average Grain size D (nm)	Average Grain size D (nm)
S1	35.46	(-111)	10.94	10.285
	38.58	(111)	9.63	
S2	35.40	(-111)	15.77	15.115
	38.56	(111)	14.46	
S3	35.16	(-111)	11.55	11.04
	38.48	(111)	10.53	

Strain and Dislocation density

The calculated strain and dislocation density of the CuO thin films as a function of thickness are summarized in **Table III.6.** The data reveal that the structural parameters are influenced by variations in film thickness. The smallest crystallite size, observed for the thinnest sample (S1, 201.060 nm), corresponds to the highest dislocation density. From the second thickness value (S2, 421.748 nm), the crystallite size increases with film thickness, leading to a decrease in dislocation density and an improvement in crystallinity. However, at a higher thickness (S3, 943.23 nm), the dislocation density increases again. on other hand, it can be noted

that the stress in CuO films is lower for a thickness of 485 nm. The stress in the films can mainly be attributed to two factors: intrinsic stress, which results from impurities and defects in the crystal, and extrinsic stress, which arises from factors such as lattice mismatch, growth conditions, and the difference in the thermal expansion coefficients of the film and the substrate. Based on these results, S2 is identified as the optimal thickness for achieving the best crystallographic quality in the CuO thin films this is in good agreement with other research work by [15].

Table III.6. Variation of strain and dislocation density in CuO thin films as a function of thickness.

Samples	S1 (6 layers)	S2 (9 layers)	S3 (12 layers)
Strain ε (x10⁻⁴)	33.06	23.015	31.45
Dislocation density δ (x10¹⁴ lines) m⁻²	9.56	4.41	8.98

III.2.2.3. Optical properties
Transmittance Spectrum:

Figure III.7. illustrates the variation in transmittance as a function of wavelength for samples with different thicknesses. The optical transmittance in the UV-VIS-NIR wavelength range for various samples is shown in **Figure III.7.** As the number of layers increases, the film transparency decreases significantly, ranging from 70% to 30%.

The mechanism behind the observed optical transmission behavior remains unclear and may be attributed to two primary factors:

i. the increase in film thickness.

ii. The increase in surface roughness of the films.

Transmittance is governed by the relationship ($T \propto e^{-\alpha d}$), where d is the film thickness and α is the absorption coefficient. Consequently, as the film thickness increases, transmittance decreases, leading to reduced transparency.

Additionally, the absence of interference fringes in the deposited films is notable. Interference fringes typically arise from multiple reflections at the film/substrate and film/air interfaces, which occur when the films are sufficiently thick and the surface is smooth. However, in this case, the roughness of the film surface promotes light scattering, which reduces reflection and suppresses the formation of interference fringes. This observation indicates that the surfaces of all deposited films are inherently rough.
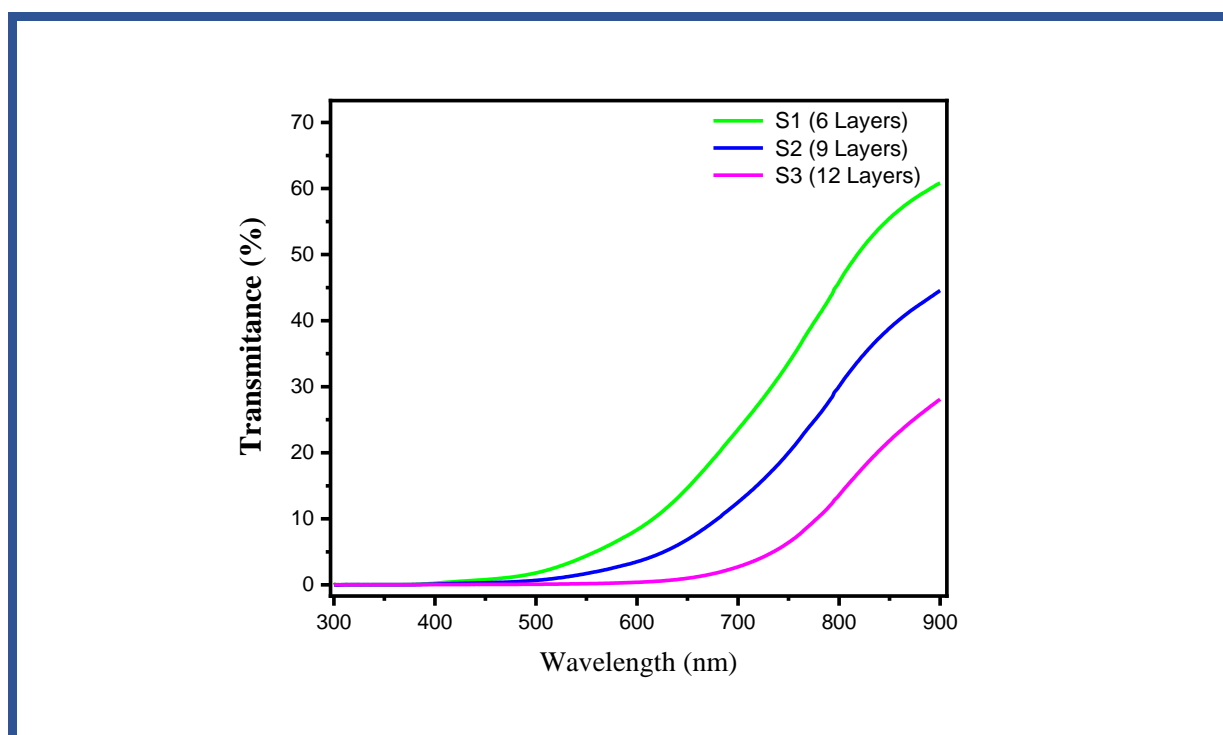
Figure III.7. illustrates the variation in transmittance as a function of wavelength for samples with different thicknesses.

Band gap energy (Eg) and Urbach energy (E*u*)

The most notable feature in this figure is the shift of the absorption band edge toward longer wavelengths, which corresponds to a narrowing of the optical band gap, as shown in **Figure III.8.** With an increase in the molarity of the precursor solution, the optical band gap decreases from 2.79 eV to 2.11 eV. This reduction in the band gap can also be attributed to an increase in disorder within the film networks. This behavior was corroborated by S. Atta [16]

The relationship between film disorder and number of layers is depicted in **Figure III.9.** It is evident that as the molarity increases, the disorder in the films rises significantly, from 328.803 meV to 389.581 meV. Conversely, the optical band gap and film disorder exhibit an inverse relationship, indicating that the variation in the optical band gap is primarily governed by the degree of disorder in the film network.
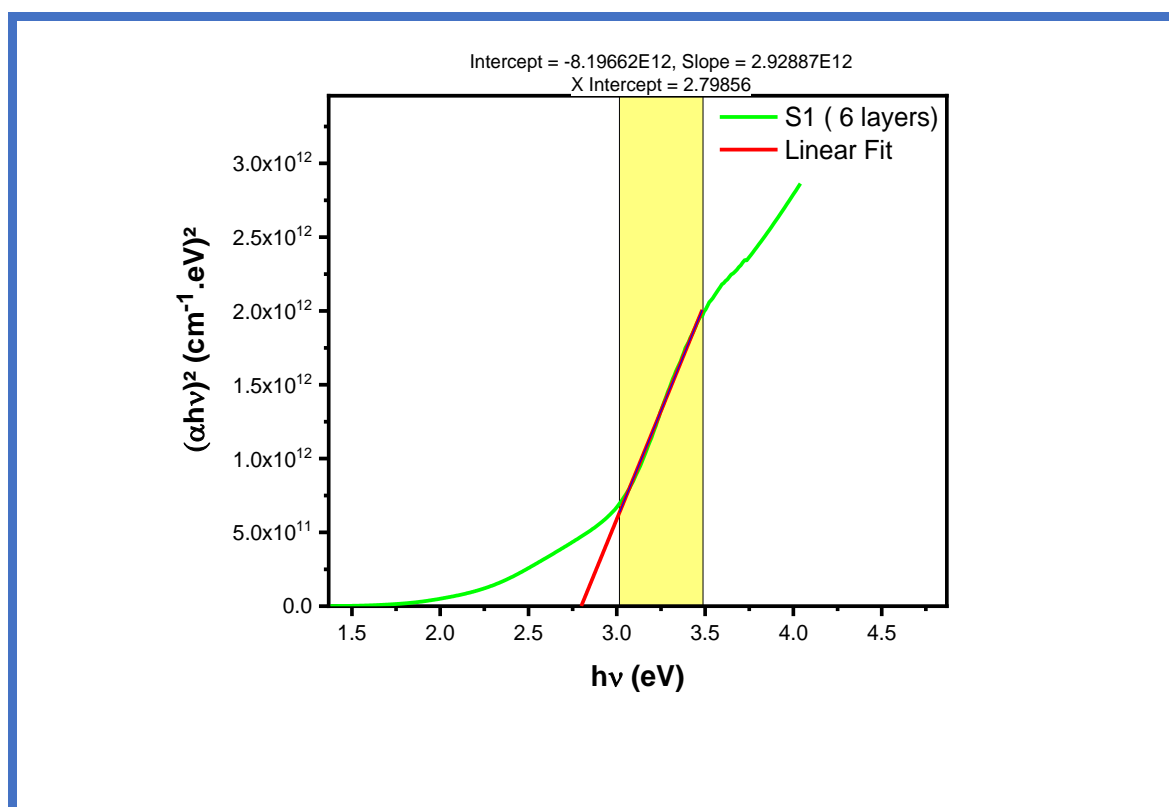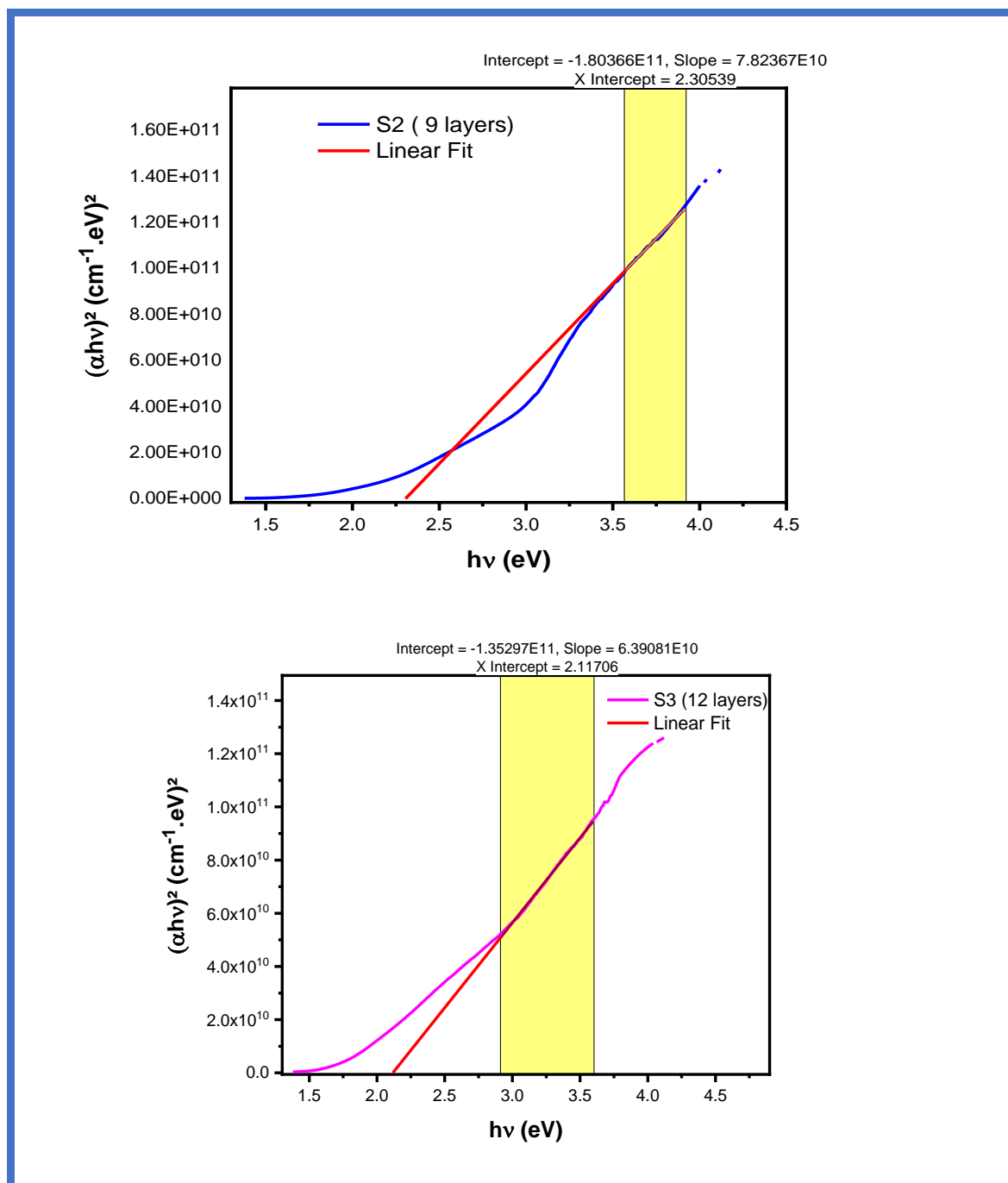
Figure III.8. Variation of $(\alpha h\nu)^{1/2}$ as a function of $h\nu$ to determine the energy gap of CuO thin films.

Intercept = 5.85128, Slope = 3.04133
X Intercept = -1.92392

Intercept = 5.48933, Slope = 2.56686
X Intercept = -2.13854
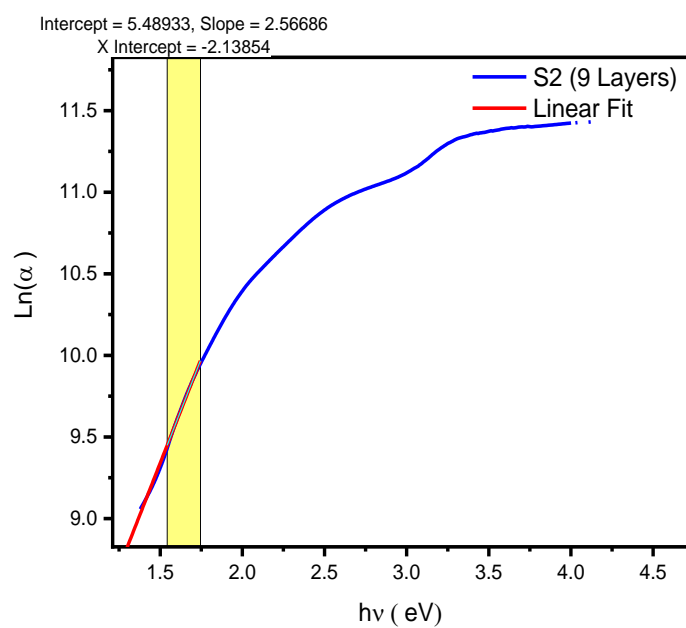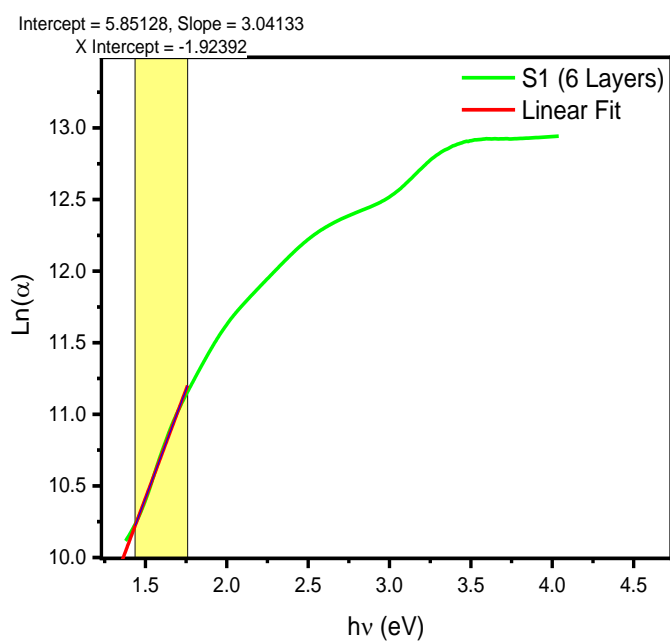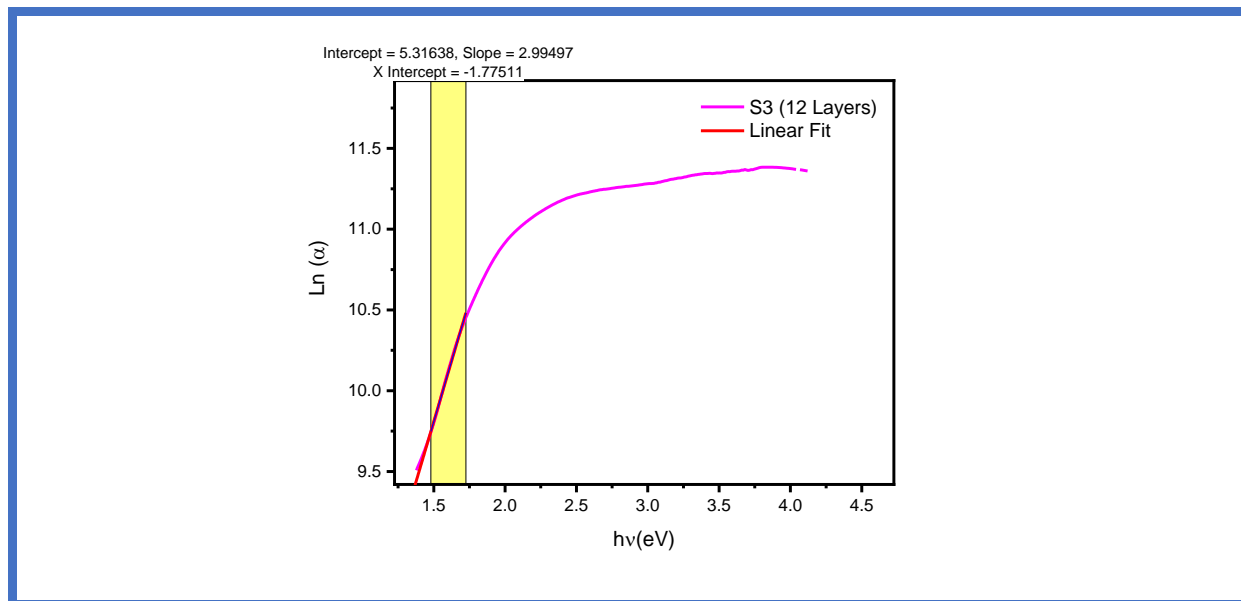
Figure III.9. Variation of Ln(α) as a function of hν for determining the Urbach energy (E*u*) of CuO thin films.

III.2.2.4. Electrical properties

This section explains how the thickness of copper oxide (CuO) thin films influences their resistivity, as shown in Table 1. The table provides the measured values of resistivity and conductivity for films with varying thicknesses. The resistivity of the CuO films decreases as their thickness increases, up to a thickness of 421.748 nm. Correspondingly, conductivity increases with thickness up to this point. This improvement in conductivity is likely due to the enhancement of crystallinity. As the crystallite size grows, the number of grain boundaries decreases, which reduces the barriers to electrical transport as seen in other studies[17]. With fewer grain boundaries, the mobility of free charge carriers increases, leading to lower resistivity. Additionally, K. Kamli and colleagues have confirmed that increasing the thickness of CuO films improves their conductivity[18].

Table III.7. The electrical conductivity and resistivity of the CuO thin films as a function of thickness.

Samples	S1 (6 layers)	S2 (9 layers)	S3 (12 layers)
R sheet $\times 10^5$	136.405	17.5	22.10
Resistivity $\times 10^2$ (Ω.cm)	2.743	0.73806	2.083
Conductivity $\times 10^{-2}$ (Ω.cm)$^{-1}$	0.3646	1.355	0.480

III.3. Annealing temperature effect

III.3.1. Introduction

In essence, the annealing temperature plays a crucial role in determining the final properties of CuO thin films. created using the spin coating technique. Annealing temperature effect on structural, optical and electrical properties of CuO films have been investigated.

III.3.2. Result and discussions

III.3.2.1. Structural properties:

XRD analysis

Figures III. (10-15). displays the X-ray diffraction (XRD) patterns of copper oxide films annealed at different temperatures, including an as-prepared sample. The film deposited at a relatively low temperature of 230°C exhibited a clear mixture of tenorite (CuO) and cuprite (Cu_2O) phases, indicative of a partially oxidized and unstable state. At this temperature, the copper oxide film may not have undergone complete oxidation. Similar behavior has been reported in previous studies [19].

Interestingly, after annealing at 300°C and above, all samples displayed peaks centered around 35.89° and 38.77°, corresponding to the (-111) and (111) planes, respectively. The CuO composition remained stable after annealing at 300°C. These observations are consistent with the findings reported by Xuyang Li et al., [20]. This observation suggests that all samples possess a polycrystalline nature and align with the characteristic peaks of a monoclinic structure.

As can perceive from the XRD spectra, the intensity of this peaks is affected by the change in annealing temperatures. It is noted that the increase in the annealing temperature leads to the increase in the peak intensity. This behavior was validated by Hussain et al., [21] The increase in the peak intensity of the layer annealed at 600°C is remarkable compared to that annealed at 400 and 550°C.The significant increase in peak intensity for the film annealed at 600°C compared to those annealed at lower temperatures indicates a substantial improvement in crystallinity
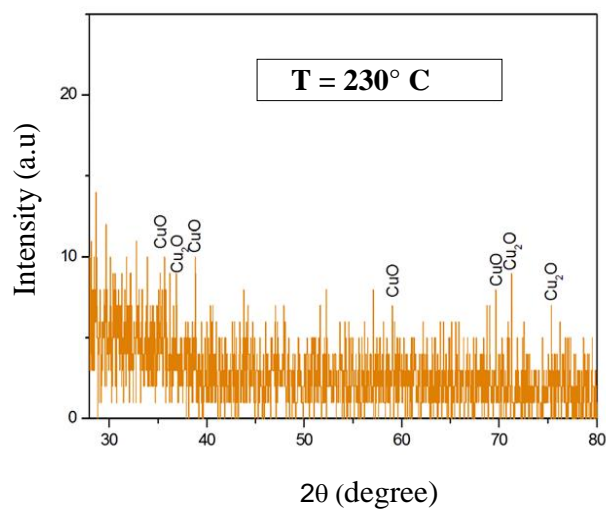
Figure III.10. X-ray diffraction pattern of CuO treated at 230°C.
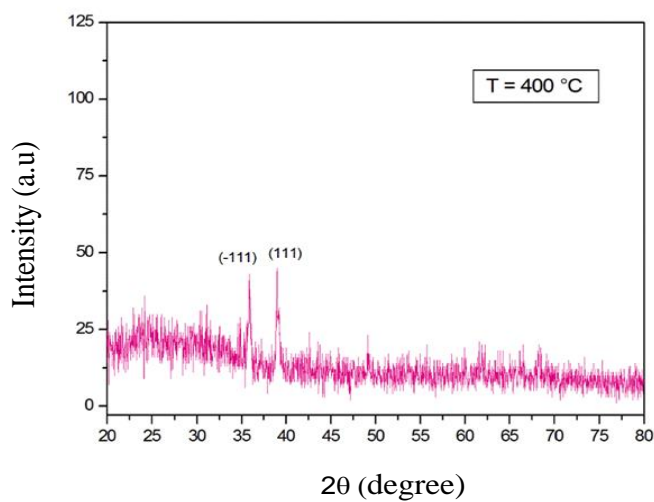
Figure III.11. X-ray diffraction spectrum of CuO annealed at 400°C.
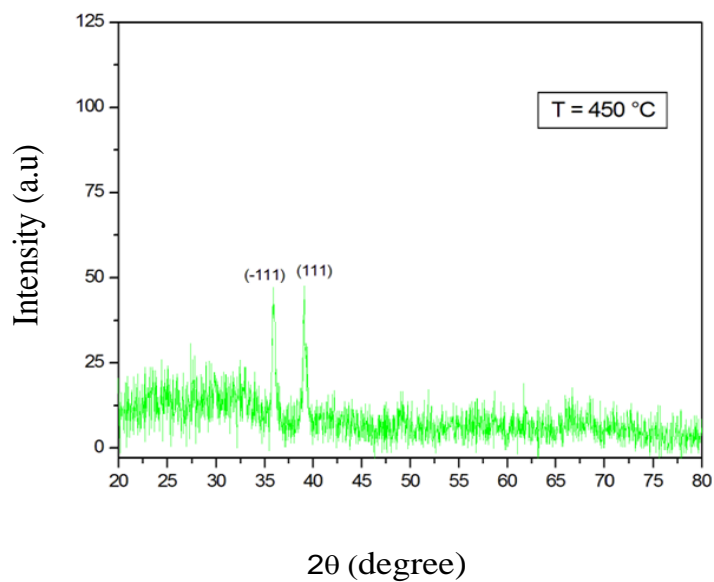
Figure III.12. X-ray diffraction spectrum of CuO annealed at 450°C.
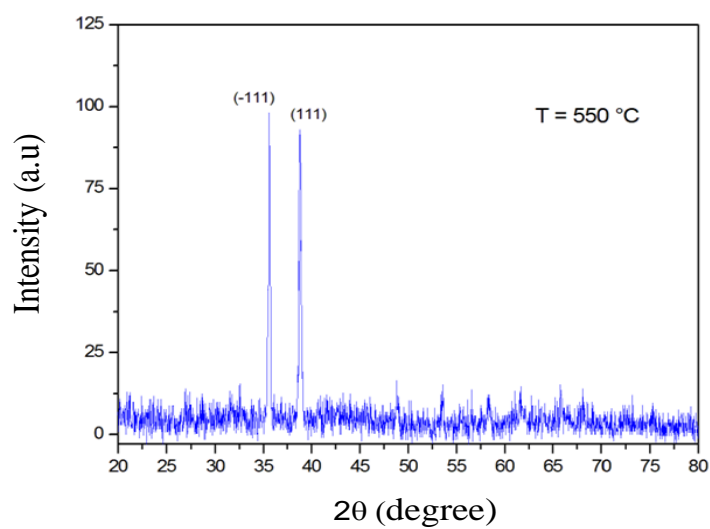
Figure III.13. X-ray diffraction spectrum of CuO annealed at 550°C.
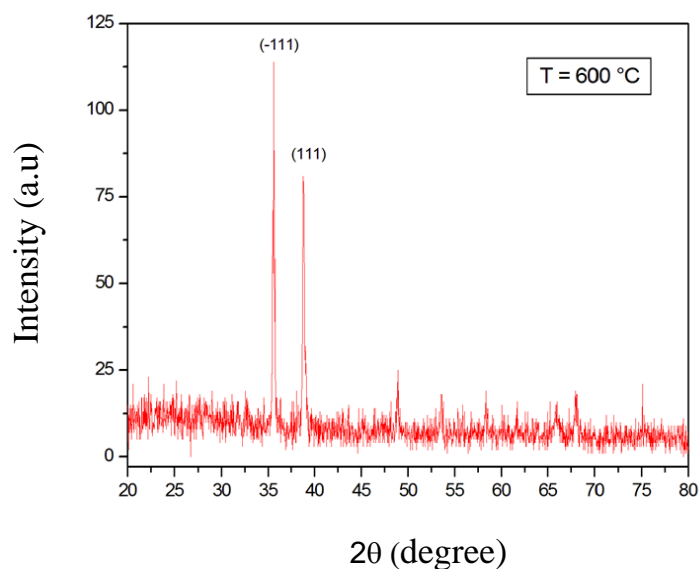
Figure III.14. X-ray diffraction spectrum of CuO annealed at 600°C.

Lattice parameters:

The various angle values for the (-111) and (111) planes of our films are compiled in **Table III.8.** These values include lattice parameters and calculations derived from the X-ray diffraction measurements.

Table III.8. Structural parameter variations of CuO thin films as a function of annealing temperature.

T (°C)	400	450	550	600
a (°A)	4.662	4.689	4.6840	4.6883
b (°A)	3.416	3.420	3.425	3.4229
c (°A)	5.118	5.13	5.129	5.1319
V (°A³)	80.39	80.42	81.16	81.22

The lattice parameter of CuO thin films is observed to increase with higher annealing temperatures. This expansion is primarily attributed to thermal expansion, where the increased thermal energy causes the lattice to expand. Additionally, changes in the crystal structure, such as phase transformations or oxygen incorporation, can influence the lattice size. These structural adjustments may result in a slight increase in the lattice parameter as the material adopts a more stable or slightly altered crystal structure [22].

Crystallite size

The grain size of each sample was determined using the Scherrer formula applied to the full width at half maximum (FWHM) of the most intense peaks (-111) and (111). The results are summarized in **Table III.9.**

Table III.9. Grain size variation as a function of annealing temperature.

Annealing Temperature (°C)	2θ (°)	Plan (hkl)	FWHM (°)	Average crystallite size D (nm)	Average crystallite size D (nm)
400	35.89	(-111)	0.433	19.285	20.05
	39.1	(111)	0.405	20.816	
450	35.86	(-111)	0.2952	28.286	27.823
	38.98	(111)	0.308	27.360	
550	35.62	(-111)	0.216	38.630	39.561
	38.8	(111)	0.208	40.493	
600	35.6	(-111)	0.156	53.485	55.984
	38.77	(111)	0.144	58.484	

The increase in crystalline size from 20.05 nm to 55.98 nm as annealing temperatures rise from 230°C to 600°C is primarily due to enhanced atomic mobility and grain growth at higher temperatures. At elevated temperatures, the increased energy allows atoms in the crystal lattice to migrate more freely, reducing defects and enabling smaller crystallites to merge into larger, more stable grains. This process, known as grain growth, leads to a gradual increase in crystalline size as the material transitions into a more ordered and thermodynamically favorable structure. Moreover, Higher annealing temperatures also help relieve internal stresses and promote phase transformations, further stabilizing the larger crystal structure and contributing to the overall growth in crystalline size [23].

Strain and Dislocation density

The calculated values of δ are presented in **Table III.10.** illustrate the variation in dislocation density and the strain with respect to annealing temperature.

Table III.10. *Variation of dislocation density and strain in CuO thin films as a function of annealing temperature.*

Temperature (°C)	400	450	550	600
Strain ε ($\times 10^{-2}$)	0.18	0.12	0.09	0.06
Dislocation density δ ($\times 10^{14}$ lines) m^{-2}	24.9	12.92	6.93	3.20

As observed in the table, dislocation density typically decreases as the annealing temperature rises. At elevated temperatures, atoms within the crystal lattice gain increased energy and mobility. This enables them to rearrange and minimize lattice imperfections, such as dislocations. Some dislocations may merge or be eliminated entirely, contributing to a more stable crystalline structure. Similarly, strain tends to decrease with higher annealing temperatures. Elevated temperatures promote stress relaxation within the material, allowing it to attain a more ordered, lower-energy state. This reduction in strain is attributed to the release of trapped defects and the reorientation of grains during recrystallization at higher temperatures [22].

III.3.2.2. Optical properties

Transmittance Spectrum:

Figure III.15. shows the variation of transmittance as a function of wavelength for samples annealed at different temperatures.
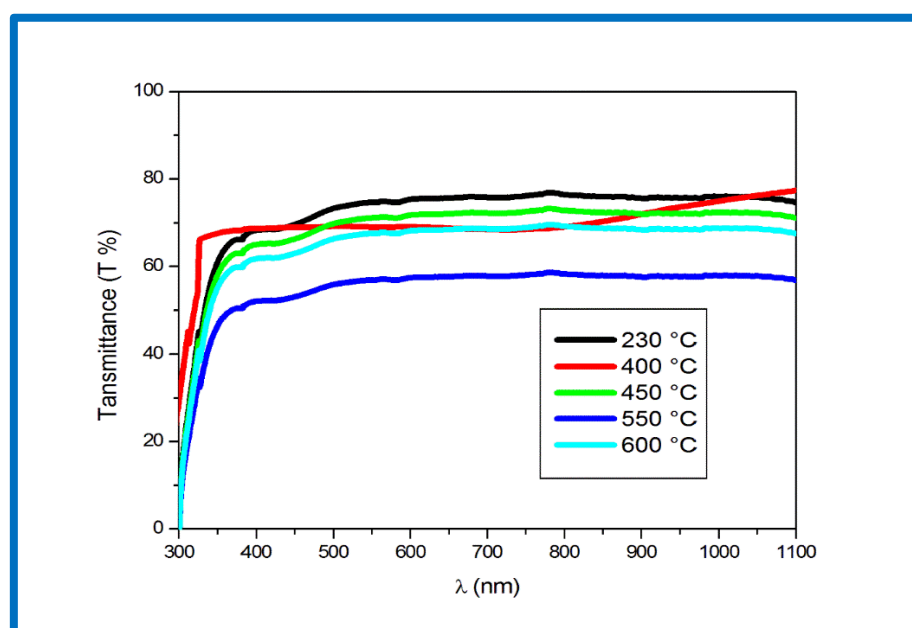
Figure III.15. Transmittance spectra as a function of wavelength**.**

Figure III.15. depicts the optical transmittance of copper oxide thin films prepared by spin coating at different annealing temperatures. The transmittance spectra were recorded over a wavelength range of 300–1100 nm, with values ranging from 59% to 80% in the 400 nm to 1100 nm range. The observed decrease in transmittance at 550°C may be due to increased surface roughness of the films annealed at this temperature. This roughness can result in the refraction of radiation at the film/air interface, causing the incident light to scatter in multiple directions instead of being reflected. Similar experimental results observation have also been reported by other works [24]

Band gap energy (Eg) and Urbach energy (Eu)
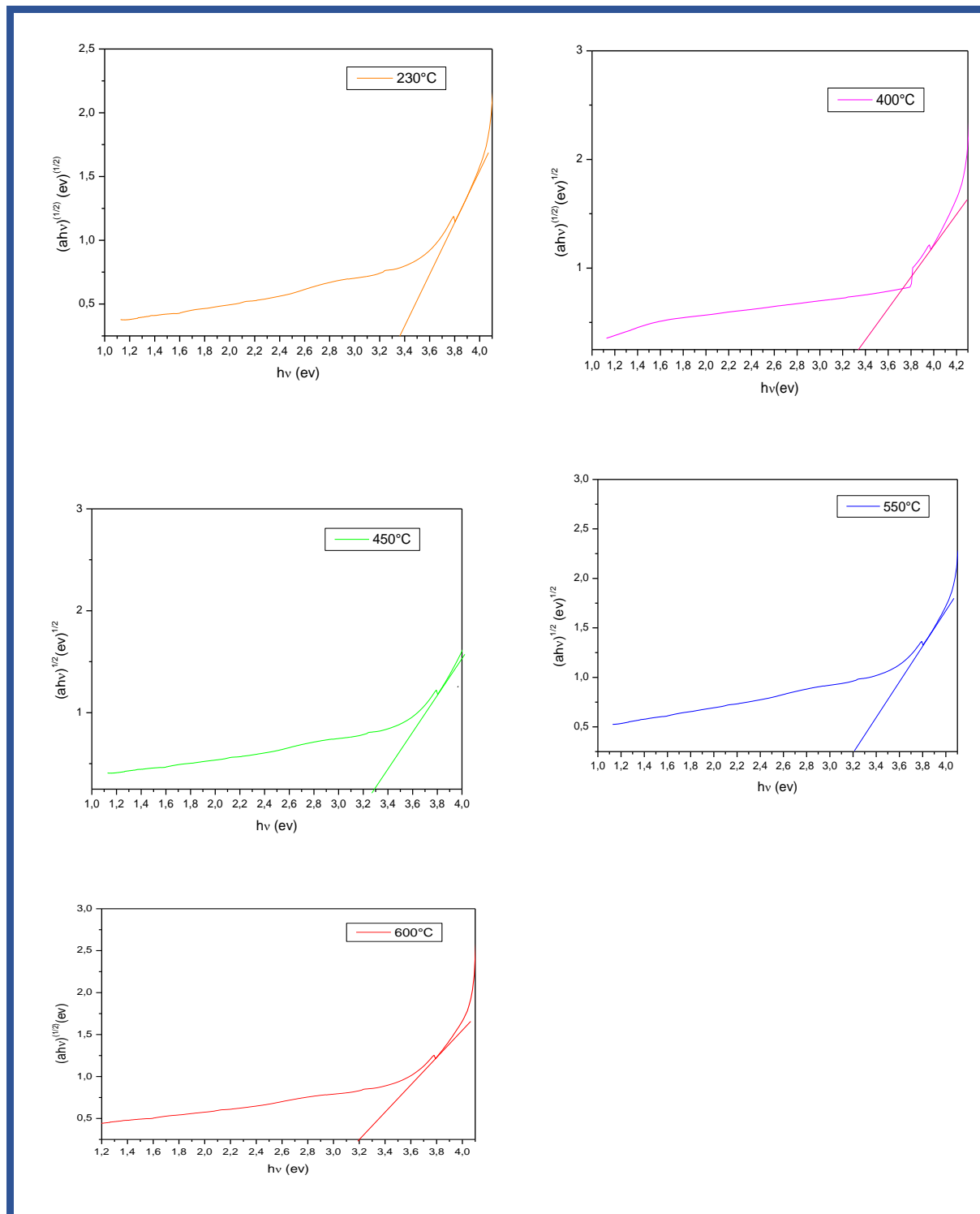
Figure III.16. Variation of $(\alpha h\nu)^{1/2}$ as a function of $h\nu$ to determine the energy gap of CuO thin films.

Table III.11. Variation the energy gap of CuO thin films.

Temperature (°C)	230	400	450	500	600
E_g (eV)	3.36	3.34	3.29	3.20	3.19

Figure III.16. shows the optical band gap (Eg) of CuO thin films as a function of annealing temperature, based on the data in **Table III.11.** Revealing a decrease in the band gap with increasing temperature. This reduction is due to two main factors: the increase in crystal size and the reduction of defects. As annealing temperature rises, the crystal grains grow larger, reducing quantum confinement effects and slightly narrowing the band gap. Additionally, higher temperatures reduce grain boundaries and defects that contribute to localized states, leading to a more uniform electronic structure and a narrower band gap. A similar decrease in the optical bandgap with increasing annealing temperature has been reported in the literature for copper oxide thin films prepared using chemical deposition and radio frequency magnetron sputtering methods [19, 25].

Disorder (Urbach Energy):

The Urbach energy E_u is a key parameter that reflects the level of disorder in the material. Using equations (II.10) and (II.11) from the previous chapter, we obtained the following curves:
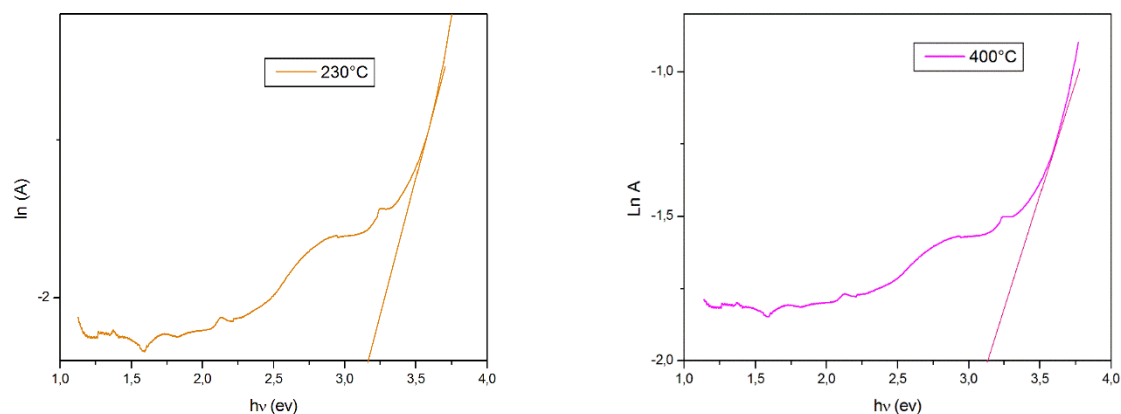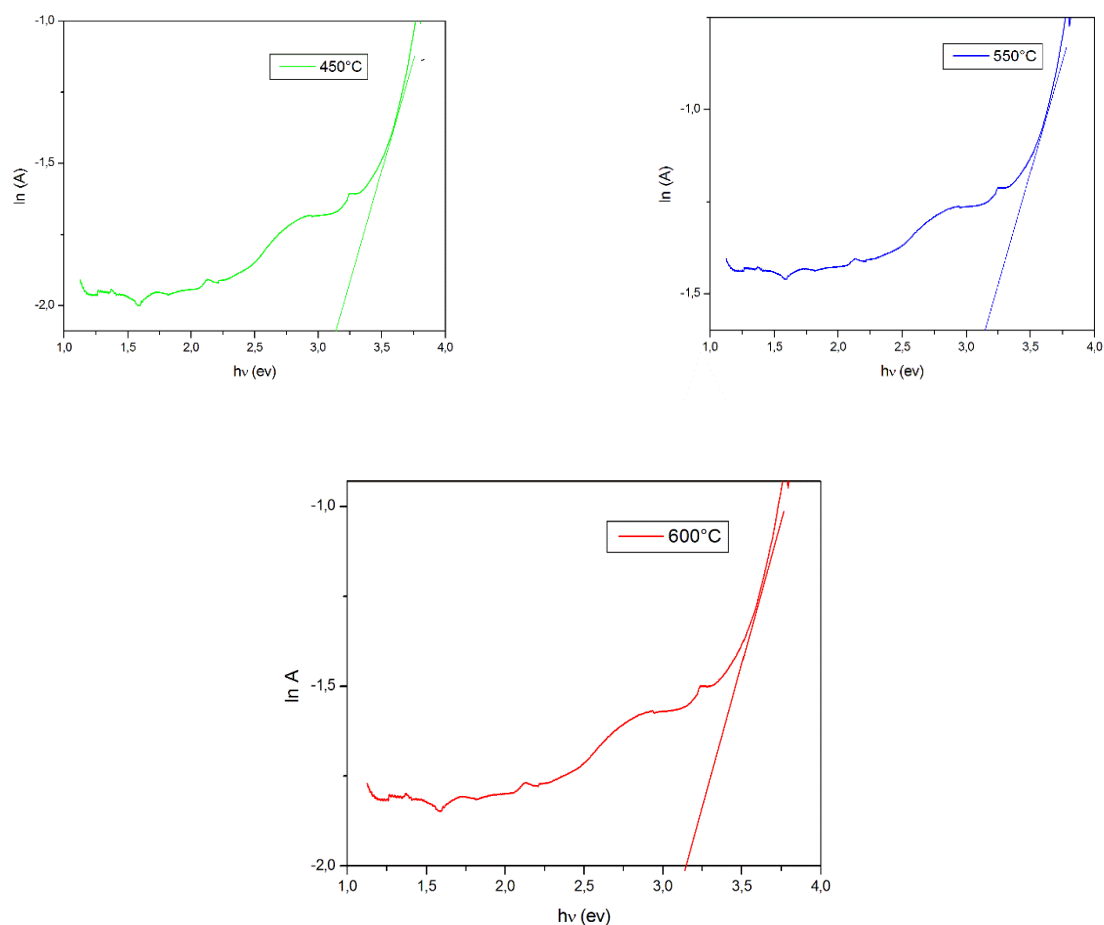
Figure III.17. Variation of Ln(A) as a function of hν for determining the Urbach energy (Eu) of CuO thin films.

Table III.12. Variation of Eu with annealing temperature.

Temperature (°C)	230	400	450	550	600
Eu (eV)	0.315	0.318	0.317	0.316	0.316

Figure III.17. shows a reduction in disorder as annealing temperature increases, which indicates improved crystallization. At higher annealing temperatures, crystal grains grow larger and more ordered, leading to fewer structural defects. This enhanced grain formation results in a more uniform and stable crystal structure, reducing the disorder within the material.

III.3.2.3. Electrical Characterization

The table below summarizes the electrical properties of our samples annealed at various temperatures. To measure the conductivity or resistivity of the CuO layers, the four-point method was applied.

Table III.13. Electrical properties of CuO films as function of annealing temperature.

Temperature (°C)	230	400	450	550	600
Resistivity $\times 10^2$ (Ω.cm)	0.0163	0.0135	0.0149	0.0067	0.0168
Conductivity $\times 10^{-2}$ (Ω.cm)$^{-1}$	61.292	73.5510	66.8645	147.1020	59.3153

The increase in conductivity and corresponding decrease in resistivity of CuO thin films with rising annealing temperatures (230°C to 600°C, peaking at 550°C) can be attributed to enhanced crystallinity and reduced defects within the material. At 550°C, the conductivity reaches its maximum, likely due to an optimal balance between grain growth and defect reduction, where the crystal structure is well-ordered with minimal structural imperfections. This temperature provides ideal conditions for maximizing grain size and minimizing defects, allowing for efficient charge carrier movement. Beyond 550°C, further structural changes or grain growth may have a diminishing effect on conductivity, and slight structural degradation may even cause a slight increase in resistivity.

III.4. Conclusion

The structural, optical, and electrical properties of CuO thin films are significantly influenced by solvent choice, film thickness, and annealing temperature.

Solvent Effects: The films exhibit a polycrystalline monoclinic structure, with solvents like Isopropanol, 1-Propanol, ethanol, and 2-Methoxyethanol promoting growth along the c-axis (002 plane), while Pentanol and Methanol favor growth along the (111) plane due to faster evaporation. Isopropanol-based films show the largest crystallite size and improved optical transmittance, while methanol leads to smaller crystallites with higher strain. Higher dielectric constants in methanol and ethanol increase conductivity by enhancing ion mobility.

Annealing Temperature Effects: Annealing at temperatures above 300°C stabilizes the CuO phase, improving crystallinity and increasing crystallite size. At higher temperatures, such as 600°C, films exhibit a marked increase in crystallite size (from 20.05 nm to 55.98 nm), reduced strain, and enhanced lattice stability. Optical properties improve with larger grains, resulting in a decrease in band gap energy from 3.36 eV to 3.19 eV. The films show improved conductivity at 550°C due to optimal grain size and minimal defects, though further temperature increases beyond this point lead to slight conductivity degradation.

In summary, by optimizing the effects of thickness, solvent, and annealing temperature, CuO thin films with ideal properties for various applications such as high optical transmittance, low resistivity, and good crystallinity can be synthesized. Selecting the appropriate solvent (ethanol) and annealing at 550°C with 9 layers, resulting in an approximate thickness of 400 nm, allows for an optimal balance between crystallite size, transparency, and conductivity.

Reference

[1]   M. Z.-C. Hu, E. A. Payzant, and C. H. Byers, "Sol–gel and ultrafine particle formation via dielectric tuning of inorganic salt–alcohol–water solutions," *Journal of colloid and interface science,* vol. 222, pp. 20-36, 2000.

[2]   A. D'Aprano, D. I. Donato, and V. Agrigento, "Static dielectric constant, viscosity, and structure of pure isomeric pentanols," *Journal of Solution Chemistry,* vol. 10, pp. 673-680, 1981.

[3]   M. Boumezrag, K. Almi, S. Lakel, and H. Touhami, "Alkali Metals Doped Cu0. 94A0. 06O (A= Li, Na and K) Thin Films: Facile Synthesis, Structural, Optical and Thermoelectric Properties," *Russian Journal of Physical Chemistry B,* vol. 18, pp. 895-906, 2024.

[4]   N. Zayyoun, B. Jaber, L. Laânab, E. Ntsoenzok, and R. Bekkari, "Effect of solvent on the morphological and optical properties of CuO nanoparticles prepared by simple sol-gel process," *J. Mater. Environ. Sci,* vol. 7, pp. 1791-1797, 2016.

[5]   M. Abaker, A. Umar, S. Baskoutas, S. Kim, and S. Hwang, "Structural and optical properties of CuO layered hexagonal discs synthesized by a low-temperature hydrothermal process," *Journal of Physics D: Applied Physics,* vol. 44, p. 155405, 2011.

[6]   K. L. Foo, M. Kashif, U. Hashim, and W.-W. Liu, "Effect of different solvents on the structural and optical properties of zinc oxide thin films for optoelectronic applications," *Ceramics International,* vol. 40, pp. 753-761, 2014.

[7]   C. Abdelmounaïm, Z. Amara, A. Maha, and D. Mustapha, "Effects of molarity on structural, optical, morphological and CO2 gas sensing properties of nanostructured copper oxide films deposited by spray pyrolysis," *Materials Science in Semiconductor Processing,* vol. 43, pp. 214-221, 2016.

[8]   A. López-Suárez and D. R. Acosta, "The Influence of Different Solvents on the Physical Properties of ZnO Thin Films," *Journal of Composites Science,* vol. 8, p. 332, 2024.

[9]   P. Kumar and K. L. Mittal, *Handbook of microemulsion science and technology*: Marcel Dekker New York, 1999.

[10]   V. Dhanasekaran and T. Mahalingam, "Physical properties evaluation of various substrates coated cupric oxide thin films by dip method," *Journal of alloys and compounds,* vol. 539, pp. 50-56, 2012.

[11]   F. Baig, M. W. Ashraf, A. Asif, and M. Imran, "A comparative analysis for effects of solvents on optical properties of Mg doped ZnO thin films for optoelectronic applications," *Optik,* vol. 208, p. 164534, 2020.

[12]   R. Bekkari, B. Jaber, H. Labrim, M. Ouafi, N. Zayyoun, and L. Laânab, "Effect of Solvents and Stabilizer Molar Ratio on the Growth Orientation of Sol-Gel-Derived ZnO Thin Films," *International Journal of Photoenergy,* vol. 2019, p. 3164043, 2019.

[13]   T. Y. Hill, "Fabrication of zinc oxide thin films for renewable energy and sensor applications," 2010.

[14]   O. Daoudi, Y. Qachaou, A. Raidou, K. Nouneh, M. Lharch, and M. Fahoume, "Study of the physical properties of CuO thin films grown by modified SILAR method for solar cells applications," *Superlattices and microstructures,* vol. 127, pp. 93-99, 2019.

[15]   H. B. Saâd, M. Ajili, S. Dabbabi, and N. T. Kamoun, "Investigation on thickness and annealing effects on physical properties and electrical circuit model of CuO sprayed thin films," *Superlattices and Microstructures,* vol. 142, p. 106508, 2020.

[16]   S. A. M. H. M. Ali and S. Makki, "The thickness effects characterization properties of copper oxide thin films prepared by thermal evaporation technique," *J. Mult. Eng. Sci. Stud.,* vol. 2, p. 532, 2016.

[17]   N. Raship, M. Sahdan, F. Adriyanto, M. Nurfazliana, and A. Bakri, "Effect of annealing temperature on the properties of copper oxide films prepared by dip coating technique," in *AIP Conference Proceedings*, 2017.

[18]   K. Kamli, Z. Hadef, B. Chouial, and B. Hadjoudja, "Thickness effect on electrical properties of copper oxide thin films," *Surface Engineering,* vol. 35, pp. 86-90, 2019.

[19]   N. Serin, T. Serin, Ş. Horzum, and Y. Celik, "Annealing effects on the properties of copper oxide thin films prepared by chemical deposition," *Semiconductor science and technology,* vol. 20, p. 398, 2005.

[20]   X. Li, J. Liang, N. Kishi, and T. Soga, "Synthesis of cupric oxide nanowires on spherical surface by thermal oxidationmethod," *Materials letters,* vol. 96, pp. 192-194, 2013.

[21]   A. N. Hussain, K. I. Hassoon, and M. A. Hassan, "Effect of annealing on copper oxide thin films and its application in solar cells," in *Journal of Physics: Conference Series*, 2020, p. 012140.

[22]   F. A. Akgul, G. Akgul, N. Yildirim, H. E. Unalan, and R. Turan, "Influence of thermal annealing on microstructural, morphological, optical properties and surface electronic structure of copper oxide thin films," *Materials Chemistry and Physics,* vol. 147, pp. 987-995, 2014.

[23]   K. Khojier, H. Savaloni, and Z. Sadeghi, "A comparative investigation on growth, nanostructure and electrical properties of copper oxide thin films as a function of annealing conditions," *Journal of Theoretical and Applied Physics,* vol. 8, pp. 1-8, 2014.

[24]   D. Ozaslan, O. Erken, M. Gunes, and C. Gumus, "The effect of annealing temperature on the physical properties of Cu2O thin film deposited by SILAR method," *Physica B: Condensed Matter,* vol. 580, p. 411922, 2020.

[25]   J. Park, T. Kwon, S. Koh, and Y. Kang, "Annealing temperature dependence on the physicochemical properties of copper oxide thin films," *Bull. Korean Chem. Soc,* vol. 32, pp. 1331-1335, 2011.

Chapter IV

Influence of alkali doping CuO thin films

IV.1. Introduction

In this chapter, we focus on presenting and analysing the findings from our research on copper oxide (CuO) thin films, including both pure and doped variations. The chapter is organized into two sections. In the first section, we investigate the structural, electrical, and optical characteristics of CuO thin films. This includes pure CuO as well as CuO doped with specific elements (Li, Na, and K), which we refer to as X-doped CuO. We explore the effect of these dopants across various concentrations (3%, 6%, 9%, and 12%) to understand how each dopant and concentration level impacts the properties of CuO. Multiple analytical techniques are employed to characterize these materials, providing a comprehensive overview of their behavior and properties. in the second section, we select the optimal doping concentration and compare the thermoelectric properties to determine the most suitable candidate for thermoelectric applications.

IV.2. Results and discussion

IV.2.1. Lithium doped Copper oxide

IV.2.1.1. Structural characterizations

XRD analysis

The impact of lithium doping on the structure of copper oxide thin films was examined using X-ray diffraction (XRD). Lithium concentrations were set at 3%, 6%, 9%, and 12% for this study. The resulting XRD patterns are shown in **Figure IV. 1.** From the diffraction patterns, peaks were observed at approximately 32.48°, 35.56°, 38.71°, 48.82°, and 61.60°, corresponding to the crystallographic planes (110), (11$\bar{1}$), (200), (20$\bar{2}$), and (113$\bar{}$) of the monoclinic CuO structure, as referenced by standard JCPDS Data No. 98-004-3179. These findings align with previous studies and confirm that the films exhibit a monoclinic CuO structure, with no additional crystalline phases introduced by the lithium doping.

The XRD patterns demonstrate that the (11$\bar{1}$) and (200) peaks of the Li-doped CuO samples have shifted slightly to lower angles compared to the undoped CuO[1]. This shift can be explained by the difference in ionic radii between lithium (Li$^+$) and copper (Cu^{2+}). The ionic radius of Li$^+$ (0.73 Å) is slightly larger than that of Cu^{2+} (0.71 Å). When Li$^+$ ions replace Cu^{2+} ions in the CuO lattice during doping, the larger Li$^+$ ions leading to an increase in the d-spacing

(the distance between atomic layers). This increase in d-spacing causes the diffraction peaks to shift to lower angles, as observed in the XRD patterns.

At lower doping levels 3% Li^+ ions can smoothly integrate into the CuO lattice, causing a slight expansion due to the larger ionic radius of Li^+ compared to Cu^{2+}. However, at 6% doping, the CuO lattice may begin to experience saturation, where it can no longer easily accommodate more Li^+ ions without inducing stress or strain. This stress could lead to lattice contraction. Instead of continuing to expand like at lower concentrations, the excess strain may cause the lattice to contract slightly, shifting the XRD peaks to higher angles. By 9% and 12%, the CuO lattice may have reorganized or stabilized, reducing the strain and distortions. As a result, the lattice expands again, causing a shift back to lower angles, as observed in the 9% and 12% samples.

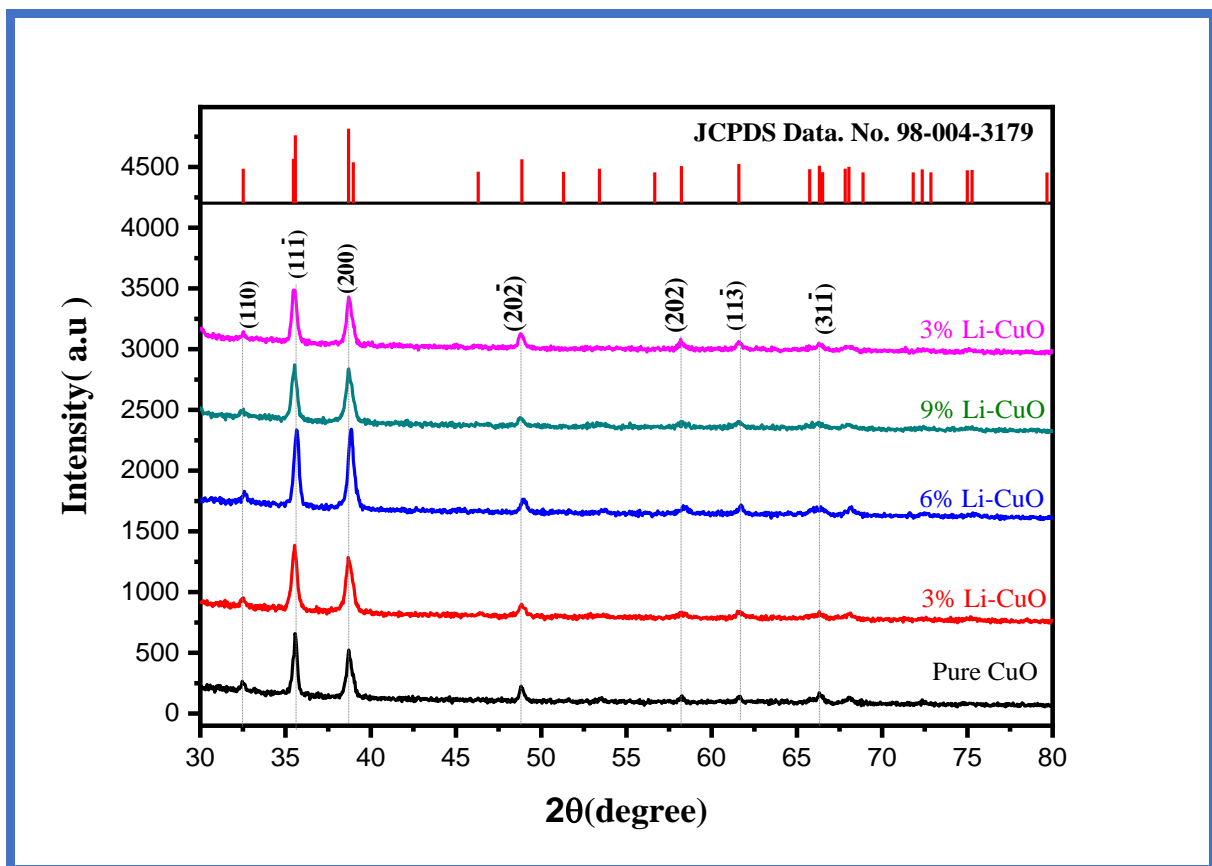**Figure IV.1.** X-ray diffraction patterns of pure and $Cu_{1-x} Li_x O$ (X=3%,6%, 9%, 12%).

The crystallite size D, Lattice parameters, strain and dislocation density

The crystallite size D is calculated using the Debye-Scherrer formula. As indicated in the table, increasing the concentration of Li dopants beyond 6% results in a decrease in the crystallite size

of CuO: Li. When Li⁺ ions substitute Cu²⁺ ions in the CuO lattice, the difference in ionic radii introduces lattice distortion. While the lattice can manage the strain at lower doping levels (up to 6%), exceeding this threshold causes the strain to intensify, leading to the formation of defects in the crystal structure.

The dislocation density (δ) and strain (ε), as shown in **Table IV.1**, increase with higher doping concentrations except at 6% of Li content. Bayansal et al., have reported that as the crystallite size decreases, the number of grain boundaries increases, which results in a higher concentration of defects such as dislocations, vacancies, and misalignments. This, in turn, leads to the degradation of the crystalline quality of the films as the doping concentration rises [2]. Hence proved, 6%Li-doped CuO sample shows the lowest lattice distortion and defects density values.

Table IV.1. shows the cell parameters a, b, c, and volume V for both pure CuO and Na-doped CuO. It is evident that the cell parameters for the doped samples are smaller compared to those of pure CuO, when Li⁺ ions substitute for Cu²⁺ ions in the CuO lattice, the smaller charge of Li⁺ (1+ compared to 2+) creates changes in the bonding environment. This often leads to a contraction of the lattice as the system accommodates the lower positive charge and rebalances the forces between the ions [3] [4]. As a result, the lattice parameters and volume tend to decrease with the introduction of Li⁺. However, the 6% Li-doped CuO behaves differently due to a critical concentration effect, where the lattice undergoes structural changes that lead to an increase in the cell parameters compared to other Li-doped samples.

Table IV.1. values of lattice parameter, grain size, dislocation density and strain for

$Cu_{1-X} Li_x O$ thin films (x = 3%, 6%, 9%, and 12%) prepared by the spin-coating method, compared to undoped CuO thin films.

Sample	Lattice parameter (Å)				Crystallite size D (nm)	Dislocation density (x10^{14} lines) m^{-2}	Strain ε × 10^{-4}
	a=	b=	c=	V=			
Pure CuO	4.6972	3.4258	5.1380	81.5450	24.53	16.61	15.80
3% Li-CuO	4.6829	3.4286	5.1307	81.4212	22.59	19.59	15.34
6% Li-CuO	4.6831	3.4291	5.1308	81.5612	23.32	18.38	14.86
9% Li-CuO	4.6826	3.4282	5.1376	81.4167	20.60	23.54	16.82
12% Li-CuO	4.6819	3.4236	5.1371	81.3865	19.53	26.20	17.74

IV.2.1.2. Optical properties

Transmittance properties

The effect of lithium doping concentration on the optical characteristics of CuO thin films was studied to understand how varying amounts of lithium influence the material's transmittance, band gap, and overall optical behaviour. Lithium was introduced at different concentrations (3%, 6%, 9%, 12%) to observe its impact on the film's microstructure, defect states, and electronic properties. In fact, we remark, from **Figure IV.2.** that a significant decrease of transmittance in both visible region after Li doping. From the same figure, we can note that the transmittance of the films increases only in infrared region. The variations in transmittance for lithium-doped CuO thin films at different doping concentrations (3%, 6%, 9%, 12%) compared to pure CuO are attributed to how lithium doping influences the film's microstructure, optical band gap, and defect states.

At 6%, 9%, and 12% Li-doping, the transmittance decreases due to the introduction of more defects, which act as centres for scattering and absorption. Additionally, increased free carrier absorption and reduced film quality contribute to greater light scattering, resulting in decreased transparency [5].
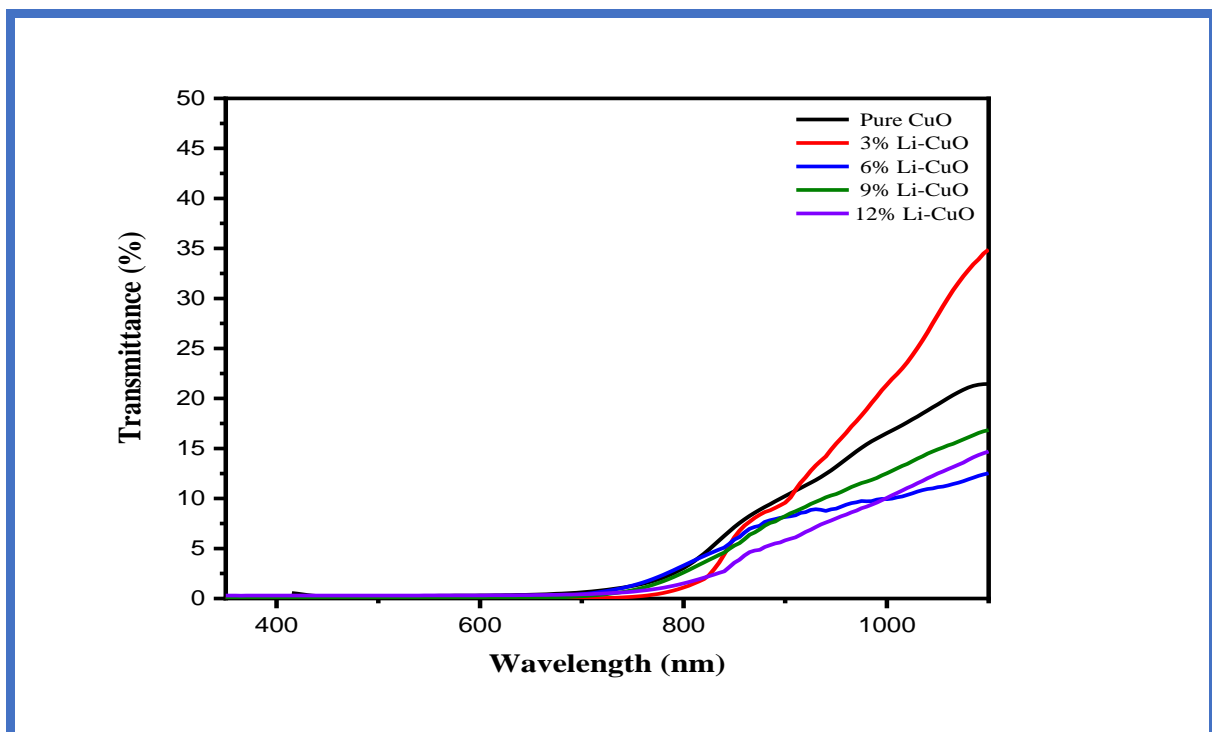
Figure IV.2. Optical transmittance spectra of spin-coating method made $Cu_{1-x} Li_x O$ (X=3%, 6%, 9% and 12%) thin films compared to those of undoped CuO one.

Band gap energy (Eg) and Urbach energy (Eu)

The variation in the band gap with different Lithium doping percentages is presented in **Table IV.2.** For Li doping, the band gap values are found to vary between 1.46 and 2.42 eV. The increase in the optical band gap can be explained by the introduction of Li, which distorts the CuO matrix as the nanostructure size decreases, leading to the formation of impurity energy levels (acceptor states) within the band gap. The combined effect of lithium doping and reduced nanostructure size results in an overall expansion of the band gap [6].

Table IV.2. Variation in optical parameters of undoped and Li-doped copper oxide thin films.

Samples	Pure CuO	Li (3%)-CuO	Li (6%)-CuO	Li (9%)-CuO	Li (12%)-CuO
Optical Band gap Eg (eV)	1.42	1.75	2.42	1.86	1.37
Urbach energy Eu (eV)	0.46	0.32	0.40	0.68	0.90
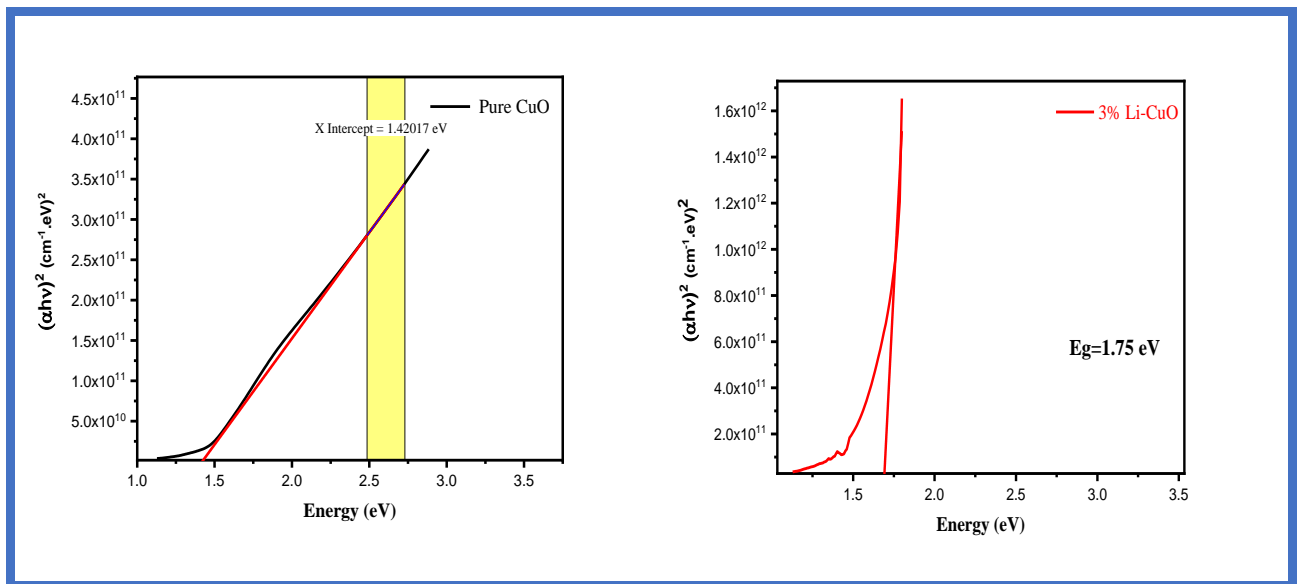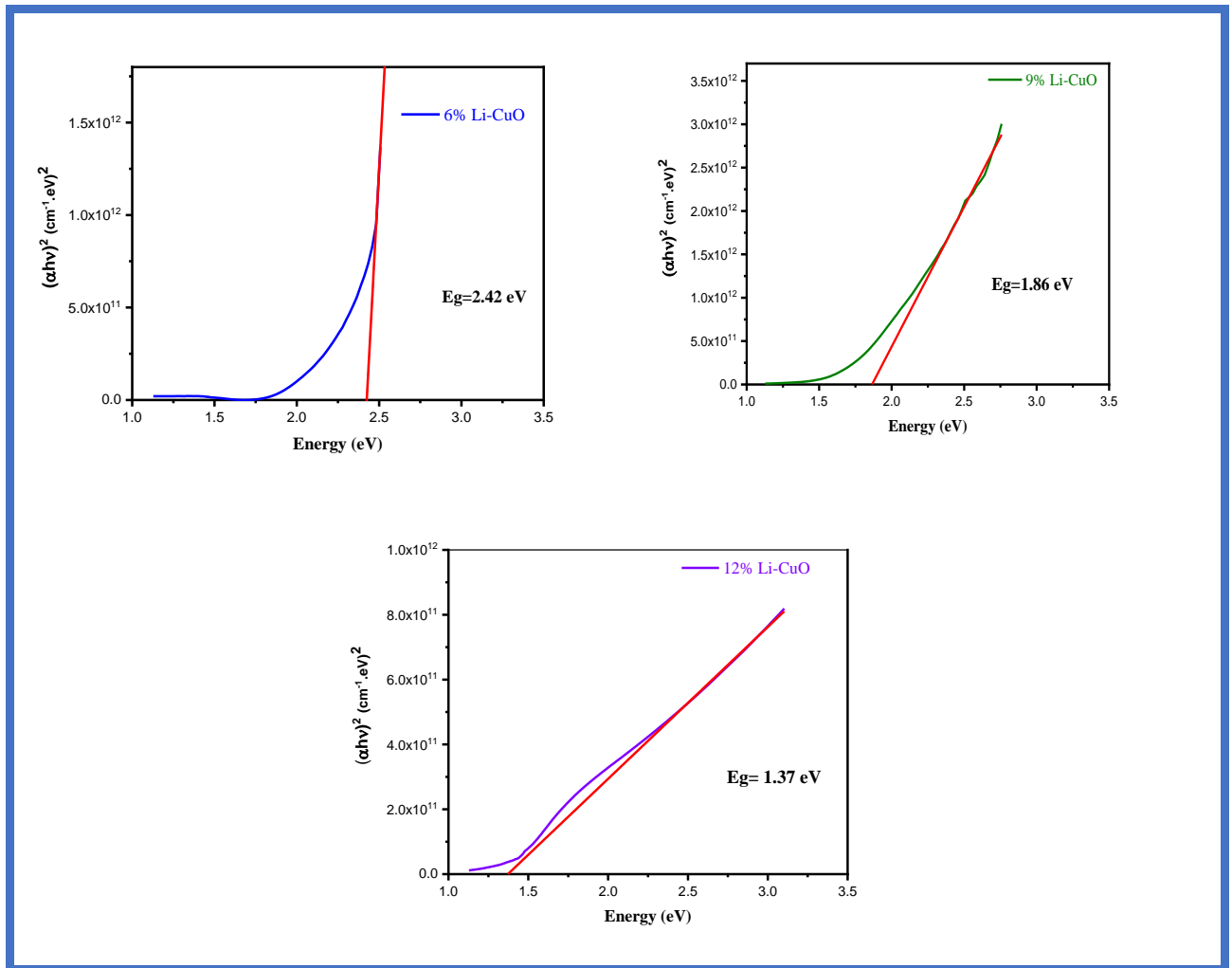
Figure IV.3. Plots of $(\alpha h\upsilon)^2$ against $h\upsilon$ of spin-coating method made $Cu_{1-x} Li_x O$ (x=3%,6%, 9% and 12%) thin films compared to those of undoped CuO one.

The substitution of Cu^{2+} by Li^+ leads to the formation of impurity energy levels between the conduction band (CB) and the valence band (VB). This increases the number of Cu^{2+} vacancies, which act as acceptor states. The marginal difference or decrease in band gap energy (Eg) is due to the high concentration of these acceptor states (cation vacancies) near the top of the valence band, associated with Cu^+ or Cu^{2+} ions. The overlap between the upper-edge states of the valence band and donor states from the conduction band, caused by doping, results in a narrowing of the band gap. An increase in the band gap energy can be attributed to the rise in Urbach energy, which reflects increased disorder and the loss of crystal structural organization.
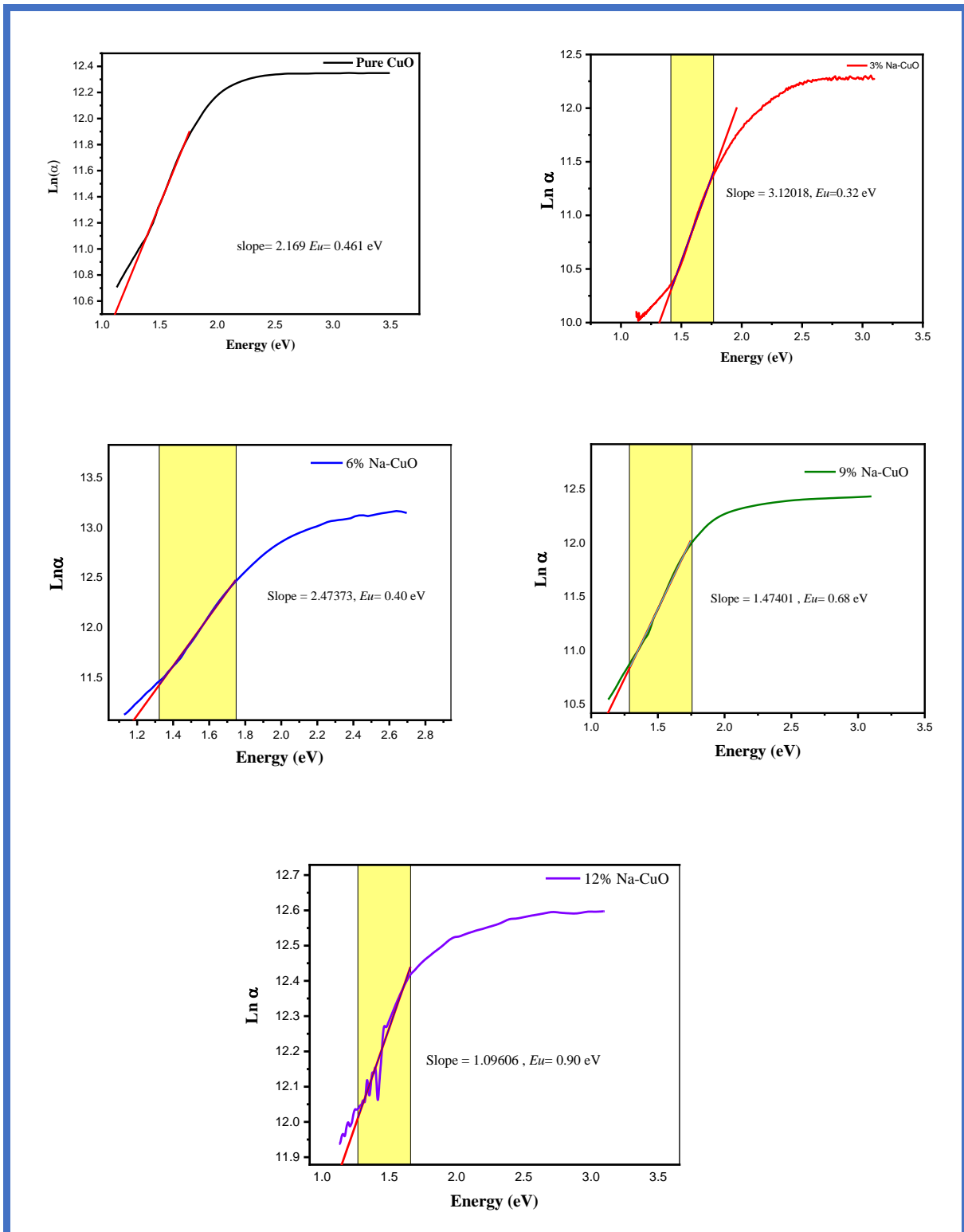
Figure IV.4. Plots of *ln α* against *hν* of spin-coating method made $Cu_{1-x} Li_x O$ (x=3%,6%, 9% and 12%) thin films compared to those of undoped CuO one.

IV.2.1.3. Electrical properties

The electrical conductivity (σ) and the resistivity (ρ)values of Li-doped CuO thin films are presented in **Table IV.3.** and their variation with Li doping concentration is shown in **Figure IV.5.** The conductivity initially increases, reaching a maximum of 0.272 at 6% Li doping, but decreases as the Li content increases further, dropping to 0.0379 $(\Omega.cm)^{-1}$ at 12% Li doping. On contrast, the resistivity (ρ) is found to decrease slightly. Then, it starts to increase significantly with further increase of Li content.

The initial rise in conductivity is attributed to an increase in hole concentration in the valence band, caused by shifts in the conduction band and the creation of holes due to oxygen non-stoichiometry in the p-type CuO grains. Additionally, as Li doping increases, grain size reduction leads to the formation of discrete energy levels, which act as electronic defects. These defects can behave like donor states, further enhancing conductivity.

However, at higher doping levels, the conductivity decreases. This reduction is attributed to the decreased crystallization of the thin films, which reduces electron scattering centers and increases the material's resistance. The higher concentration of dopant ions disrupts the crystal structure, leading to diminished electrical conductivity.
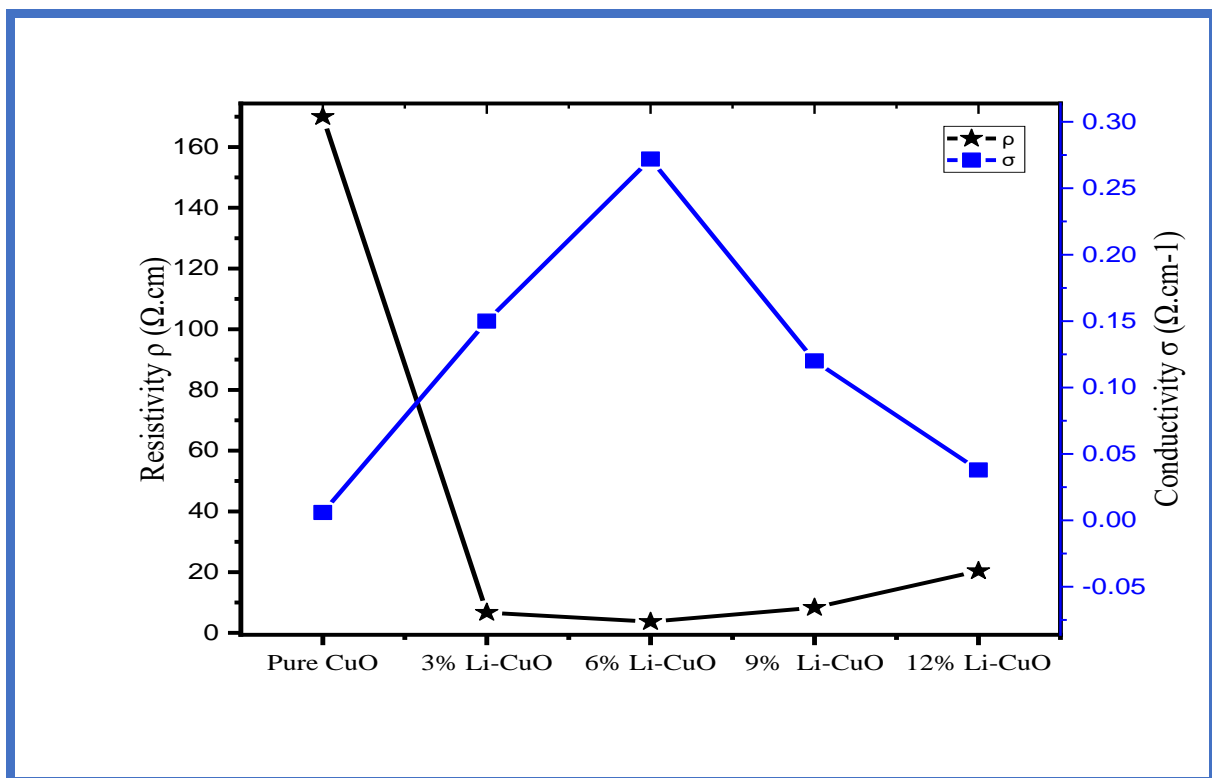
Figure IV.5. Electrical conductivity and resistivity of the Cu_{1-x} Li_x O (x=3%,6%, 9% and 12%) and undoped CuO thin films as a function of doping concentration.

Table.IV.3. Electrical conductivity and resistivity of the $Cu_{1-x} Li_x O$ (x=3%,6%, 9% and 12%) and undoped CuO thin films.

Samples	Pure CuO	3% Li-CuO	6% Li-CuO	9% Li-CuO	12% Li-CuO
Resistivity × 10^2 (Ω.cm)	1.7	0.066	0.0367	0.083	0.202
Conductivity ×10^{-2} (Ω.cm)$^{-1}$	0.58	15.00	27.2	12.00	3.790

IV.2.2. Sodium doped copper oxide
IV.2.2.1. Structural characterization

*XRD analysis*

The X-ray diffraction (XRD) patterns of the as-deposited thin films, each containing varying percentages of sodium doping, consistently exhibit a monoclinic phase. This was confirmed by comparison with the standard JCPDS Card No. 98-004-3179. Various diffraction peaks were detected in CuO thin films at specific diffraction angles (2θ) of 32.48°, 35.56°, 38.71°, 48.82°, and 61.60°, corresponding to the crystallographic planes (110), (11$\bar{1}$), (200), (20$\bar{2}$), and (11$\bar{3}$), respectively. It was observed that the preferred ($^-$111) and (111) peaks, orientation remains unchanged as the sodium concentration increases. The full width at half maximum (FWHM) values, as shown in Table 1, increased by 3%, 9%, and 12% for Na-doped CuO samples compared to pure CuO thin films. This increase suggests that sodium doping inhibits crystallite growth, leading to reduced crystallinity.

The decrease in crystallization can be attributed to factors such as the type of chemical bonds between the atoms in the film material, the specific heat of the solid, or the differences in melting points of the material's components. Similar effects were observed by A. Sobhani et al., [7] where the FWHM values decreased due to crystal defects introduced by doping. Notably, the peak intensities also diminished as sodium doping levels increased.

As sodium doping increases, the peak positions gradually shift towards lower 2θ values, indicating an increase in interplanar spacing according to Bragg's Law, as the spacing increases, the diffraction angle must decrease to satisfy the equation. This shift is due to the difference in ionic radii between Na^+ (0.102 nm) and Cu^{2+} (0.065 nm) ions. The formation of vacancies, which leads to lattice contraction through electrostatic interactions, along with lattice expansion caused by the change in cation radius (steric effect), increases the distance between atomic

planes, as reported by Marrocchelli et al [8] . It is well known that CuO is prone to vacancy defects, and in this work, the observed lattice contraction is attributed to the creation of vacancies after sodium doping. However, the 6% Na-doped CuO sample exhibited a different behavior, suggesting that this doped sample may have better crystallinity than the others.

The average crystallite size (D) for the nanostructured thin films was calculated using the Scherrer equation **(II.14)** for the (111) preferred orientation. The average crystallite size was found to range from 13.67 nm to 24.53 nm, with the size decreasing as sodium doping concentration increased from 0% to 12%. The decrease in crystallite size can be explained by the internal strain introduced when larger Na^+ ions (1.02 Å) replace smaller Cu^{2+} ions (0.65 Å) in the CuO lattice. This size mismatch destabilizes the crystal structure, and to relieve the strain, the system undergoes a spontaneous reduction in particle size, helping to stabilize the structure. This phenomenon, where ion size differences lead to lattice distortions, is commonly observed in doped or substituted crystal systems [9] [10].

The lattice parameters of the monoclinic unit cell were calculated using Debye-Scherrer relationship, lattice parameter a, b and c for monoclinic structure, and V volume of unit cell of tenorite.

Table IV.4 shows the cell parameters a, b, c, and volume V for both pure CuO and Na-doped samples. It is evident that the cell parameters for the doped samples are smaller compared to those of pure CuO, indicating that lattice compression has occurred in the doped material. This compression is caused by the difference in ionic radii between Na and Cu, which introduces lattice distortion. To accommodate the size mismatch and reduce strain, the unit cell contracts, leading to a reduction in the lattice parameters.
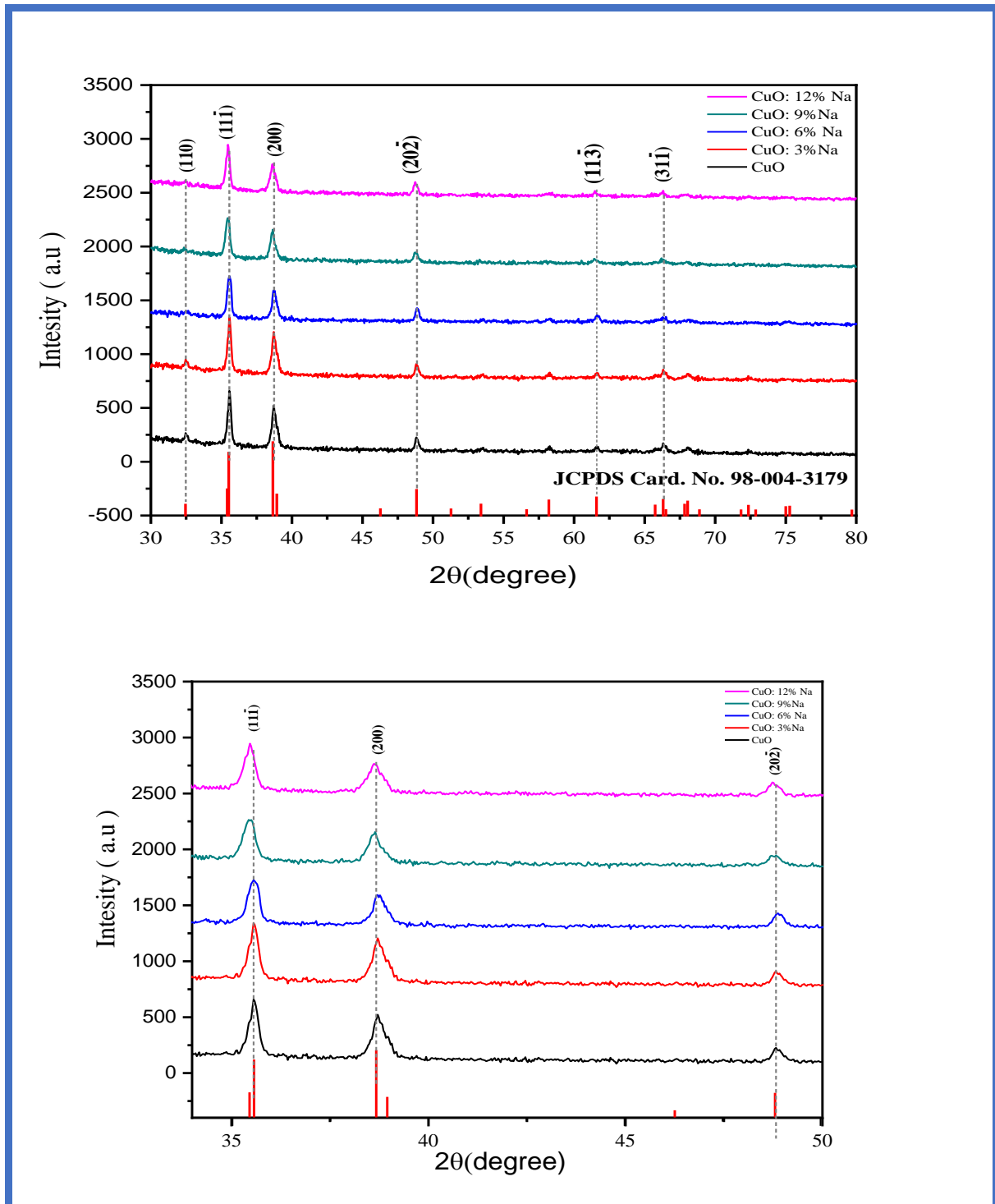
Figure IV.6. X-ray diffraction patterns of pure and $Cu_{1-x}Na_xO$ (x=3%,6%, 9%, 12%).

Together, dislocation density and micro-strain give a more complete understanding of a material's defect structure and how those defects impact its physical and mechanical properties. have been calculated using equations. The dislocation density of CuO nanostructure thin films exhibited an upward trend with increasing Na dopant levels, except at 6 mol% Li concentration.

This anomaly could be linked to a rise in grain boundaries, likely caused by variations in crystallite size, as demonstrated in **Table.IV.4**. These observations align with the research of F. Bayansal et al, [11] which noted a reduction in grain size alongside a rise in dislocation density as the dopant concentration increased.
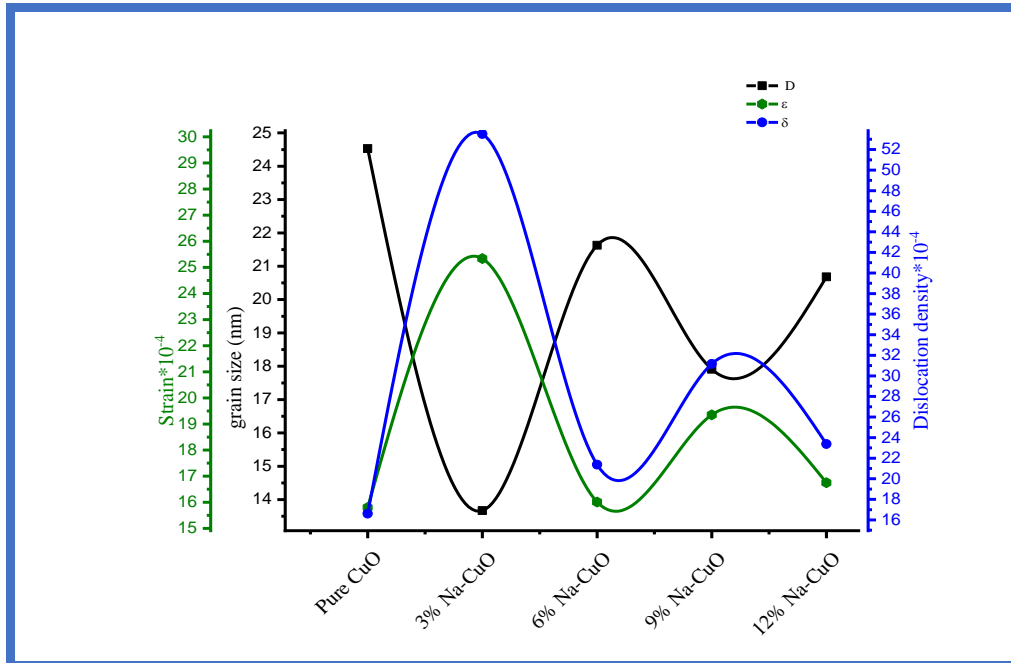
Figure IV.7. Variation of grain size, strain and dislocation density of CuO thin films as function of Na concentration

Table IV.4. values of lattice parameter, grain size, dislocation density and strain for

$Cu_{1-x} Na_x O$ thin films (x = 3%, 6%, 9%, and 12%) prepared by the spin-coating method, compared to undoped CuO thin films.

Sample	FHWM (°)	Lattice parameter (Å)				Crystallite size D (nm)	Dislocation density (x10^14 lines) m^-2	Strain ε × 10^-4
		a=	b=	c=	V=			
Pure CuO	0.34	4.6972	3.4258	5.1380	81.5450	24.53	16.61	15.80
3% Na-CuO	0.61	4.6969	3.4251	5.1381	81.5222	13.67	53.51	25.34
6% Na-CuO	0.38	4.6979	3.4259	5.1382	81.5612	21.63	21.37	16.01
9% Na-CuO	0.46	4.6971	3.4254	5.1376	81.5274	17.91	31.17	19.35
12% Na-CuO	0.40	4.6970	3.4256	5.1379	81.5441	20.68	23.38	16.75

IV.2.2.2. Optical properties

The optical characteristics of pristine and sodium-doped CuO thin films were examined through UV-Visible spectroscopy. The transmittance spectra for the produced CuO thin films, including those without doping and those doped with sodium at concentrations of 3%, 6%, 9%, and 12%, are displayed in **Figure IV.8.** It can be said that the change in transmittance values did not follow a systematic trend, which may suggest that the impurity ions were not uniformly incorporated into the CuO lattice. In the domain below 800 nm, there is generally low transmission and consequently strong light absorption by both undoped and Na-doped CuO layers. However, in this region, the average transmission increases as the percentage of Na doping increases. Additionally, the 6% Na-doped CuO sample exhibited the highest transmittance values compared to all other produced CuO samples. The increased transmittance at 6% doping can be attributed to a reduction in defects, enhanced crystallinity, and decreased scattering or absorption of incident light, indicating low surface roughness and improved homogeneity. This is further supported by experimental results obtained through X-ray analysis. The high transparency observed in the film with 6% Na doping in the visible region suggests its potential for optoelectronic applications, including use in flat plate collectors and photovoltaic devices, as a transparent conducting oxide material. Decreased transmittance is attributed to surface roughness and higher defect density due to the incorporation of excess Na in copper oxide lattice as well as the pores present in the thin films which increased the scattering of photons.
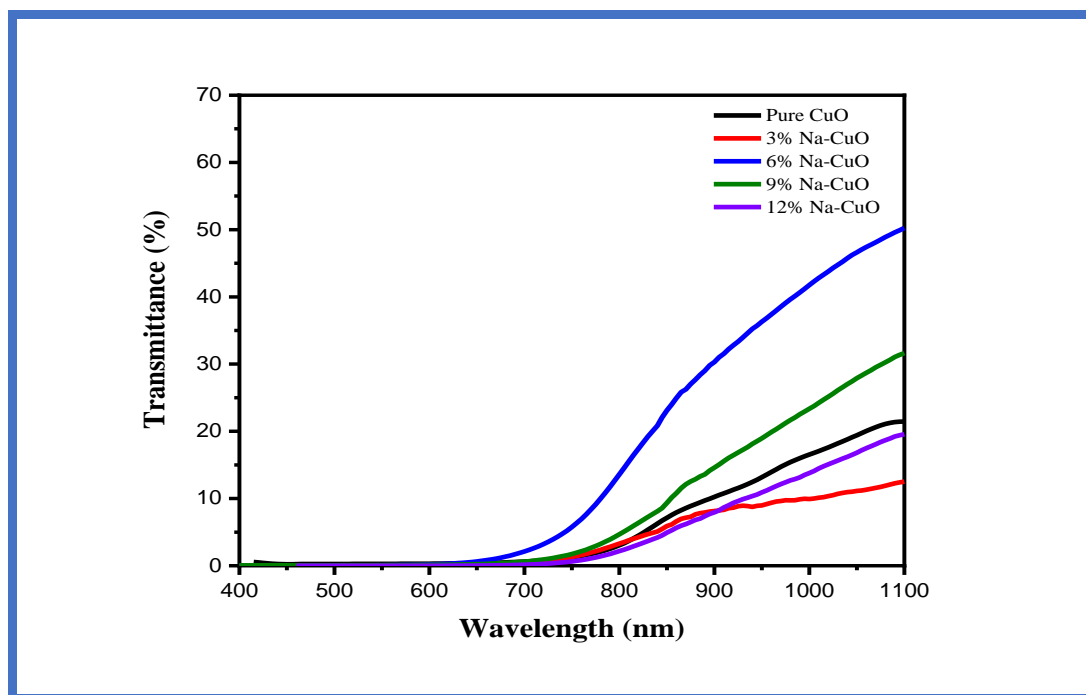
Figure IV.8. Transmittance spectra of undoped and Na-doped CuO**.**

Table IV.5. Variation in optical parameters of undoped and Na-doped copper oxide thin films

Samples	Pure CuO	Na (3%)-CuO	Na (6%)-CuO	Na (9%)-CuO	Na (12%)-CuO
Optical Band gap Eg (e V)	1.42	1.85	1.70	1.52	1.39
Urbach energy Eu (e V)	0.46	0.32	0.40	0.68	0.90

The variation in the band gap with different sodium doping percentages is presented in **Table IV.5.** Pure copper oxide exhibited a band gap of 1.42 eV, while sodium-doped copper oxide showed a range of band gaps from 1.85 eV to 1.39 eV, depending on the doping level. The optical band gap energy increases with higher sodium dopant concentrations **Figure IV.9** This increase can be attributed to the increase in grain boundaries, resulting from the reduction in crystallite size and the increase in film thickness. This behavior was also obtained for copper oxide films deposited by spray pyrolysis [12], and chemical deposition [13].
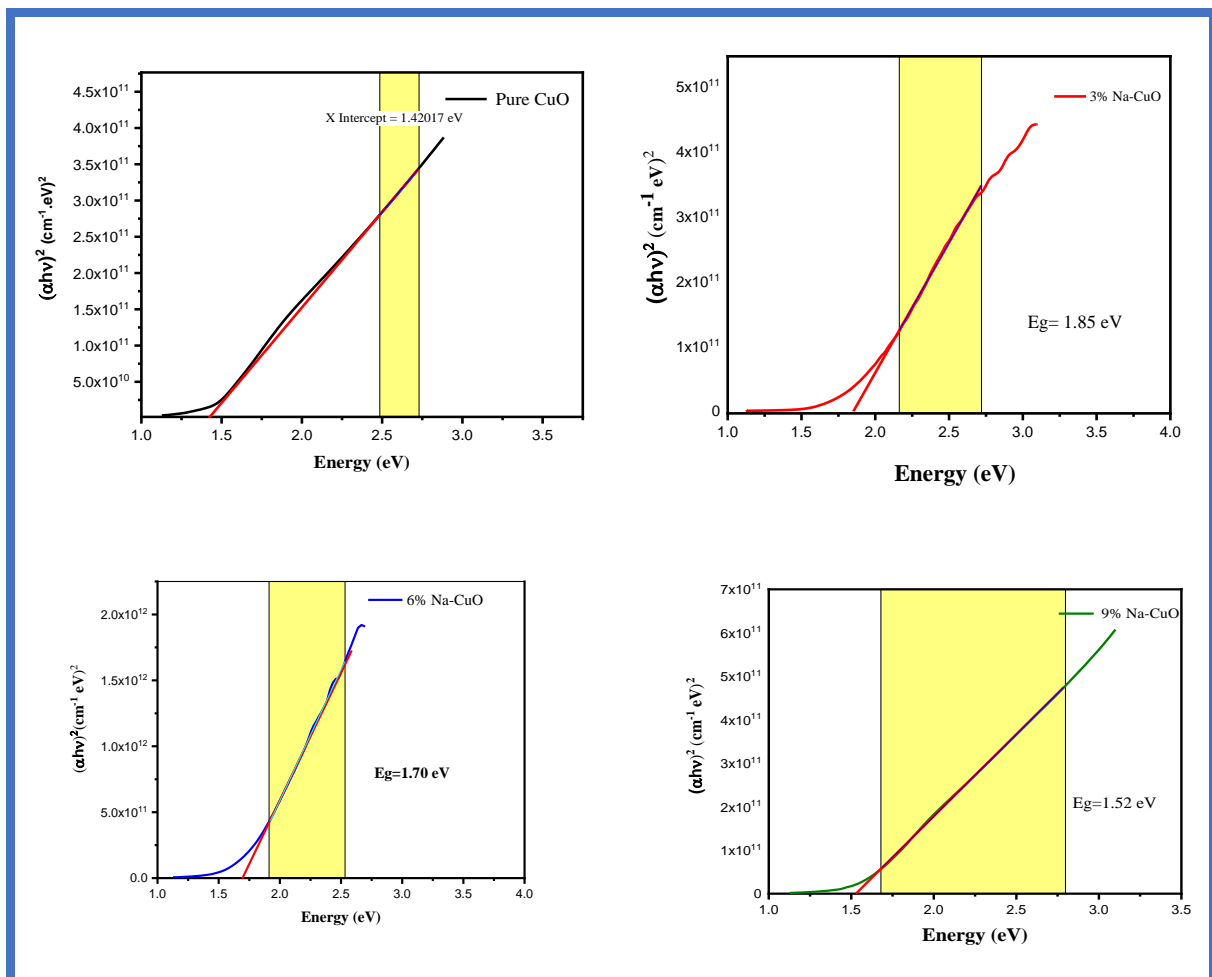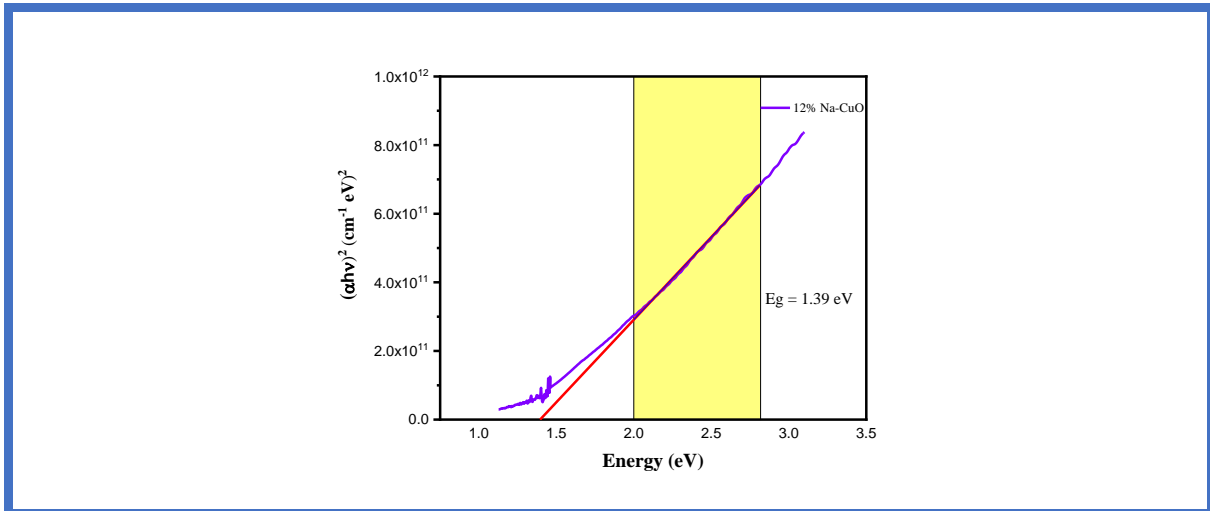
Figure IV.9. Graphs of $(\alpha h\nu)^2$ plotted against $h\nu$ for $Cu_{1-x}Na_xO$ thin films (x = 3%, 6%, 9%, and 12%) prepared by the spin-coating method, compared to undoped CuO thin films.

The introduction of impurities into a semiconductor typically leads to the formation of band tailing within the band gap. Optical transitions from the occupied states in the valence band tail to the unoccupied states at the conduction band edge result in an exponential relationship between the absorption coefficient (α) and photon energy near the band edge.

This effect is represented by the band tail energy, or Urbach energy Eu, which indicates the presence of local defects and follows the empirical Urbach law. As illustrated in **figure IV.10.** with the calculated values summarized in **Table IV.5.** The results show that the Urbach energy of doped samples is higher than that of undoped ones. The findings indicate that the Urbach energy in doped samples is higher compared to undoped ones. Where, a reduction in grain size results in an increase in the number of grain boundaries, creating regions of disorder that disturb the regular crystal lattice and introduce defects, dislocations, and localized states. This heightened disorder leads to a rise in Urbach energy, which is reflected in the widening of the absorption edge.
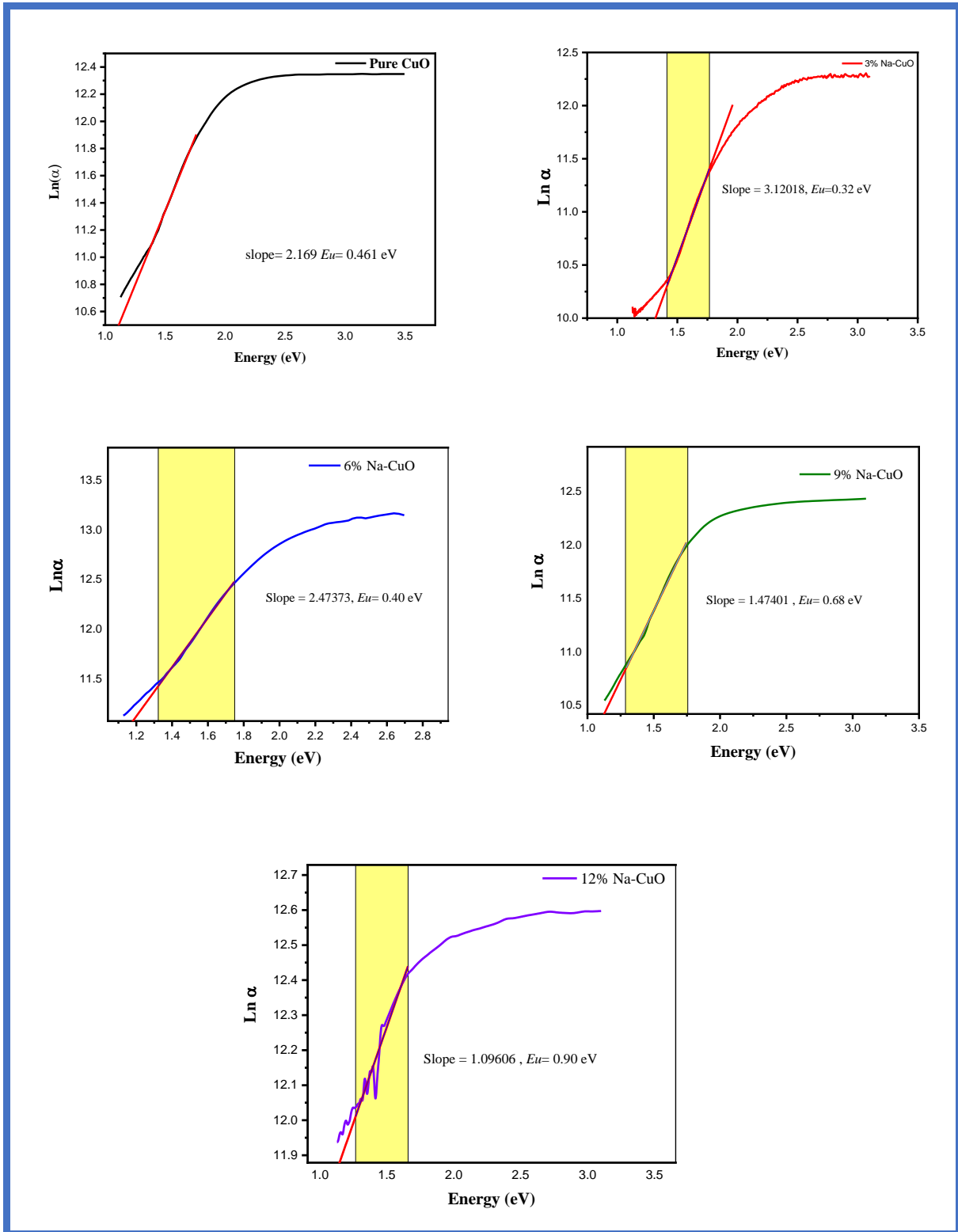
Figure IV.10. Graphs of Ln α plotted against $h\upsilon$ for Cu_{1-x} Na_xO thin films (x = 3%, 6%, 9%, and 12%) prepared by the spin-coating method, compared to undoped CuO thin films.

IV.2.2.3. Electrical properties

To examine the impact of Na doping on the electrical properties of CuO thin films, we calculated the electrical resistivity (ρ) and conductivity (σ) of CuO films at room temperature using the equation from. **Figure IV.11.** illustrates the variation in electrical conductivity and resistivity for both pure and Na-doped CuO thin films.

As shown, increasing the Na dopant concentration up to 3% results in a rise in electrical conductivity from 5.87×10^{-3} to 9.09×10^{-3} (Ω cm)$^{-1}$, followed by a further increase to 5.93×10^{-2} (Ω cm)$^{-1}$ at 6% Na concentration. However, beyond this point, the conductivity decreases to 5.49×10^{-2} and 4.74×10^{-2} (Ω.cm)$^{-1}$ at 9% and 12% Na concentrations, respectively. Conversely, the resistivity decreases from 170 Ω cm to 110 Ω cm at 6% Na concentration, reaching 16.9 Ω cm at 6%, but then increases slightly to 18.2 Ω cm and 21.1 Ω cm at 9% and 12% Na concentrations, respectively.
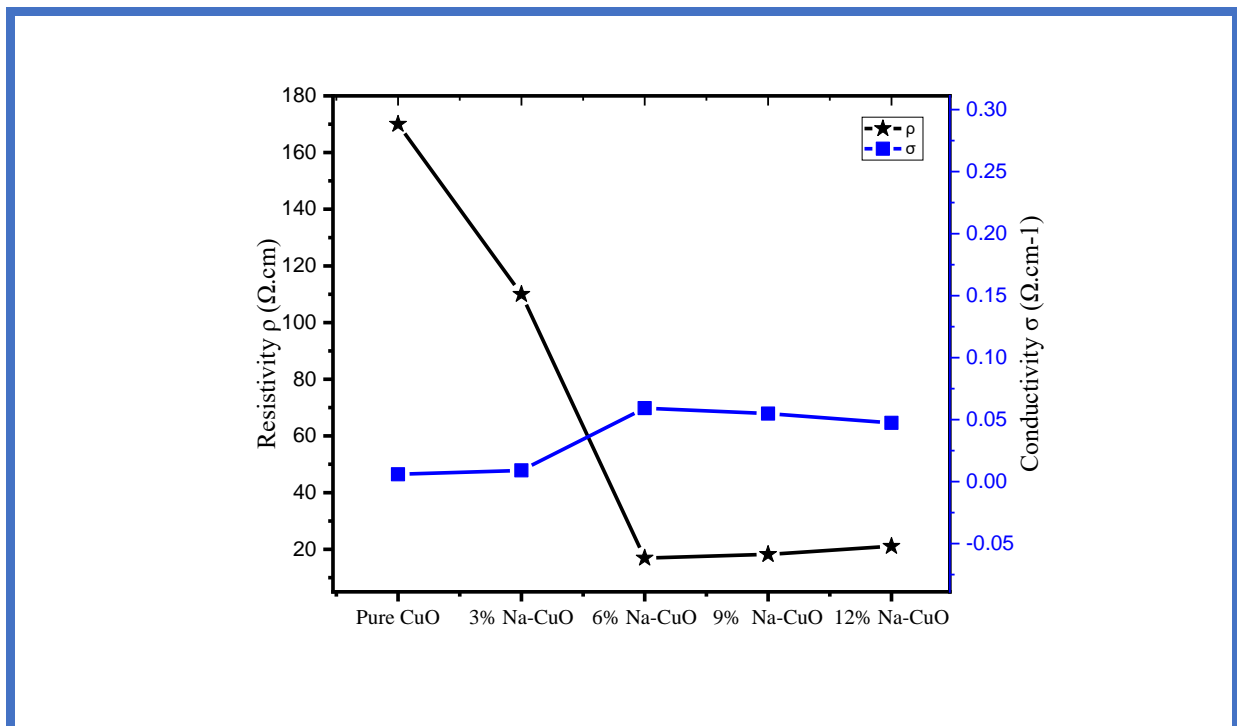
Figure IV.11. Electrical conductivity and resistivity of $Cu_{1-x}Na_xO$ thin films (x = 3%, 6%, 9%, and 12%) and undoped CuO thin films as a function of Na doping concentration.

In Na-doped copper oxide (CuO), the initial reduction in resistivity with increasing Na concentration is due to an increase in charge carrier density and mobility introduced by the doping process. When sodium (Na) atoms substitute for copper (Cu) atoms or integrate into the CuO structure, they generate additional free charge carriers (mainly holes), which enhances electrical conductivity and reduces resistivity. However, at higher Na concentrations, the

resistivity begins to rise due to the increased structural disorder, defect formation, and reduced carrier mobility. Where, these defects act as scattering centers for charge carriers, hindering their mobility and reducing overall conductivity. This explains the higher resistivity observed in the 9% and 12% Na-doped CuO samples compared to the 6% Na-doped sample.

IV.2.3. Potassium doped copper oxide

IV.2.3.1. Structural characterizations

The structural properties play a pivotal role in elucidating the electrical and optical characteristics of thin films. It's noteworthy that copper oxide (CuO) primarily exists in two structural forms: orthorhombic and monoclinic structures. **In Figure IV.12.** the characteristic X-ray diffraction patterns of undoped and potassium-doped copper oxide with variable potassium contents are depicted. First of all, Various diffraction peaks were detected in CuO thin films at specific diffraction angles (2θ) of 32.48°, 35.56°, 38.71°, 48.82°, and 61.60°. which belong to orientations at (110), (11$\bar{1}$),(200), (20$\bar{2}$),and (11$\bar{3}$),respectively, as per the standard data from JCPDS Card No.: 98-004-3179, consistent with the monoclinic crystal structure of the copper oxide phase. Furthermore, the addition of potassium (K) didn't alter the structure of the copper oxide thin films. This is supported by the lack of additional impurity peaks in the X-ray diffraction pattern, indicating the successful integration of the doped elements into the CuO lattice without the formation of distinct compounds. Moreover, the presence of K atoms is indicated by changes in peak position and intensity. When atoms occupy lattice sites, the reflection intensity on specific planes varies. These variations reflect slight alterations in crystal symmetry, likely due to the emergence of defects and vacancies at lattice sites. It is evident that the diffraction peak position values monotonically increase overall with higher K doping concentration, by comparing the diffraction peak position values of major peaks the standard XRD pattern, it can be deduced due to Poisson's effect that the undoped CuO film had residual compressive stress. As K^+ ions substitute Cu^{2+} at CuO lattice sites or enter interstitial sites, the lattice constant of $Cu_{1-x}K_x O$ should expand with increasing K doping concentration, attributed to the larger ionic radius of K^+ ions (1.38 Å) compared to Cu^{2+} ions (0.72 Å). Consequently, the diffraction peaks of $Cu_{1-x}K_xO$ films are anticipated to shift to lower angles overall. The lattice parameters of the monoclinic unit cell were calculated using Debye-Scherrer relationship (1), lattice parameter a, b and c for monoclinic structure (2), and V volume of unit cell of tenorite (3).

as detailed in Table 1. The data reveal that the slight difference in the ionic sizes of copper and zinc results in changes to the lattice parameters when zinc is added to copper oxide.

All CuO samples exhibit prominent ($\bar{1}11$) and (111) peaks, which are significantly more intense than the other peaks. The ($\bar{1}11$) plane is identified as the preferential growth plane, corresponding to the crystal face perpendicular to the c-axis. This plane is known for its relatively lower surface energy compared to other crystallographic directions. As a result, atoms experience a higher thermodynamic driving force to attach to this face, facilitating the formation of new layers and promoting faster growth in that direction.
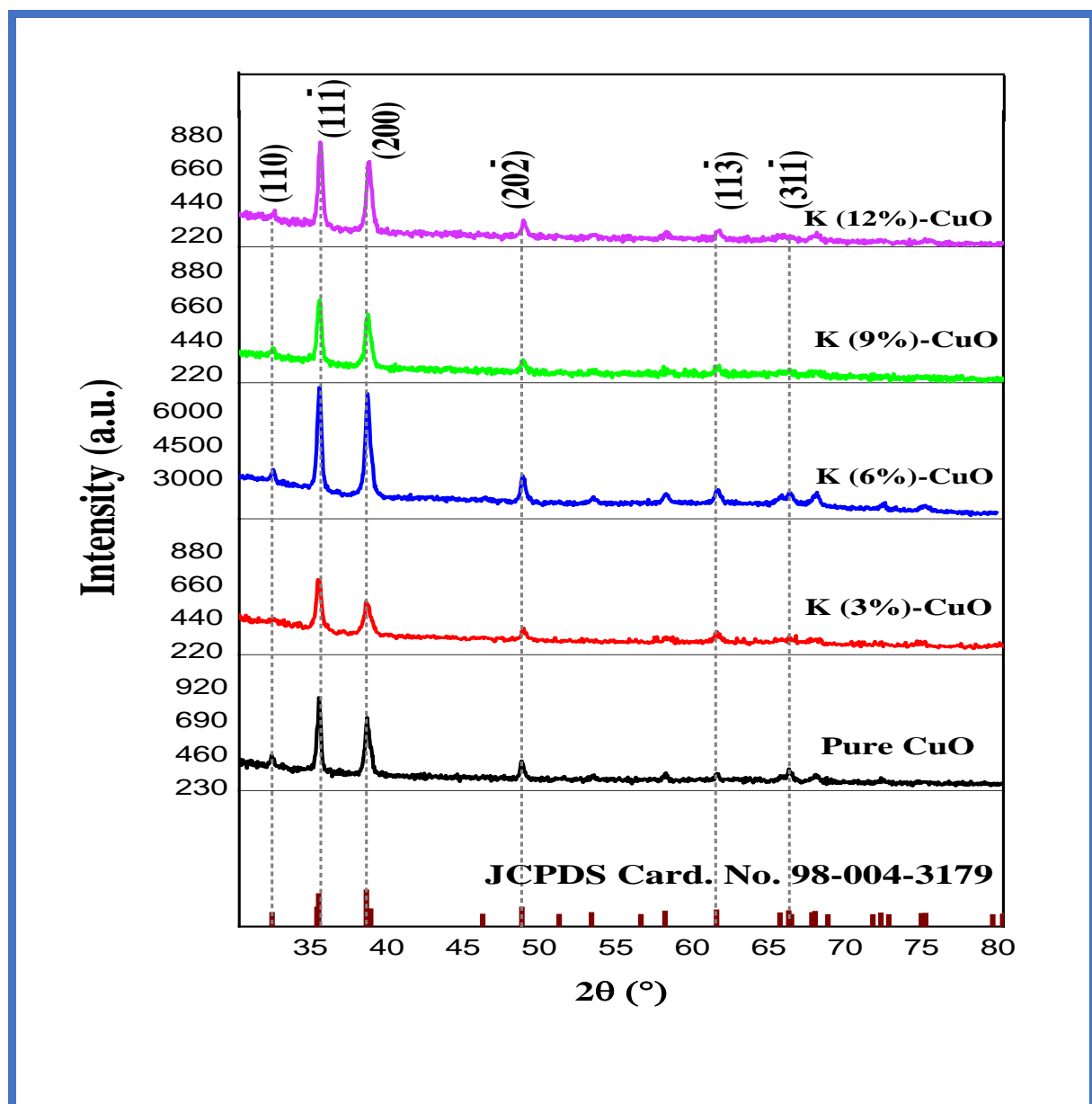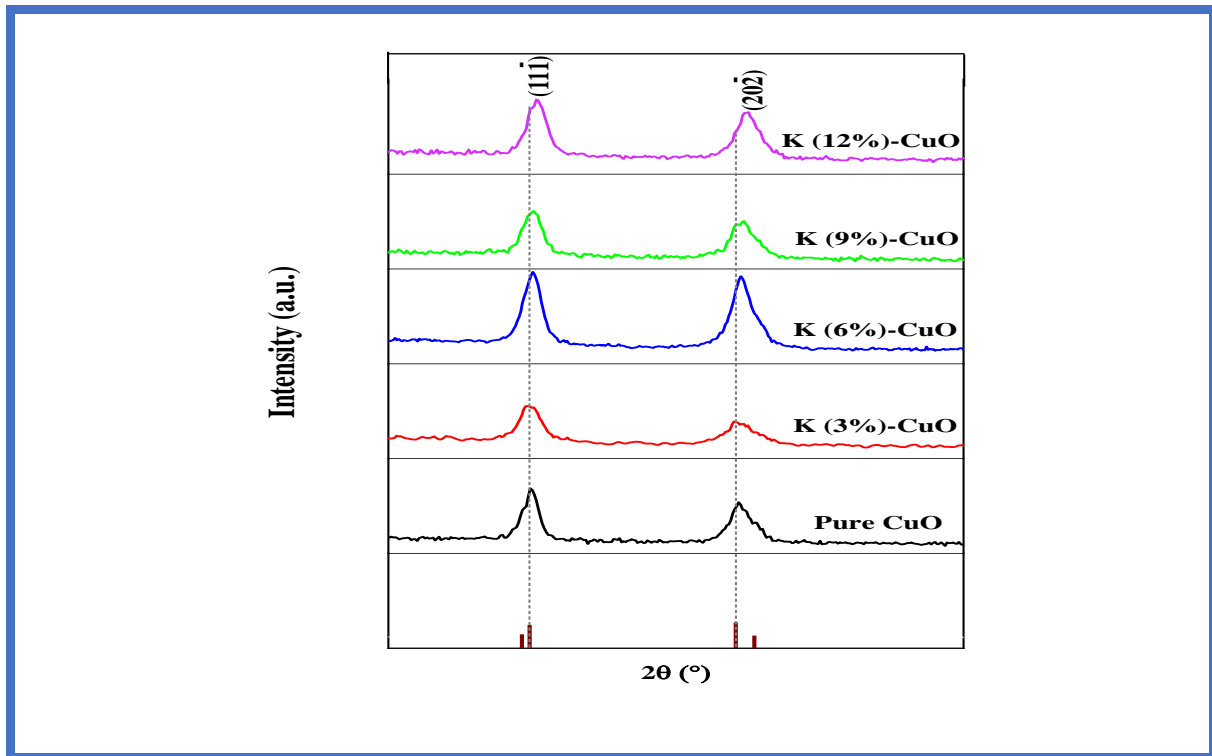
Figure IV.12. X-ray diffraction patterns of pure and $Cu_{1-x} K_x O$ (x=3%,6%, 9%, 12%).

The crystallite size of the as-prepared samples was determined using both the Debye-Scherrer formula and the Williamson-Hall relation. Several microstructural parameters like crystallite size (D), dislocation density (δ), micro-strain (ε), have been calculated.
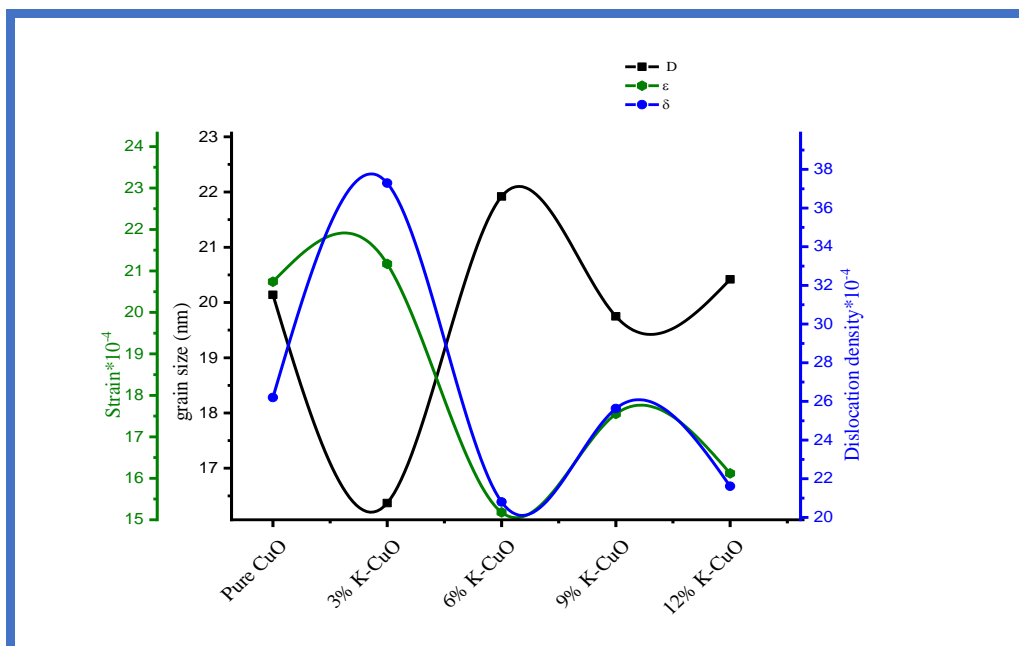
Figure IV.13. Variation of grain size, strain and dislocation density of CuO thin films as function of k concentration.

Doped CuO samples exhibit a smaller crystallite size compared to pure CuO. where, The crystallite size decreases for doping ratios of 3, 9 and 12 wt% and then increases for 6 wt% when compared with pure CuO thin. film as the incorporation of dopants limits grain growth by accumulating at the grain boundaries during nucleation, thereby increasing lattice distortion and introducing more defects such as dislocations. However, when the K doping concentration reaches 6%, the lattice parameter values of CuO films begin to increase, while dislocation density and micro-strain values decrease. The larger crystallite size and lower dislocation density at this concentration indicate an enhancement in crystallinity. Therefore, the minimal values of micro-strain and dislocation density suggest that 6% K-doped CuO thin films have reduced lattice defects and dislocations along the grain boundaries. The decrease in crystallite size with higher doping concentrations may be attributed to an increase in nucleation sites resulting from potassium doping or the saturation of potassium within the CuO samples. Similar behavior has been reported in previous studies [14].

Table IV.6. values of lattice parameter, grain size, dislocation density, strain and stacking fault probability for $Cu_{1-x} K_x O$ thin films (x = 3%, 6%, 9%, and 12%) prepared by the spin-coating method, compared to undoped CuO thin films

| Sample	Lattice parameter (Å)				Crystallite size D (nm)	Dislocation density (x10^14 lines) m^-2	Strain ε × 10^-4
	a=	b=	c=	V=			
Pure CuO	4.6972	3.4258	5.1380	81.5450	20.14	26.20	21.40
3% K-CuO	4.7131	3.4210	5.1028	81.1467	16.37	37.20	23.34
6% K-CuO	4.6880	3.4257	5.1301	81.2578	21.92	20.80	17.44
9% K-CuO	4.7025	3.4139	5.0120	81.0701	19.75	25.63	19.36
12% K-CuO	4.6956	3.4134	5.1244	81.0073	20.42	21.61	17.77

IV.2.3.2. Morphological (SEM) and chemical composition (EDX) analysis

Scanning Electron Microscopy (SEM) provides clear insight into the morphology of thin film surfaces, reflecting their internal structures. The morphology of as-synthesized pure and K-doped CuO thin films was investigated using SEM. By comparing the micrographs, it can be observed that the spin-coated layers exhibit distinct surface morphologies. where, the undoped CuO film displays a nanofiber-like morphology, with interconnected nanofibers and

no micropores, voids, or holes on the surface. However, this nanofiber-like morphology begins to disappear when the film is doped with potassium (K).

With K doping, the morphology transitions to irregularly shaped grains dispersed across the film surface. Thus, the concentration of K doping significantly influences the surface morphology of the CuO thin film, resulting in round grains of various sizes distributed almost uniformly across the film surfaces.
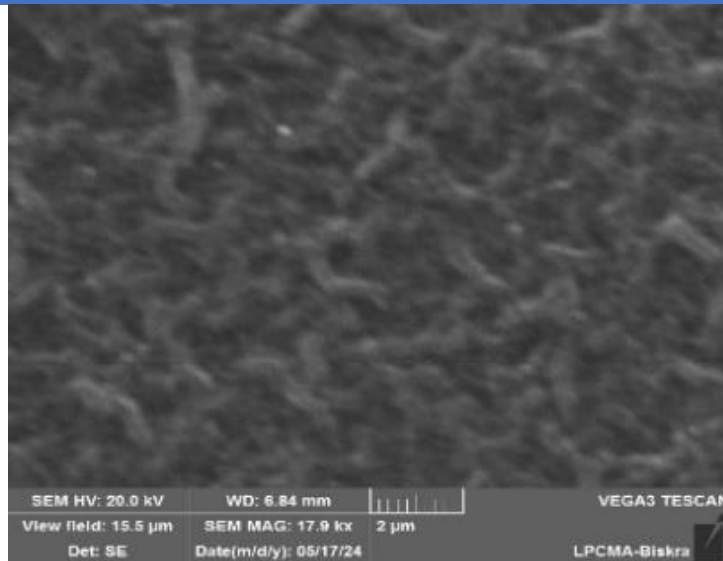
Pure CuO
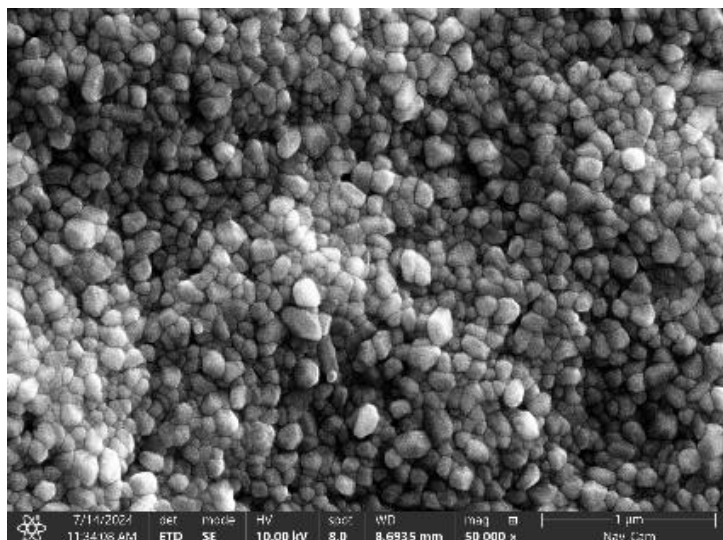
(3%) K-CuO
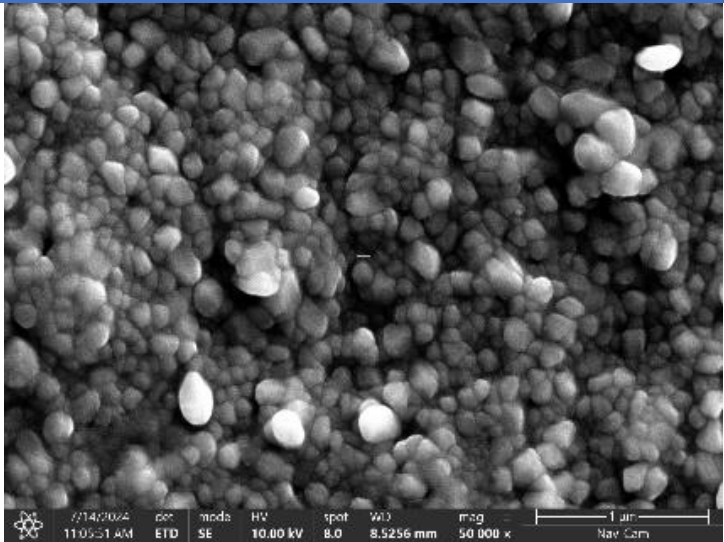
(6% K-CuO)
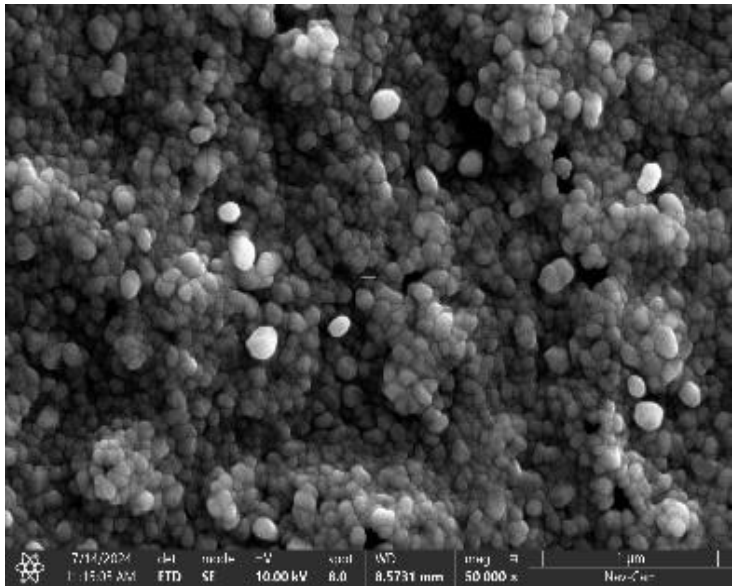
(9% K-CuO)

(12% K-CuO)
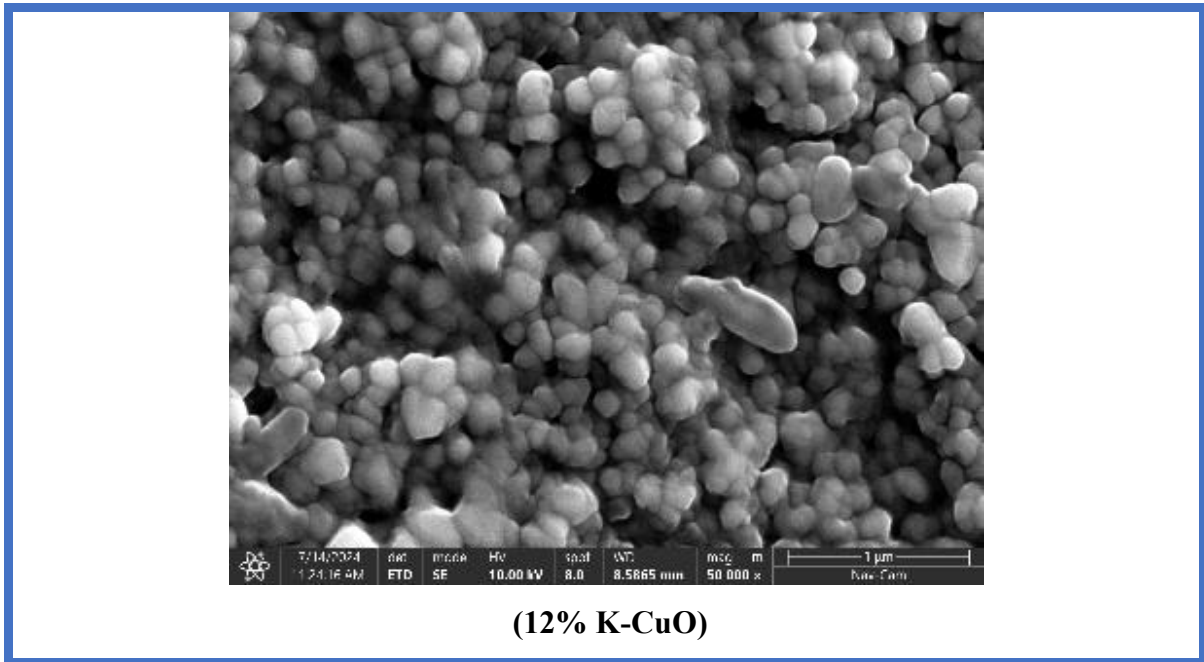
Figure IV.15. SEM images of undoped and K-doped CuO thin films.

EDX analysis is an analytical technique used for the elemental analysis or chemical characterization of a sample. The energy dispersive X-ray spectroscopy examinations of all thin films were performed at a lower magnification (500x), and the EDX spectrograph is presented in **Figure IV.16**. The analysis reveals that pure CuO films contain strong signals of Cu and O peaks. Additionally, the doped samples with different concentrations (3, 6, 9, and 12 %) show characteristic peaks of Cu, O, and K. confirming the incorporation of K into CuO thin films.

Pure CuO

Element	Weight %	Atomic %
O K	24.1	55.8
K K	0.3	0.3
Cu K	75.6	44.0

(3% K-CuO)

Element	Weight %	Atomic %
O K	29.4	62.1
K K	0.5	0.6
Cu K	70.1	37.3

(6% K-CuO)

Element	Weight %	Atomic %
O K	43.4	75.2
K K	0.8	0.9
Cu K	55.8	23.9

(9% K-CuO)

Element	Weight %	Atomic %
O K	47.9	78.2
K K	1.2	0.8
Cu K	50.9	20.9
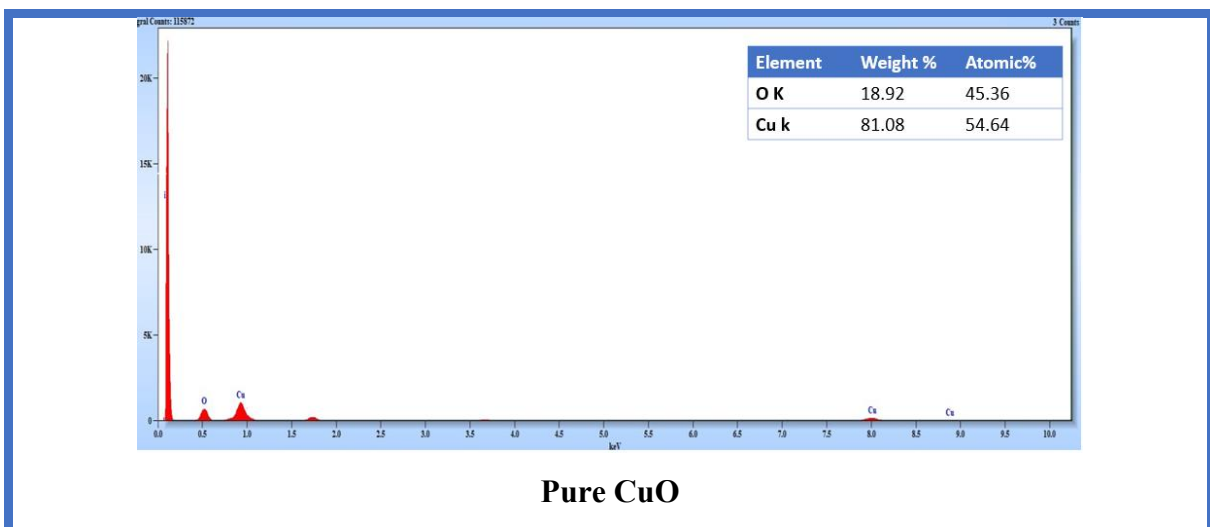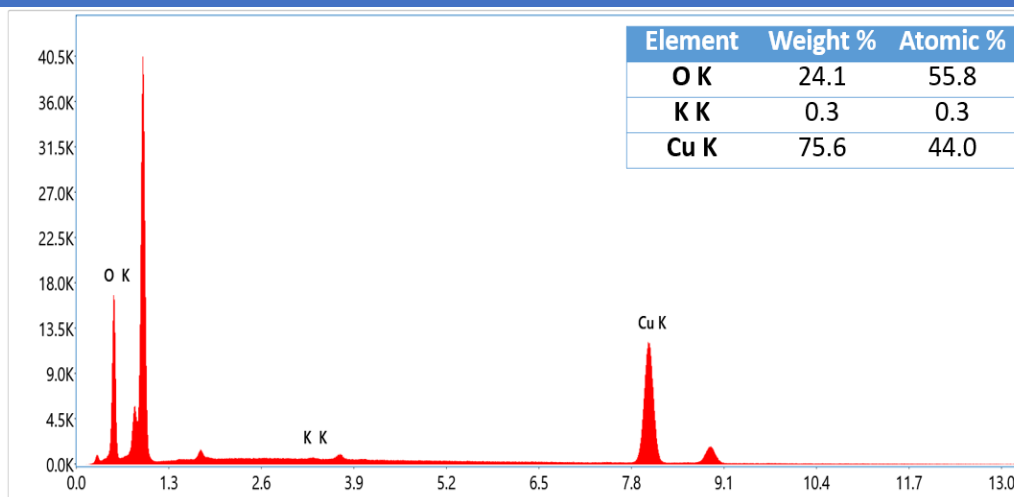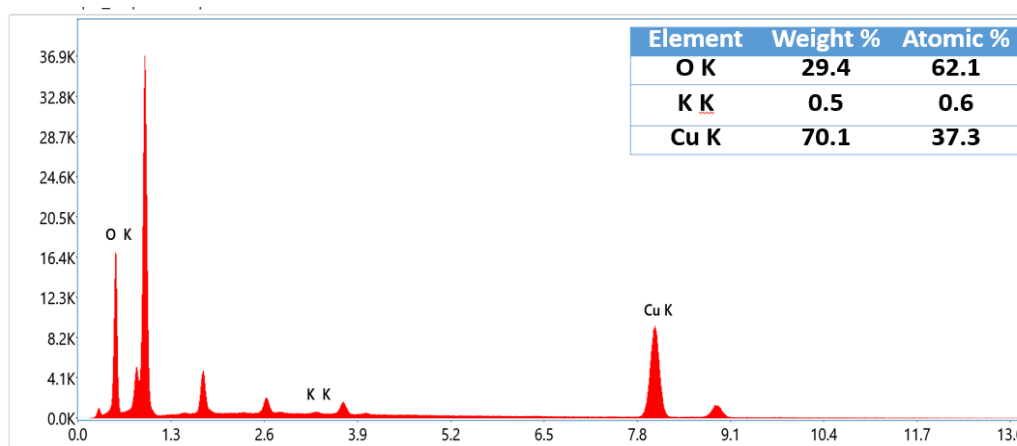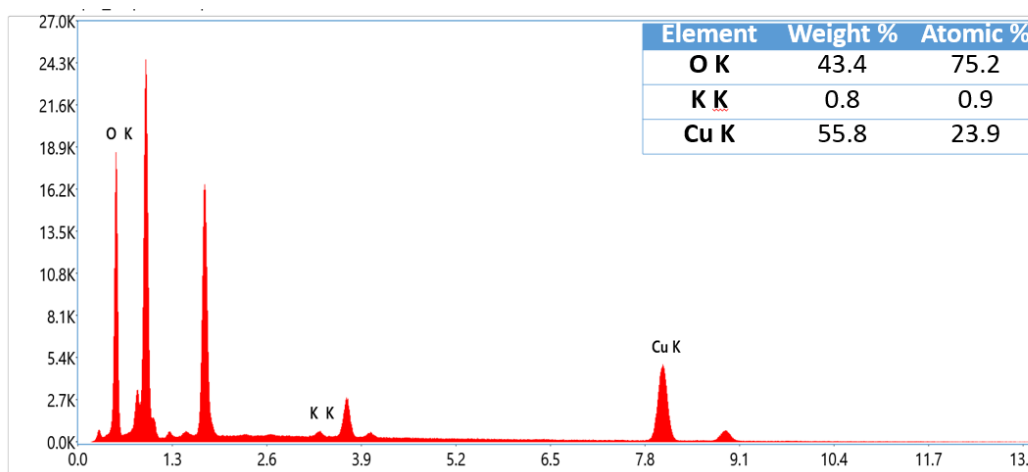
(12% K-CuO)
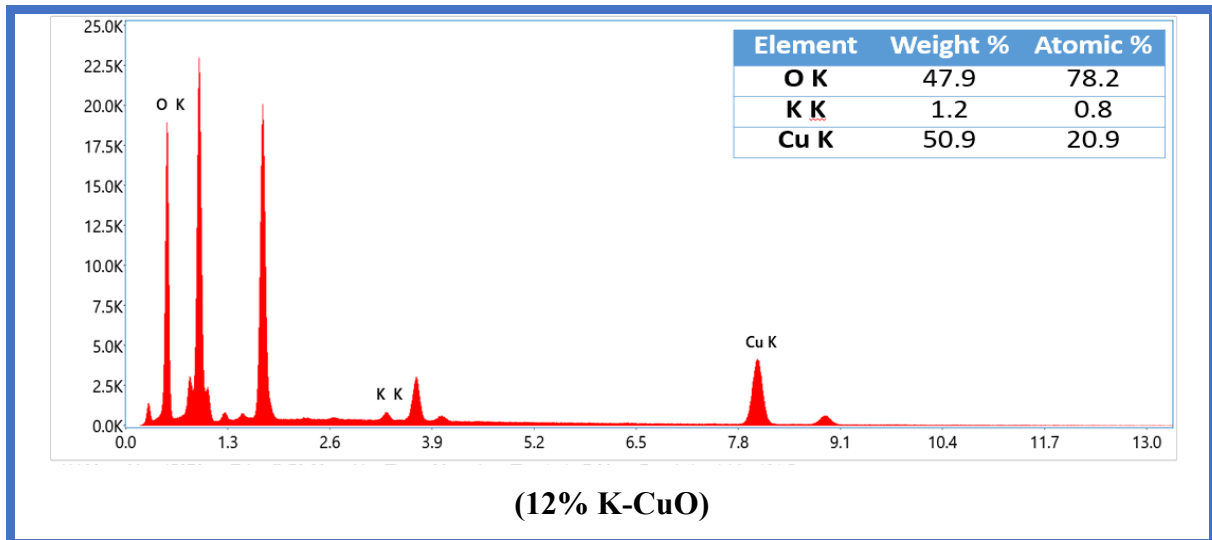
Figure IV.16. EDS spectra of undoped and K-doped CuO thin films.

IV.2.3.3. Optical properties

The optical properties of pure and potassium-doped CuO thin films were investigated using UV-Visible spectroscopy. The optical transmittance spectra of the fabricated CuO thin films, including undoped and potassium-doped samples with ratios of 3%, 6%, 9%, and 12%, are presented in **Figure IV.18.** The transmittance versus wavelength data revealed lower transmission in the visible region of the light spectrum, accompanied by an increase in transmittance in the near-infrared (NIR) region. This suggests that the prepared CuO thin films are highly effective for light absorption up to the visible range. Additionally, the overall transmittance increased with higher dopant concentrations. Besides, the highest transmittance values were reached with the 6% K doped CuO sample among the all produced CuO. These changes in optical transmittance can be attributed to the improved crystal structure resulting from doping, which reduces light scattering within the material and enhances transmittance, as corroborated by experimental results obtained using X-ray analysis [15].
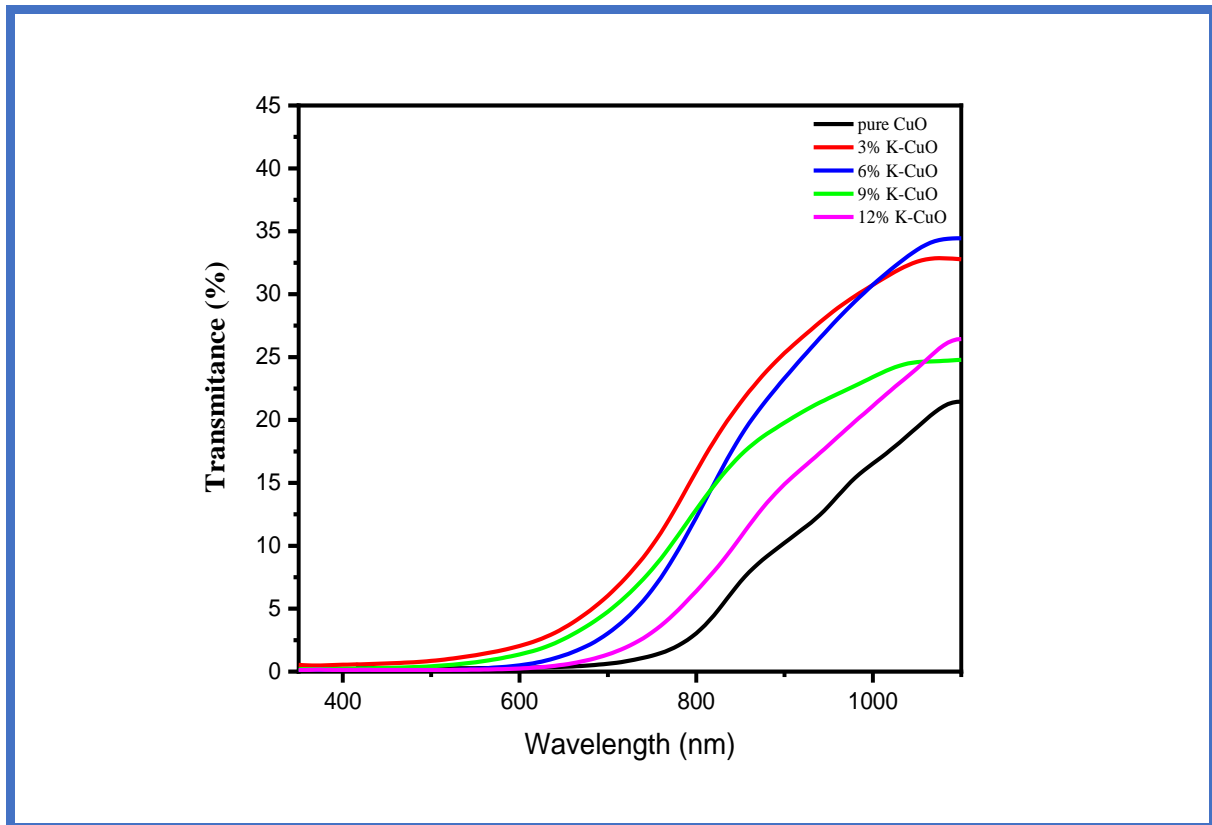
Figure IV.17. Transmittance spectra of undoped and K-doped CuO.

The absorption coefficient (α) and Extinction coefficient (κ)

The figure indicates lower absorption and extinction coefficients in the UV-region. However, an increasing trend is observed in the visible and NIR regions. In potassium-doped copper oxide (CuO), a lower absorption coefficient means that the films absorb less light or electromagnetic radiation than undoped CuO. This decrease in absorption may result from changes in the electronic structure and morphology of CuO when potassium ions K^+ are incorporated into its lattice. Potassium doping can shift the energy levels within the CuO lattice, potentially altering how electrons interact with photons. If these shifts reduce the likelihood of electronic transitions that absorb light at specific wavelengths, the film's overall absorption may decrease, thus reducing the absorption coefficient. On the other hand, the diminished absorption observed in potassium-doped CuO can be attributed to its lower extinction coefficient as reported by A. Ansari et al., [16].
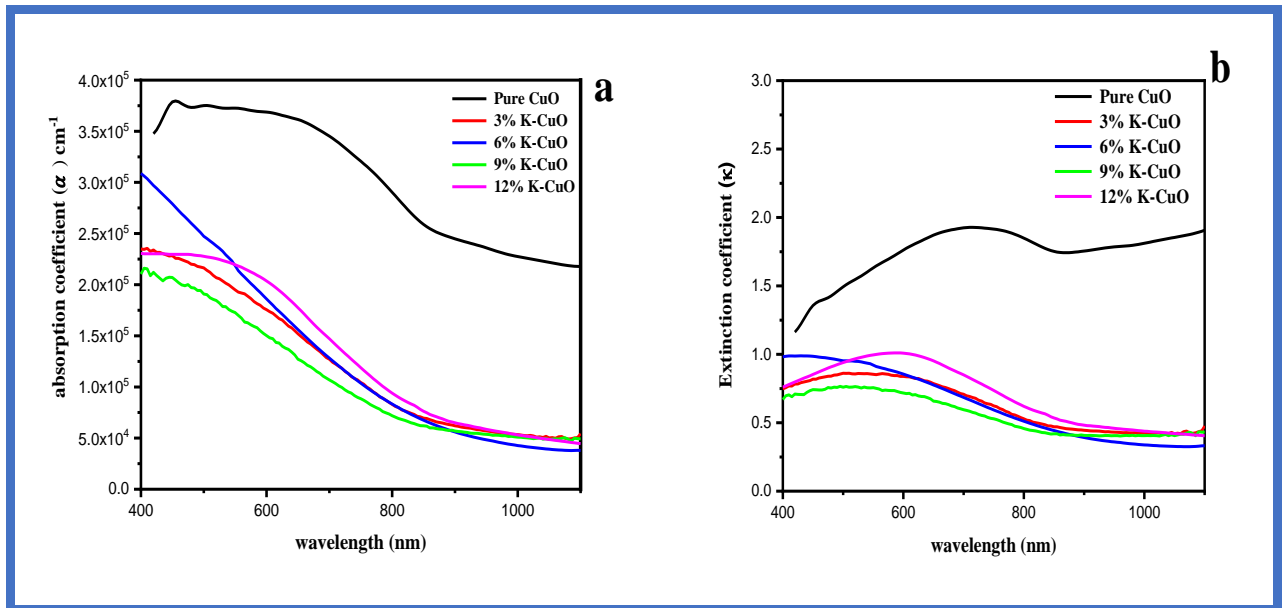
Figure IV.18. a) absorption coefficient (α), b) Extinction coefficient (κ) with wavelength of undoped and K-doped CuO thin films**.**

Band gap energy (Eg) and Urbach energy (Eu)

The transition type in the pure and K-doped CuO is the direct transition. Therefore, the optical band gaps were determined using Tauc's plot method. The Tauc plots were employed to evaluate the band gap energy by plotting $(\alpha h\nu)^2$ versus $(h\nu)$ and extrapolating the linear portion to find the intercept with the energy axis. This process is illustrated in **Figure IV.19.** and **IV.20.** and the resulting band gap energy values
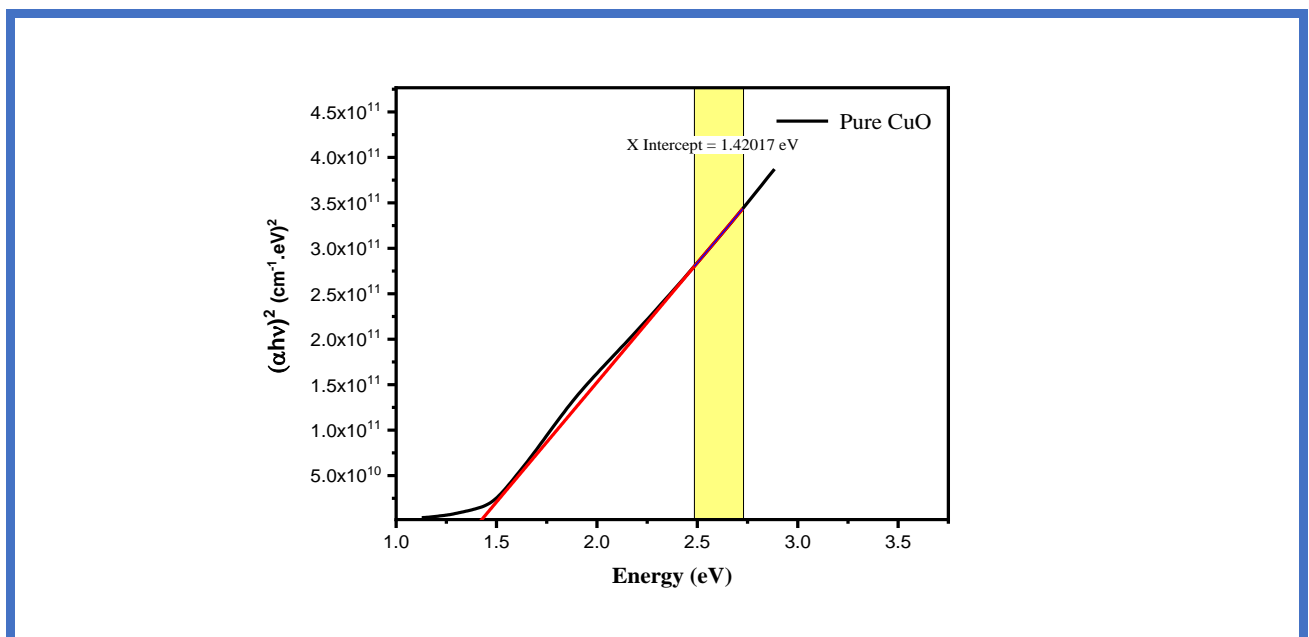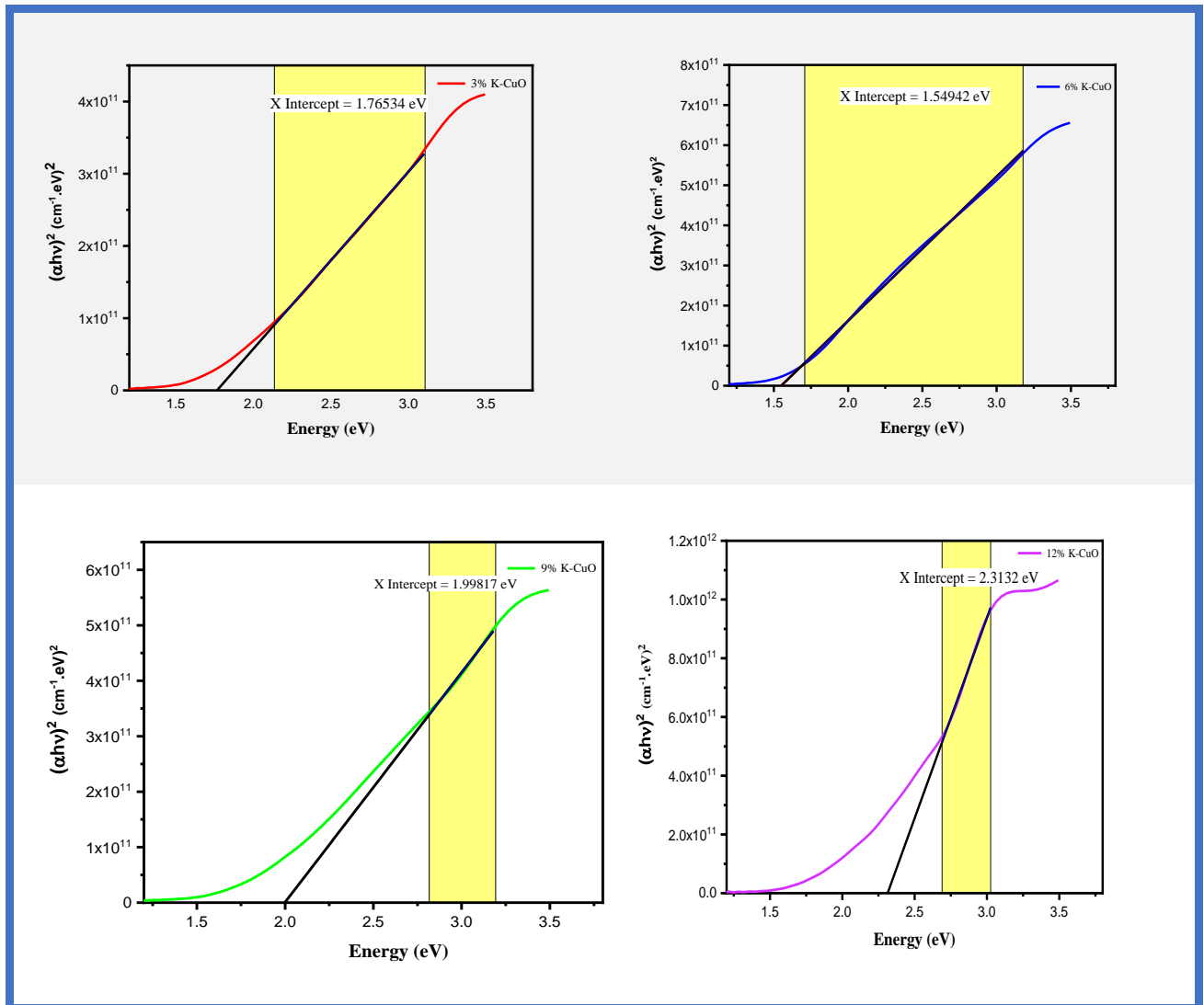
Figure IV.19. plot of $(\alpha h\upsilon)^2$ plotted against $h\upsilon$ for Cu_{1-x} K_xO thin films (x = 3%, 6%, 9%, and 12%) prepared by the spin-coating method, compared to undoped CuO thin films.

It is clear that as the doping process happened, the band gap value varied. The change in the band gap is the result of the existence of K levels within the CuO lattice. Concerning band gap values for undoped CuO (1.42 eV) in close accord with the data presented. while it is found that the band gap of 3% K-doped CuO (1.78 eV) which is decreased to (1.54 eV) for 6% K- doped CuO. Later increased to (1.99 eV) and (2.31 eV) for 9% and 12% K- doped CuO respectively. Our results are comparable by other experimental result [17]. In this case, the broadening of Eg in K-doped CuO thin films may be due to the high oxygen content observed in EDX analysis. Oxygen impacts the bandgap by modifying the electronic structure and creating oxygen-related defects, like vacancies and interstitials, which introduce new energy states and alter the crystal structure, affecting atomic spacing and bonding. Higher oxygen

levels can also increase charge carrier density, collectively raising Eg by shifting energy levels and influencing electron interactions. Notably, oxygen content peaks in the 12 at% K-doped CuO film, which also has the highest Eg. Since Eg depends on the film's composition and stoichiometry, its increase can be attributed to variations in elemental composition in K-doped CuO. A similar behavior was reported in previous work by [18]
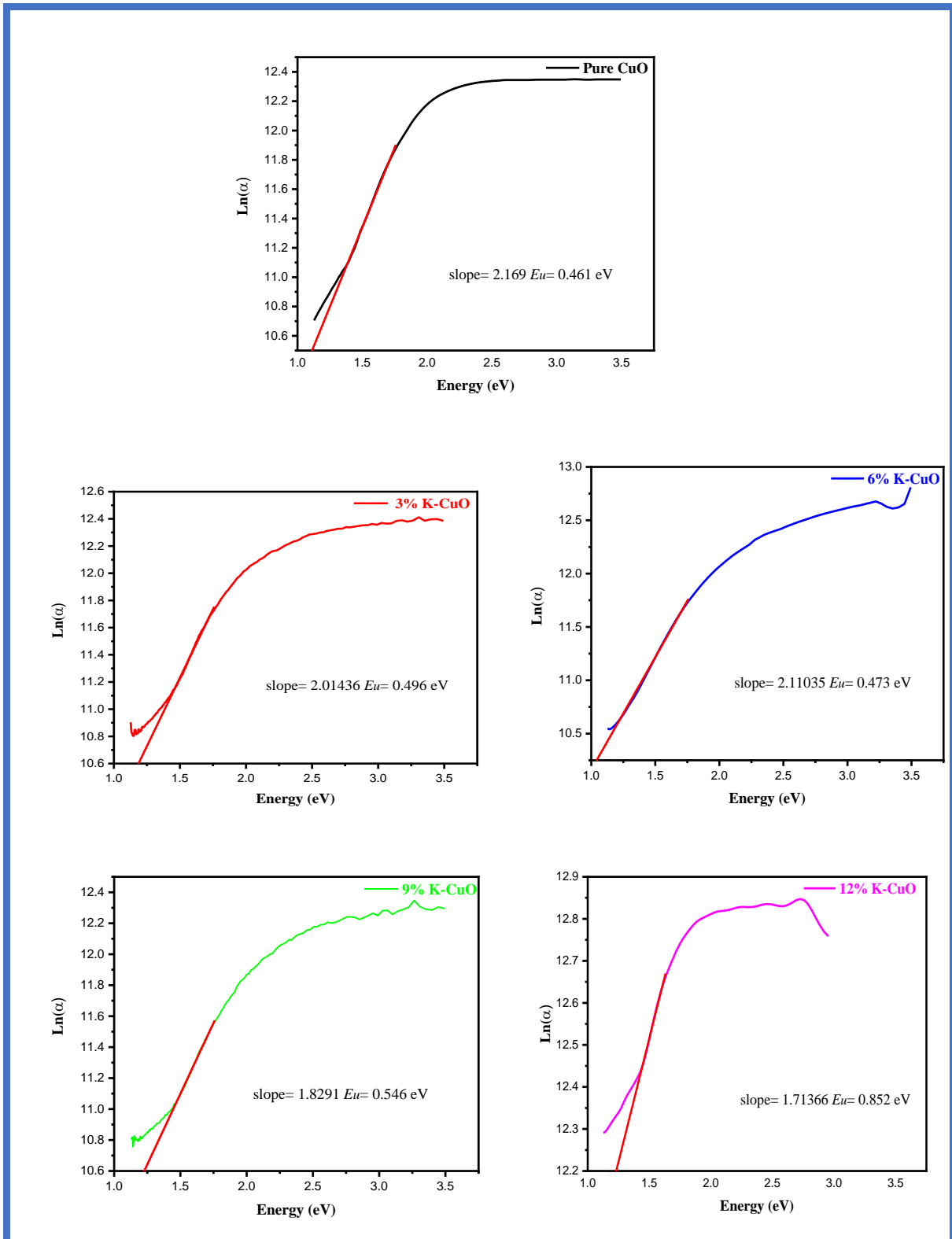
Figure IV.20. plot of Ln(α)plotted against *hv* for $Cu_{1-x}K_xO$ thin films (x = 3%, 6%, 9%, and 12%) prepared by the spin-coating method, compared to undoped CuO thin films.

IV.2.3.4. Electrical properties

This section describes how potassium (K) doping affects the resistivity of copper oxide (CuO) thin films, as shown in Table 1. The table presents the measured resistivity values of both undoped CuO and CuO doped with various potassium levels (3%, 6%, 9%, and 12%). As potassium concentration increases, the resistivity of the material decreases significantly, indicating that K-doped CuO films conduct electricity more efficiently. In fact, Pure CuO exhibits p-type conductivity, meaning it primarily conducts through holes, which result from its structural properties: copper vacancies and interstitial oxygen atoms [19]. These copper vacancies create Cu^{2+}ions, each of which introduces a hole in the valence band. When CuO is doped with potassium, resistivity further decreases because potassium increases the concentration of Cu^{2+} ions. The presence of K^+ ions in the CuO lattice introduces additional holes, thereby enhancing p-type conductivity [20].

Structural analysis suggests that defects, such as grain boundaries and dislocations, act as traps for free carriers, reducing their mobility and thus increasing the resistivity of the thin film. This may account for the observed reduction in resistivity of the 6% k-doped CuO compared to other doping. This could explain the lower resistivity observed in the 6% K-doped CuO compared to other doping levels[21].

Table IV.7. Electrical conductivity and resistivity of the $Cu_{1-x} K_x O$ (x=3%,6%, 9% and 12%) and undoped CuO thin films.

Samples	Pure CuO	3% K-CuO	6% K-CuO	9% K-CuO	12% K-CuO
Resistivity $\times 10^2$ (Ω.cm)	1.7	0.154	0.101	0.173	0.168
Conductivity $\times 10^{-2}$ (Ω.cm)$^{-1}$	0.58	6.49	9.92	5.79	5.97

IV.2.4. Thermoelectric properties

IV.2.4.1. Conductivity Type

In P-type thin films, the majority carriers, referred to as 'holes,' migrate from the cold probe to the hot probe. This movement of holes between the probes creates an electric field and a potential gradient. The potential difference generated is measured by a voltmeter connected in parallel. The hot probe indicates positive polarity (indicating an excess of holes), while the

cold probe displays negative polarity (indicating a deficiency of holes), resulting in a negative reading on the voltmeter. In contrast, for N-type thin films, the behavior is reversed, producing a positive reading on the voltmeter. The negative reading observed in all samples confirms their classification as P-type conductivity, aligning well with existing literature.

IV.2.4.2. The Seebeck coefficient

The Seebeck coefficient was determined experimentally by calculating the slope of the graph of ΔV as a function of ΔT, as illustrated in the figure. The graph demonstrates that the electromotive force increases linearly with the temperature difference between the cold and hot ends of the sample.

Figure IV.21.   Graph showing the relationship between electric potential and temperature difference (between 290 K and 383 K) for undoped and 6% X-doped (X = Li, Na, K) CuO thin films. The Seebeck coefficient for the undoped films is approximately ($736.83 \pm 10 \, \mu V/K$), which is consistent with previous research on CuO. This value is significantly higher than those observed for the doped samples. Specifically, the Li-doped CuO sample exhibited a Seebeck coefficient of ($599.5 \pm 10 \, \mu V/K$), while the Na-doped CuO showed ($528.67 \pm 10 \, \mu V/K$), and the K-doped CuO sample had ($172.17 \pm 10 \, \mu V/K$). This variation in values can be attributed to an increase in the number of defects, which is typically accompanied by enhanced vibrations within the material's internal structure. These vibrations interact and impede the flow of scattered phonons, leading to lower thermal conductivity. Consequently, these changes affect the Seebeck coefficient, as concluded by the authors of this study[22]. Notably, the highest Seebeck coefficient values were achieved with Li doping[23], a finding that aligns with similar results reported by N. Yoshida et al,.[20] .
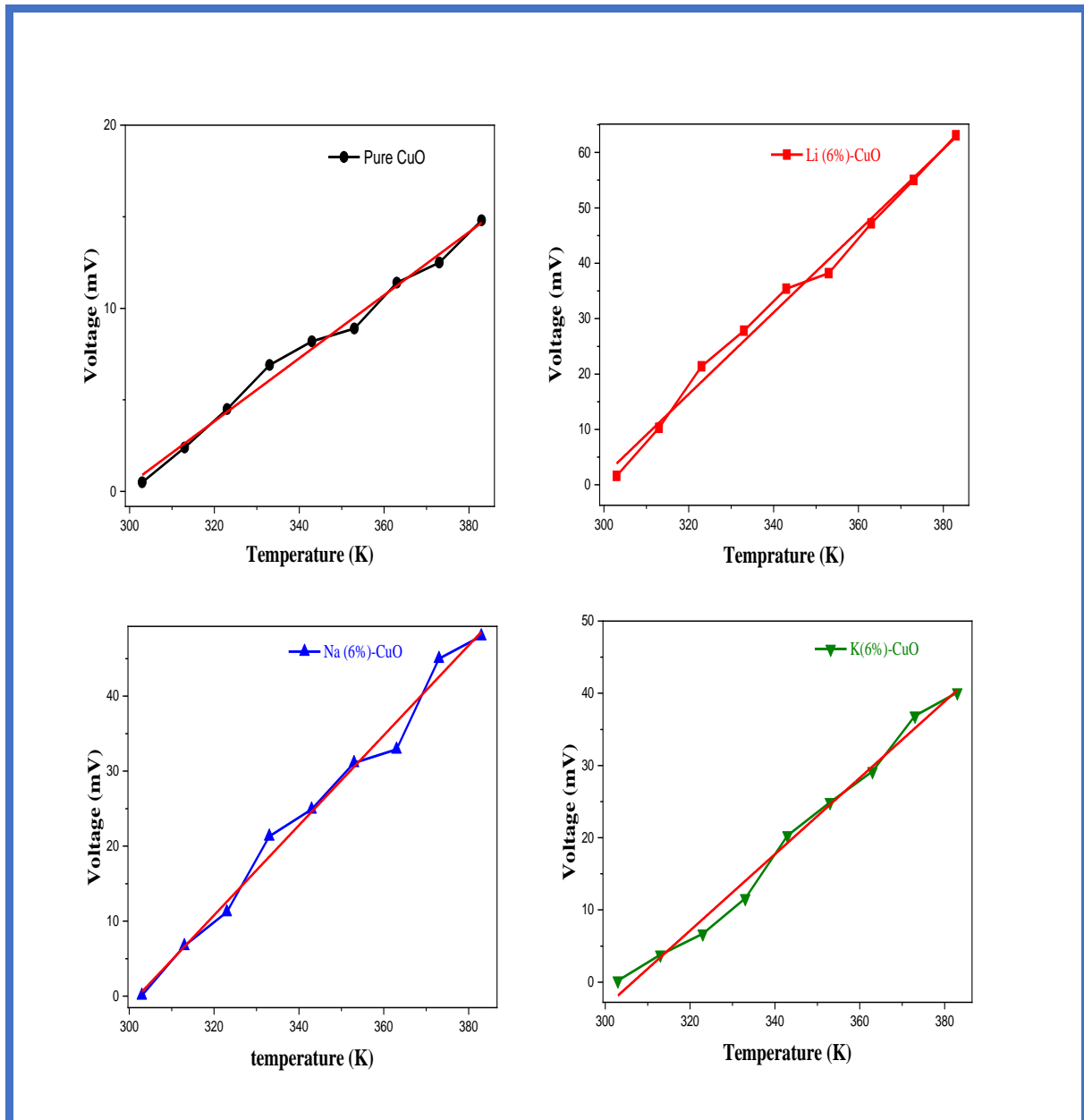
Figure IV.21. Graph between electric potential and temperature difference (between 290 - 383K) of undoped and 6% X-doped (X= Li, Na, K) CuO thin films.

IV.2.4.3. The Power Factor (PF)

Figure IV.22. illustrates the magnitude of the power factor (PF), which is influenced by both the electrical conductivity and the Seebeck coefficient of the copper oxide samples. The maximum PF value observed in the Li-doped CuO samples is approximately (9.776×10^{-10} $W.m^{-1}.K^{-2}$). In comparison, the Na-doped CuO shows a PF of (1.657×10^{-11} $W.m^{-1}.K^{-2}$), while the K-doped CuO has a PF of (2.944×10^{-11} $W.m^{-1}.K^{-2}$). These values are comparable to that of the undoped samples, which exhibit a PF of (3.186×10^{-11} $W.m^{-1}.K^{-2}$).

One plausible explanation for this phenomenon could be linked to increased disorder in this material system, improving the thermoelectric properties, as conclude by R. Mulla [24].
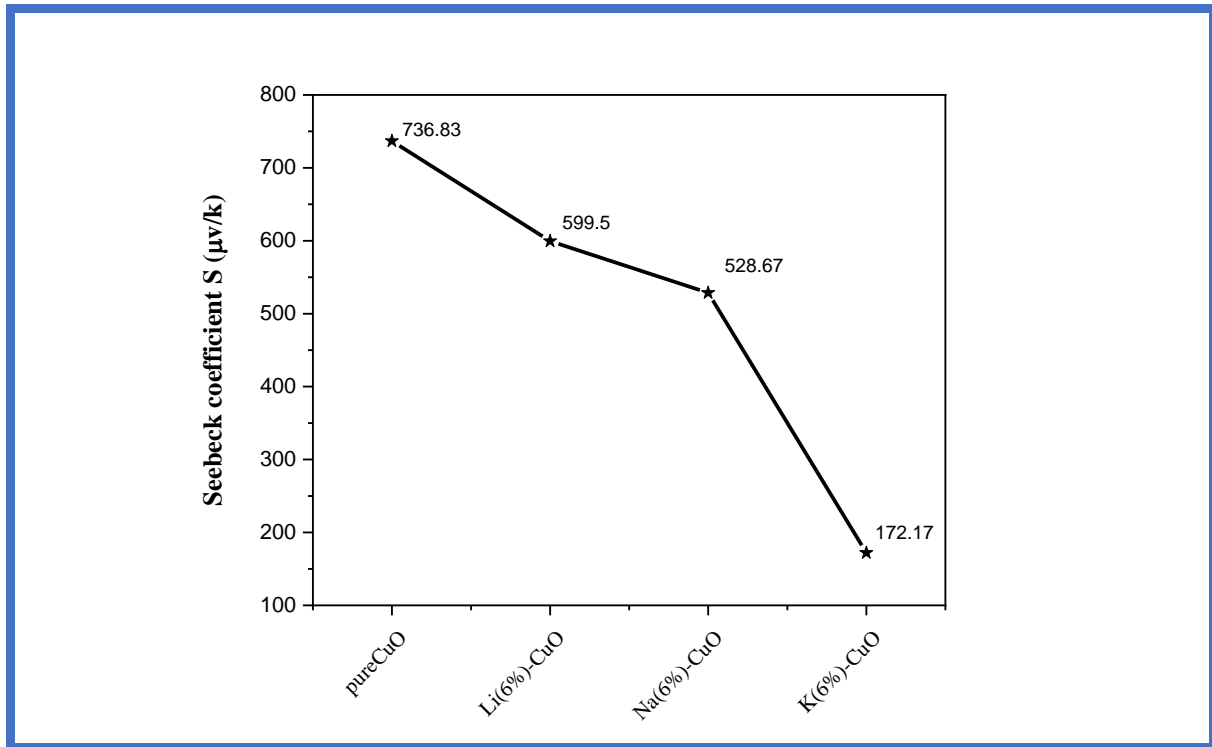
Figure IV.22. Variation of the Seebeck coefficient of undoped and 6% X-doped (X= Li, Na, K) CuO thin films between 290 -383K.

IV.2.5. Elastic constants and mechanical properties

IV.2.5.1. Elastic constants of single crystal

Elastic constants are very crucial material parameters. The study of elastic constants provides a link between the mechanical properties and dynamic information concerning the nature of the forces operating in solids, especially for the stability and stiffness of materials. The elastic constants relate to various fundamental solid-state phenomena such as stiffness, stability, brittleness, ductility, anisotropy of material and propagation of elastic waves in normal mode. The CASTEP calculates the elastic properties from the first-principles using the finite strain theory, which gives the elastic constants as the proportionality coefficients relating the applied strain to the computed stress, $\sigma_i = C_{ij} \varepsilon_j$.

The elastic properties of the monoclinic CuO crystal are characterized in terms of thirteen independent elastic constants: C_{11}, C_{22}, C_{33}, C_{44}, C_{55}, C_{66}, C_{12}, C_{13}, C_{15}, C_{23}, C_{25}, C_{35} and C_{46}. In the present work, the predicted single-crystal elastic constants C_{ij} of considered compounds are determined using the stress-strain approach [25]. Our calculated elastic constants C_{ij} and S_{ij}

for CuO are presented in **Table IV.8.** For a monoclinic crystal, the thirteen independent elastic constants C_{ij} as shown below.

$$\begin{bmatrix} C_{11} & C_{12} & C_{13} & 0 & C_{15} & 0 \\ C_{12} & C_{22} & C_{23} & 0 & C_{25} & 0 \\ C_{13} & C_{23} & C_{33} & 0 & C_{35} & 0 \\ 0 & 0 & 0 & C_{44} & 0 & C_{46} \\ C_{15} & C_{25} & C_{35} & 0 & C_{55} & 0 \\ 0 & 0 & 0 & C_{46} & 0 & C_{66} \end{bmatrix} \qquad \text{(IV.1)}$$

The requirement of mechanical stability in a monoclinic structure leads to the following restrictions on the elastic constants [26]:

$$C_{ii} > 0 \quad \forall\, i \in \{1, 6\},$$

$$(C_{33}C_{55} - C_{35}^2) > 0, \quad (C_{44}C_{66} - C_{46}^2) > 0, \quad (C_{22} + C_{33} - 2C_{23}) > 0$$

$$(C_{11} + C_{22} + C_{33} + 2C_{12} + 2C_{13} + 2C_{23}) > 0$$

$$C_{22}(C_{33}C_{55} - C_{35}^2) + 2C_{23}C_{25}C_{35} - C_{23}^2 C_{55} - C_{25}^2 C_{33} > 0 \qquad \text{, and} \qquad \text{(IV.2)}$$

$$2\big[C_{15}C_{25}(C_{33}C_{12} - C_{13}C_{23}) + C_{15}C_{35}(C_{12}C_{13} - C_{12}C_{23}) + C_{25}C_{35}(C_{11}C_{23} - C_{12}C_{13})\big]$$
$$-\big[C_{15}^2(C_{22}C_{33} - C_{23}^2) + C_{25}^2(C_{11}C_{33} - C_{13}^2) + C_{35}^2(C_{11}C_{22} - C_{12}^2)\big] + g\, C_{55} > 0,$$

Where: $g = C_{11}C_{22}C_{33} - C_{11}C_{23}^2 - C_{22}C_{13}^2 - C_{33}C_{12}^2 + 2C_{12}C_{13}C_{23}$

It is clear that the elastic constants C_{ij} satisfy the mechanical stability criteria, indicating that CuO crystal are mechanically stable. The calculated C_{33} values are larger than that of C_{11} and C_{22}, which indicate that the resistance to deformation along the [001] direction is higher than that along the [100] and [010] directions. Additionally, it is observed that the value of the elastic constants C_{44}, C_{55} and C_{66} are smaller than the elastic constants C_{11}, C_{22} and C_{33}, implying that the resistances of the studied materials to the compressional deformations, are stronger than their resistances to shear deformations. The elastic constants C_{25} and C_{46} of the monoclinic CuO are found to be negative.

Table IV.8. Calculated elastic constants Cij (in GPa) and Sij (in TPa^{-1}) of monoclinic CuO

C$_{11}$	C$_{22}$	C$_{33}$	C$_{44}$	C$_{55}$	C$_{66}$	C$_{12}$	C$_{13}$	C$_{15}$	C$_{23}$	C$_{25}$	C$_{35}$	C$_{46}$
235	120.79	347.68	25.94	35.45	70.09	127.5	142.6	-26.64	118.93	-15.88	-30.25	-6.56
S$_{11}$	S$_{22}$	S$_{33}$	S$_{44}$	S$_{55}$	S$_{66}$	S$_{12}$	S$_{13}$	S$_{15}$	S$_{23}$	S$_{25}$	S$_{35}$	S$_{46}$
9.4651	12.0916	4.9836	28.841	24.5004	18.6929	-5.864	-1.2231	1.7720	-2.6212	2.169	-2.3241	2.2431

IV.2.5.2. Polycrystalline elastic constants

The mechanical properties of polycrystalline materials, bulk modulus B and shear modulus G can be evaluated using the Voigt [27], Reuss [28]and Hill approximation [29] methods. For a monoclinic crystal, the Voigt, Reuss, and Hill bulk (B$_V$, B$_R$, B$_H$) and shear (G$_V$, G$_R$, G$_H$) moduli are given by [26]: :

$$B_V = \frac{1}{9}(C_{11} + C_{22} + C_{33}) + \frac{2}{9}(C_{12} + C_{13} + C_{23}) \tag{IV.3}$$

$$G_V = \frac{1}{15}(C_{11} + C_{22} + C_{33} - C_{12} - C_{13} - C_{23}) + \frac{1}{5}(C_{44} + C_{55} + C_{66}) \tag{IV.4}$$

$$B_R = \left[(S_{11} + S_{22} + S_{33} + 2(S_{12} + S_{13} + S_{23})\right]^{-1} \tag{IV.5}$$

$$G_R = 15\left[4(S_{11} + S_{22} + S_{33}) - 4(S_{12} + S_{13} + S_{23}) + 3(S_{44} + S_{55} + S_{66})\right]^{-1} \tag{IV.6}$$

$$B = B_H = \frac{1}{2}(B_V + B_R) \tag{IV.7}$$

$$G = G_H = \frac{1}{2}(G_V + G_R) \tag{IV.8}$$

Where the S$_{ij}$ (=C$_{ij}^{-1}$) are the elastic compliance constants. The Young's modulus *E* and

Poisson's ratio *v* can be given by

$$E_V = \frac{9\,B_V\,G_V}{3B_V + G_V} \quad ; \quad E_R = \frac{9\,B_R\,G_R}{3B_R + G_R} \quad ; \quad E = E_H = \frac{9\,B_H\,G_H}{3B_H + G_H} \tag{IV.9}$$

$$v_V = \frac{3B_V - 2G_V}{2(3B_V + G_V)} \quad ; \quad v_R = \frac{3B_R - 2G_R}{2(3B_R + G_R)} \quad ; \quad v = v_H = \frac{3B_H - 2G_H}{2(3B_H + G_H)} \tag{IV.10}$$

Our calculated polycrystalline bulk modulus (B_V, B_R, B_H=B), shear modulus (G, G_R, G_H=G), Young's modulus (E_V, E_R, E_H=B), Poisson's ratio, B/G ratio of monoclinic CuO are presented in **Table IV.9.** and **Table IV.10.** The bulk modulus and shear modulus that measure the resistance to volume change under applied hydrostatic pressure, and the resistance to reversible deformation upon shear stress, respectively. The Young's modulus E which measures of the stiffness of a solid material, it defines the relationship between stress and strain. A material with a very large Young's modulus can be approximated as stiff. The B/G value indicates that the material is ductile (or brittle). According to the criterion of Pugh [30], a material behaves in a ductile manner if B/G ratios > 1.75, and it should be brittle if B/G is less than 1.75. Our obtained values are 1.39 for CuO, indicating that CuO can be classified as ductile materials. The value of Poisson's ratio is greater than 0.26 [31], indicating that a material behaves in a ductile manner, otherwise, it shows a brittle manner. The Poisson's ratio value is 0.365, meaning that the monoclinic CuO shows brittle nature. The result from Poisson's ratio is consistent with the conclusion from B/G.

Table IV.9. Computed values of bulk modulus B (in GPa), Young's modulus E (in GPa), shear modulus G (in GPa) and Poisson's ratio (unitless) of CuO in monoclinic phase.

Average scheme	Bulk modulus B (in GPa)	Young's modulus E (in GPa)	Shear modulus G (in GPa)	Poisson's ratio (unitless)
Voigt	B_V = 166.84	E_V = 132.88	G_V = 48.592	v_V = 0.367
Reuss	B_R = 113.32	E_R = 92.786	G_R = 34.024	v_R = 0.363
Hill	B_H = 140.08	E_H = 112.83	G_H = 41.308	v_H = 0.365

A universal measure of anisotropy which is applicable to all types of single crystal can be obtained by accounting for both the bulk component and shear component and the formula can be expressed as [32]:

$$A^U = 5\frac{G_V}{G_R} + \frac{B_V}{B_R} - 6 \geq 0 \tag{IV.11}$$

It is aware that B_V and G_V and are the upper bounds of bulk and shear modulus, so the universal anisotropy should be larger than zero for the anisotropic single crystal and equal to zero for isotropic materials. The calculated results in **Table IV.10.** show that CuO is the anisotropic equal A^U (2.61).

Using the polycrystalline shear modulus G and bulk modulus B, we can obtain the longitudinal and transverse elastic wave velocity [30, 31],:

$$V_l = \frac{3B + 4G}{3\rho} \qquad (IV.12)$$

$$V_t = \frac{G}{\rho} \qquad (IV.13)$$

So the average wave velocity V_m can be approximately given by

$$V_m = \left[\frac{1}{3} \left(\frac{2}{V_t^3} + \frac{1}{V_l^3} \right) \right]^{-\frac{1}{3}} \qquad (IV.14)$$

From the average wave velocity, the Debye temperature can be determined by the following formula:

$$\theta_D = \frac{h}{k_B} \left[\frac{3n}{4\pi} \left(\frac{N_A \rho}{M} \right) \right]^{\frac{1}{2}} V_m \qquad (IV.15)$$

Where h is Planck's constant, k is Boltzmann's constant, N_A is Avogadro's number, n is the number of atoms per formula unit, M is the molecular mass per formula unit, $\rho = (M/V)$ is the density.

As an important fundamental parameter of solids, Debye temperature has close relationships with specific heat, bonding types and melting temperature.

The estimation results for CuO are 398 K. Since the vibrational excitation at 0 K contains only the acoustic components, the Debye temperature determined by elastic constants should have no difference from the measurement of specific heat method at low temperature [33].

The shear and longitudinal sound velocities V_t, V_l, average wave velocities V_m and Debye temperatures θ_D are determined and listed in **Table IV.10.** According to our knowledge, there are no data available in the literature concerning the shear, longitudinal sound velocities and Debye temperatures θ_D of CuO in monoclinic phase. Our results are predictions and may serve as a reference for future experimental investigations.

Table IV.10. The calculated bulk modulus (B), shear modulus (G), Pugh's ratio (G/B), Young's modulus (E), Poisson's ratio, longitudinal (V_l), shear (V_t), average (V_m) elastic wave velocities and Debye temperature (θ_D) of CuO in monoclinic phase.

Material	B (GPa)	G (GPa)	B/G	E (GPa)	ν	A^U	ρ(g/cm³)	V_t (m/s)	V_l (m/s)	V_m (m/s)	$θ_D$ (K)
CuO	140.08	41.308	3,39	112.83	0.365	2.61	6.31	2717	6038	3065	398

IV.2.4.3. Anisotropy of elastic moduli

Materials whose physical properties vary according to direction are called anisotropic materials. This is due to the different atomic densities in the crystal directions. The study of elastic anisotropy is important as it influences a variety of physical processes including the development of plastic deformation in crystals, microscale cracking in materials, and plastic relaxation in thin-film metallic. In the isotropic case elastic properties are easily represented, but for anisotropic (non-isotropic) materials, even in the simple cubic symmetry, it can be difficult to visualize how properties such as linear compressibility, Young's modulus, Shear modulus or Poisson's ratio vary with stress/strain orientation.

For a monoclinic crystal system, the directional dependence of Young's modulus (E) and shear modulus (G) can be expressed as [34-37]:

For a monoclinic system, the direction-dependent linear compressibility can be described as:

$$\beta = \left(S_{11} + S_{12} + S_{13}\right)l_1 + \left(S_{12} + S_{22} + S_{23}\right)l_2 + \left(S_{13} + S_{23} + S_{33}\right)l_3 + \left(S_{15} + S_{25} + S_{35}\right)l_3\,l_1 \quad \text{(IV.16)}$$

Young's modulus (E)

$$\frac{1}{E(\overline{l})} = S'_{1111} = S_{ijkt}\, l_i\, l_j\, l_k\, l_t = l_1^4 S_{11} + 2l_1^2 l_2^2\, S_{12} + 2l_1^2 l_3^2\, S_{13} + 2l_1^2 l_3\, S_{15} + l_2^4 S_{22} +$$
$$2l_2^2 l_3^2\, S_{23} + 2l_1 l_2^2\, l_3 S_{25} + l_3^4 S_{33} + 2l_1 l_3^2\, l_3 S_{35} + l_2^2\, l_3^2\, S_{44} + 2l_1 l_2^2\, l_3 S_{46} + l_1^2\, l_3^2\, S_{55} + l_1^2\, l_2^2\, S_{44} \quad \text{(IV.17)}$$

Shear modulus (G)

$$G' = l_1^2\, m_1^2 S_{11} + 2l_1\, l_2\, m_1 m_2\, S_{12} + 2l_1\, l_3\, m_1 m_3\, S_{13} + l_2^2\, m_2^2 S_{22} + 2l_2\, l_3\, m_2 m_3\, S_{23} + l_3^2\, m_3^2 S_{33} +$$
$$\left(l_1^2 m_1 m_3 + l_1 l_3 m_1^2\right)S_{15} + \left(l_1 l_2 m_2 m_3 + l_2 l_3 m_1 m_2\right)S_{25} + \left(l_3^2 m_1 m_3 + l_1 l_3 m_3^2\right)S_{35} +$$
$$\frac{1}{4}\left(l_2^2 l_3^2 + 2l_2 l_3 m_2 m_3 + l_3^2 m_2^2\right)S_{44} + \frac{1}{2}\left(l_1 l_2 m_2 m_3 + l_2^2 m_1 m_3 + l_1 l_3 m_2^2 + l_2 l_3 m_1 m_2\right)S_{46} +$$
$$\frac{1}{4}\left(l_1^2 m_3^2 + 2l_1 l_3 m_1 m_3 + l_3^2 m_1^2\right)S_{55} + \frac{1}{4}\left(l_1^2 m_2^2 + 2l_1 l_2 m_1 m_2 + l_2^2 m_1^2\right)S_{55} \quad \text{(IV.18)}$$

$$G = \frac{1}{4\,G'}$$

The Poisson ratio can be expressed as [38]

$$v\left(\theta,\varphi,\chi\right)=-\frac{S_{12}^{'}\left(\theta,\varphi,\chi\right)}{S_{11}^{'}\left(\theta,\varphi,\chi\right)} \tag{IV.19}$$

In these equations, S_{ij} are the components of the compliance elastic constant matrix, which have been determined in last section. l_i and m_i are two groups of direction cosines are the directions between the loading direction and three l_i coordinate axials, while m_i determines a vector perpendicular to the loading direction, which plays important roles in calculations of Shear modulus, representing the shear planes. The relationships between the two groups of direction cosines and the Euler angles are as follows:

$$\vec{l}=\begin{pmatrix} l_1=\sin\theta\ \cos\varphi \\ l_2=\sin\theta\ \sin\varphi \\ l_3=\cos\theta \end{pmatrix} \quad,\quad \vec{m}=\begin{pmatrix} m_1=\cos\theta\cos\varphi\cos\chi-\sin\theta\sin\chi \\ m_2=\cos\theta\sin\varphi\cos\chi+\cos\theta\sin\chi \\ m_3=-\sin\theta\cos\chi \end{pmatrix} \tag{IV.20}$$

Using the above equations, some representation surfaces can be constructed in 3D space to give a straight visualization of the direction-dependent mechanical properties for arbitrary directions. Each point on the surface of 3D plot corresponds to a loading direction and the distance between this point and the origin is equal to the value of modulus in this direction. For the isotropic material, its mechanical properties are of independence of direction and the 3D curved surface will exhibit a shape of sphere. But the sphere will deviate if the material is anisotropic and a large deviation corresponds to strong anisotropic characters.

The maximum and minimum values of Young's modulus (E), linear compressibility (β), shear modulus (G) and Poisson's ratio (v) for these alloys are also listed in **Table IV.11.**

Table IV.11. The maximum and minimum values of Young's modulus (E, in GPa), linear compressibility (β, in TPa^{-1}), shear modulus (G, in GPa) and Poisson's ratio (v) of monoclinic CuO.

| Material	Young's modulus (GPa)		Linear Compressibility(TPa^{-1})		Shear modulus(GPa)		Poisson's ratio	
	E_{max}	E_{min}	β_{max}	β_{min}	G_{max}	G_{min}	v_{max}	v_{min}
CuO	230.75	48.58	8.66	1.954	79.03	20.98	9.64	0.105

The linear compressibility is defined as a relative change in length when a material is subjected to hydrostatic pressure. For most known materials, such as metals, alloys and ceramics, their linear compressibility are around 5TPa^{-1}, which means that each 1GPa increase in pressure will

cause a 5% reduction in length. Using the elastic constants calculated above, we can give a quantitatively description of the linear compressibility of CuO as a function of direction. As shown in **Figure IV.23**, their representation surfaces are constructed according to equation (IV.17), together with planar projections for some specific crystal planes. The 3D plot of linear compressibility of CuO in different directions show big differences, implying their obvious anisotropy in linear compressibility. It is also noted that the linear compressibility of CuO become negative in some directions in our present calculation. From the planar projections through (010) crystal planes of CuO in **Figure IV.23**, we can clearly see that the CuO possesses the maximum linear compressibility and the linear compressibility of CuO is unchanged on (010) crystal plane but its value is relatively small.

The representation surfaces of Young's modulus for CuO are illustrated in **Figure IV.24.** in 3D space. CuO possesses the most pronounced anisotropy because the shape of its representation surface is strongly curved and almost collapses in several directions as shown in **Figure IV.24.** The relative elastic anisotropy exhibited by Coop can be simply measured by the ratio of maximum to minimum orientation-dependent moduli. The maximum modulus occurs in the diagonal direction of crystal structure. A high Young's modulus in a specific direction usually corresponds to high strength of chemical bonds in that direction. The extreme moduli for CuO are determined numerically from the representation surface as 230.75. GPa / 48.58 GPa.

The surface contours of the shear modulus as well as the projections in different planes for CuO are shown in **Figure IV.25.** Because in one loading direction there are plenty of shear planes and different shear modulus, so we give the minimum and maximum shear modulus in every loading direction (**Figure IV.25**). One can see from **Figure IV.25.** that the minimum shear modulus for CuO are not equal in every crystalline direction, which shows the obvious anisotropy in shear modulus. In **Figure IV.25.**, the maximum shear modulus also shows significant anisotropy.

We have shown 3D plots of directional dependence of Poisson's ratio for monoclinic CuO in **Figure IV.26.** above. The 3D plot of Poisson's ratio exhibits high level of anisotropy. This is originating from the character of the monoclinic structure of CuO. The deviations from the spherical shape in the figures of these physical properties show the degree of anisotropy. In **Figure IV.23, IV.24, IV.25, and IV.26.** the blue curves represent the maximum values and the green curves represent the minimum values for the (β, E, G and ν).

Figure IV.23. Orientation dependence of linear compressibility for monoclinic CuO.
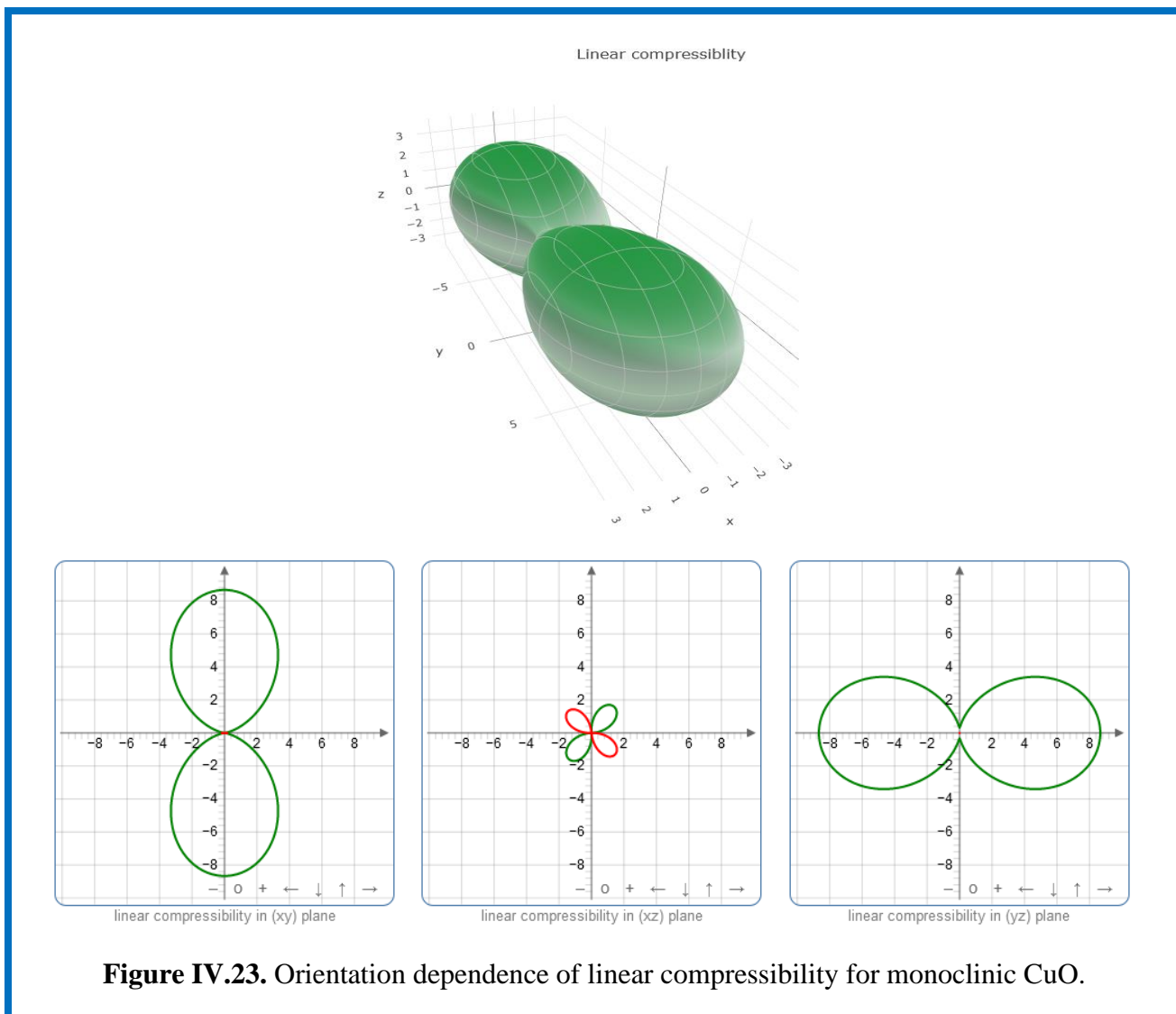
Figure IV.24. Directional dependence of Young's modulus *E*, and planar projections of monoclinic CuO , (The unites are in GPa).
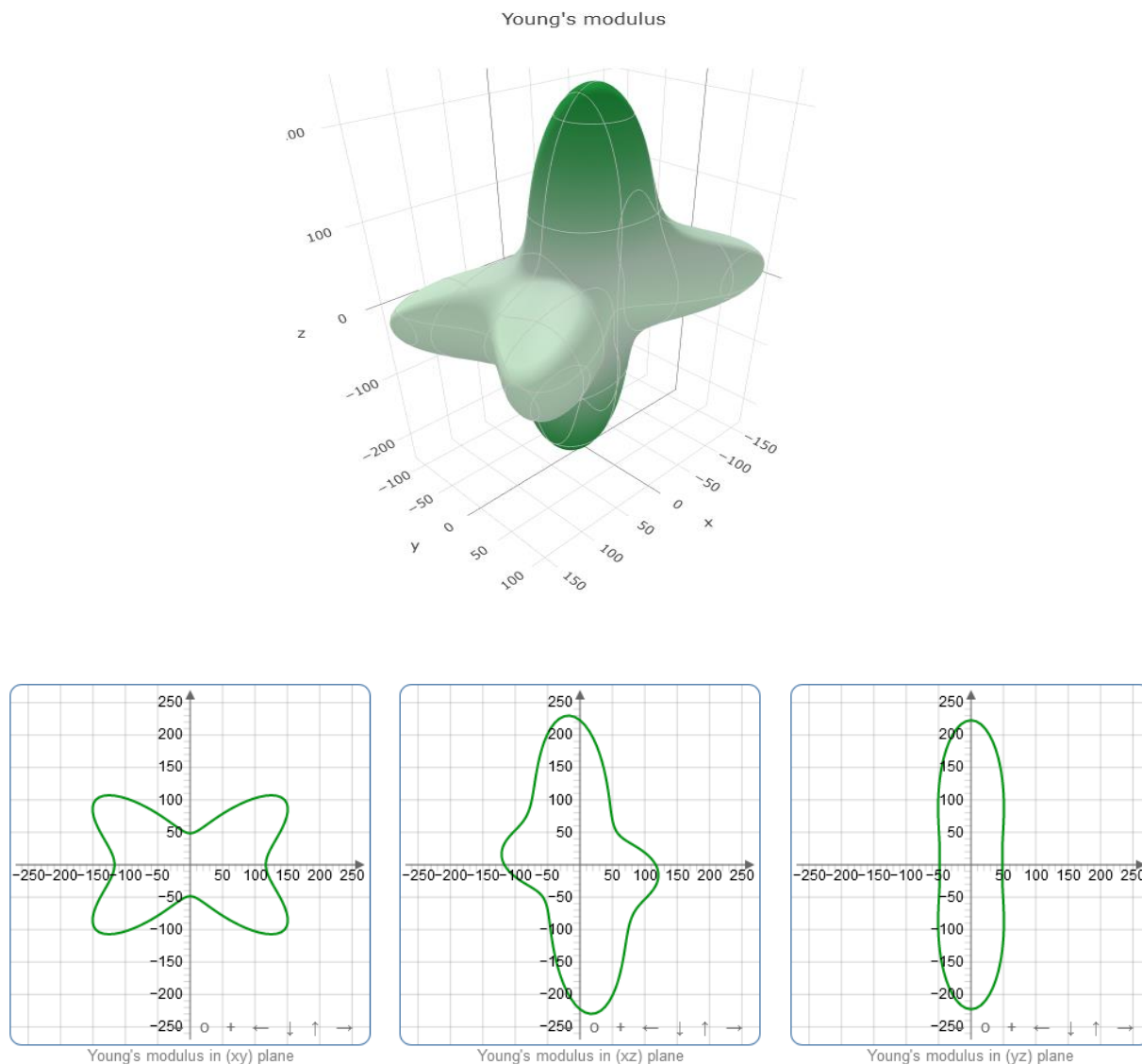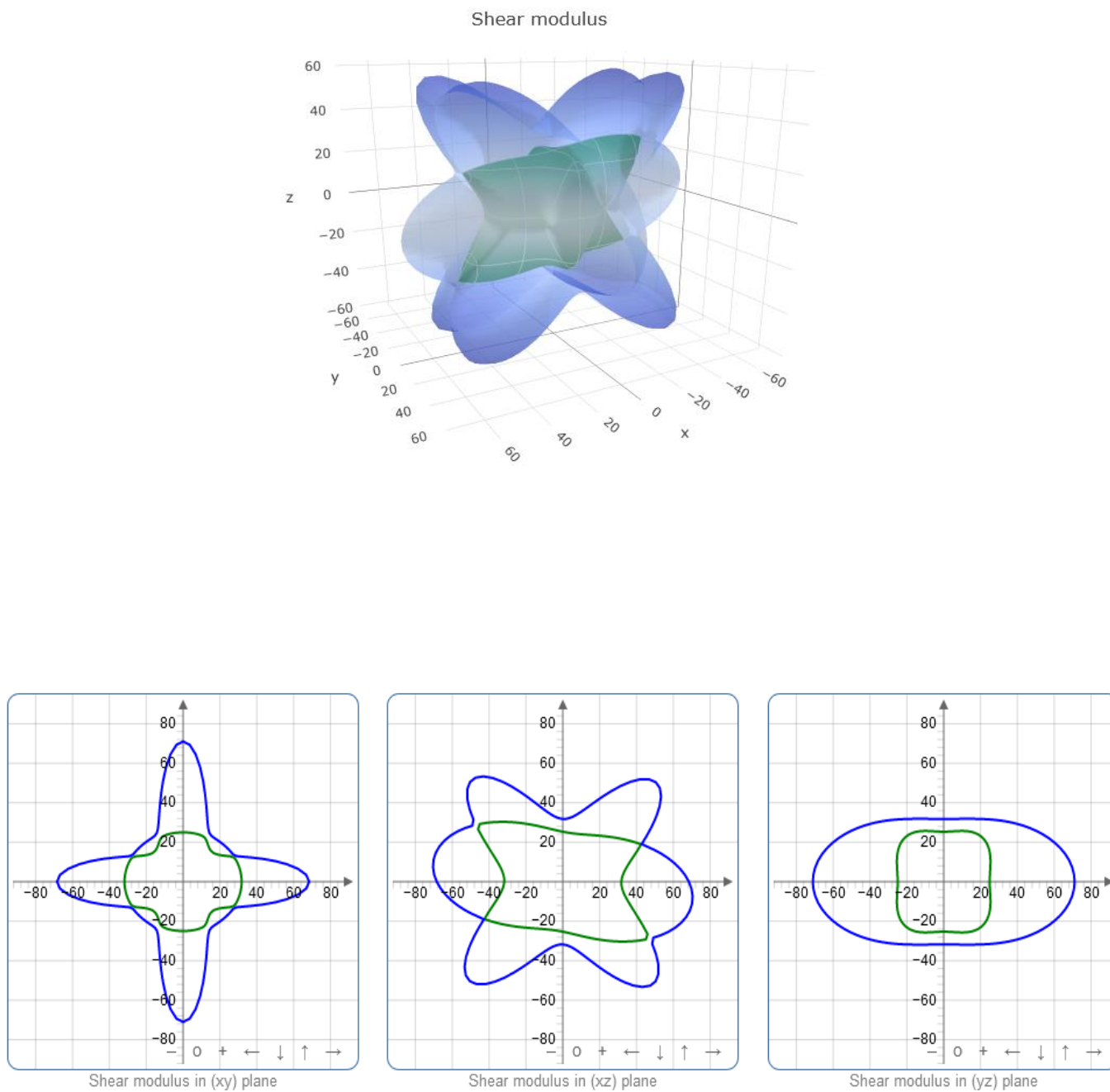
Shear modulus

Figure IV.25. Directional dependence of shear modulus G and planar projections of monoclinic CuO, (The unites are in GPa).
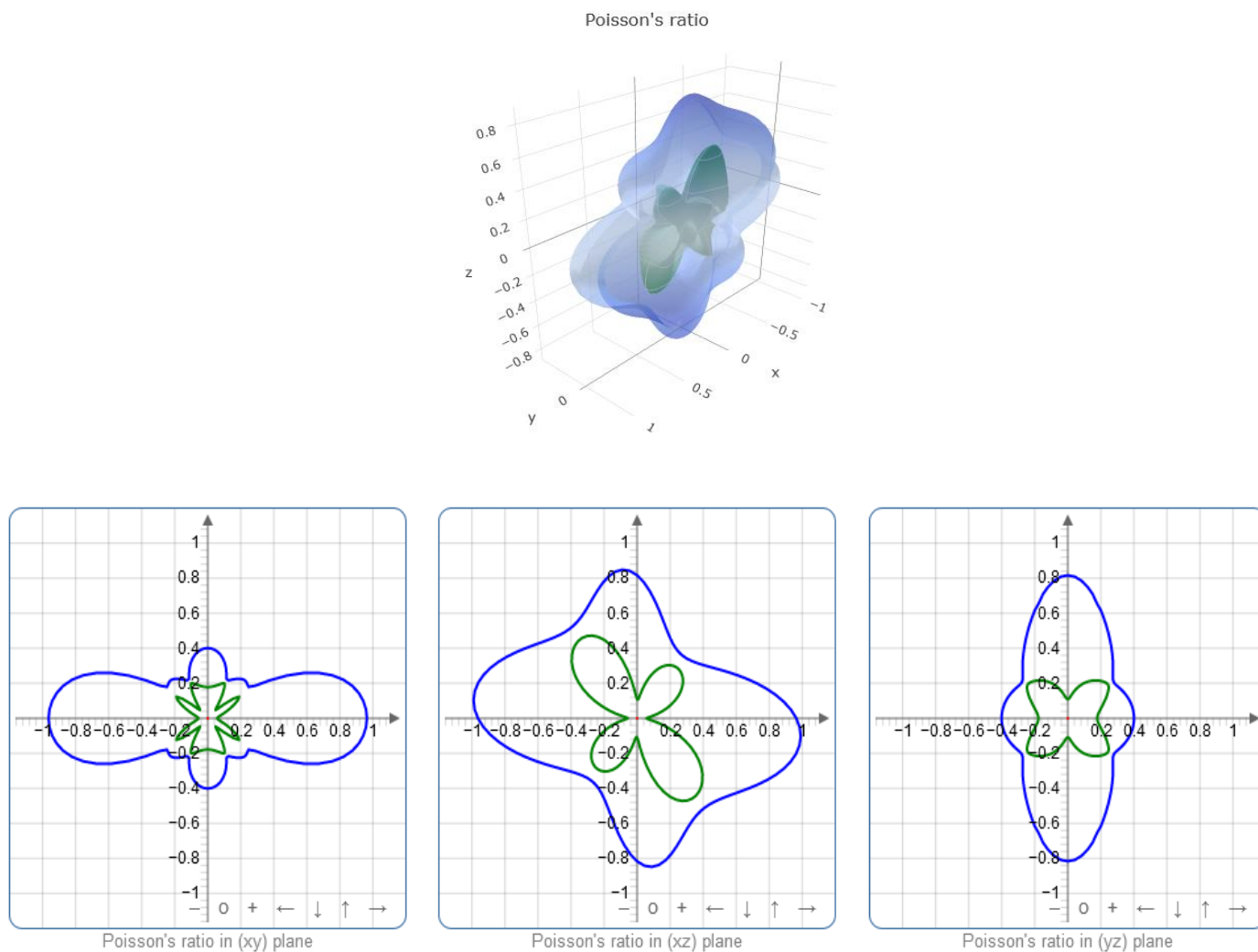
Figure IV.26. Directional dependence of Poisson's ratio ν, and planar projections of monoclinic CuO, (The unites are in GPa).

IV.3. Conclusion:

In summary, doping copper oxide (CuO) with sodium (Na), potassium (K), and lithium (Li) leads to distinct yet comparable effects on its structural, optical, electrical, and thermoelectric properties. Across all doping levels, the monoclinic phase is preserved, with sodium and potassium doping inducing peak shifts due to the ionic radius differences, while lithium doping shows a shift corresponding to larger ions, particularly at 6% doping. Sodium and potassium doping lead to lattice compression, while lithium causes a decrease in lattice volume at higher concentrations.

At 6% doping, sodium and potassium reduce crystallite size and enhance crystallinity, while lithium doping results in a decrease at higher concentrations. Strain is minimal in potassium-doped CuO, particularly at 6%, but increases with sodium and lithium doping at higher concentrations.

In optical properties, sodium and potassium doping result in higher transmittance, with potassium doping providing the best optical clarity at 6%. Lithium doping generally leads to a decrease in transmittance, while the band gap increases in sodium and potassium-doped films. Urbach energy is higher in all doped films, indicating increased disorder, with potassium showing the least disorder at 6%.

Electrical conductivity is enhanced with sodium and potassium doping, peaking at 6%, with sodium achieving a conductivity of 5.93×10^{-2} $(\Omega\ cm)^{-1}$ and potassium exhibiting the lowest resistivity. Lithium doping improves conductivity up to 6%, but further doping reduces it due to crystallization issues. Charge carrier density increases with doping, though excessive doping introduces defects that hinder mobility.

In thermoelectric properties, the Seebeck coefficient decreases in all doped films, with potassium doping showing the lowest value. The power factor is highest for lithium-doped CuO, followed by potassium and sodium doped films, indicating that lithium doping is more favorable for thermoelectric performance.

Regarding mechanical and elastic properties, CuO is mechanically stable based on elastic constants.

Reference

[1]   G. Yıldırım and E. Yücel, "Variation of the key structural, morphological, and optical properties of nanostructured copper (II) oxide (CuO) thin films using surfactant CAPB as a capping agent," *Journal of Materials Science: Materials in Electronics,* vol. 33, pp. 19057-19070, 2022.

[2]   A. R. West, *Solid state chemistry and its applications*: John Wiley & Sons, 2022.

[3]   A. R. West, "Basic solid state chemistry," *(No Title),* 1999.

[4]   D. W. Bruce and D. O'Hare, *Inorganic materials*: John Wiley & Sons, 1997.

[5]   L. Xu, G. Zheng, J. Miao, and F. Xian, "Dependence of structural and optical properties of sol–gel derived ZnO thin films on sol concentration," *Applied Surface Science,* vol. 258, pp. 7760-7765, 2012.

[6]   O. Diachenko, J. Kováč Jr, O. Dobrozhan, P. Novák, J. Kováč, J. Skriniarova, and A. Opanasyuk, "Structural and optical properties of CuO thin films synthesized using spray pyrolysis method," *Coatings,* vol. 11, p. 1392, 2021.

[7]   A. Sobhani, "Hydrothermal synthesis of CuMn2O4/CuO nanocomposite without capping agent and study its photocatalytic activity for elimination of dye pollution," *International Journal of Hydrogen Energy,* vol. 47, pp. 20138-20152, 2022.

[8]   D. Marrocchelli, S. R. Bishop, H. L. Tuller, and B. Yildiz, "Understanding chemical expansion in non-stoichiometric oxides: ceria and zirconia case studies," *Advanced Functional Materials,* vol. 22, pp. 1958-1965, 2012.

[9]   R. Sahraei, S. Shahriyar, M. Majles Ara, A. Daneshfar, and N. Shokri, "Preparation of nanocrystalline CdS thin films by a new chemical bath deposition route for application in solar cells as antireflection coatings," *Progress in Color, Colorants and Coatings,* vol. 3, pp. 82-90, 2011.

[10]   L. Singh and M. Hussain, "Effect of doping concentration on the optical properties of nanocrystalline Zn Doped PbS thin films deposited by CBD method," *Chalcogenide Lett,* vol. 17, pp. 583-591, 2020.

[11]   F. Bayansal, B. Şahin, M. Yüksel, N. Biyikli, H. Çetinkara, and H. Güder, "Influence of coumarin as an additive on CuO nanostructures prepared by successive ionic layer adsorption and reaction (SILAR) method," *Journal of alloys and compounds,* vol. 566, pp. 78-82, 2013.

[12]   A. S. Kumar, K. Perumal, and P. Thirunavukkarasu, "Structural and optical properties of chemically sprayed CuO thin films," *Optoelec. Advan. Mater.–Rapid Commun,* vol. 4, pp. 831-833, 2010.

[13]   M. R. Johan, M. S. M. Suan, N. L. Hawari, and H. A. Ching, "Annealing effects on the properties of copper oxide thin films prepared by chemical deposition," *International Journal of Electrochemical Science,* vol. 6, pp. 6094-6104, 2011.

[14]   D. Naveena, T. Logu, K. Sethuraman, and A. C. Bose, "Significant enhancement of photo-physicochemical properties of Yb doped copper oxide thin films for efficient solid-state solar cell," *Journal of Alloys and Compounds,* vol. 795, pp. 187-196, 2019.

[15]   M. E. Güldüren, D. İskenderoğlu, H. Güney, E. Gür, M. Acar, and S. M. Karadeniz, "Investigating the influence of Ni doping on the CuO thin films deposited via ultrasonic spray pyrolysis: Structural, optical and H2 gas sensing analyses," *International Journal of Hydrogen Energy,* vol. 48, pp. 828-839, 2023.

[16]   A. R. Ansari, A. H. Hammad, M. S. Abdel-wahab, M. Shariq, and M. Imran, "Structural, optical and photoluminescence investigations of nanocrystalline CuO thin films at different microwave powers," *Optical and Quantum Electronics,* vol. 52, p. 426, 2020.

[17]   İ. Y. Erdoğan and Ö. Güllü, "Optical and structural properties of CuO nanofilm: its diode application," *Journal of Alloys and Compounds,* vol. 492, pp. 378-383, 2010.

[18]   M. Nesa, M. Sharmin, K. S. Hossain, and A. Bhuiyan, "Structural, morphological, optical and electrical properties of spray deposited zinc doped copper oxide thin films," *Journal of Materials Science: Materials in Electronics,* vol. 28, pp. 12523-12534, 2017.

[19]   H. Touhami, K. Almi, S. Lakel, and M. Boumezrag, "Alkali Doping Nickel Oxide Thin Films Using Sol-Gel Spin Coated and Density Functional Theory: Structural and Physical Properties," *Russian Journal of Physical Chemistry B,* vol. 17, pp. 1057-1068, 2023.

[20]   N. Yoshida, T. Naito, and H. Fujishiro, "Thermoelectric Properties of Li-Doped CuO," *Japanese Journal of Applied Physics,* vol. 52, p. 031102, 2013.

[21]   M. E. Boumezrag, K. Almi, S. Lakel, and H. Touhami, "A Mini Review on Synthesis and Characterization of Copper Oxide Some Properties and Potential Applications," *Russian Journal of Physical Chemistry B,* vol. 18, pp. 873-894, 2024.

[22]   S. V. Faleev and F. Léonard, "Theory of enhancement of thermoelectric properties of materials with nanoinclusions," *Physical Review B,* vol. 77, p. 214304, 2008.

[23]   M.-J. Guan, P.-F. Qiu, Q.-F. Song, J. Yang, D.-D. Ren, X. Shi, and L.-D. Chen, "Improved electrical transport properties and optimized thermoelectric figure of merit in lithium-doped copper sulfides," *Rare Metals,* vol. 37, pp. 282-289, 2018.

[24]   R. Mulla and M. Rabinal, "CuO/Cu x S composites fabrication and their thermoelectric properties," *Materials for Renewable and Sustainable Energy,* vol. 10, pp. 1-7, 2021.

[25]   J. F. Nye, *Physical properties of crystals: their representation by tensors and matrices*: Oxford university press, 1985.

[26]   Z.-j. Wu, E.-j. Zhao, H.-p. Xiang, X.-f. Hao, X.-j. Liu, and J. Meng, "Crystal structures and elastic properties of superhard Ir N 2 and Ir N 3 from first principles," *Physical Review B—Condensed Matter and Materials Physics,* vol. 76, p. 054115, 2007.

[27]   W. Voigt, "Lehrbuch der Kristallphysik (Teubner, Leipzig, 1928)," *There is no corresponding record for this reference,* 1908.

[28]   A. Reuss and Z. Angnew, "A calculation of the bulk modulus of polycrystalline materials," *Math Meth,* vol. 9, p. 55, 1929.

[29]   R. Hill, "The elastic behaviour of a crystalline aggregate," *Proceedings of the Physical Society. Section A,* vol. 65, p. 349, 1952.

[30]   H. Charrouf, K. Almi, A. Lakel, F. Okbi, and S. Lakel, "Elastic and mechanical properties of Y 1–x Sc x N alloying system as a function of Sc content: First principles study," *Mechanics of Solids,* vol. 56, pp. 1028-1038, 2021.

[31]   S. Saada, S. Lakel, and K. Almi, "Optical, electronic and elastic properties of ScAlN alloys in WZ and ZB phases: Prospective material for optoelectronics and solar cell applications," *Superlattices and Microstructures,* vol. 109, pp. 915-926, 2017.

[32]   M. Hadi, "New ternary nanolaminated carbide Mo2Ga2C: A first-principles comparison with the MAX phase counterpart Mo2GaC," *Computational Materials Science,* vol. 117, pp. 422-427, 2016.

[33]   S. I. Ranganathan and M. Ostoja-Starzewski, "Universal elastic anisotropy index," *Physical review letters,* vol. 101, p. 055504, 2008.

[34]   H. Fu, X. Chen, J. Fu, and Y. Ma, "Orientation dependence of elastic constants and electronic properties of rhenium nitrides first-principle calculations," *Journal of Materials Science,* vol. 48, pp. 4284-4296, 2013.

[35]   Y. Ding and B. Xiao, "Anisotropic elasticity, sound velocity and thermal conductivity

of TiO2 polymorphs from first principles calculations," *Computational materials science,* vol. 82, pp. 202-218, 2014.

[36]   J. Ning, X. Zhang, J. Qin, S. Zhang, M. Ma, and R. Liu, "Distinct electron density topologies and elastic properties of two similar omega phases: ω-Zr and Zr2Al," *Journal of Alloys and Compounds,* vol. 660, pp. 316-323, 2016.

[37]   A. Marmier, Z. A. Lethbridge, R. I. Walton, C. W. Smith, S. C. Parker, and K. E. Evans, "ElAM: A computer program for the analysis and representation of anisotropic elastic properties," *Computer Physics Communications,* vol. 181, pp. 2102-2115, 2010.

[38]   T. Ting, "On Anisotropic Elastic Materials for which Young's Modulus E (n) is Independent of n or the Shear Modulus G (n, m) is Independent of n and m," *Journal of Elasticity,* vol. 81, pp. 271-292, 2005.

Conclusion

Conclusion

The development of CuO thin films on glass substrates was achieved using the spin-coating technique, utilizing copper acetate monohydrate (Cu $(CH_3COO)_2 \cdot H_2O$) as the precursor and monoethanolamine (MEA) as the stabilizing agent. Optimal experimental conditions, informed by prior research, were refined by adjusting parameters such as solvent-to-metal ion molar ratio, stirring, aging, substrate preparation, spinning speed, preheating, and annealing to ensure ideal crystallization. The choice of precursor materials was found to significantly impact film crystallinity and overall performance.

This thesis also focused on producing pure, alkali-doped, and alkali-co-doped NiO thin films with doping concentrations of 3%, 6%, 9%, and 12% using the sol-gel method. Characterization methods included X-ray diffraction (XRD), UV-visible (UV-Vis) spectrophotometry, and the four-point probe technique.

The primary findings are summarized as follows:

- XRD Analysis: Results showed polycrystalline structure with a strong peak at (11-1) and no impurities, indicating film purity. Peak intensity was affected by deposition conditions.

- Impact of Solvent and Temperature: Increasing the carbon chain length of alcoholic solvents led to a decrease in film quality, with ethanol providing the best properties. Higher temperatures improved film crystallinity, reaching an optimum at 500°C, and nine layers yielded the best results.

Li-Doped NiO

- Crystallite size in Li-doped NiO films initially decreased then increased with higher Li concentrations, ranging from 24.53 to 26.20 nm. Higher Li concentrations reduced transmittance, while the bandgap decreased to 1.37 eV at 12% Li doping but increased to 2.42 eV for 6% Li.

Na-Doped CuO:

- The average crystallite size for pure CuO, initially 31.56 nm, decreased with Na doping, reaching 24.53, 13.67, 21.63, 17.91, and 20.68 nm at 3%, 6%, 9%, and 12% Na concentrations.
- Na-doped CuO samples exhibited lower transmittance compared to undoped and Li-doped CuO at similar concentrations. The bandgap decreased with higher Na concentration, from 1.85 eV to 1.39 eV.

Conclusion

- Resistivity declined as Na concentration increased, reaching a minimum at the highest doping level.

K-Doped NiO:

- At low K concentrations, the (111) peak was the preferred orientation, shifting to the (200) peak at higher concentrations. Lattice parameter increased with K doping, while dislocation density dropped from 26.20 x10^{-4} to 21.61 10 $^{-4}$.
- The highest transmittance among K-doped samples was observed at 6% K. The bandgap for undoped CuO (1.42 eV) increased with 3% K doping (1.78 eV), slightly decreased at 6% K doping (1.54 eV), and then rose to 1.99 eV and 2.31 eV at 9% and 12% K doping, respectively.

- K doping initially enhanced electrical conductivity, peaking at 6% but decreasing thereafter. Resistivity declined sharply to 16.9 Ω cm at 6% Na, then slightly increased at 9% and 12%.

Doping also improved the power factor (PF), with Li-doped CuO reaching a maximum PF of (9.776×10^{-10} W m^{-1} K^{-2}). Compared to an initial value of (3.186×10^{-11} W m^{-1} K^{-2})

In conclusion, this class of materials shows significant potential for enhancement, as thermoelectric properties can be precisely tailored.

Elastic Constants of Single Crystal:

- For monoclinic CuO, there are 13 independent elastic constants (C11, C22, C33, etc.) calculated using the stress-strain approach.
- The mechanical stability of CuO is confirmed, with elastic constants satisfying stability criteria.
- CuO shows higher resistance to deformation along the [001] direction compared to [100] and [010].
- Smaller values for C44, C55, and C66 indicate stronger resistance to compressional deformations than shear deformations.
- Negative values were observed for C25 and C46.

Polycrystalline Elastic Constants:

- The Voigt, Reuss, and Hill methods were used to calculate the bulk modulus (B), shear modulus (G), Young's modulus (E), and Poisson's ratio (v) for CuO.
- CuO has a B/G ratio of 1.39, indicating ductile behavior, but the Poisson's ratio of 0.365 suggests a brittle nature.
- The Debye temperature was estimated at 398 K, providing insights into the material's vibrational properties.

Anisotropy of Elastic Moduli:

Conclusion

- CuO exhibits strong anisotropy, meaning its mechanical properties vary with direction due to different atomic densities in crystal directions.
- Young's modulus, shear modulus, and Poisson's ratio show significant directional dependence, as seen in 3D plots.
- CuO's linear compressibility and moduli vary across directions, highlighting its anisotropic behavior.
- The maximum and minimum values of Young's modulus, shear modulus, and Poisson's ratio demonstrate the degree of anisotropy in CuO.

Abstract

Study of mechanical and physical properties of thermoelectric materials for energy conversion.

This study investigates the fabrication and characterization of CuO thin films on glass substrates using the spin coating technique. Key experimental parameters, including solvent type, annealing temperature, film thickness, and alkali metal (Li, Na, K) doping at concentrations of 3%, 6%, 9%, and 12%, were optimized to enhance the structural, optical, electrical, and thermoelectric properties of the films. X-ray diffraction (XRD) analysis confirmed the polycrystalline monoclinic structure of CuO, with variations in crystalline peaks and lattice structure influenced by different solvents. Isopropanol, 1-propanol, ethanol, and 2-methoxyethanol promoted growth along the c-axis (002 plane), whereas pentanol and methanol favored (111) plane growth. Isopropanol-based films exhibited the largest crystallite size and improved optical transmittance, while crystallinity improved with annealing up to 500°C. Optimized film deposition with nine layers resulted in an approximate thickness of 400 nm, leading to smaller crystallites with higher strain. Other hand, across all doping levels, the monoclinic phase was preserved. Sodium and potassium doping led to lattice compression, whereas lithium reduced lattice volume at higher concentrations. Optically, sodium and potassium doping enhanced transmittance, with potassium providing the best optical clarity at 6%, while lithium reduced transmittance and increased the band gap. Urbach energy increased in all doped films, indicating higher disorder, with potassium-doped films showing the least disorder at 6%. For the electrical properties, electrical conductivity was improved with sodium and potassium doping, peaking at 6%, with sodium achieving a conductivity of 5.93×10^{-2} (Ω cm)$^{-1}$ and potassium exhibiting the lowest resistivity. Lithium doping enhanced conductivity up to 6%, but further doping led to a decline. The best thermoelectric performance was observed in Li-doped CuO, which exhibited the highest power factor (9.776×10^{-10} W. m^{-1}.K^{-2}). Additionally, the study of mechanical and elastic properties confirmed CuO's strong anisotropy and mechanical stability. These findings highlight the potential of doped CuO thin films for applications in optoelectronics, thermoelectric, and flexible electronics, demonstrating the ability to fine-tune their properties through controlled doping and processing techniques.

الملخص

دراسة الخواص الميكانيكية والفيزيائية للمواد الحرارية الكهربائية لتحويل الطاقة

تتناول هذه الدراسة تصنيع وتوصيف أغشية أكسيد النحاس (CuO) الرقيقة على ركائز زجاجية باستخدام تقنية الطلاء بالدوران. تم تحسين المعايير التجريبية الرئيسية، بما في ذلك نوع المذيب، ودرجة حرارة التلدين، وسمك الفيلم، وتشويب المعادن القلوية (Li, Na, K) بتركيزات 3%، 6%، 9%، و12%، لتعزيز الخصائص التركيبية والبصرية والكهربائية والحرارية لهذه الأغشية. أكدت تحليلات حيود الأشعة السينية (XRD) أن البنية البلورية لأكسيد النحاس متعددة البلورات وأحادية الميل، مع تغيرات في القمم البلورية وبنية الشبكة البلورية تحت تأثير أنواع المذيبات المختلفة. عززت المذيبات مثل الأيزوبروبانول، 1-بروبانول، الإيثانول، و2-ميثوكسي إيثانول النمو على طول المحور (002)، بينما فضل البنتانول والميثانول النمو على طول المحور (111). أظهرت الأفلام المحضرة باستخدام الأيزوبروبانول أكبر حجم بلوري ونفاذية بصرية محسنة، بينما تحسنت البنية البلورية مع التلدين حتى C°500. أدى ترسيب تسع طبقات إلى الحصول على فيلم بسماكة تقارب 400 نانومتر، مما أدى إلى تكوين بلورات أصغر مع إجهاد أعلى. من جهة أخرى حافظت جميع مستويات التشويب على الطور احادي الميل، وأدى التشويب بالصوديوم والبوتاسيوم إلى ضغط الشبكة البلورية، في حين تسبب الليثيوم في تقليل حجم الشبكة البلورية عند التركيزات الأعلى. بصريًا، أدى التشويب بالصوديوم والبوتاسيوم إلى زيادة النفاذية، مع تحقيق البوتاسيوم لأفضل وضوح بصري عند 6%، بينما أدى الليثيوم إلى تقليل النفاذية وزيادة فجوة الطاقة. ارتفعت طاقة أورباخ في جميع الأفلام المشوبة، مما يشير إلى زيادة الاضطراب، حيث أظهر التشويب بالبوتاسيوم أقل اضطراب عند 6.% بالنسبة للخصائص الكهربائية تحسنت التوصيلية الكهربائية مع التشويب بالصوديوم والبوتاسيوم، وبلغت ذروتها عند 6%، حيث حقق الصوديوم أعلى قيمة للتوصيلية بلغت 5.93×10^{-2} (Ω cm)$^{-1}$ بينما سجل البوتاسيوم أقل مقاومة. حسن التشويب بالليثيوم التوصيلية حتى 6%، لكن التشويب الإضافي أدى إلى انخفاضها. أظهر أكسيد النحاس المشوب بالليثيوم أفضل أداء حراري، حيث سجل أعلى معامل قدرة 9.776×10^{-10} W. m^{-1}.K^{-2}. بالإضافة إلى ذلك، أكدت دراسة الخصائص الميكانيكية والمرنة وجود تباين قوي في خصائص أكسيد النحاس، مع ثوابت مرونة تدعم استقراره الميكانيكي. تسلط هذه النتائج الضوء على الإمكانات الكبيرة لأغشية أكسيد النحاس المشوبة في تطبيقات الإلكترونيات الضوئية، والحرارية، والإلكترونيات المرنة، مما يثبت إمكانية ضبط خصائصها من خلال التحكم في عملية التشويب والتصنيع.

الكلمات المفتاحية: أكسيد النحاس المطعم بالذرات القلوية، الطلاء بالتدوير، المذيب، الخصائص البنيوية، الخصائص الكهرو حرارية

.